APPLIED COMPUTATIONAL ELECTROMAGNETICS SOCIETY JOURNAL

April 2016
Vol. 31 No. 4
ISSN 1054-4887

The ACES Journal is abstracted in INSPEC, in Engineering Index, DTIC, Science Citation Index Expanded, the Research Alert, and to Current Contents/Engineering, Computing & Technology.

The illustrations on the front cover have been obtained from the research groups at the Department of Electrical Engineering, The University of Mississippi.

EMERITUS EDITORIAL ASSISTANTS

APRIL 2016 REVIEWERS

THE APPLIED COMPUTATIONAL ELECTROMAGNETICS SOCIETY

JOURNAL

Vol. 31 No. 4 April 2016

TABLE OF CONTENTS

A Multiscale Algorithm for Eddy-Current Nondestructive Evaluation Based On Volume-Integral Equations: Initial Concepts
R. Kim Murphy, Harold A. Sabbagh, and Elias H. Sabbagh 333

Wire Fault Diagnosis Based on Time-Domain Reflectometry and Backtracking Search Optimization Algorithm
Hamza Boudjefdjouf, Houssem R. E. H. Bouchekara, Francesco de Paulis, Mostafa K. Smail, Antonio Orlandi, and Rabia Mehasni 340

Compact UWB Antenna with Triple Band-Notches Using C-Shaped and S-Shaped Structures
Zhenyang Ma, Feifei Dong, Zheng Han, Shaocheng Han, and Qiannan Xue 348

FR4-Only Microstrip Reflectarray Antennas for 5.8 GHz Dual-Polarized Wireless Bridges
Babak Honarbakhsh 355

Optimal Design of PCS Ceramic Microwave Filters using the Differential Evolution Algorithm
Theodoros I. Kosmanis, Ioannis T. Rekanos, and Stelios P. Tsitsos 361

An Accurate High-Speed Method for Mutual Inductance Calculations of Coplanar Disk Coils Using Generalized Hypergeometric Functions
Yao Luo 366

A New High Performance Hibiscus Petal Pattern Monopole Antenna for UWB Applications
Md. Zulfiker Mahmud, Salehin Kibria, Md. Samsuzzaman, Norbahiah Misran, and Mohammad T. Islam 373

A Planar Monopole Antenna with Switchable Dual Band-Notched UWB/Dual-Band WLAN Applications
Mohammad M. Fakharian, Pejman Rezaei, and Vahid Sharbati 381

Ultra-Wideband Planar Antenna with Notched Bands at 3.5/5.5 GHz
Rezaul Azim and Mohammad T. Islam 388

Design of a Compact Wideband Balun Bandpass Filter with High Selectivity
Hui Ma, Jiayuan Lu, Yuran Li, Lin Liu, and Jianpeng Wang 396

Novel Compact Branch-Line Coupler Using Non-Uniform Folded Transmission Line and Shunt Step Impedance Stub With Harmonics Suppressions
Shalaleh Nouri, Javad Nourinia, Nooshin Valizade, Bahman Mohammadi, and Arash Valizade 401

CPW Dependent Loss Analysis of Capacitive Shunt RF MEMS Switch
Santhanam Suganthi, Karuppusamy Murugesan, and Singaravelu Raghavan 410

Dual Band and Dual Mode Microstrip Antenna for Body Centric Wireless Communication
Seiran Khaledian and Zahra Atlasbaf 417

A Novel Coupling Structure for Changing the Coupling Nature Between TE01delta -mode Dielectric Resonator and Combline Resonator
Bin Yu, Bao-Fu Jia, and Zhao-Jun Zhu 423

The Substrate Integrated Waveguide T-junction Power Divider with Arbitrary Power Dividing Ratio
Asrin Piroutiniya and Pejman Mohammadi 428

Small Wearable Meta Materials Antennas for Medical Systems
Albert Sabban 434

A Hybrid Explicit-Implicit Scheme for Spectral-Element Time-Domain Analysis of Multiscale Simulation
Hao Xu, Dazhi Z. Ding, and Rushan Chen 444

Broadband CRLH Beam Scanning Leaky-Wave Antenna Designed on Dual-Layer SIW
Mohsen Niayesh and Zahra Atlasbaf 450

Evaluation of E-Field Distribution and Human Exposure for a LTE Femtocell in an Office
Hsing-Yi Chen and Shu-Huan Wen 455

Light-Weight Wide-Band Metal-Only Reflectarray Antennas
Babak Honarbakhsh 468

A Multiscale Algorithm for Eddy-Current Nondestructive Evaluation Based On Volume-Integral Equations: Initial Concepts

R. Kim Murphy, Harold A. Sabbagh, and Elias H. Sabbagh

Victor Technologies, LLC
PO Box 7706, Bloomington, IN 47407-7706, USA
rkmurphy@att.net, has@sabbagh.com, ehs@sabbagh.com

Abstract **−** The use of coupled integral equations and anomalous currents allows us to efficiently remove 'background effects' in either forward or inverse modeling. This is especially true when computing the change in impedance due to a small flaw in the presence of a larger background anomaly. It is more accurate than simply computing the response with and without the flaw and then subtracting the two nearly equal values to obtain the small difference due to the flaw. In this paper, we compute the change in impedance of a probe due to a flaw in the presence of a much larger background anomaly, when the probe, which consists of a coil with a ferrite core, lies within the host region, and then apply the model and algorithm to the problem of inspecting a bolt hole in a plate or other layered medium with a 'SplitD' eddy-current probe.

Index Terms **−** Aircraft structures, computational, electromagnetics, eddy-current nondestructive evaluation, volume-integral equations.

I. INTRODUCTION

In [1] we developed a systematic procedure for analyzing problems in eddy-current nondestructive evaluation (NDE) by means of volume-integral equations (method of moments), and applied it to problems in aerospace, nuclear power, materials characterization, and other areas. One problem of interest to aerospace, and described in [1], is computing the response of a small crack located adjacent to a bolt hole. This requires the solution of a 'multiscale problem', with the bolt hole being the larger scale and the crack a much smaller scale. A method for solving this problem was developed using coupled integral equations, one for the anomalous currents within the bolt hole and the other for the anomalous currents within the crack. The algorithm was validated using measured data acquired by a 'conventional' surface coil scanned past the bolt hole and crack. By 'conventional' we mean that the coil was circular, with its axis normal to the surface of the host material, and containing no ferritic cores. The response of such coils can be computed analytically, as shown in [1]. That problem was chosen because of its relative simplicity in acquiring the data.

In this paper, we attack the more complicated, but common, problem in which inspections are performed by a complex probe positioned within the bolt hole. The probes typically used for inspections are complex, often of the 'SplitD' variety, with a transmit coil exciting the system, and two receive coils picking up the response. Furthermore, none of the three coils is circular, and they all enclose two ferritic cores, split longitudinally to give the 'SplitD' characteristic. See [1] for a description and application of these probes. This model then calls for three coupled integral equations, two as above, and the third for the probe.

We develop the 'probe-in-host' algorithm in Section II, and apply it to the SplitD probe problem in Section III. In order to keep the paper of reasonable length, we invite the reader to peruse [1] in order to get the background for understanding the terminology and concepts that are used throughout the paper. The development of the circuit response for the probe-in-host algorithm follows Chapter 5, 'Computing Network Immitance Functions from Field Calculations' of [1]. Also for length considerations, we have opted to discuss only the theoretical underpinnings of the algorithm. We will give a thorough presentation of **VIC-3D®** model results, as well as experimental validation in a second paper.

II. THE 'PROBE-IN-HOST' ALGORITHM

This algorithm is an extension of our multiscale background-removal algorithm. Both algorithms were developed to compute the change in impedance of a probe due to a flaw in a sample which also contains a much larger background anomaly. The background-removal algorithm addresses problems in which the flaw and background lie in one planar region, referred to as the 'host' region, and the probe, consisting of coil elements only, lies in a separate planar region. This permits the modeling of a coil scanned across the surface of a plate containing a bolt hole (the background) with an adjacent flaw.

The problem of modeling a probe containing a

Submitted On: October 4, 2015
Accepted On: February 25, 2016

ferrite core, and positioned within a bolt hole is addressed by the probe-in-host algorithm, which solves the more complex problem of a ferrite-cored probe that lies within the host region. The problem is illustrated in Fig. 1, but the algorithm is more general than shown, since the flaw may lie wholly or partially inside or outside the background, and this is true for the probe as well.

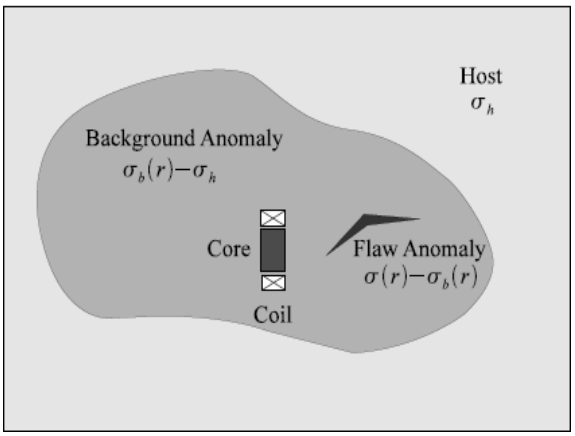

Fig. 1. The 'probe-in-background' problem. The conductivity within the host region is $\sigma(\mathbf{r})$. With background only (no flaw or probe) the conductivity is $\sigma_b(\mathbf{r})$. Outside the flaw (and probe), $\sigma(\mathbf{r}) = \sigma_b(\mathbf{r})$. Outside the background $\sigma(\mathbf{r}) = \sigma_b(\mathbf{r}) = \sigma_h$.

The conductivity at all points within the host region is given by $\sigma(\mathbf{r})$. For the corresponding unflawed problem with background and probe only, the function is $\sigma_u(\mathbf{r})$. Thus $\sigma(\mathbf{r})$ agrees with $\sigma_u(\mathbf{r})$ at all points outside the flaw. For the corresponding unflawed problem with background only (i.e., probe removed), the function is $\sigma_b(\mathbf{r})$. Thus, $\sigma_u(\mathbf{r})$ agrees with $\sigma_b(\mathbf{r})$ at all points outside probe. The conductivity of the host region has a uniform value of σ_h outside the background and flaw, where $\sigma(\mathbf{r}) = \sigma_u(\mathbf{r}) = \sigma_b(\mathbf{r}) = \sigma_h$. Finally, the permeabilities $\mu(\mathbf{r})$, $\mu_u(\mathbf{r})$, $\mu_b(\mathbf{r})$ and μ_h are defined analogously, and hence obey analogous relations.

Perhaps it would be more clear to think of building up to $\sigma(\mathbf{r})$ and $\mu(\mathbf{r})$ as follows: Start with the uniform conductivity and permeability, σ_h and μ_h of the host. Add the background to get $\sigma_b(\mathbf{r})$ and $\mu_b(\mathbf{r})$. Add the probe to get $\sigma_u(\mathbf{r})$ and $\mu_u(\mathbf{r})$. Finally, add the flaw to get $\sigma(\mathbf{r})$ and $\mu(\mathbf{r})$.

The anomalous current and magnetization, $\mathbf{J}_a(\mathbf{r})$ and $\mathbf{M}_a(\mathbf{r})$ respectively, satisfy the equations:

$$\mathbf{J}_a(\mathbf{r}) = (\sigma(\mathbf{r}) - \sigma_h)\mathbf{E}(\mathbf{r}), \tag{1}$$

$$\mathbf{M}_a(\mathbf{r}) = \left(\frac{1}{\mu_h} - \frac{1}{\mu(\mathbf{r})}\right)\mathbf{B}(\mathbf{r}), \tag{2}$$

where

$$\mathbf{E}(\mathbf{r}) = \mathbf{E}^{(i)}(\mathbf{r}) + \mathbf{E}(\mathbf{r})[J_a] + \mathbf{E}(\mathbf{r})[M_a], \tag{3}$$

$$\mathbf{B}(\mathbf{r}) = \mathbf{B}^{(i)}(\mathbf{r}) + \mathbf{B}(\mathbf{r})[J_a] + \mathbf{B}(\mathbf{r})[M_a], \tag{4}$$

and $\mathbf{E}^{(i)}(\mathbf{r})$ and $\mathbf{B}^{(i)}(\mathbf{r})$ are the incident electric and magnetic fields of the probe coil. Functionals, such as $\mathbf{E}(\mathbf{r})[\cdot]$ and $\mathbf{B}(\mathbf{r})[\cdot]$, are volume integrals with Green's function kernels.

We rewrite the right hand side of (1) and (2) as follows:

$$\begin{aligned}\mathbf{J}_a(\mathbf{r}) = {} & (\sigma_b(\mathbf{r}) - \sigma_h)\mathbf{E}(\mathbf{r}) \\ & + \big(\sigma_u(\mathbf{r}) - \sigma_b(\mathbf{r})\big)\mathbf{E}(\mathbf{r}) \\ & + \big(\sigma(\mathbf{r}) - \sigma_u(\mathbf{r})\big)\mathbf{E}(\mathbf{r}),\end{aligned} \tag{5}$$

$$\begin{aligned}\mathbf{M}_a(\mathbf{r}) = {} & \left(\frac{1}{\mu_h} - \frac{1}{\mu_b(\mathbf{r})}\right)\mathbf{B}(\mathbf{r}) \\ & + \left(\frac{1}{\mu_b(\mathbf{r})} - \frac{1}{\mu_u(\mathbf{r})}\right)\mathbf{B}(\mathbf{r}) \\ & + \left(\frac{1}{\mu_u(\mathbf{r})} - \frac{1}{\mu(\mathbf{r})}\right)\mathbf{B}(\mathbf{r}).\end{aligned} \tag{6}$$

Now notice that if we find solutions $\mathbf{J}_b(\mathbf{r})$, $\mathbf{J}_c(\mathbf{r})$, $\mathbf{J}_f(\mathbf{r})$, $\mathbf{M}_b(\mathbf{r})$, $\mathbf{M}_c(\mathbf{r})$, $\mathbf{M}_f(\mathbf{r})$ to the coupled equations,

$$\mathbf{J}_b(\mathbf{r}) = (\sigma_b(\mathbf{r}) - \sigma_h)\mathbf{E}(\mathbf{r}), \tag{7}$$

$$\mathbf{J}_c(\mathbf{r}) = \big(\sigma_u(\mathbf{r}) - \sigma_b(\mathbf{r})\big)\mathbf{E}(\mathbf{r}), \tag{8}$$

$$\mathbf{J}_f(\mathbf{r}) = \big(\sigma(\mathbf{r}) - \sigma_u(\mathbf{r})\big)\mathbf{E}(\mathbf{r}), \tag{9}$$

$$\mathbf{M}_b(\mathbf{r}) = \left(\frac{1}{\mu_h} - \frac{1}{\mu_b(\mathbf{r})}\right)\mathbf{B}(\mathbf{r}), \tag{10}$$

$$\mathbf{M}_c(\mathbf{r}) = \left(\frac{1}{\mu_b(\mathbf{r})} - \frac{1}{\mu_u(\mathbf{r})}\right)\mathbf{B}(\mathbf{r}), \tag{11}$$

$$\mathbf{M}_f(\mathbf{r}) = \left(\frac{1}{\mu_u(\mathbf{r})} - \frac{1}{\mu(\mathbf{r})}\right)\mathbf{B}(\mathbf{r}), \tag{12}$$

where

$$\begin{aligned}\mathbf{E}(\mathbf{r}) = {} & \mathbf{E}^{(i)}(\mathbf{r}) + \mathbf{E}(\mathbf{r})[J_b] + \mathbf{E}(\mathbf{r})[J_c] \\ & + \mathbf{E}(\mathbf{r})\big[J_f\big] + \mathbf{E}(\mathbf{r})[M_b] + \mathbf{E}(\mathbf{r})[M_c] \\ & + \mathbf{E}(\mathbf{r})\big[M_f\big],\end{aligned} \tag{13}$$

$$\begin{aligned}\mathbf{B}(\mathbf{r}) = {} & \mathbf{B}^{(i)}(\mathbf{r}) + \mathbf{B}(\mathbf{r})[J_b] + \mathbf{B}(\mathbf{r})[J_c] \\ & + \mathbf{B}(\mathbf{r})\big[J_f\big] + \mathbf{B}(\mathbf{r})[M_b] + \mathbf{B}(\mathbf{r})[M_c] \\ & + \mathbf{B}(\mathbf{r})\big[M_f\big],\end{aligned} \tag{14}$$

then the sums $\mathbf{J}_a(\mathbf{r}) = \mathbf{J}_b(\mathbf{r}) + \mathbf{J}_c(\mathbf{r}) + \mathbf{J}_f(\mathbf{r})$ and $\mathbf{M}_a(\mathbf{r}) = \mathbf{M}_b(\mathbf{r}) + \mathbf{M}_c(\mathbf{r}) + \mathbf{M}_f(\mathbf{r})$ satisfy (1) and (2).

Noting from (7-12) that $\mathbf{J}_b(\mathbf{r})$ and $\mathbf{M}_b(\mathbf{r})$ are zero outside the background, $\mathbf{J}_c(\mathbf{r})$ and $\mathbf{M}_c(\mathbf{r})$ are zero outside the probe core, and $\mathbf{J}_f(\mathbf{r})$ and $\mathbf{M}_f(\mathbf{r})$ are zero outside the flaw, we identify these anomalous currents and magnetizations as those of the background, probe core and flaw, respectively.

Since we will be solving for $\mathbf{J}_c(\mathbf{r})$ and $\mathbf{M}_c(\mathbf{r})$ only within the space occupied by the probe core, and the flaw does not intrude into that space, we can replace $\sigma_u(\mathbf{r})$ and $\mu_u(\mathbf{r})$ by $\sigma(\mathbf{r})$ and $\mu(\mathbf{r})$ in (8) and (11), respectively. Similarly, since we will be solving for $\mathbf{J}_f(\mathbf{r})$ and $\mathbf{M}_f(\mathbf{r})$ only within the space occupied by the flaw, and the probe

does not intrude into that space, we can replace $\sigma_u(\mathbf{r})$ and $\mu_u(\mathbf{r})$ by $\sigma_b(\mathbf{r})$ and $\mu_b(\mathbf{r})$ in (9) and (12), respectively.

With these substitutions, and in preparation for discretization, we reorder (7-12) as well as their unknowns, and rewrite them in the form:

$$\begin{aligned}\mathbf{E}^{(i)}(\mathbf{r}) = {} & \frac{1}{\sigma_b(\mathbf{r})-\sigma_h}\mathbf{J}_b(\mathbf{r}) - \mathbf{E}(\mathbf{r})[J_b] \\ & - \mathbf{E}(\mathbf{r})[M_b] - \mathbf{E}(\mathbf{r})[J_c] \\ & - \mathbf{E}(\mathbf{r})[M_c] - \mathbf{E}(\mathbf{r})\big[J_f\big] \\ & - \mathbf{E}(\mathbf{r})\big[M_f\big], \end{aligned} \tag{15}$$

$$\begin{aligned}\mathbf{B}^{(i)}(\mathbf{r}) = {} & -\mathbf{B}(\mathbf{r})[J_b] + \frac{\mu_b(\mathbf{r})\mu_h}{\mu_b(\mathbf{r})-\mu_h}\mathbf{M}_b(\mathbf{r}) \\ & - \mathbf{B}(\mathbf{r})[M_b] - \mathbf{B}(\mathbf{r})[J_c] \\ & - \mathbf{B}(\mathbf{r})[M_c] - \mathbf{B}(\mathbf{r})\big[J_f\big] \\ & - \mathbf{B}(\mathbf{r})\big[M_f\big], \end{aligned} \tag{16}$$

$$\begin{aligned}\mathbf{E}^{(i)}(\mathbf{r}) = {} & -\mathbf{E}(\mathbf{r})[J_b] - \mathbf{E}(\mathbf{r})[M_b] \\ & + \frac{1}{\sigma(\mathbf{r})-\sigma_b(\mathbf{r})}\mathbf{J}_c(\mathbf{r}) - \mathbf{E}(\mathbf{r})[J_c] \\ & - \mathbf{E}(\mathbf{r})[M_c] - \mathbf{E}(\mathbf{r})\big[J_f\big] \\ & - \mathbf{E}(\mathbf{r})\big[M_f\big], \end{aligned} \tag{17}$$

$$\begin{aligned}\mathbf{B}^{(i)}(\mathbf{r}) = {} & -\mathbf{B}(\mathbf{r})[J_b] - \mathbf{B}(\mathbf{r})[M_b] \\ & - \mathbf{B}(\mathbf{r})[J_c] + \frac{\mu(\mathbf{r})\mu_b(\mathbf{r})}{\mu(\mathbf{r})-\mu_b(\mathbf{r})}\mathbf{M}_c(\mathbf{r}) \\ & - \mathbf{B}(\mathbf{r})[M_c] - \mathbf{B}(\mathbf{r})\big[J_f\big] \\ & - \mathbf{B}(\mathbf{r})\big[M_f\big], \end{aligned} \tag{18}$$

$$\begin{aligned}\mathbf{E}^{(i)}(\mathbf{r}) = {} & -\mathbf{E}(\mathbf{r})[J_b] - \mathbf{E}(\mathbf{r})[M_b] \\ & - \mathbf{E}(\mathbf{r})[J_c] - \mathbf{E}(\mathbf{r})[M_c] \\ & + \frac{1}{\sigma(\mathbf{r})-\sigma_b(\mathbf{r})}\mathbf{J}_f(\mathbf{r}) - \mathbf{E}(\mathbf{r})\big[J_f\big] \\ & - \mathbf{E}(\mathbf{r})\big[M_f\big], \end{aligned} \tag{19}$$

$$\begin{aligned}\mathbf{B}^{(i)}(\mathbf{r}) = {} & -\mathbf{B}(\mathbf{r})[J_b] - \mathbf{B}(\mathbf{r})[M_b] \\ & - \mathbf{B}(\mathbf{r})[J_c] - \mathbf{B}(\mathbf{r})[M_c] \\ & - \mathbf{B}(\mathbf{r})\big[J_f\big] + \frac{\mu(\mathbf{r})\mu_b(\mathbf{r})}{\mu(\mathbf{r})-\mu_b(\mathbf{r})}\mathbf{M}_f(\mathbf{r}) \\ & - \mathbf{B}(\mathbf{r})\big[M_f\big]. \end{aligned} \tag{20}$$

Note that $\sigma_b(\mathbf{r}) = \sigma_h$ and $\mu_b(\mathbf{r}) = \mu_h$ in (17) and (18) for parts of the probe that lie outside the background, and in (19) and (20) for parts of the flaw that lie outside the background.

We will discretize these equations using three grids: a core grid, a coarse 'background' grid, and a fine 'flaw' grid. First we expand $\mathbf{J}_b(\mathbf{r})$, $\mathbf{J}_c(\mathbf{r})$ and $\mathbf{J}_f(\mathbf{r})$ in tent functions, and $\mathbf{M}_b(\mathbf{r})$, $\mathbf{M}_c(\mathbf{r})$ and $\mathbf{M}_f(\mathbf{r})$ in edge-elements, defined on the background, core and flaw grids, respectively. Then we use these same functions to test our equations. We multiply the equations by these functions, which have compact support spanning one or two grid cells along each direction, and integrate over space. We test (15), (17), and (19) with the tent functions, and (16), (18), and (20) with the edge-elements, defined on the background, core and flaw grids respectively. This gives the discretized matrix equation:

$$\begin{bmatrix} \mathbf{A}_{bb}^{(ee)} & -\mathbf{G}_{bb}^{(em)} & -\mathbf{G}_{bc}^{(ee)} & -\mathbf{G}_{bc}^{(em)} \\ -\mathbf{G}_{bb}^{(me)} & \mathbf{A}_{bb}^{(mm)} & -\mathbf{G}_{bc}^{(me)} & -\mathbf{G}_{bc}^{(mm)} \\ -\mathbf{G}_{cb}^{(ee)} & -\mathbf{G}_{cb}^{(em)} & \mathbf{A}_{cc}^{(ee)} & -\mathbf{G}_{cc}^{(em)} \\ -\mathbf{G}_{cb}^{(me)} & -\mathbf{G}_{cb}^{(mm)} & -\mathbf{G}_{cc}^{(me)} & \mathbf{A}_{cc}^{(mm)} \\ -\mathbf{G}_{fb}^{(ee)} & -\mathbf{G}_{fb}^{(em)} & -\mathbf{G}_{fc}^{(ee)} & -\mathbf{G}_{fc}^{(em)} \\ -\mathbf{G}_{fb}^{(me)} & -\mathbf{G}_{fb}^{(mm)} & -\mathbf{G}_{fc}^{(me)} & -\mathbf{G}_{fc}^{(mm)} \end{bmatrix} \begin{bmatrix} -\mathbf{G}_{bf}^{(ee)} & -\mathbf{G}_{bf}^{(em)} \\ -\mathbf{G}_{bf}^{(me)} & -\mathbf{G}_{bf}^{(mm)} \\ -\mathbf{G}_{cf}^{(ee)} & -\mathbf{G}_{cf}^{(em)} \\ -\mathbf{G}_{cf}^{(me)} & -\mathbf{G}_{cf}^{(mm)} \\ \mathbf{A}_{ff}^{(ee)} & -\mathbf{G}_{ff}^{(em)} \\ -\mathbf{G}_{ff}^{(me)} & \mathbf{A}_{ff}^{(mm)} \end{bmatrix} \begin{bmatrix} \mathbf{J}_b \\ \mathbf{M}_b \\ \mathbf{J}_c \\ \mathbf{M}_c \\ \mathbf{J}_f \\ \mathbf{M}_f \end{bmatrix} = \begin{bmatrix} \mathbf{E}_b^{(i)} \\ \mathbf{B}_b^{(i)} \\ \mathbf{E}_c^{(i)} \\ \mathbf{B}_c^{(i)} \\ \mathbf{E}_f^{(i)} \\ \mathbf{B}_f^{(i)} \end{bmatrix}, \tag{21}$$

which we solve for the vectors $\mathbf{J}_b$, $\mathbf{J}_c$ and $\mathbf{J}_f$ of expansion coefficients for the anomalous currents, and the vectors $\mathbf{M}_b$, $\mathbf{M}_c$ and $\mathbf{M}_f$ of expansion coefficients for the anomalous magnetizations, of the background, probe core and flaw respectively. Here, $\mathbf{A} = \mathbf{Q} - \mathbf{G}$, where the matrix $\mathbf{Q}$ contains the dependence on the anomalous electromagnetic material properties of the probe core, background and flaw.

III. THE PROBE-IN-BACKGROUND PROBLEM

Now we consider the simple case in which: 1) The permeability of the background, flaw and host are the same, and 2) The probe lies within the background and has the same conductivity as the background. From (10) and (12) we see that the first condition implies $\mathbf{M}_b = \mathbf{M}_f = 0$, and from (8) the second condition implies that $\mathbf{J}_c = 0$. Then the field equations (15-20) reduce to the three equations,

$$\begin{aligned}\mathbf{E}^{(i)}(\mathbf{r}) = {} & \frac{1}{\sigma_b(\mathbf{r})-\sigma_h}\mathbf{J}_b(\mathbf{r}) - \mathbf{E}(\mathbf{r})[J_b] \\ & - \mathbf{E}(\mathbf{r})[M_c] - \mathbf{E}(\mathbf{r})\big[J_f\big], \end{aligned} \tag{22}$$

$$\begin{aligned}\mathbf{B}^{(i)}(\mathbf{r}) = {} & -\mathbf{B}(\mathbf{r})[J_b] + \frac{\mu(\mathbf{r})\mu_h}{\mu(\mathbf{r})-\mu_h}\mathbf{M}_c(\mathbf{r}) \\ & -\mathbf{B}(\mathbf{r})[M_c] - \mathbf{B}(\mathbf{r})\big[J_f\big], \end{aligned} \tag{23}$$

$$\begin{aligned}\mathbf{E}^{(i)}(\mathbf{r}) = {} & -\mathbf{E}(\mathbf{r})[J_b] - \mathbf{E}(\mathbf{r})[M_c] \\ & + \frac{1}{\sigma(\mathbf{r})-\sigma_b(\mathbf{r})}\mathbf{J}_f(\mathbf{r}) - \mathbf{E}(\mathbf{r})\big[J_f\big], \end{aligned} \tag{24}$$

and the discretized matrix equation reduces to:

$$\begin{bmatrix} [\mathbf{Q}_{bb}^{(ee)} - \mathbf{G}_{bb}^{(ee)}] & -\mathbf{G}_{bc}^{(em)} & -\mathbf{G}_{bf}^{(ee)} \\ -\mathbf{G}_{cb}^{(me)} & [\mathbf{Q}_{cc}^{(mm)} - \mathbf{G}_{cc}^{(mm)}] & -\mathbf{G}_{cf}^{(me)} \\ -\mathbf{G}_{fb}^{(ee)} & -\mathbf{G}_{fc}^{(em)} & [\mathbf{Q}_{ff}^{(ee)} - \mathbf{G}_{ff}^{(ee)}] \end{bmatrix} \begin{bmatrix} \mathbf{J}_b \\ \mathbf{M}_c \\ \mathbf{J}_f \end{bmatrix} = \begin{bmatrix} \mathbf{E}_b^{(i)} \\ \mathbf{B}_c^{(i)} \\ \mathbf{E}_f^{(i)} \end{bmatrix}. \quad (25)$$

We recast this matrix equation in the form of the three coupled equation:

$$[\mathbf{Q}_{cc}^{(mm)} - \mathbf{G}_{cc}^{(mm)}]\mathbf{M}_c = \mathbf{B}_c^{(i)} + \mathbf{G}_{cb}^{(me)}\mathbf{J}_b + \mathbf{G}_{cf}^{(me)}\mathbf{J}_f, \quad (26)$$

$$[\mathbf{Q}_{bb}^{(ee)} - \mathbf{G}_{bb}^{(ee)}]\mathbf{J}_b = \mathbf{E}_b^{(i)} + \mathbf{G}_{bc}^{(em)}\mathbf{M}_c + \mathbf{G}_{bf}^{(ee)}\mathbf{J}_f, \quad (27)$$

$$[\mathbf{Q}_{ff}^{(ee)} - \mathbf{G}_{ff}^{(ee)}]\mathbf{J}_f = \mathbf{E}_f^{(i)} + \mathbf{G}_{fb}^{(ee)}\mathbf{J}_b + \mathbf{G}_{fc}^{(em)}\mathbf{M}_c. \quad (28)$$

If the grids for the probe core, background and flaw are evenly spaced along the *x*, *y*, and *z* directions, then the **G** matrices that appear on the left-hand side of these equations have a Toeplitz/Hankel structure. This, along with the sparse nature of the **Q** matrices, allows the matrix multiplications on the left-hand side of the equations to be performed quickly. Therefore, for a given value of the right-hand side, the equations can be solved efficiently using a conjugate-gradient matrix equation solver. The **G** matrices on the right-hand side of the equations lack this structure, so evaluation of the right-hand side is much more computationally expensive.

We start with initial values of zero for $\mathbf{M}_c$, $\mathbf{J}_b$, and $\mathbf{J}_f$ and cycle through the equations, updating the right-hand sides and solving for updated unknowns until changes in the magnetizations and currents are insignificant.

For small flaws, $\mathbf{J}_f$ will have little effect on $\mathbf{M}_c$ and $\mathbf{J}_b$. In this case, we can set $\mathbf{J}_f = 0$ in (26) and (27), and cycle through these equations to solve for $\mathbf{M}_c$ and $\mathbf{J}_b$, which amounts to solving the unflawed problem. Then, we insert these values into (28) and solve for $\mathbf{J}_f$. Experimental evidence supports this 'small flaw' approximation for flaws typical in nondestructive evaluation.

IV. BOLT-HOLE INSPECTION WITH THE SPLITD PROBE

We now consider the problem of inspecting a bolt hole in a plate or other layered planar medium with the 'SplitD' probe that is depicted in Fig. 2.

The probe is pulled along the direction of the bolt hole axis while it is spinning in the circumferential direction, thereby generating a two-dimensional raster scan. This is an important problem in the aircraft industry, and led to the development of this probe. The probe comprises a racetrack driver coil in combination with a pickup coil wound in a differential configuration around a 'SplitD' ferrite core. See pages 81-91 of [1] for a description of such a probe, with examples of its use in characterizing surface cracks within bolt holes in a benchmark test case.

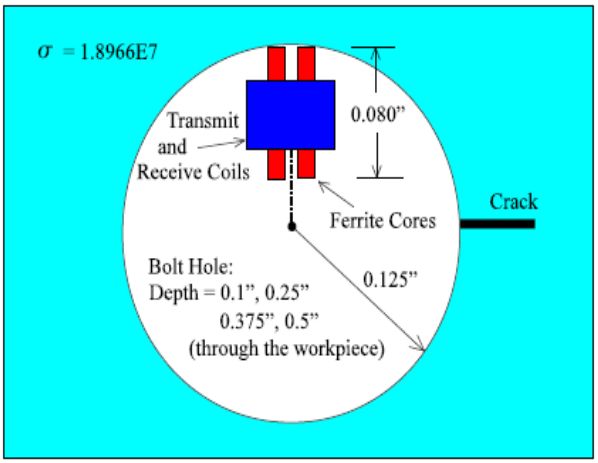

Fig. 2. Illustrating the SplitD probe within the bolt hole. The probe is spun about the axis of the bolt hole (out of page).

We compute the change in the pickup impedance due to the flaw. The corresponding circuit diagram is shown in Fig. 3. The ferrite core has the effect of increasing the inductances, L_d and L_p, of the driver and pickup coils. We model this effect with additional coil turns represented in the figure by L_μ and L_μ, respectively. Setting the sum of the voltage drops around each of the circuits for driver coil with core, pickup coil with core, background and flaw to zero gives:

$$V_1(\alpha) = (Z_{dd} + Z_{d\mu} + Z_{\mu d} + Z_{\mu\mu})I_1 + (Z_{dp} + Z_{d\mu'} + Z_{\mu p} + Z_{\mu\mu'})I_2(\alpha) + (Z_{d3} + Z_{\mu 3})I_3(\alpha) + \alpha(Z_{d4} + Z_{\mu 4})I_4, \quad (29)$$

$$V_2(\alpha) = (Z_{pd} + Z_{p\mu} + Z_{\mu' d} + Z_{\mu' \mu})I_1 + (Z_{pp} + Z_{p\mu'} + Z_{\mu' p} + Z_{\mu'\mu'})I_2(\alpha) + (Z_{p3} + Z_{\mu' 3})I_3(\alpha) + \alpha(Z_{p4} + Z_{\mu' 4})I_4, \quad (30)$$

$$0 = (Z_{3d} + Z_{3\mu})I_1 + (Z_{3p} + Z_{3\mu'})I_2(\alpha) + Z_{33}I_3(\alpha) + \alpha Z_{34}I_4, \quad (31)$$

$$0 = (Z_{4d} + Z_{4\mu})I_1 + (Z_{4p} + Z_{4\mu'})I_2(1) + Z_{43}I_3(1) + Z_{44}I_4. \quad (32)$$

The equations are parameterized by α, which has a value of unity for the problem we are solving, which includes a flaw, and a value of zero for the corresponding unflawed problem. Since the flaw current, I_4, is zero when $\alpha = 0$, we write it as αI_4.

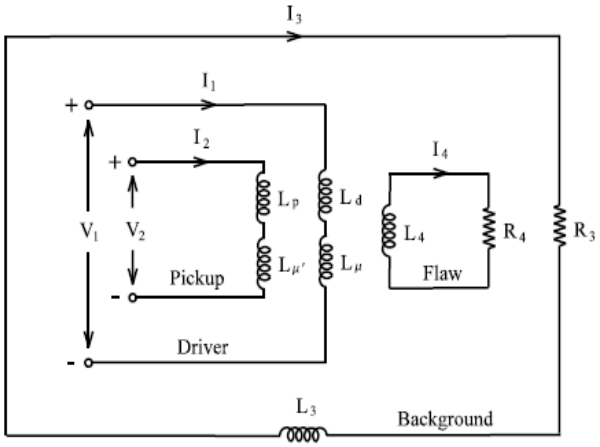

Fig. 3. Equivalent circuit diagram for the probe-in-background problem with the SplitD probe. L_d and L_p are the inductances of the driver and pickup coils. L_μ and L_μ, model the increased inductance due to the ferrite core.

The current I_2 in the pickup coil will be very small (theoretically zero), so we will ignore the terms in (29-32) that involve I_2. And we will combine L_d and L_μ into a single inductance, L_1, and L_p and L_μ, into a single inductance, L_2. The circuit equations then become:

$$V_1(\alpha) = Z_{11}I_1 + Z_{13}I_3(\alpha) + \alpha Z_{14}I_4, \quad (33)$$
$$V_2(\alpha) = Z_{21}I_1 + Z_{23}I_3(\alpha) + \alpha Z_{24}I_4, \quad (34)$$
$$0 = Z_{31}I_1 + Z_{33}I_3(\alpha) + \alpha Z_{34}I_4, \quad (35)$$
$$0 = Z_{41}I_1 + Z_{43}I_3(1) + Z_{44}I_4, \quad (36)$$

where

$$\begin{aligned} Z_{11} &= Z_{dd} + Z_{d\mu} + Z_{\mu d} + Z_{\mu\mu} \\ Z_{21} &= Z_{pd} + Z_{p\mu} + Z_{\mu' d} + Z_{\mu'\mu} \\ Z_{1j} &= Z_{dj} + Z_{\mu j} \\ Z_{i1} &= Z_{id} + Z_{i\mu} \\ Z_{2j} &= Z_{pj} + Z_{\mu' j}. \end{aligned} \quad (37)$$

Solving (35) for I_3 when $\alpha = 0$ (no flaw) gives:

$$I_3(0) = -\frac{Z_{31}}{Z_{33}} I_1, \quad (38)$$

and solving (35) and (36) for $\alpha = 1$ (with flaw) gives

$$I_3(1) = -\frac{\begin{vmatrix} Z_{31} & Z_{34} \\ Z_{41} & Z_{44} \end{vmatrix}}{\begin{vmatrix} Z_{33} & Z_{34} \\ Z_{43} & Z_{44} \end{vmatrix}} I_1, \quad (39)$$

$$I_4 = -\frac{\begin{vmatrix} Z_{33} & Z_{31} \\ Z_{43} & Z_{41} \end{vmatrix}}{\begin{vmatrix} Z_{33} & Z_{34} \\ Z_{43} & Z_{44} \end{vmatrix}} I_1. \quad (40)$$

Equations (38-40) give the distributed currents for the background and flaw in terms of the driver current I_1. Putting these into (34) gives the pickup voltage without and with the flaw:

$$V_2(0) = \left(Z_{21} - Z_{23}\frac{Z_{31}}{Z_{33}}\right) I_1, \quad (41)$$

$$V_2(1) = \left(Z_{21} - Z_{23}\frac{\begin{vmatrix} Z_{31} & Z_{34} \\ Z_{41} & Z_{44} \end{vmatrix}}{\begin{vmatrix} Z_{33} & Z_{34} \\ Z_{43} & Z_{44} \end{vmatrix}} - Z_{24}\frac{\begin{vmatrix} Z_{33} & Z_{31} \\ Z_{43} & Z_{44} \end{vmatrix}}{\begin{vmatrix} Z_{33} & Z_{34} \\ Z_{43} & Z_{44} \end{vmatrix}} \right) I_1. \quad (42)$$

The change in the transfer impedance due to the flaw is thus,

$$\begin{aligned} dZ_{21} &= \frac{V_2(1)}{I_1} - \frac{V_2(0)}{I_1} \\ &= -\left(Z_{23}\frac{\begin{vmatrix} Z_{31} & Z_{34} \\ Z_{41} & Z_{44} \end{vmatrix}}{\begin{vmatrix} Z_{33} & Z_{34} \\ Z_{43} & Z_{44} \end{vmatrix}} + Z_{24}\frac{\begin{vmatrix} Z_{33} & Z_{31} \\ Z_{43} & Z_{44} \end{vmatrix}}{\begin{vmatrix} Z_{33} & Z_{34} \\ Z_{43} & Z_{44} \end{vmatrix}} - Z_{23}\frac{Z_{31}}{Z_{33}} \right). \end{aligned} \quad (43)$$

We now re-solve the equations in a form more useful for the calculation of dZ_{21}. From (35) the background current is:

$$I_3(\alpha) = -\left(\frac{Z_{31}}{Z_{33}} I_1 + \alpha \frac{Z_{34}}{Z_{33}} I_4\right), \quad (44)$$

and putting this result into (34) we get:

$$\begin{aligned} V_2(\alpha) &= Z_{21}I_1 - \frac{Z_{23}}{Z_{33}}(Z_{31}I_1 + \alpha Z_{34}I_4) + \alpha Z_{24}I_4 \\ &= \left(Z_{21} - \frac{Z_{23}Z_{31}}{Z_{33}}\right) I_1 \\ &\quad + \alpha\left(Z_{24} - \frac{Z_{23}Z_{34}}{Z_{33}}\right) I_4. \end{aligned} \quad (45)$$

The first terms in the two parentheses represent the direct coupling of the pickup to the driver and the flaw. The second terms represent the coupling, through the background, of the pickup to the driver and the flaw. The background produces a field that opposes that due to the direct coupling, thus reducing the impedance.

To find the voltage produced at the flaw by a current flowing through the pickup coil, we need to add the terms from I_2 to (35) and (36), which we rewrite as:

$$0 = Z_{31}I_1 + Z_{32}I_2(1) + Z_{33}I_3(1) + Z_{34}I_4, \quad (46)$$
$$0 = Z_{41}I_1 + Z_{42}I_2(1) + Z_{43}I_3(1) + Z_{44}I_4. \quad (47)$$

Solving (46) for I_3 gives:

$$I_3(1) = -\frac{1}{Z_{33}}(Z_{31}I_1 + Z_{32}I_2(1) + Z_{34}I_4), \quad (48)$$

and putting this into (47) gives:

$$\begin{aligned} 0 &= \left(Z_{41} - \frac{Z_{43}Z_{31}}{Z_{33}}\right) I_1 + \left(Z_{42} - \frac{Z_{43}Z_{32}}{Z_{33}}\right) I_2 \\ &\quad + \left(Z_{44} - \frac{Z_{43}Z_{34}}{Z_{33}}\right) I_4. \end{aligned} \quad (49)$$

The second term of (49) gives the voltage across the flaw due to the pickup current, and includes the coupling through the background as well as the direct coupling.

Now we evaluate the voltage across the pickup coil due to the flaw in terms of field quantities, for the purpose of computation. From (45) we have:

$$V_2(1) - V_2(0) = \left(Z_{24} - \frac{Z_{23}Z_{34}}{Z_{33}}\right) I_4. \qquad (50)$$

This is equal to the line integral around the pickup coil,

$$dV_2 = -\int_{coil} \mathbf{E}^{(4)}(\mathbf{r}) \cdot \mathbf{dl}, \qquad (51)$$

where $\mathbf{E}^{(4)}(\mathbf{r})$ is the field produced at the pickup coil by the flaw current I_4. We rewrite this as:

$$dV_2 = \frac{-\int_{coil} \mathbf{E}^{(4)}(\mathbf{r}) \cdot I_2(1)\mathbf{dl}}{I_2(1)} = \frac{-\int_{coil} \mathbf{E}^{(4)}(\mathbf{r}) \cdot \mathbf{J}^{(2)}(\mathbf{r})dV}{I_2(1)}, \qquad (52)$$

where the volume integral in the last expression is the integral over the coil volume of the dot product of the field, $\mathbf{E}^{(4)}(\mathbf{r})$, at the pickup coil due to the flaw with the current density, $\mathbf{J}^{(2)}(\mathbf{r})$, of the pickup current.

Now by the reciprocity theorem we have the symmetry:

$$\int_{coil} \mathbf{E}^{(4)}(\mathbf{r}) \cdot \mathbf{J}^{(2)}(\mathbf{r})dV = \int_{flaw} \mathbf{E}^{(2)}(\mathbf{r}) \cdot \mathbf{J}^{(4)}(\mathbf{r})dV, \qquad (53)$$

where the right hand side of (53) is the integral over the flaw of the dot product of the field, $\mathbf{E}^{(2)}(\mathbf{r})$, at the flaw due to the pickup current with the current density, $\mathbf{J}^{(4)}(\mathbf{r})$, of the flaw current. This symmetry is reflected in the coefficients of I_4 and I_2 in (45) and (49) respectively, which are equal as are the Z_{ij} under the interchange of i and j.

With this equality we can now write the change in the transfer impedance due to the flaw as:

$$dZ_{21} = \frac{dV_2}{I_1} = \frac{-\int_{flaw} \mathbf{E}^{(2)}(\mathbf{r}) \cdot \mathbf{J}^{(4)}(\mathbf{r})dV}{I_2(1)I_1}. \qquad (54)$$

The current $\mathbf{J}^{(4)}(\mathbf{r})$ is the flaw current due to the driver current, and is therefore proportional to I_1. The field $\mathbf{E}^{(2)}(\mathbf{r})$is the field at the flaw due to the pickup current, and is therefore proportional to $I_2(1)$. From the second term of (49), it's clear that $\mathbf{E}^{(2)}(\mathbf{r})$ includes the field at the flaw generated by the action of the pickup current on the background. And from (37) it's clear that it's computation includes the contributions of the ferrite core as well.

Thus, we can write the change in impedance due to the flaw as:

$$dZ_{21} = -\int_{flaw} \mathbf{E}^{(2)}(\mathbf{r}) \cdot \mathbf{J}^{(4)}(\mathbf{r})dV = \sum_{KLM} E^{(x)}_{KLM} J^{(x)}_{KLM} + E^{(y)}_{KLM} J^{(y)}_{KLM} + E^{(z)}_{KLM} J^{(z)}_{KLM}, \qquad (55)$$

where in the last expression the sum is over the x, y, and z indices, K, L, and M of the flaw grid, J is the solution $\mathbf{J}_f$ obtained in solving (28) for a driver coil current of unity, and E is given by the right-hand side of that equation, where $\mathbf{M}_c$ and $\mathbf{J}_b$ are the solutions obtained in solving (26) and (27) for a pickup coil current of unity.

V. COMMENTS AND CONCLUSIONS

We have developed a model for computing solutions to multiscale problems based on coupled integral equations, and have reduced the equations to matrix form using the usual techniques of the method of moments. We have shown, further, that the development of the model equations and the interpretation of the model results is facilitated by the use of classical electrical equivalent circuits. This is one of the advantages in choosing electrical impedance to be the observable in the solution of the field equations.

The algorithm developed in this paper is being coded into the commercial product, **VIC-3D®**. In future papers, we will describe its application to a number of problems in aircraft inspection, as well as discuss our success with such coding concerns as parallelization and the use of GPU hardware.

ACKNOWLEDGEMENT

This work was supported by the Air Force Research Laboratory under SBIR contract FA8650-13-C-5011 with Victor Technologies, LLC.

REFERENCES

[1] H. A. Sabbagh, R. K. Murphy, E. H. Sabbagh, J. C. Aldrin, and J. S. Knopp, *Computational Electromagnetics and Model-Based Inversion: A Modern Paradigm for Eddy-Current Nondestructive Evaluation*, Springer, New York, 2013.

R. Kim Murphy received his B.A. in Physics from Rice University in 1978, and his Ph.D. in Physics from Duke University in 1984. Since 1989, he has worked as a Senior Physicist for Sabbagh Associates Inc., and Victor Technologies, LLC. Murphy has been active in formulating models and coding in VIC-3D, performing validation numerical experiments, and solving one-dimensional and three-dimensional inverse problems.

Harold A. Sabbagh received his BSEE and MSEE from Purdue University in 1958, and his Ph.D. from Purdue in 1964. In 1980, he formed Sabbagh Associates, Inc., and did research in the application of computational electromagnetics to nondestructive evaluation (NDE). This research evolved into the commercial volume-integral code, VIC-3D. In 1998, he formed Victor Technologies, LLC, in order to continue this research and further development of VIC-3D. His past professional activities have included a stint as President of ACES, and in 2010, he was elected to the grade of Fellow in ACES.

Elias H. Sabbagh received the B.Sc. in Electrical Engineering and the B.Sc. in Economics from Purdue University in 1990 and 1991. He has worked as System Administrator, Software Engineer, and Researcher for Victor Technologies since its inception. His interests include object-oriented programming, database administration, system architecture, scientific programming, and distributed programming.

Wire Fault Diagnosis Based on Time-Domain Reflectometry and Backtracking Search Optimization Algorithm

Hamza Boudjefdjouf [1], Houssem R. E. H. Bouchekara [1,2], Francesco de Paulis [3], Mostafa K. Smail [4], Antonio Orlandi [3], and Rabia Mehasni [1]

[1] Constantine Electrical Engineering Laboratory, LEC, Department of Electrical Engineering
University of Freres Mentouri Constantine, 25000 Constantine, Algeria
hamza.boudjefdjouf@lec-umc.org, Houssem.bouchekara@gmail.com, mehasni@yahoo.fr

[2] Laboratory of Electrical Engineering of Constantine, LGEC, Department of Electrical Engineering
University of Freres Mentouri Constantine, 25000 Constantine, Algeria

[3] UAq EMC Laboratory, Department of Industrial and Information Engineering and Economics
Via G. Gronchi, 18, 67100 - L'Aquila – Italy
antonio.orlandi@univaq.it, francesco.depaulis@univaq.it

[4] Institut Polytechnique des Sciences Avancées (IPSA)
15-21 Rue Maurice Grandcoing, 94200 Ivry-sur-Seine, France
mostafa-kamel.smail@ipsa.fr

Abstract ─ The development of a robust and accurate fault diagnosis approach under various system and fault conditions is a research area of great interest. The objective of this paper is to develop a new non-destructive approach for wiring diagnosis based on Time Domain Reflectometry (TDR) in one hand and on Backtracking Search Optimization Algorithm (BSA) in the other hand. Real-world case studies are investigated to demonstrate the effectiveness and robustness of the proposed approach. Simulation results evaluated from experimental data demonstrate that the proposed approach can be used for effective diagnosis of complex wiring networks.

Index Terms ─ Backtracking search optimization algorithm, time domain reflectometry, wiring diagnosis.

I. INTRODUCTION

Electrical wiring diagnosis is a challenge for maintenance engineers. Aging of wires can result in: loss of critical functions of the equipment energized by the system, loss of critical information relevant to the decision making process and operator actions and may cause a break in power supply [1].

In order to detect electrical failures and reduce maintenance cost in electrical wiring networks, diagnosis approaches that can detect, localize and characterize defects are required. Ideally, the approach should be non-destructive and accurate [2], [3].

Time Domain Reflectometry (TDR) is a measurement technique used to determine the characteristics of electrical lines by observing reflected waveforms [4]. The key benefit of TDR over other testing technique is that is non-destructive [5]. It has been proven that TDR is able to detect hard faults in coaxial cables. However, a TDR response is not self-explanatory and consequently it cannot be used alone for complex wiring networks. Over the last decade, many inverse techniques were used along with TDR in order to detect faults in wiring networks [6], [7], [8], [9].

The Backtracking Search Optimization Algorithm (BSA) is a new Evolutionary Algorithm (EA) developed to solve real-valued numerical optimization problems. It is based on three basic and well-known operators that are selection, mutation and crossover [10].

The aim of this paper is to develop an efficient approach for wire fault diagnosis based on TDR and BSA. This approach is used to detect, localize and characterize hard faults (open or short circuit) that can affect a wiring network.

The rest of this paper is organized as follows. In Section II the developed approach is presented. In Section III, the developed approach is applied to three case studies. Finally, conclusions are drawn in Section IV.

II. APPROACH

The proposed TDR-BSA based approach consists of using a forward model in order to generate the TDR response, and the BSA in order to solve the inverse problem as shown in Fig. 1. Therefore, BSA is used to

Submitted On: July 25, 2015
Accepted On: February 25, 2016

minimize the difference between the measured TDR response and the generatedone. Mathematically, we can formulate the inverse problem as an optimization problem with the following objective function:

$$\mathrm{F} = \left(\frac{1}{N} \sum_{n=1}^{N} \left(\mathrm{M\_TDR\_res}(\mathbf{x}) - \mathrm{G\_TDR\_res}(\mathbf{x}) \right)^2 \right)^{\frac{1}{2}}, \quad (1)$$

where F is the objective function to be minimized, N the number of points, M_TDR_res and G_TDR_res are the measured and generated TDR responses, respectively and **x** is the vector of design variables that are the lengths (L_i) and the termination loads (R_i) of different branches.

In other words, knowing the topology of the network (healthy one), the target is to detect, to localize and to characterize faults in a given wiring network through finding the length and the termination load of each branch. If a calculated length L_i is different (shorter) than the length of the healthy branch, then a fault has occurred in that branch where L_i represents the location of the fault and R_i indicates whether the fault is an open circuit or a short circuit. If $R_i = 1$ the fault is an open circuit otherwise if $R_i = 0$, the fault is a short circuit.

In the following sections, both the forward model and the BSA are described. It is worth mentioning that the forward model has been presented and discussed in detail in [9] and in the following only briefly recalled for sake of completeness and clarity.

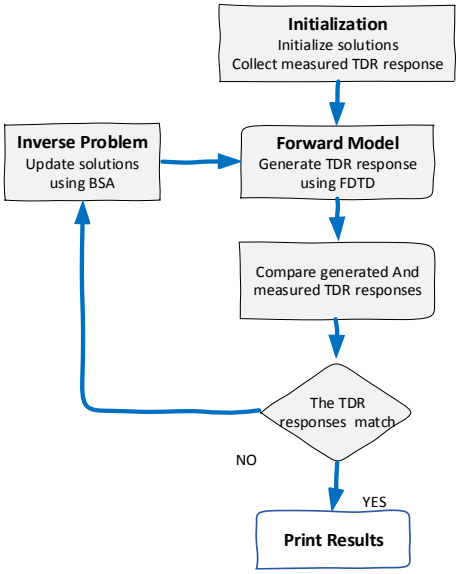

Fig. 1. The proposed TDR-BSA approach for wiring diagnosis.

A. The forward model

The TDR response is computed by solving the Kirchhoff law applied on the electrical model of the multiconductor transmission line [11], using the Finite Difference Time Domain (FDTD) method [14]:

$$\frac{\partial \mathrm{V}(z,t)}{\partial z} = -\mathrm{RI}(z,t) - \mathrm{L}\frac{\partial \mathrm{I}(z,t)}{\partial t}, \quad (2)$$

$$\frac{\partial \mathrm{I}(z,t)}{\partial z} = -\mathrm{GV}(z,t) - \mathrm{C}\frac{\partial \mathrm{V}(z,t)}{\partial t}. \quad (3)$$

In (2) and (3) V and I are the vectors of line voltages and line currents, respectively. The position along the line is denoted as *z* and time is denoted as *t*. The R (resistance), L (inductance), C (capacitance) and G (conductance) are the matrices of the per-unit-length parameters. The values of these parameters are computed analytically as in [9].

B. Experimental setup

The principle of TDR is to inject a signal into the inner conductor of the coaxial cable, which propagates along the cable; when the signal meets a discontinuity of impedance, a part of its energy is reflected back to the injection point where it is observed. The analysis of the response (the reflected signal) is used to detect, localize and characterize defects based on the amplitude and timing (or location) of the reflected signal.

The echo responses of the different network configurations are measured by means of a Vector Network Analyzer (VNA) connected to the testing network, as shown in Fig. 2. The VNA is an Anritsu MS4624B network analyzer, with a frequency range of 10 MHz to 9 GHz.

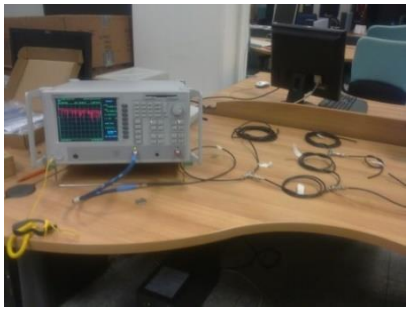

Fig. 2. Experimental setup.

The measured one-port scattering parameter S_{11} represents the frequency response of the network, thus it can be simply multiplied by the spectrum of the same input pulse used in the FDTD simulation. The Inverse Fast Fourier Transform is applied to convert the frequency domain response to the time domain response.

In order to measure, using VNA, the same network, the frequency band is 10 MHz - 1 GHz, and for the complex configuration we use a frequency band of 1 GHz - 2 GHz; then the two sets of data are combined together to achieve a 2 GHz bandwidth data with a doubled frequency resolution (f = 618 kHz based on

1601 samples per measurement). The reconstructed S_{11} is multiplied by the spectrum of the input pulse. The input pulse is a raised cosine pulse, with a rising time of 4 ns and amplitude of 1 Volt.

C. The backtracking search optimization algorithm

The BSA is used for solving the inverse problem. As previously mentioned, the BSA is a new EA and global optimization method developed in [10] for solving real-valued numerical optimization problems. It uses the three basic and well-known EA operators that are selection, mutation and crossover.

The main steps of the BSA are given in Algorithm 1. BSA is a population based optimization method; thus, it starts by randomly generating a population in the search space. In the Selection-I stage, the historical population that is used for calculating the search direction is determined. In the Mutation stage, the initial form of the trial population is generated while in the Crossover stage the final form of this trial population is generated. In this stage the best trial individuals for the optimization problem are used to evolve the target population individuals [10]. At the end of the Crossover stage, the individuals that go beyond the search space limits are redefined inside these limits. In the Selection-II stage, the trial population is used to update the population using a greedy selection. More details about the BSA can be found in [10].

Algorithm 1: General structure of BSA [10]
1. Initialization
repeat
2. Selection-I
Generation of Trial-Population
3.Mutation
4.Crossover
End
5. Selection-II
until stopping conditions are met

III. APPLICATIONS AND RESULTS

A. Model validation

Before using the developed TDR-BSA approach for the diagnosis of wiring networks, the validation of our forward model is carried out using the healthy YY-shaped network shown in Fig. 3. The measured and generated (using the forward model) TDR responses of this network are given in Fig. 4. The comparison between these two TDR responses shows the accuracy of the developed forward model. This is also confirmed by the small values of GRADE and SPREAD (GRADE = 2, SPREAD = 1) that are the figures of merits of the Feature Selective Validation (FSV) technique [12], [13] that is suggested by the IEEE Standard [14] as the preferred algorithm for quantitative data comparison.

(a)

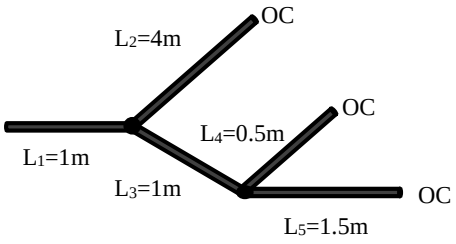

(b)

Fig. 3. The YY-shaped network: (a) the experimental network and (b) the schematic representation.

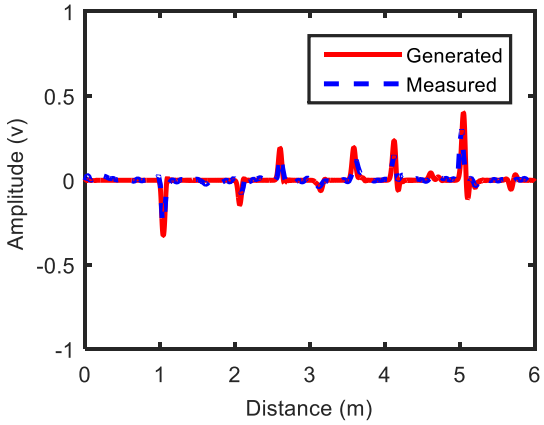

Fig. 4. Comparison between the healthy measured and generated TDR responses of the YY-shaped network.

B. Case studies

In order to evaluate the performance of the developed TDR-BSA approach we consider in this paper three case studies.

1. CASE 1

The first case study investigated in this paper is a YY-shaped network affected by an open circuit in L_2 at 2 m from the first junction as shown in Fig. 5. Thus, the design variables for this case are L_2, L_4, L_5, R_2, R_4 and R_5. It is worth mentioning that, the main branches L_1 and L_3 are assumed to be healthy, i.e., they are not considered as design variables. Because if the first main branch L_1 is affected by a fault it means that the investigated YY-

shaped network is reduced to a simple line. Now if the second main branch L_3 is affected by a fault the network is reduced to a simpler network which is the Y-shaped network.

A simple comparison between the healthy and the faulty measured TDR responses of Fig. 6 allows us to make a first comment about the status of the wiring network under study: the network is not healthy. This phase is called the detection and it constitutes the first phase in our diagnosis as previously mentioned.

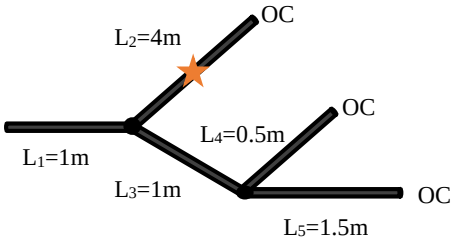

Fig. 5. The wiring network for CASE 1.

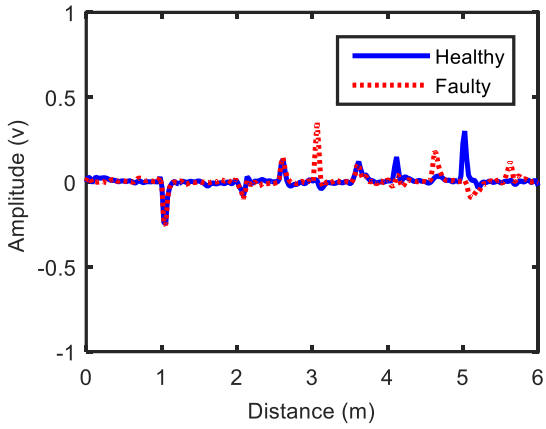

Fig. 6. Comparison between the healthy and the faulty measured TDR responses for CASE 1.

The developed TDR-BSA approach has been run for this case and the obtained results are given in Fig. 7 and in Table 1.

It can be seen from Fig. 7 that there is a good matching (FSV GRADE = 2 and SPREAD = 1) between the TDR response generated using the developed approach and the one obtained from measurements.

Table 1 compares the lengths and termination loads that correspond to the healthy network with those generated using the developed TDR-BSA approach. From this table, we can make the following conclusions: the analyzed network has a fault in L_2 at 2.04 m and the type of fault is an open circuit because $R_2 = 1$. It is worth mentioning here that, there is an error of estimating the fault distance of 0.04 m. These two conclusions represent the second and third phases of our diagnosis that are localization and characterisation, respectively.

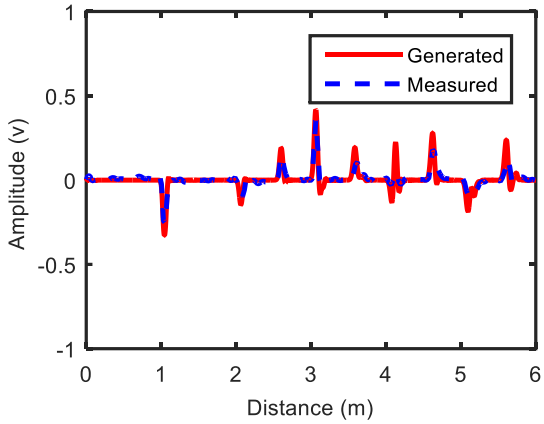

Fig. 7. Comparison between the measured and the generated TDR responses for CASE 1 (FSV GRADE = 2 and SPREAD = 1).

Table 1: Optimal results found for CASE 1

Design Variables		
Name	Generated Values	Healthy Network Values
L_2	2.04	4.00
L_4	0.50	0.50
L_5	1.50	1.50
R_2	1	1
R_4	1	1
R_5	1	1

2. CASE 2

The second case investigated is a faulty YY-shaped network with a short circuit in L_4 at 0.4 m from the second junction as shown in Fig. 8. Thus, the design variables for this case are L_2, L_4, L_5, R_2, R_4 and R_5. For the same reasons explained before, L_1 and L_3 are not considered as design variables here.

For the detection phase, a simple analysis of the TDR responses of Fig. 9 allows to detect the presence of faults.

The developed TDR-BSA approach has been run for this case and the obtained results are given in Fig. 10 and in Table 2.

From Fig. 10 we can say that there is a good agreement (FSV GRADE = 2 and SPREAD = 1) between the TDR generated using the proposed approach and the one measured using experimental setup. From Table 2 we can make the following conclusions about the localization and characterization of faults: the analyzed network has a fault in L_4 at 0.42 m and the type of fault is a short circuit because R_4=0.It is worth to mention here that, there is an error of 0.02 m and 0.021 m in estimating L_2 and L_4, respectively.

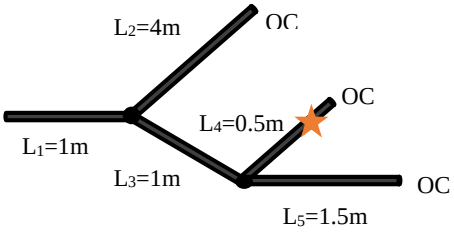

Fig. 8. The wiring network for CASE 2.

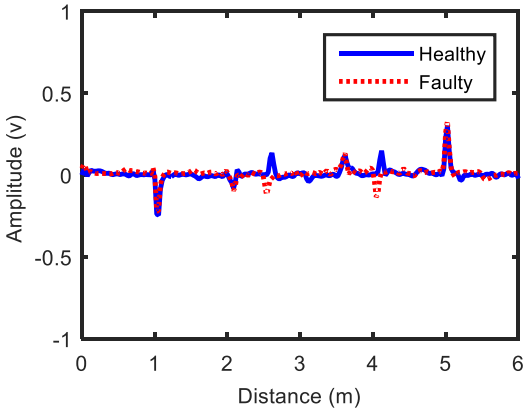

Fig. 9. Comparison between the healthy and the faulty measured TDR responses for CASE 2.

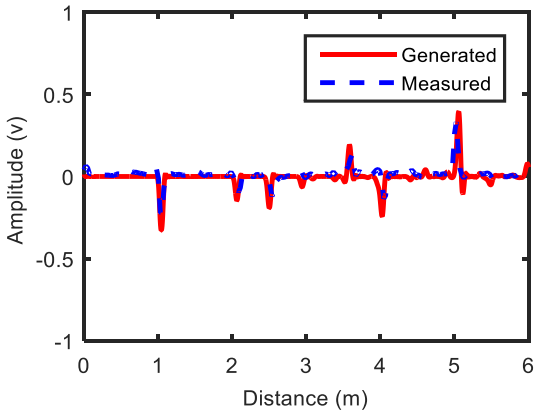

Fig. 10. Comparison between the measured and the generated TDR responses for CASE 2 (FSV GRADE = 2 and SPREAD = 1).

Table 2: Optimal results found for CASE 2

Design Variables		
Name	Generated Values	Healthy Network Values
L_2	3.98	4.00
L_4	0.42	0.40
L_5	1.50	1.50
R_2	1	1
R_4	0	1
R_5	1	1

3. CASE 3

To prove the robustness of the developed approach against more complex networks, the third case study investigated in this paper is a YYY-shaped network affected by two hard faults, a short circuit in L_2 at 2 m from the first junction and an open circuit in L_4 at 0.4 m from the second junction as shown in Fig. 11.

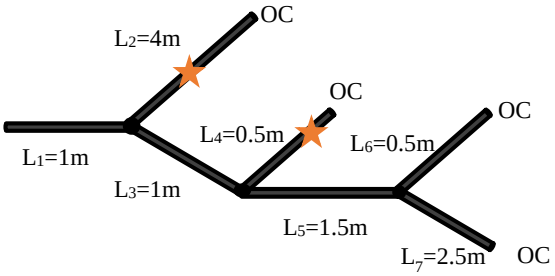

Fig. 11. The wiring network for CASE 3.

Therefore, the design variables for this case are L_2, L_4, L_6, L_7, R_2, R_4, R_6 and R_7.The detection phase is similar to the ones explained in CASE 1, and CASE 2. In order to avoid undesired repetition, we have not put it here.The developed TDR-BSA approach has been run for this complex case and the obtained results are given in Fig. 12 and in Table 3. Figure 12 shows the good matching (FSV GRADE = 2 and SPREAD = 2) between the TDR generated and the one measured experimentally. From Table 3 we can make the following conclusions about the localization and characterization of faults: there is a short circuit (R_2=0) in L_2 at 2.02 m from the first junction and an open circuit (R_4=1) in L_4 at 0.42 m from the second junction. The error in estimating fault locations is0.02m for both L_2 and L_4.

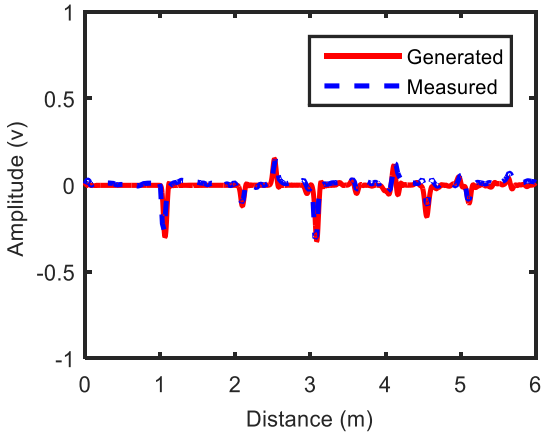

Fig. 12. Comparison between the measured and the generated TDR responses for CASE 3 (FSV GRADE = 2 and SPREAD = 2).

Table 3: Optimal results found for CASE 3

Design Variables		
Name	Generated Values	Healthy Network Values
L_2	2.02	4.00
L_4	0.42	0.50
L_6	0.50	0.50
L_7	2.50	2.50
R_2	0	1
R_4	1	1
R_6	1	1
R_7	1	1

IV. CONCLUSION

In this paper, a new approach using TDR and BSA is developed and used for the diagnosis of wiring networks. The TDR is used to measure the TDR response of a given network. The BSA is used to compare this response with a generated one using a developed forward model.

In order to assess the effectiveness and robustness of the proposed approach, three different case studies using YY-shaped and YYY-shaped networks are tested. The obtained results show that the developed approach has excellent performance and it is very accurate for the diagnosis of wiring networks. Moreover, by using the same values of convergence threshold there is an improvement (a decreasing) of around 70% of CPU time between the BSA that is proposed in this paper and the TLBO that was used in [9].

REFERENCES

[1] J. Wang, P. Crapse, Y. J. Shin, and R. Dougal, "Diagnostics and prognostics of electric cables in ship power systems via joint time-frequency domain reflectometry," *Proceedings of the IEEE Instrumentation and Measurement Technology Conference*, pp. 917-921, May 2008.

[2] J. Wang, P. Crapse, Y. J. Shin, and R. Dougal, "Diagnostics and prognostics of electric cables in nuclear power plants via joint time-frequency domain reflectometry," *IEEE International Symposium on Electrical Insulation*, pp. 24-27, June 2008.

[3] P. F. Fantoni and A. Nordlund, *Wire System Aging Assessment and Condition Monitoring (WASCO)*, ISBN 87-7893-192-4 Electronic Report, Apr. 2006.

[4] C. Lo and C. Furse, "Noise-domain reflectometry for locating wiring faults," *IEEE Trans. Electromagnetic Compatibility*, 47, pp. 97-104, Feb. 2005.

[5] P. Smith, C. Furse, and J. Gunther, "Analysis of spread spectrum time domain reflectometry for wire fault location," *IEEE Sensors Journal*, vol. 5, no. (6), pp. 1469-78, Dec. 2005.

[6] M. K. Smail, T. Hacib, L. Pichon, and F. Loete, "Detection and location of defects in wiring networks using time-domain reflectometry and neural networks," *IEEE Trans. Magnetics*, 47, pp. 1502-1505, 2011.

[7] H. R. E. H. Bouchekara, M. K. Smail, and G. Dahman, "Diagnosis of multi-fault wiring network using time-domain reflectometry and electromagnetism-like mechanism," *Electromagnetics*, 33, pp. 131-143.

[8] M. K. Smail, H. R. E. H. Bouchekara, L. Pichon, H. Boudjefdjouf, and R. Mehasni, "Diagnosis of wiring networks using particle swarm optimization and genetic algorithms," *Computers and Electrical Engineering*.

[9] H. Boudjefdjouf, R. Mehasni, A. Orlandi, H. R. E. H. Bouchekara, F. de Paulis, and M. K. Smail, "Diagnosis of multiple wiring faults using time-domain reflectometry and teaching–learning-based optimization," *Electromagnetics*, vol. 35, no. 1, pp. 10-24, Dec. 2014.

[10] P. Civicioglu, "Backtracking search optimization algorithm for numerical optimization problems," *Appl. Math. Comput*., vol. 219, no. 15, pp. 8121-8144, Apr. 2013.

[11] C. R. Paul, *Analysis of Multiconductor Transmission Lines*, New York. Wiley 1994.

[12] A. P. Duffy, A. J. M. Martin, A Orlandi, G Antonini, T. M. Benson, and M. S. Woolfson, "Feature selective validation (FSV) for validation of computational electromagnetics (CEM). Part I – The FSV method," *IEEE Trans. on Electromagn. Compatibility*, vol. 48, no. 3, pp. 449-459, Aug. 2006.

[13] A. Orlandi, A. P. Duffy, B Archambeault, G Antonini, D. E. Coleby, and S Connor, "Feature selective validation (FSV) for validation of computational electromagnetics (CEM). Part II – Assessment of FSV performance," *IEEE Trans. on Electromagn. Compatibility*, vol. 48, no. 3, pp. 460-467, Aug. 2006.

[14] IEEE Standard P1597, *Standard for Validation of Computational Electromagnetics Computer Modeling and Simulation – Part 1*, 2, 2008.

Hamza Boudjefdjouf was born in Mila, Algeria, in 1982. He received his master degree in 2009 from Constantine University, Algeria. He is currently a Ph.D. student at the University of Constantine, Member of the LEC Laboratory and Engineer in Dam Monitoring & Maintenance at the National Agency of Dams and Transfers. He had

several internships at the UAq EMC Laboratory, University of L'Aquila, Italy. His main research interests are wave propagation, wiring networks diagnosis, non-destructive testing, electromagnetic compatibility, inverse modeling, optimization techniques and dams control and monitoring.

Houssem R. E. H. Bouchekara is an Associate Professor in the Electrical Engineering Department of University of Freres Mentouri Constantine. He has received his B.S. in Electrical Engineering from University Mentouri Constantine, Algeria, in 2004. He has received his Master in Electronic Systems and Electrical Engineering from Polytechnic School of the University of Nantes, France, 2005. He received his Ph.D. in Electrical Engineering from Grenoble Institute of Technology, France, in 2008. His research interest includes: Optimization techniques, Magnetic refrigeration, Electromagnetics, Electric machines and Power systems.

Francesco de Paulis was born in L'Aquila, Italy in 1981. He received the Specialist degree (summa cum laude) in Electronic Engineering from University of L'Aquila, L'Aquila, Italy, in 2006, the M.S. degree in Electrical Engineering in May 2008 from Missouri University of Science and Technology (formerly University of Missouri-Rolla), USA, and the Ph.D. degree in Electrical and Information Engineering in 2012 from the University of L'Aquila, L'Aquila, Italy. He was involved in the research activities at the UAq EMC Laboratory from August 2004 to August 2006, L'Aquila, Italy and at the MST EMC Laboratory from August 2006 to May 2008, Rolla MO, USA. From June 2004 to June 2005 he had an internship at Selex Communications, L'Aquila, within the layout/SI/PI design group. He is currently a Research Assistant at the UAq EMC Laboratory, University of L'Aquila, Italy. His main research interests are in developing fast and efficient analysis techniques for SI/PI and design of high speed signals on PCB and packages, analysis and characterization of composite materials for shielding and absorbing materials, RF interference in mixed-signal system, TSVs in silicon chips and interposers, EMI problem investigation, remote fault and degraded joint detection in power transmission lines.

Mostafa Kamel Smail is an Associate Professor in the Aerospace Systems Department of Polytechnic Institute of Advanced Science – Paris – France. He received the master degree in Components and Antennas for Telecommunications in 2007 and the Ph.D. degree from University of Paris-Sud XI, France in 2010. His current research interests are wave propagation modeling, reliability of wiring, electromagnetic compatibility and Inverse modeling.

Antonio Orlandi (M'90-SM'97-F'07) was born in Milan, Italy in 1963. He received the Laurea degree in Electrical Engineering from the University of Rome "La Sapienza", Italy, in 1988 and the Ph.D. degree in Biomedical Engineering from the University "Campus Biomedico", Italy, in 2012. He was with the Department of Electrical Engineering, University of Rome "La Sapienza" from 1988 to 1990. Since 1990 he has been with the Department of Electrical Engineering of the University of L'Aquila where he is currently Full Professor and Chair of the UAq EMC Laboratory. Author of more than 300 technical papers, he has published in the field of electromagnetic compatibility in lightning protection systems and power drive systems. Current research interests are in the field of numerical methods and modeling techniques to approach signal/power integrity, EMC/EMI issues in high speed digital systems. Orlandi received the IEEE Transactions on Electromagnetic Compatibility Best Paper Award in 1997, IEEE Transactions on Advanced Packaging Best Paper Award in 2011, the IEEE EMC Society Technical Achievement Award in 2003 and 2012 the IBM Shared University Research Award in 2004, 2005, 2006 and 2012, the CST University Award in 2004, the IEEE International Symposium on EMC Best Paper Award in 2009, 2010, 2013, the Designcon Best Paper Award in 2011 and 2012 and the IEEE Transactions on Electromagnetic Compatibility Best Paper Award Honorable Mention in 2015. He is co-recipient of the 2015 CISCO University Program Fund Award on "TSV modeling and measurement". From 1996 to 2000, and from 2010 up to December 2015 has been Associate Editor of the IEEE Transactions on Electromagnetic Compatibility. Since January 2016 he is the Editor in Chief of the IEEE Transactions on Electromagnetic Compatibility.

Rabia Mehasni was born in Grarem, Algeria in 1970. He received the Ph.D. in Electrical Engineering from the University of Constantine, Algeria in 2007. He is with the Department of Electrical Engineering, University of Constantine since 2000. He is currently Professor and Member of the LEC Laboratory. He has published in the field of magnetic separation. His research interests are in the field of numerical methods and modeling techniques to approach the multidisciplinary problems.

Compact UWB Antenna with Triple Band-Notches Using C-Shaped and S-Shaped Structures

Zhenyang Ma [1], Feifei Dong [2], Zheng Han [3], Shaocheng Han [3], and Qiannan Xue [1]

[1] Tianjin Key Laboratory of Civil Aircraft Airworthiness and Maintenance
Civil Aviation University of China, Tianjin, 300300, China
zyma@mail.xidian.edu.cn, qiannanxue@163.com

[2] Chengdu Monitoring Station of the State Radio Monitoring Center
Chengdu, 610000, China
dong.f.f@srrc.org.cn

[3] Basic Experimental Center
Civil Aviation University of China, Tianjin, 300300, China
hanzhengcauc@163.com, schan_cauc@163.com

Abstract ─ A semi-ellipse planar monopole UWB antenna with triple band-notched characteristics is presented. The proposed antenna with three band notches can operate in 3-13.9 GHz which covers the UWB (3.1-10.6 GHz) frequency range. Triple band-notched characteristics is achieved by etching a C-shaped slot on main radiator and adding two novel modified S-shaped cells on either side of microstrip line. The antenna is designed to reject the WiMAX (3.3-3.7 GHz), WLAN (5.15-5.825 GHz), and the downlink of X-band satellite communication systems (7.25-7.75 GHz). The proposed antenna is designed on FR4 substrate of size 20×26×1 mm^3. Details of the antenna design and analysis are presented in this paper.

Index Terms ─ Modified S-shaped structure, semi-ellipse antenna, triple notched bands, UWB.

I. INTRODUCTION

With the rapid development of ultra wideband technology, UWB antennas with band-notched characteristics have gained wide attention in academic fields. Over the UWB frequency range, there are some other wireless communication systems, such as microwave access (WiMAX) in 3.3-3.7 GHz, wireless local-area network (WLAN) in 5.15-5.825 GHz and the downlink of X-band satellite communication systems in 7.25-7.75 GHz, etc. So, in order to filter the interference, new UWB antennas with band-notched characteristics need to be designed.

Lots of band-notched antennas have been proposed in literature. Some papers use the method of etching various types of slots in the patch of the antenna or ground floor (i.e., U-shaped [1-3], H-shaped [4-5], L-shaped [6], E-shaped [7], C-shaped [8-10], π-shaped [11], ɾ-shaped [12], and SRR-shaped [13-16]) to generate notched bands. In some other literatures, the rejection bands can also be realized by adding various structures in antenna. In [17-19], various types of electromagnetic band gap (EBG) structures are applied to obtain notched bands. In [14-15, 20-21], some structures are placed adjacent to the feed-line to achieve one or two band-notched performance. Nevertheless, in order to achieve long current path, the structures closing to the feed-line general have large length, and one structure corresponds to one notched band. For instance, the size of the split rectangular ring filter is 6.2×16 mm^2 in [15], the L-shaped stub is 2.25×9.5 mm^2 in [20], and the G-shaped structure is 1.25×4.75 mm^2 in [21]. In this work, we have designed a novel modified S-shaped structure. From the results of the simulation, we can found the single modified S-shaped cell can generate dual notched bands, and we can increase current path with the modified S-shaped structure.

The proposed UWB antenna is composed of a semi-ellipse patch and fed by a microstrip line. A C-shaped slot is etching in the patch to achieve the WiMAX notched band, and two symmetrical modified S-shaped patches are put nearing the feed-line to avoid the interference of WLAN and the downlink frequency of X-band satellite communication systems. The simulation results of voltage standing wave radio (VSWR), current distribution, radiation pattern, gain, and efficiency are carried out using CST Microwave Studio.

II. ANTENNA DESIGN

The geometry of the proposed monopole antenna is illustrated in Fig. 1. A patch is printed on FR-4 substrate

Submitted On: November 26, 2015
Accepted On: March 18, 2016

with a relative dielectric constant of ε_r =4.4, size of 20×26 mm^2 and thickness of 1 mm. The semi-ellipse patch is the main radiating element with radius a=9 mm, b=14 mm. In order to achieve triple band-notches, one slit and two S-shaped cells are used in the proposed antenna, as shown in Fig. 1 (a). A rectangular ground plane with gap is placed on the other side of the substrate and a 50 Ω microstrip line is used to excite the monopole antenna. The dimensions of the designed antenna after optimization are as follows: W_1=20 mm, L_1=26 mm, L_2=2 mm, L_3=2 mm, W_2=11 mm, W_3=3 mm, L_4=8 mm, h=0.5 mm, L_5=2.45 mm, W_4=2 mm, d=0.2 mm, W_5=2 mm, L_6=2.6 mm, L_7=9.6 mm, W_6=0.3 mm, L_i=2.8 mm, L_o=4.3 mm.

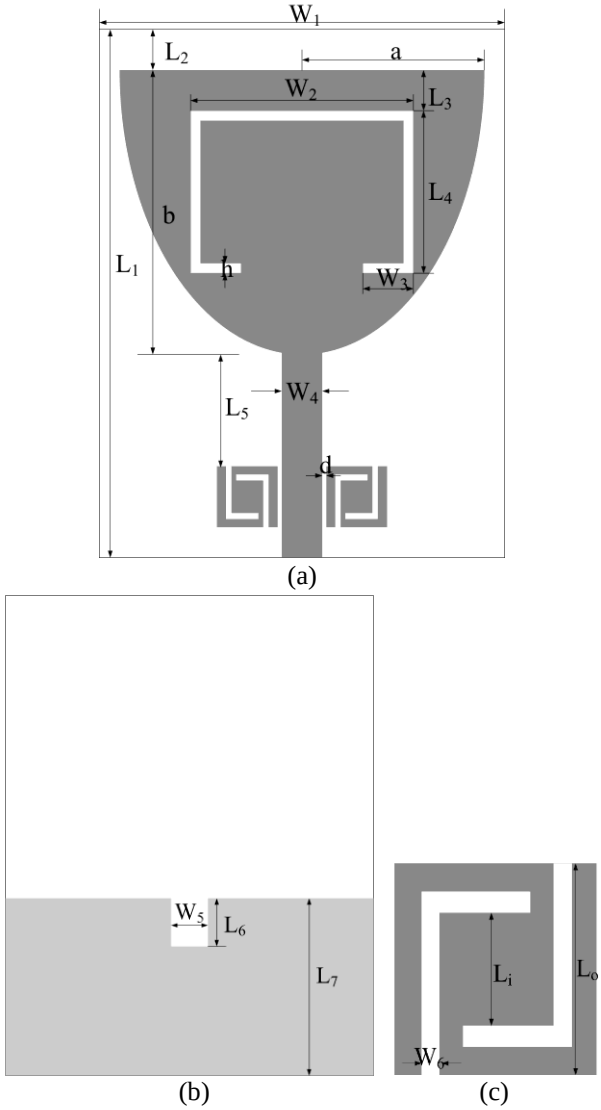

Fig. 1. Configuration and parameters of the UWB antenna: (a) top view, (b) bottom view, and (c) modified S-shaped cell.

A. C-shaped slot design

The design of the first notched band is obtained by etching a C-shaped slot in the semi-ellipse patch. Generally speaking, the length of the slot is about half wave-length at the center frequency of the notch-band. In [15], the notch frequency given the dimensions of the band notched feature can be assumed as:

$$f_{notch} = \frac{c}{2L\sqrt{\frac{\varepsilon_r + 1}{2}}}, \quad (1)$$

where f_{notch} is the center frequency of the notch band, c is the velocity of light in free space, L is the total length of the C-shaped slot, and ε_r is the dielectric constant. By adjusting the length of slot, we can get the optimal parameter, $L=W_2+W_3\times2+L_4\times2$.

B. Modified S-shaped patch design

The notched band can be achieved by adding some structures closing to the feed-line. In order to achieve long current path, structures with large length are needed to generate band-notched characteristics. In this paper, a modified S-shaped structure is proposed as shown in Fig. 1 (c). The modified S-shaped structure has the advantage of small size, relatively long current path, and dual band-notched characteristics. The two band stop filters are designed to reject the WLAN band (5.15-5.825 GHz) and the downlink of X-band satellite communication systems (7.25-7.75 GHz).

The modified S-shaped structure is composed by a square patch and two L-shaped slots with center symmetry. The structure is help to generate dual band-notched and increase current path. The size of the square patch, width and length of slots, and size of the central patch are the parameters that we need to be further studied based on previous research experience and CST software. By using CST Microwave Studio, we observe the influence of the parameters (L_o, L_i, and W_6) on the modified S-shaped structure. Simulations with different variables are carried out as shown in Fig. 2. The first notch corresponds to WLAN, and the second notch corresponds to the downlink frequency of X-band satellite communication systems. From Fig. 2 (a), it can be seen that with the increasing of L_o, the center frequencies of the two notched bands decrease and vice versa. And the outer length of L_o has more obvious effects on the first notch. Similarly, Fig. 2 (b) shows the center frequencies of the two notched bands decrease with the increasing of L_i. But the inner length of L_i has a larger impact on the second notch. Figure 2 (c) indicates the center frequencies of the two notched bands change with the slit width of W_6. So, by selecting proper parameters of the S-shaped patch, wanted band-notches will be received.

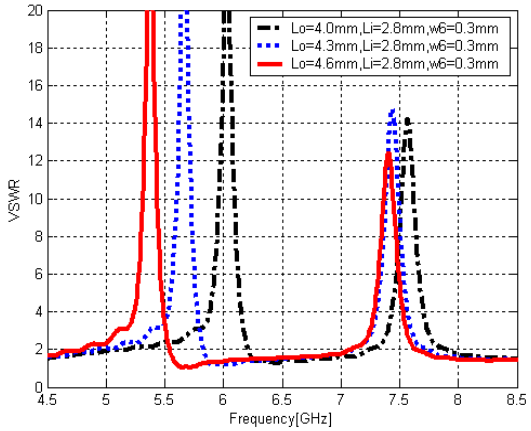

(a) L_o

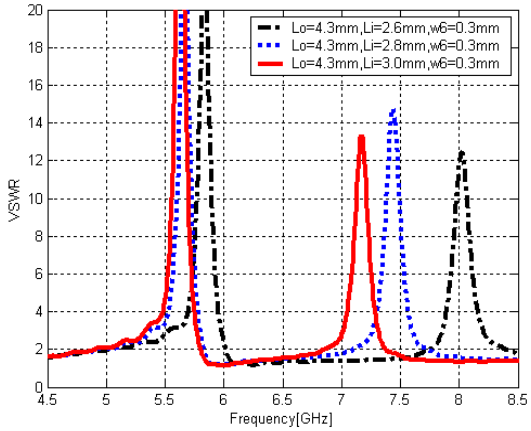

(b) L_i

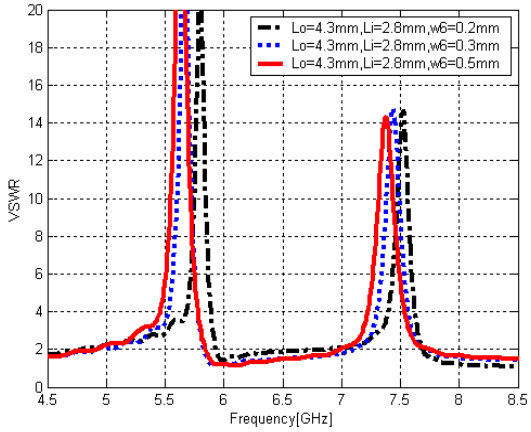

(c) W_6

Fig. 2. Simulated VSWR versus frequency with different parameters.

Furthermore, we study the effect of the symmetrical S-shaped structure on the property of the proposed antenna. The S-shaped cell equivalents two *LC* resonators, and it can produce two stop bands. We use symmetrical S-shaped cells on either side of the microstrip line rather than a single S-shaped cell on one side can enhance radiation effect and increase bandwidth as shown in Fig. 3.

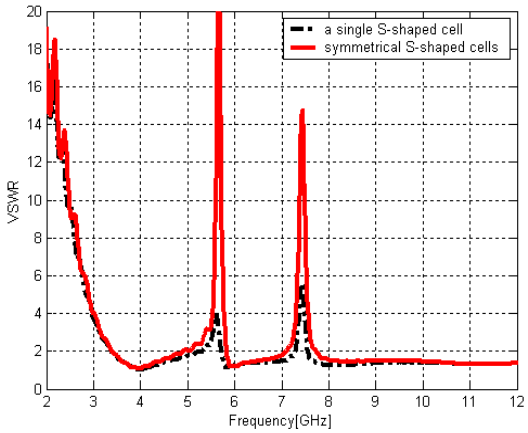

Fig. 3. Simulated VSWR of the antenna with a single S-shaped cell and symmetrical S-shaped cells.

III. RESULTS AND ANALYSIS

To better understand the design process and the band-notched characteristics of the proposed antenna, three different antennas were investigated for comparison. As shown in Fig. 4, antenna (a) is a UWB antenna with a C-shaped slot resonator in the radiation element. Antenna (b) is designed with two S-shaped resonator configurations on both sides of microstrip line. And both the C-shaped slot and S-shaped patches are integrated in antenna (c). The simulated VSWR of the three types of antennas are represented in Fig. 5. The VSWR of antenna (c) basically coincides with antenna (a) and (b). It indicates the structures in (a) and (b) are independent of each other. And the three notch bands are 3.23-3.77 GHz, 5.09-5.86 GHz and 7.11-7.77 GHz, which can filter the interference of WIMAX, WLAN and the downlink of X-band satellite communication systems, respectively.

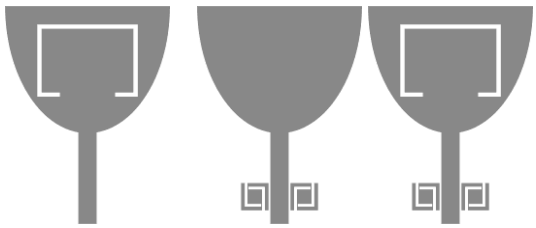

(a) (b) (c)

Fig. 4. Three types of antennas: (a) UWB antenna with C-shaped slot, (b) UWB antenna with S-shaped patches, and (c) proposed UWB antenna.

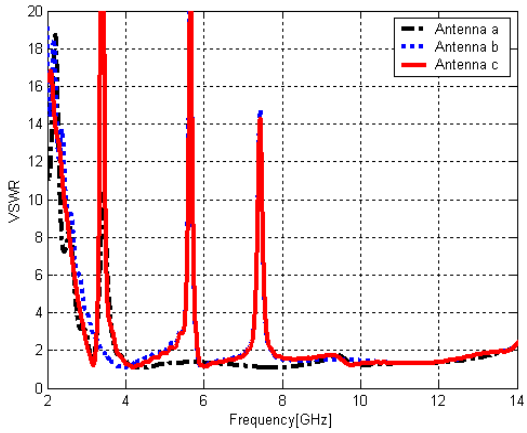

Fig. 5. Simulated VSWR of three types of antennas.

The simulated current distribution of the proposed antenna at frequency of 3.4, 5.6, 7.4, and 9 GHz is presented in Fig. 6. It can be observed in Fig. 6 (a) that the current concentrated around the C-shaped slot, and only a small amount of current flows on the other area at 3.4 GHz. Similarly, we can see more and stronger current distributions on the two S-shaped patches than any other area at 5.6 and 7.4 GHz in Figs. 6 (b) and (c). Most of the current is drawn to band notched structures at notched frequencies. In other words, the antenna resonates near the notched frequencies, and the energy cannot be radiated effectively. Compared with current distribution at notched frequencies, the current flows along the feed and wave is propagated in forward to the antenna at pass frequency form Fig. 6 (d). Also, the current density is smaller than the other three pictures. The current distribution results confirm that the independence of the C-shaped slot and S-shaped patches, and we can change the rejection characteristic of antenna by changing the structure.

Figure 7 depicts the radiation patterns in both E- and H-planes at four frequencies of 4, 6, 8 and 10 GHz. As can be seen from Fig. 8, the antenna has a stable bidirectional radiation patterns in E-plane and nearly omni-directional radiation characteristic in H-plane over the whole UWB frequency range.

The simulated antenna gain and total efficiency is shown in Fig. 8. The gain varies approximately from 2 dBi to 5.2 dBi over the operating frequency range except three notched bands. And the gain is very low at the notched bands, which drops to -2.3 dBi at 3.4 GHz, -6.1 dBi at 5.7 GHz, and -0.38 dBi at 7.5 GHz. The radiation efficiency is bigger than 80% except three notched bands. The frequencies of the efficiency minimum are as the same as the gain, which verify the design of triple band-notched characteristics once again.

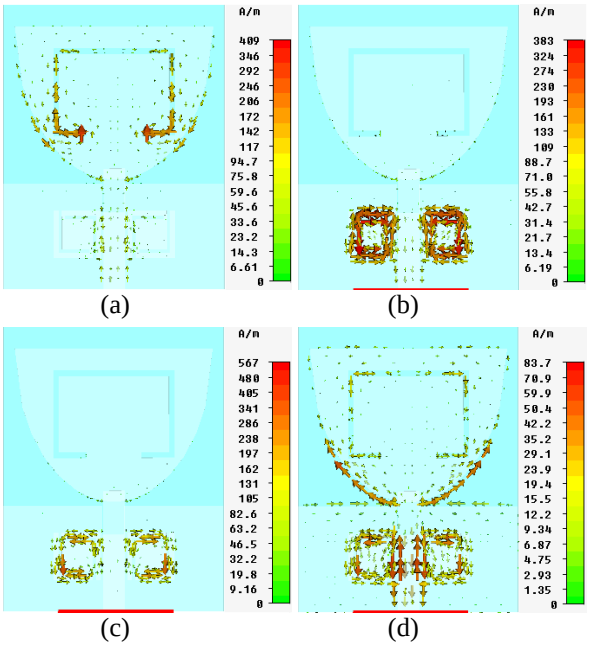

Fig. 6. Simulated current distribution at frequencies of: (a) 3.4 GHz, (b) 5.6 GHz, (c) 7.4 GHz, and (d) 9 GHz.

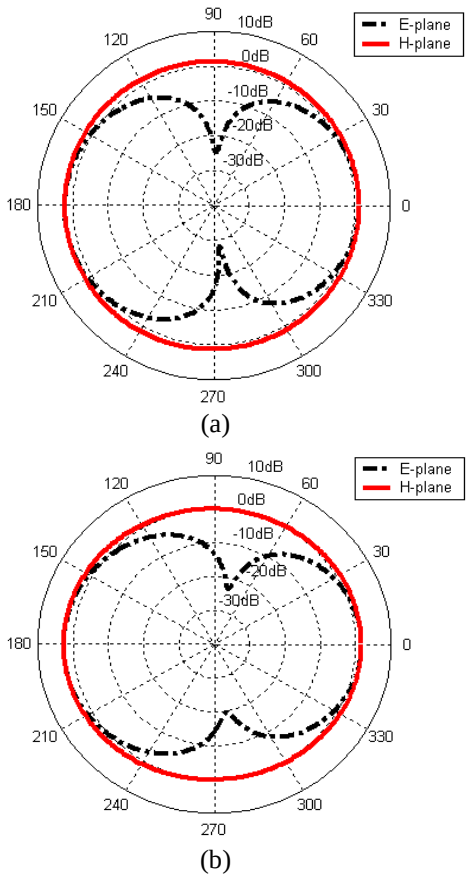

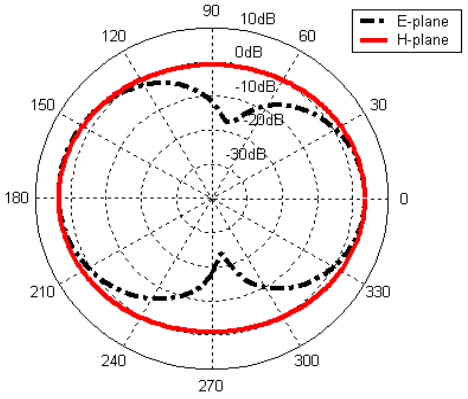

(c)

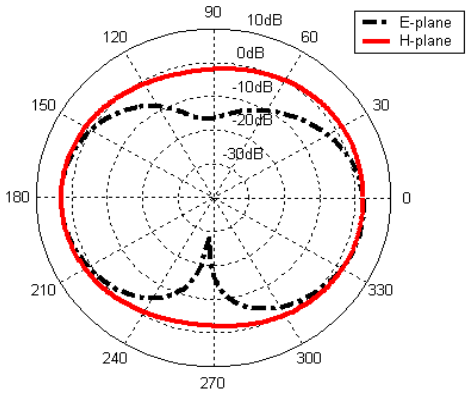

(d)

Fig. 7. Simulated radiation pattern at frequencies of: (a) 4 GHz, (b) 6 GHz, (c) 8 GHz, and (d) 10 GHz.

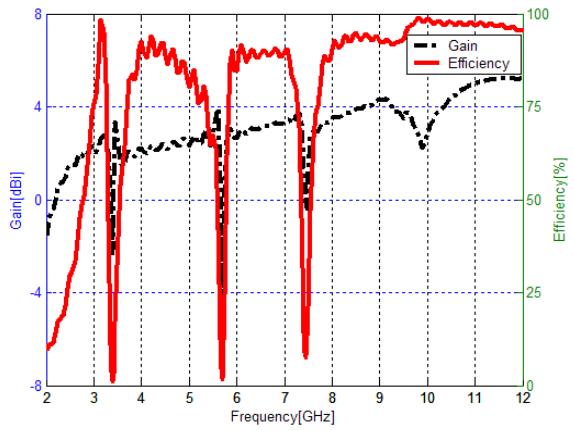

Fig. 8. Simulated gain and total efficiency of the proposed antenna.

At last, the proposed antenna and the other antennas with triple band-notched characteristics are compared in Table 1. From the table, the antenna in [12] has the similar size and performance with the proposed antenna, but it adopts four ɾ-shaped slits and a G-slot. So, it is more complex in structure and difficult to manufacture relative the antenna in this work. By comparison, the antenna proposed in this paper has certain advantages on the property.

Table 1: Performance comparison

Antennas	Dimensions (mm^2)	UWB Ranges (GHz)	Gain (dBi)
Ref. [1]	28×32	2.9-13.4	-4-4
Ref. [2]	42×46	3.1-13	2.8-6.6
Ref. [5]	24×35	Not reported	-2-11.5
Ref. [12]	20×24	2-17.6	0-5
This work	20×26	3-13.9	2.5-5

IV. CONCLUSION

A novel UWB antenna with triple notched bands has been presented. The proposed antenna has the advantages of small size, simple configuration and good band notched feature. By etching a C-shaped slot on the radiator and employing two symmetrically S-shaped patches, three bands are obtained to filter the interference of WiMAX, WLAN and the downlink frequency of X-band satellite communication systems in UWB band. The design is simulated and optimized by using CST Microwave Studio. From the results, stable radiation pattern, good gain and efficiency of the antenna make it suitable for UWB applications.

ACKNOWLEDGMENT

This research was supported by the Joint Funds of the National Natural Science Foundation of China (U1433105) and the Fundamental Research Funds for the Central Universities (3122014C024).

REFERENCES

[1] Q. Wang and Y. Zhang, "Design of a compact UWB antenna with triple band-notched characteristics," *International Journal of Antennas & Propagation*, vol. 2014, pp. 1-9, 2014.

[2] A. Shaker, S. H. Zainud-Deen, K. R. Mahmoud, and S. M. Ibrahem, "Compact Bluetooth/UWB antenna with multi-band notched characteristics," *Journal of Electromagnetic Analysis and Applications*, vol. 3, pp. 512-518, 2011.

[3] L. Xu, Y. Luo, and Z. Xin, "A compact monopole antenna for Bluetooth and UWB applications with dual band notched characteristics," *2013 International Workshop on Microwave and Millimeter Wave Circuits and System Technology (MMWCST). IEEE*, Mount Emei, China, pp. 50-53, October 2013.

[4] Y. S. Li, X. D. Yang, C. Y. Liu, and T. Jiang, "Compact CPW-fed ultra-wideband antenna with dual band-notched characteristics," *Electronics Letters*, vol. 46, no. 14, pp. 967-968, 2010.

[5] J. Y. Deng, Y. Z. Ying, S. G. Zhou, and Q. Z. Liu,

"Compact ultra-wideband antenna with tri-band notched characteristic," *Electronics Letters*, vol. 44, no. 21, pp. 1231-1233, 2008.

[6] Z. F. Yao, X. Wang, S. G. Zhou, L. Sun, B. H. Sun, and Q. Z. Liu, "A novel dual band-notched ultra-wideband slot antenna," *Antennas, Propagation and EM Theory, 2008. ISAPE 2008. 8th International Symposium on, IEEE*, Kunming, China, pp. 66-69, 2008.

[7] N. Ojaroudi, M. Ojaroudi, and N. Ghadimi, "UWB monopole antenna with WLAN frequency band-notched performance by using a pair of E-shaped slits," *Applied Computational Electromagnetics Society Journal*, vol. 28, no. 12, pp. 1244-1249, 2013.

[8] D. H. Bi and Z. Y. Yu, "Study of dual stopbands UWB antenna with U-slot and v-slot DGS," *Journal of Electromagnetic Waves & Applications*, vol. 22, no. 17, pp. 2335-2346, 2008.

[9] Q. X. Chu and Y. Y. Yang, "A compact ultra wideband antenna with 3.4/5.5 GHz dual band-notched characteristics," *IEEE Transactions on Antennas and Propagation*, vol. 56, no. 12, pp. 3637-3644, 2008.

[10] A. Boutejdar, A. A. Ibrahim, and E. P. Burte, "A compact multiple band-notched planer antenna with enhanced bandwidth using parasitic strip lumped capacitors and DGS-Technique," *TELKOMNIKA Indonesian, Journal of Electrical Engineering*, vol. 13, no. 2, pp. 203-208, 2015.

[11] Y. S. Li, W. Li, and Q. Ye, "A reconfigurable triple-notch-band antenna integrated with defected microstrip structure band-stop filter for ultra-wideband cognitive radio applications," *International Journal of Antenna &Propagation*, vol. 2013, pp. 721-724, 2013.

[12] A. Abdollahvand, A. Pirhadi, M. R. Hosseinnezhad, and H. Ebrahimian, "A compact UWB printed monopole antenna with triple-band notched characteristics," *Applied Computational Electromagnetics Society Journal*, vol. 30, no. 4, pp. 374-380, 2015.

[13] M. C. Tang, S. Q. Xiao, T. W. Deng, D. Wang, J. Guan, B. Z. Wang, and G. D. Ge,"Compact UWB antenna with multiple band-notches for WiMAX and WLAN," *IEEE Transactions on Antennas and Propagation*, vol. 59, no. 4, pp. 1372-1376, 2011.

[14] N. Wang and P. Gao, "A novel printed UWB and Bluetooth antenna with quad band-notched characteristics," *2013 International Workshop on Microwave and Millimeter Wave Circuits and System Technology (MMWCST)*, Mount Emei, China, pp. 150-153, October 2013.

[15] Z. Q. Li and C. L. Ruan, "A small integrated bluetooth and UWB antenna with WLAN band-notched characteristic," *2010 International Symposium on Signals Systems and Electronics (ISSSE)*, Nanjing, China, pp. 1-4, September 2010.

[16] Y. Minyeong and L. Sungjoon, "SRR- and CSRR-loaded ultra-wideband (UWB) antenna with tri-band notch capability," *Journal of Electromagnetic Waves & Applications*, vol. 27, no. 17, pp. 2190-2197, 2013.

[17] H. Liu and Z. Xu, "Design of UWB monopole antenna with dual notched bands using one modified electromagnetic-bandgap structure," *The Scientific World Journal*, vol. 2013, pp. 1-9, 2013.

[18] P. Kumar and Z. C. Alex, "Realization of band-notch UWB monopole antenna using AMC structure," *International Journal of Engineering & Technology*, vol. 5, no. 3, pp. 3020-3028, 2013.

[19] T. Y. Yang, C. Y. Song, W. W. Lin, and X. L. Yang, "A new band-notched UWB antenna based on EBG structure," *2013 International Workshop on Microwave and Millimeter Wave Circuits and System Technology (MMWCST)*, Mount Emei, China, pp. 146-149, October 2013.

[20] M. Naser-Moghadasi and A. A. Kalteh, "Elliptical slot antenna with dual band-notched characteristics for UWB applications," *Applied Computational Electromagnetics Society Journal*, vol. 30, no. 5, pp. 558-563, 2015.

[21] S. Ojaroudi, Y. Ojaroudi, N. Ghadimi, and N. Ojaroudi, "UWB monopole antenna with dual band-stop performance using G-shaped SRR and SIR structures at feed line," *Applied Computational Electromagnetics Society Journal*, vol. 29, no. 10, pp. 807-812, 2014.

Zhenyang Ma received the B.S. degree in Applied Physics from Shandong Normal University, Jinan, China, in 2008, and the Ph.D. degree in Microelectronics and Solid State Electronics from XiDian University, Xi'an, China, in 2013. His research interests include VLSI technology and reliability, the damage effect and mechanism of micro-devices and circuits induced by high-power microwaves and lightning/HIRF protection technology.

Feifei Dong was born in Gansu Province. She graduated from the University of Electronic Science and Technology of China (UESTC) in 2009. Now she is working for State Radio Regulating Committee. Her research interests are the radio monitoring, antenna and magnetron design.

Zheng Han received the B.S. degree in Communication Engineering from Tianjin University of Technology in 2006, and the M.S. degree in Signal and Information Processing from Civil Aviation University of China in 2009. Her research interests include analysis and design of microstrip antenna, ultra-wideband antenna, and electromagnetic compatibility of airborne equipment.

Shaocheng Han received the B.S. degree in Information and Communication Engineering from North University of China in 2004, and the M.S. degree in Signal and Information Processing from Civil Aviation University of China in 2009. His research interests include image processing, digital watermarking and finger vein identification.

Qiannan Xue received the B.S. degree in Physical Electronics from Institute of Electronics, Chinese Academy of Sciences, China, in 2012. Her research interests include Micro Sensor and System, Microwave Sensor, System on a Chip, and Wireless Sensor Network.

FR4-Only Microstrip Reflectarray Antennas for 5.8 GHz Dual-Polarized Wireless Bridges

Babak Honarbakhsh

Department of Electrical Engineering
Shahid Beheshti University, Tehran, 1983963113, IRAN
b_honarbakhsh@sbu.ac.ir

Abstract ─ Low-cost antennas are suggested for 5.8 GHz narrow-band, low-power and dual-polarized wireless bridges based on pure microstrip flat reflectarrays. A single layer of the cheapFR4 epoxy is exploited as the substrate for both of the feed and reflector. Detailed design procedure for the feed is reported. Three different elements are used for designing the reflector including rectangular dipole, unbalanced cross and square patch. Using method of moments, performance of the designs is compared from various aspects, including reflector diameter, computational cost, gain, half-power beam-width and polarization purity.

Index Terms ─ Cross-polarization, dual-polarized, ethernet, FR4, microstrip, reflectarray, WiMAX.

I. INTRODUCTION

In spite of their relative ease of fabrication, microstrip reflectarray antennas (MRAs) [1], have not yet replaced parabolic reflectors in commercial systems. This is mainly due to high-cost of low-loss microstrip substrates which makes them expensive even in mass production. At present, wireless bridges are seen to be responsive for many commercial applications and are often narrowband and low-power [2, 3]; e.g., fixed point-to-point (PTP) ethernet and WiMAX links. Specifically, channel bandwidths are in the order of 10 MHz at 5.8 GHz with output power about 30 dBm. Among possible architectures, dual-polarized systems are one of the most attractive. Such systems can be considered as a 2×2 wireless MIMO communication system with polarization diversity and can be exploited in both of LOS and NLOS links [2]. The effective ranges of these bridges can be up to 250 km, using high-gain out-door antennas. Currently, suggestions of producers are limited to parabolic reflectors [2].

Thus far, some attempts have been taken for lowering the cost of MRAs [4-12]. Specifically, the idea of exploiting the FR4 epoxy in the flat reflector is formerly enlightened in [5]. Yet, in all of these works, either the dielectric media of the reflector is double-layer [4, 7, 8-9, 10], or exploits a low-loss dielectric [4, 7, 12] or the feed antenna is not microstrip [4-7, 9-12].

In the present work, low-cost antennas are suggested for narrow-band, low-power and dual-polarized wireless bridges based on pure microstrip flat reflectarrays. A single layer of the cheap FR4 epoxy is exploited as the substrate for both of the feed and reflector. A complete design is suggested for 5.8 GHz PTP applications, including detailed design procedure of the feed. Three different re-radiating elements are used for designing the reflector, i.e., rectangular dipole, unbalanced cross and square patch. Based on full-wave simulation, performance of the designs is compared from various aspects of reflector diameter (D), computational cost, gain, half-power beam-width (HPBW) and polarization purity. During the paper, the dielectric constant, loss tangent and height of the FR4 is assumed to be 4.4, 0.02 and 1.6 mm, respectively. The relatively large dielectric thickness is selected to ensure mechanical robustness to make the designs appropriate for out-door applications. Simulation results are carried out using 32-bit FEKO® suit 5.5 software.

II. ANTENNA SYSTEM ARCITECHTURES

The desired specifications of the antenna system are: low-cost, simple-to-realize, high-isolation and low cross-polarization (X-pol). To satisfy the first two properties, both of the feed and reflector are selected to be single-layer microstrip with FR4 substrate. Due to inevitable excitation of surface waves in the microstrip substrate, high port isolation can be reached using two separated single-polarized feeding microstrip antennas (MSAs). High-polarization purity is achieved by proper selection of reflector elements. Three simple-to-realize such structures are dipole, cross and square patch. Since dipoles support only one polarization, their exploitation required two individual single-polarized reflectors. In contrast, cross and square supports both polarization and thus, one dual-polarized reflector suffices. However, the design tolerance of cross is less than the others. For reducing the blockage, offset-feed configuration is selected with $\theta_i = 30°$ illumination angle with respect to the reflector normal direction. The said two antenna

Submitted On: November 25, 2015
Accepted On: February 26, 2016

systems are schematically described in Fig. 1, which are in accordance with the solutions suggested in [2].

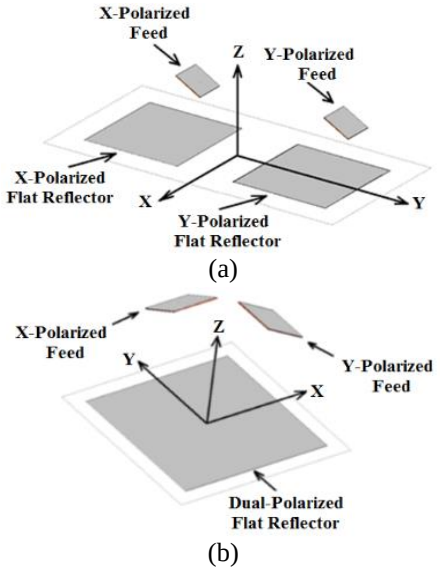

Fig. 1. Responsive antenna system architectures: (a) double-feed single-polarized MSA, and (b) double-feed dual-polarized MSA.

III. MICROSTRIP FEED DESIGN

It is aimed to feed the reflector by single-layered linear-polarized MSAs with FR4 substrate. Since one of the most important design criteria is polarization purity, the feed is designed to provide low X-pol. The normal range of F/D is 0.3 to 1.0 [13], where F designates the focal length of the reflector. Higher values of F/D lead to better X-pol performance at the cost of larger dimensions [13]. Thus, a proper feed should marginally provide $F/D \cong 1$. Following [14], the feed pattern is assumed to be of the form $\cos^n\theta$. As the first feed scheme, a single square patch on a finite square substrate is studied, as depicted in Fig. 2. The side lengths of the patch and the substrate are $L_p \cong \lambda_g/2$ and $L_s = 3\lambda_0/2$, respectively, where λ_0 is free-space wavelength and $\lambda_g = \lambda_0/\sqrt{\varepsilon_r}$. The corresponding radiation pattern is depicted in Fig. 3. This design is improper, due to pattern asymmetry. Nevertheless, E-plane pattern and its related efficiencies are computed and reported in Figs. 4 and 5, respectively [14]. As usual, illumination, spillover and total efficiency are, respectively, designated by η_i, η_s and η. The optimum valued for F/D is 0.4 which is far from unity and leads to poor η.

Next, a 2×2 array of square patches is investigated. This scheme is depicted in Fig. 6, where L_s and L_p are the same as the previous case and the length L is used as the optimization parameter to provide $F/D \cong 1$. Noting to Fig. 7, the optimum value for L is 15 mm, ensuring the most symmetric pattern due to the close values of F/D in E- and H-planes. The length L, also, affects the reflection from the feed, as reported in Fig. 8 for L = 15 and 18 mm, which shows superiority of L = 18 mm. Figure 9 indicates that the difference in η for the said values is negligible, suggesting L = 18 mm. However, since the wire port is used in simulations, it is likely that capacitive behaviour of the real connector compensates the shift in $|S_{11}|$ of the L = 15 mm case. Hence, L and F/D are taken to be 15 mm and 0.9, respectively. The radiation pattern is reported in Fig. 10, which in accordance to Fig. 7, is symmetric and ensures proper illumination of the reflector. Besides, its low X-pol, shown in Fig. 10 (b), ensures sufficient polarization purity for commercial applications. Thus, efficiency curves can be computed based on the average n factor of E- and H-plane patterns, which is found to be 7.69 [4]. The corresponding efficiency curves for the second feed scheme are depicted in Fig. 11.

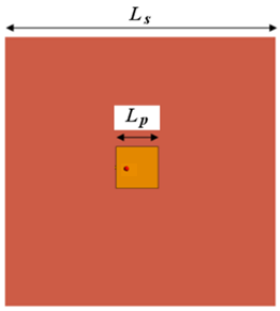

Fig. 2. The first feed with L_s = 78 mm and L_p = 12 mm (red spot: excitation).

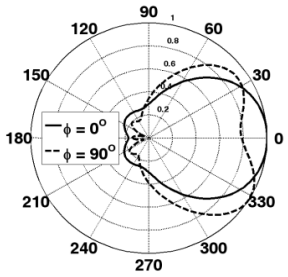

Fig. 3. Radiation patterns of the first feed.

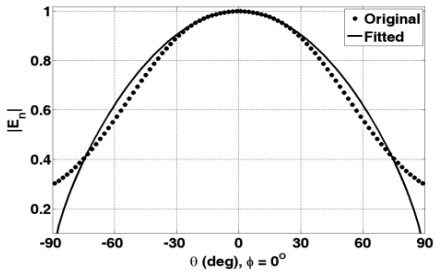

Fig. 4. E-plane pattern of the first feed (n = 0.69).

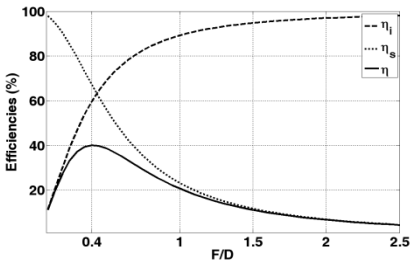

Fig. 5. *E*-plane efficiencies of the first feed.

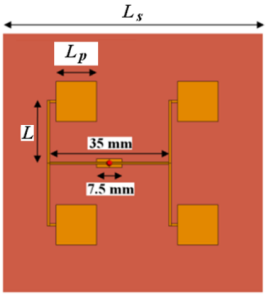

Fig. 6. The second feed (red spot: excitation).

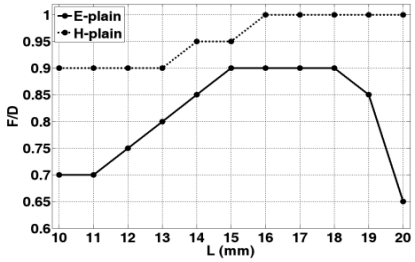

Fig. 7. *F*/*D* vs. *L* for the second feed.

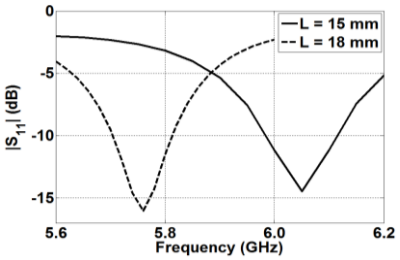

Fig. 8. Simulated $|S_{11}|$ for the second feed.

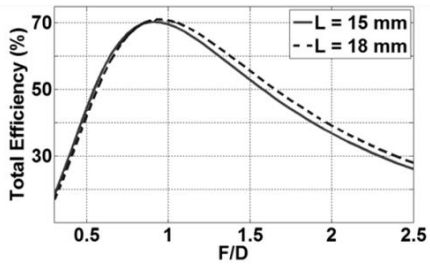

Fig. 9. Total efficiency vs. *F*/*D* for the second feed.

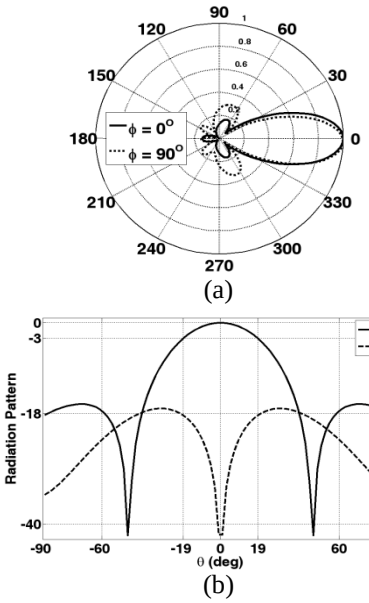

Fig. 10. Radiation pattern of the second feed: (a) Co-pol at orthogonal planes, and (b) Co- and X-pol at *E*-plane.

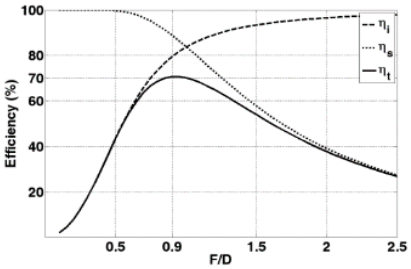

Fig. 11. Efficiencies of the second feed (n_{av} = 7.69).

IV. UNIT CELL DESIGN

To cover both antenna architectures introduced in Section II, three unit cells are investigated for designing the reflector: dipole, cross and square. Geometry of these cells is described in Fig. 12. These are selected due to their low fabrication complexity and low X-pol. The dipole width is taken to be 2.5 mm ≅ 0.05λ_0, ensuring negligible transversal current density distribution. This allows computing the delay characteristic of the cross by considering only one of its arms. Thus, delay response of the cross is assumed to be the same as the dipole. The delay characteristics of the dipole and square are reported in Fig. 13, assuming offset-fed configuration with illumination angle of θ_i = 30°.The dipole supports only one and the rest, supports both polarizations. It can be predicted that the square provides more gain due to its more metallic surface with respect to the others. Due to their narrow width, dipole and cross are expected to exhibit less X-pol compared to the square. However, the design tolerance of cross is less than the others. It should be noted that due to narrow bandwidth of commercial

wireless bridges, the narrow bandwidth of these unit cells is tolerable.

Although the infinite array approach is currently the most used method for computing the delay characteristic, here, the finite array approach is exploited wherein, a unit cell is surrounded by eight other cells of the same size with inter-element spacing of $P = 0.95\lambda_g$. This method is followed because of its less simulation time. Specifically, due to relatively large dielectric constant of FR4, even using a course mesh, the eigen-mode analysis becomes too slow at 5.8 GHz. Yet, using the said approach, Green's function of the substrate can be exploited which significantly speeds up the analysis.

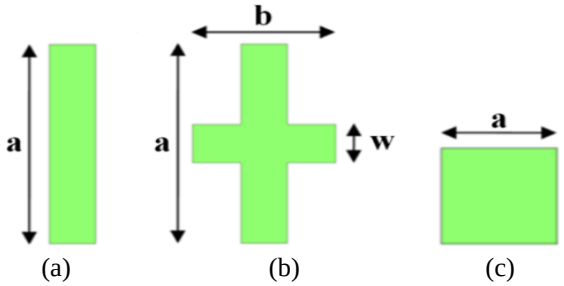

Fig. 12. Geometry of the investigated unit cells: (a) dipole, (b) cross, and (c) square.

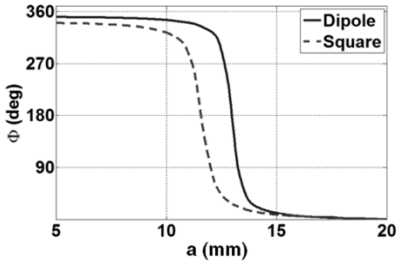

Fig. 13. Delay characteristics of unit cells.

V. MICROSTRIP REFLECTOR DESIGN AND PERFORMANCE COMPARISON

By the introduced unit cells, a variety of reflectors is designed with different number of elements (N) and analyzed using method of moments (MoM). For efficient usage of computational resources and minimizing the simulation time, three tricks are applied. The first is making use of symmetry for the feed antenna and reflectors with dipole and square elements. This cannot be done when cross elements are used due to the imposed asymmetry in the reflector. The second is infinite substrate assumption for reflectors and thus, exploitation of the Green's function. The third is decoupling the analysis of the feed and the reflector.

The reflectors are all square shaped, consisting of a single-layer of FR4, grounded by a metallic PEC plane. The dependence of N on D and the peak memory usage are reported, respectively, in Figs. 14 and 15. As can be seen, the required memory for the analysis of reflectors with square elements increases dramatically with N. This, put limitation on the range of N for full-wave simulation of MSAs with such elements. Noting to Fig. 16, gain of MSAs with dipole and cross elements are essentially the same. As well, it shows that MRA with square elements provides about 3 dB more gain with respect to the others. The HPBWs are reported in Fig. 17, showing that this parameter depends on D and not the element shape. Please note to monotonic increase of gain in Fig. 16 and monotonic decrease of HPBW in Fig. 17 as D increases. These can be regarded as a convergence analysis which validates the design procedure and the exploited simplifying tricks [15]. Comparison of the polarization purity of the designs can be made by Fig. 18, where the average X-pol in the HPBW is reported for MRAs with cross and square elements. This figure demonstrates that cross elements provide about 20 dB less X-pol compared to square elements. Since the said two elements have the same performance in the sense of HPBW, this result justifies using cross elements for secure dual-polarized links. Gain patterns of MRAs with cross and square elements with 22.8 dB gain and, respectively, 49 cm and 35 cm diameter are reported in Fig. 19. The related layout and the 3D pattern for MRA with cross elements are depicted in Figs. 20 and 21. Based on Figs. 16 and 17, the performance of dipole and cross elements is expected to be the same. This can be verified by considering the gain patterns of MRAs with the said elements and $D = 49$, which is depicted in Fig. 22. Thus, gain pattern of the high-gain low X-pol MRA with $D = 115$ cm can be predicted from its dipole equivalent, as depicted in Fig. 23.

It should be noted that all the results reported in this section are derived using only one feed antenna with single polarization. This may seem to be in contradiction with the claim of the work. Nevertheless, both of the architectures introduced in Fig. 1 ensure extension of the aforementioned results to the situation wherein both feed antennas illuminate the reflector with two orthogonal polarizations. This can be justified noting that first, in both of the responsive antenna systems the feed antennas are placed on separated substrates and second, the X-pol of the feeds are sufficiently low, as reported in Fig. 10 (b).

At last, the design procedure of the antenna system can be summarized as follows: First, the compromise should be made between X-pol and gain; this determines the shape of unit-cells. Second, the diameter of the reflector is determined based on the desired HPBW from Fig. 17. Third, the design tolerance determines the proper choice of architecture, shown in Fig. 1.

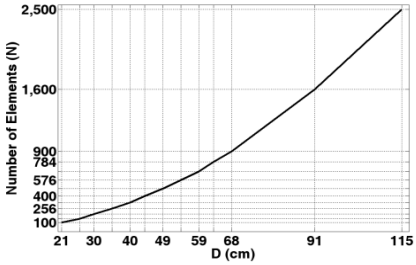

Fig. 14. Number of elements vs. reflector diameter.

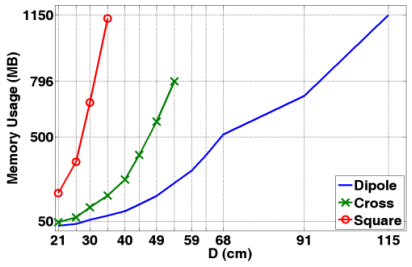

Fig. 15. Peak memory usage vs. *N*.

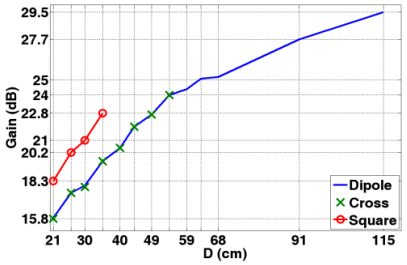

Fig. 16. Gain vs. *D*.

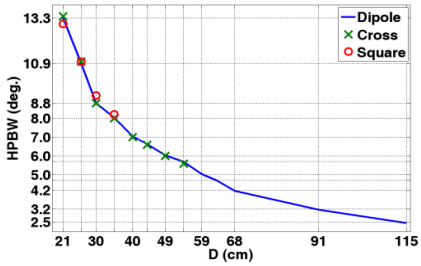

Fig. 17. Half-power beam-width vs. *D*.

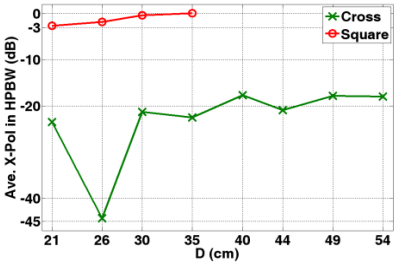

Fig. 18. Average X-pol in HPBW vs. *D*.

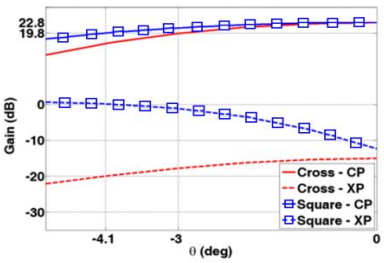

Fig. 19. Co-pol (CP) and X-pol (XP) gain patterns.

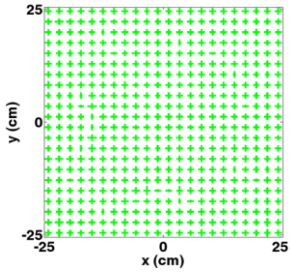

Fig. 20. MRA layout for D = 49 cm and cross elements.

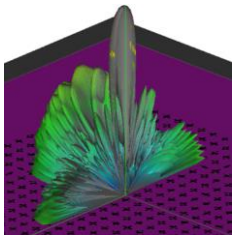

Fig. 21. Radiation pattern for D = 49 cm in dB.

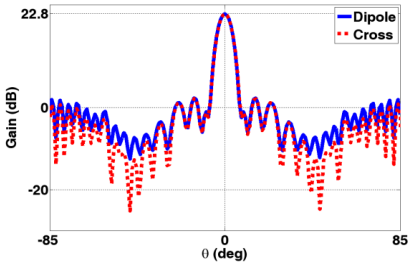

Fig. 22. Gain patterns for MRAs with D = 49 cm.

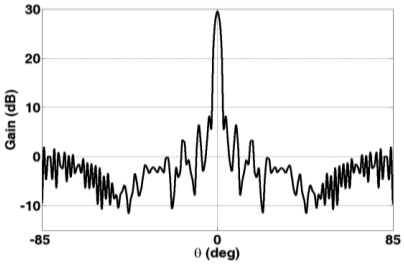

Fig. 23. Predicted gain pattern for MRA with D = 115 cm and unbalanced cross elements.

VI. CONCLUSION

Low-cost antenna architectures can be realized for dual-polarized commercial point-to-point wireless bridges using pure microstrip reflectarray antennas based on FR4 epoxy. A 2×2 array of square patches on a FR4 substrate can be used as a feed antenna for each of the link polarizations. Such a feed provides sufficient pattern symmetry and low cross-polarization. Rectangular dipole, unbalanced cross and square patches as reflector elements are demonstrated to be responsive for providing desired specifications. Cross elements can provide about 20 dB more polarization purity compared to square elements. However, square elements provide about 3 dB more gain compared to dipole and cross elements. Co-pol radiation pattern using dipole and cross elements are essentially the same. Half-power beam-width depends on the reflector diameters and not on the shape of reflector elements. Computational cost for designs based on dipole elements is considerably less than the others. The performance of MRAs based on square and cross elements can be well predicted from corresponding dipole designs.

REFERENCES

[1] J. Huang and A. Encinar, *Reflectarray Antennas*, New York: IEEE/John Wiley, 2008.

[2] *PTP Solutions Guide Motorola Fixed Point-to-Point Wireless Bridges*, Motorola Inc., 2008.

[3] *Cambium PTP 500 and PTP 300 Series User Guide*, Cambium Networks, 2012.

[4] Y. Pan, Y. Zhang, and S. Karimkashi, "Broadband low-cost reflectarray for multi-mission radar applications," *IEEE Radar Conference (RADAR)*, Atlanta, GA, pp. 613-617, 2012.

[5] J. Ethier, M. R. Chaharmir, J. Shaker, and D. Lee, "Development of novel low-cost reflectarrays," *IEEE Antennas Propagat. Mag.*, vol. 54, no. 3, pp. 277-287, 2012.

[6] L. Haitao, S. Gao, and L. Tian-Hong, "Low cost beam switchable reflectarray antenna," *Int. Workshop Smart Antennas (WSA)*, Dresden, pp. 8-11, 2012.

[7] E. Carrasco, M. Barba, J. A. Encinar, and M. Arrebola, "Design, manufacture and test of a low-cost shaped-beam reflectarray using a single layer of varying-sized printed dipoles," *IEEE Trans. Antennas Propagat.*, vol. 61, no. 6, pp. 3077-3085, 2013.

[8] K. Zhang, L. Jianzhou, W. Gao, and X. Jiadong, "Low-cost single-layer broadband reflectarray for satellite communications," *Antennas Propagat. Conf. (LAPC)*, Loughborough, pp. 78-83, 2013.

[9] K. Zhang, F. Yangyu, X. Jiadong, and Q. Chen, "Design of broadband, low cost single layer reflectarray using phoenix cell," *IEEE Region 10 TENCON Conf.*, Xi'an, pp. 1-4, 2013.

[10] G. Carluccio, A. Mazzinghi, and A. Freni, "Low cost complementary reflectarray for transportable radar applications," *ICEAA Conf.*, Palm Beach, pp. 723-725, 2014.

[11] Q. Wang, H. S. Zhen, C. J. Yu, and L. K. Peng, "Broadband low-cost reflectarray using modified double-square loop loaded by spiral stubs," *IEEE Trans. Antennas Propagat.*, vol. 63, no. 9, pp. 4224-4229, 2015.

[12] D. R. Prado, A. Campa, M. Arrebola, M. R. Pino, J. A. Encinar, and F. Las-Heras, "Design, manufacture and measurement of a low-cost reflectarray for global earth coverage," *IEEE Antennas Wireless Propagat. Lett.*, vol. 14, pp. 1-4, 2015.

[13] W. L. Stutzman and G. A. Thiele, *Antenna Theory and Design*, John Wiley, 1998.

[14] J. Huang, "Analysis of a microstrip reflectarray antenna for microspacecraft applications," *JPL TDA Progress Report*, no. 42-120, February 15, 1995.

[15] J. C. Rautio, "The microwave point of view on software validation," *IEEE Antennas Propagat. Mag.*, vol. 38, no. 2, pp. 68-71, 1996.

Babak Honarbakhsh born in Tehran, Iran, in 1981. He received his B.S., M.S. and Ph.D. degrees in Electrical Engineering, all from Amirkabir University of Technology (Tehran Polytechnic), in 2004, 2007 and 2012. He is currently an Assistant Professor in the Department of Electrical Engineering at Shahid Beheshti University. His research interest is CEM.

Optimal Design of PCS Ceramic Microwave Filters using the Differential Evolution Algorithm

Theodoros I. Kosmanis [1], Ioannis T. Rekanos [2], and Stelios P. Tsitsos [3]

[1] Department of Vehicles Engineering
Alexandrion Technological and Educational Institute, Thessaloniki, PO Box 141, GR-57400, Greece
kosmanis@vt.teithe.gr

[2] School of Electrical and Computer Engineering
Aristotle University, Thessaloniki, GR-54124, Greece
rekanos@auth.gr

[3] Department of Computer Engineering
Technological and Educational Institute of Central Macedonia, Serres, GR-62124, Greece
s.tsitsos@teicm.gr

Abstract ─ The optimal geometrical design of a ceramic microwave filter according to the specifications of the downlink band of the PCS-1900 mobile communications protocol is investigated in this paper. An efficient combination of the Differential Evolution Algorithm and the Finite Element Method leads to the optimal values of four design parameters.

Index Terms ─ Evolutionary algorithm, microwave filter design, PCS.

I. INTRODUCTION

A major issue in the design of modern microwave structures is the compliance with strict communication specifications, obtained mainly through optimal geometry characteristics [1]. The evident complexity of microwave structures connects the fulfilment of their specifications with a significant number of design parameters, mainly geometrical ones. The design is usually formulated as an optimization problem where the objective is to minimize an appropriately defined cost function. The cost function is nonlinear with respect to the design parameters with many local or even global minima. As a result, traditional deterministic optimisation techniques based on the use of the optimization function gradients (gradient-based techniques) do not guarantee a successful approach. They may easily be trapped in local minima, while the final optimal solution directly depends on the selection of the initial values of design parameters. Moreover, the gradient-based techniques may not be implemented in minimization problems due to the lack of convexity of the minimization function.

A more successful alternative to this problem may be attained by the so-called global optimization algorithms. Evolutionary algorithms such as the Particle Swarm Optimization (PSO) method [2] and the Differential Evolution Algorithm (DEA) [3] are very promising in achieving global optimization because they offer ease of implementation and faster convergence than the conventional gradient-based optimization methods. Furthermore, they have been successfully used in design and optimization problems of various scientific fields as well as computational electromagnetics [4-9]. The counterpart to their efficiency is the significant time consumption they require since the original simulation is multiply executed.

In this paper, the DEA is combined with the Finite Element Method (FEM) towards the optimal shape design of ceramic microwave filters in order to meet specific requirements. This type of filter is widely used in cellular telephony and operates under the Personal Communication System (PCS-1900) protocol, one of the three versions of the Global System for Mobile Communications (GSM). The optimal design of microwave filters, which satisfies the PCS-1900 downlink specifications, is investigated through a multi-parametric DEA-FEM analysis, where precision is of great importance.

II. THE PCS-1900 MICROWAVE FILTER

The ceramic microwave filter under design is meant to be used in one of the three versions of the GSM cellular communications and particularly the GSM-1900 or PCS-1900 as it is well known [1]. It is used mainly in the U.S.A. and characterized by two bands; the uplink frequency band (1825-1885 MHz), and the downlink frequency band (1930-1990 MHz). The interest of the present work is focused on the downlink band, which is

Submitted On: November 14, 2015
Accepted On: March 18, 2016

characterized by the specifications given in Table 1.

Table 1: Filter specifications in the downlink band

Specification	Desired Value
Lower cut-off frequency	1930 MHz
Upper cut-off frequency	1990 MHz
Central frequency	1960 MHz
Bandwidth	60 MHz
Band pass insertion loss	< -3 dB
Band pass return loss	> -10 dB
Band stop attenuation	-7 dB at 1910 MHz, -17 dB at 2090 MHz

Figure 1 presents a 3D view of a PCS ceramic microwave band-pass filter used in mobile handsets [10]. Figures 2 (a) and 2 (b) illustrate its facial and top cut respectively. The filter consists of three metalized coupled $\lambda/4$ resonators, where λ is the wavelength corresponding to the central frequency of the pass-band. Each resonator employs a metallic cup that defines the coupling capacitances between the resonators and the loading capacitances between the resonators and the metallic case of the filter. The air part appearing at the top of the filter was used to prevent the electromagnetic energy radiation. The surrounding ceramic material has a relative dielectric constant, ε_r=92 and dielectric losses, tanδ=0.0007, while the material of the resonators, the metallic cups and the filter case is a silver paste with a conductivity of 5.219×10^7 S/m.

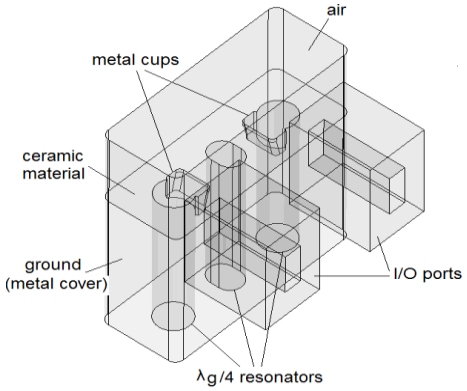

Fig. 1. 3D view of the PCS ceramic filter.

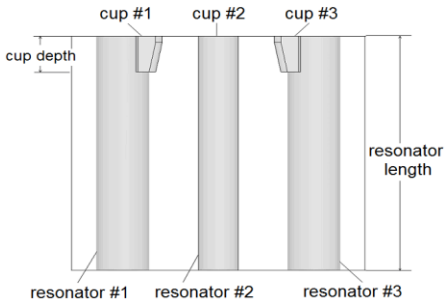

(a)

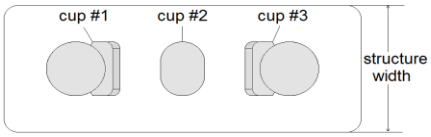

(b)

Fig. 2. PCS ceramic filter: (a) side view and (b) top view.

III. DESIGN TECHNIQUE

The overall design technique aimed at the compliance of the ceramic filter (described in the previous section) with the PCS-1900 downlink band specifications of Table 1. Particularly, the values of four geometrical characteristics of the microwave filter that allow this compliance are investigated. These are the resonator length, the structure width, the central resonator width and the cup depth of the side resonators.

The optimization scheme used for this purpose was an efficient combination of the DEA and the FEM. The overall algorithm is implemented by a two-step procedure, which is repeated iteratively. In the first step, for a given set of the design parameters values, the electromagnetic analysis problem is solved using the Ansoft HFSS [11] computational package, which is based on FEM [12]. In the second step, the DEA updates the values of the design parameters based on their performance in meeting the design specifications.

A. Differential Evolution Algorithm (DEA)

The common characteristic of all optimization algorithms that are based on the principles of evolutionary optimization algorithms is the mimic of natural phenomena and mechanisms for the quest of an optimal solution [3]. They are based on a population of possible solutions and not on a unique one, unlike standard optimization algorithms.

For the design of the PCS-1900 microwave filter, the initial population of DEA was selected to consist of 100 members (candidate solutions). Each member was characterized by a different set of values of the four design parameters, thus providing a different FEM solution of the microwave filter analysis problem.

The initial population of the algorithm was randomly generated where each design parameter is uniformly distributed within specific value ranges whose lower and upper limits are given in Table 2. Each new generation was produced iteratively after three operators, namely mutation, crossover and selection were applied on each candidate solution, assuring that the best candidate solution (the one with the lowest cost function) of the new generation performs at least as good as the best candidate of the previous generation. This procedure is repeated iteratively until the cost function of the candidate solution is lower than a predefined threshold, or until a predefined total number of generations have been generated. The DEA algorithm was implemented in

the MATLAB environment. The heart of the overall procedure is a MATLAB code that, first, updates the design parameters of the filter and, second, it calls the HFSS for the evaluation of the filter performance. The MATLAB/HFSS interface can be easily created. The time required for the algorithm to complete one optimization depends on the initial solutions that are randomly produced and the discretization required by HFSS. However, the average execution time was found to be around 3 hours.

The choice of the cost function is of crucial importance for the convergence of the algorithm. For the case of the PCS-1900 microwave filter the cost function was selected to be the following:

$$C = \begin{cases} 160 - 4\left|S_{11}^{\mathrm{dB}}(\mathrm{f_c})\right| + 20\sum_{k=1}^{2}\left|3 + S_{12}^{\mathrm{dB}}(\mathrm{f_k})\right| & if\ S_{11}^{dB}(f_c) > -40\,dB \\ 20\sum_{k=1}^{2}\left|3 + S_{12}^{\mathrm{dB}}(\mathrm{f_k})\right| & if\ S_{11}^{dB}(f_c) \le -40\,dB, \end{cases} \quad (1)$$

where f_1 = 1.93 GHz, f_2 = 1.99 GHz and f_c = 1.96 GHz. S_{11} and S_{12} stand for the S-parameters of the microwave filter. In (1), coefficient 3 corresponds to the -3dB of the reflection coefficient (parameter S_{11}) that is the goal in the upper and lower cut-off frequencies of the filter. Coefficients 160, 4 and 20 are produced via a trial and error procedure. However, coefficients 160 and 4 are connected via the maximum 40 dB which was set as a goal for the filter's central frequency reflection coefficient (parameter S_{11}). The maximum number of iterations of the DEA-FEM design technique was 250. The value of the cost function, corresponding to the best candidate solution in each generation versus the number of iterations is depicted in Fig. 3. The specific figure was chosen to prove the convergence of the algorithm to a specific solution following a convergence stopping criterion.

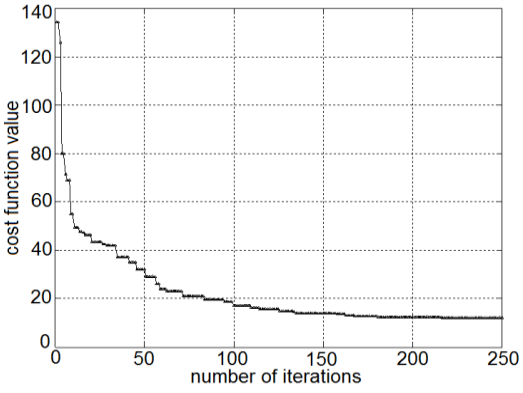

Fig. 3. Cost function vs. number of iterations.

B. Results and discussion

The final optimal solution resulted from the optimization algorithm was found to meet the specifications of Table 1. This is clearly illustrated in Fig. 4 where the S-parameter values are presented. In this figure the scattering parameters S_{11} and S_{21} of the filter's response are compared in two cases. The best initial solution corresponds to the solution which results in a minimum value of the cost function, among all candidate solutions produced at the very first step of the simulation. The optimal solution corresponds to the solution which results in a minimum value of the cost function as a result of the overall simulation. The extracted results are compared well with the results obtained by the HFSS and an equivalent circuit frequency response as presented in [13]. The ceramic filter under investigation was manufactured by TDK Corporation, Japan. Some technical details were made available to the authors; however, measured results were not made available. Measured results are available for a similar technology GSM filter in the 900 MHz frequency band [14].

In particular, the scattering parameters S_{11} and S_{12} of the best candidate solution in the initial population are compared with those of the final optimal solution. It is evident that the optimal solution completely meets the bandwidth requirements of the PCS-1900 protocol. The values of the design parameters that led to the optimal solution are given in Table 2. The upper and lower dimension bounds were determined according to the manufacturing process and the dimensional tolerances information given by the manufacturer (TDK Corporation, Japan).

The variation in the design parameter values during simulation is not presented, since any effort to plot the design parameters would lead to rather abstract figures. Having 100 candidate solutions and a maximum of 250 iterations would give four sets of almost 2000 values. Moreover, the optimal solution per iteration is a function of all four design parameters which means that they should all be treated as one. The ideal representation would be in a four-dimensional space.

Table 2: Design parameter values

Design Parameter	Lower Limit (mm)	Upper Limit (mm)	Final Value (mm)
Resonator length	3.60	4.30	3.9709
Structure width	0.75	1.50	0.6704
Cup depth	0.15	0.70	0.4552
Resonator radius	0.01	0.32	0.2988

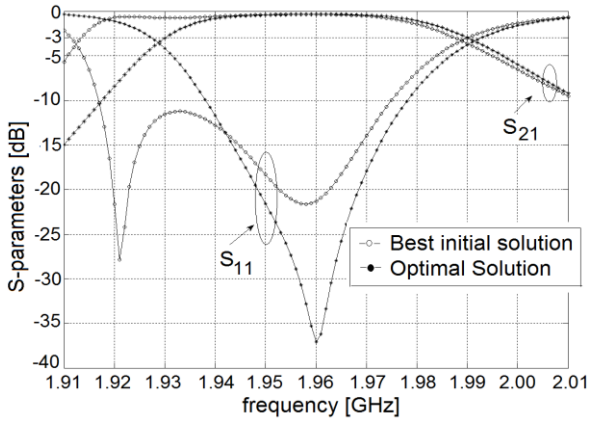

Fig. 4. S-parameters of the microwave PCS filter before and after optimization.

ACKNOWLEDGMENT

The authors wish to acknowledge the financial support provided by the Research Committee of the Technological and Educational Institute (T.E.I.) of Central Macedonia, Serres, Greece, under grant SAT/IC/020316-34P/6.

REFERENCES

[1] A. F. Molisch, *Wireless Communications*, J. Wiley & Sons Ltd., 2005.

[2] J. Kennedy and R. C. Eberhart, *Swarm Intelligence*, Morgan Kaufmann, 2001.

[3] R. Storn and K. Price, "Differential evolution – A simple and efficient heuristic for global optimization over continuous space," *J. Global Optimization*, vol. 11, pp. 341-359, 1997.

[4] J. Robinson and Y. Rahmat-Samii, "Particle swarm optimization in electromagnetic," *IEEE Trans. Antennas Propagat.*, vol. AP-52, pp. 397-407, 2004.

[5] S. Caorsi, M. Donelli, A. Lommi, and A. Massa, "Location and imaging of two-dimensional scatterers by using a particle swarm algorithm," *J. Electromagn. Waves Applicat*., vol. 18, pp. 481-494, 2004.

[6] A. Qing, "Electromagnetic inverse scattering of multiple two-dimensional perfectly conducting objects by a differential evolution strategy," *IEEE Trans. Antennas Propagat*., vol. AP-51, pp. 1251-1262, 2003.

[7] I. T. Rekanos and T. V. Yioultsis, "Convergence enhancement for the vector finite element modeling of microwaves and antennas via differential evolution," *AEÜ Int. J. Electron. Commun.*, vol. 60, pp. 428-434, 2006.

[8] I. T. Rekanos, "Shape reconstruction of a perfectly conducting scatterer using differential evolution and particle swarm optimization," *IEEE Trans. Geosci. Remote Sens*., vol. 46, pp. 1967-1974, 2008.

[9] K. E. Parsopoulos and M. N. Vrahatis, "Recent approaches to global optimization problems through particle swarm optimization," *Natural Comput.*, vol. 1, pp. 235-306, 2002.

[10] S. Tsitsos, A. A. P. Gibson, L. E. Davis, and I. T. Rekanos, "Design of a 3-pole PCS-type monoblock filter using an equivalent circuit approach," *AEÜ Int. J. Electron. Commun.*, vol. 60, pp. 638-646, 2006.

[11] Ansoft High Frequency Structure Simulation (HFSS), ver. 10, Ansoft Corporation, Pittsburgh, PA, 2005.

[12] S. R. H. Hoole, *Computer-Aided Analysis and Design of Electromagnetic Devices*, Elsevier, 1989.

[13] P. Kyriazidis, S. Tsitsos, A. Kouiroukidis, and A. A. P. Gibson, "Equivalent circuit parameter extraction techniques for a PCS ceramic filter, using commercial electromagnetic software," *Proc. of the 36th European Microwave Conf.*, pp. 1159-1162, Manchester, UK, 2006.

[14] S. Tsitsos, A. A. P. Gibson, and L. E. Davis, "A new technique for the extraction of equivalent circuit parameters from 3-D monoblock filters," *Int. Journal of RF and Microwave Computer-Aided Engineering*, vol. 15, no. 2, pp. 210-217, 2005.

Theodoros I. Kosmanis was born in Thessaloniki, Greece in 1974. He was awarded the Diploma in Electrical Engineering and the Ph.D. in Electrical and Computer Engineering from the Aristotle University of Thessaloniki, in 1997 and 2002, respectively. From 2003 until 2007, he was an Associate Lecturer in the Department of Mechanical Engineers of the University of Thessaly, Greece and the Departments of Mechanical Engineering and Computer Engineering of the Technological and Educational Institute of Central Macedonia, Serres, Greece. Since 2008, he is with the Department of Automotive Engineering of the Alexander Technological and Educational Institute of Thessaloniki, Greece, where he is now an Associate Professor. His research interests include electrical drive-trains, power signal management algorithms and computational electromagnetics. Kosmanis is a Member of the TCG (Technical Chamber of Greece), SAE (Society of Automotive Engineers), IEEE (Institute of Electrical and Electronics Engineers) and Hel.E.V. (Hellenic Institute of Electric Vehicles).

Ioannis T. Rekanos was born in Thessaloniki, Greece, in 1970. He was awarded the Diploma in Electrical Engineering and the Ph.D. in Electrical and Computer Engineering from the Aristotle University of Thessaloniki, in 1993 and 1998, respectively. From 2000 to 2002 he was a Post-doctoral Researcher in the Department of Radio Science and Engineering of the Aalto University (former Helsinki University of Technology), Finland. His research was funded by the European Commission through the Marie Curie Individual Fellowships program. In 2006 he joined the Aristotle University of Thessaloniki, Greece, where he is now a Professor in the School of Electrical and Computer Engineering. His research interests include wave propagation, inverse scattering, microwave tomography, computational electromagnetics, optimization techniques and signal processing. Rekanos is a Member of the TCG (Technical Chamber of Greece), and Senior Member of the IEEE (Institute of Electrical and Electronics Engineers).

Stelios P. Tsitsos was born in Giannitsa, Greece in 1966. He was awarded the Diploma in Electrical and Computer Engineering from the Democritus University of Thrace, Greece, in 1989. In 1991 he was awarded the Master's degree in Telecommunications Engineering and Digital Electronics from the University of Manchester Institute of Science and Technology (UMIST), UK. In 1994 he was awarded his Ph.D. degree in Microwave Engineering from the same University. From 1996 to 1999, he worked as a Research Associate at UMIST, UK, where he conducted research on the design and optimization of ceramic filters for mobile phones, for TDK Corporation, Japan. From 1999 to 2002, he worked for the Greek Telecommunications Company (OTE) as a Senior Engineer. In 2002 he joined the Department of Computer Engineering of the Technological and Educational Institute of Central Macedonia, Serres, Greece, where he is now an Associate Professor. His research interests include passive and active microwave components and devices for wireless communications and computational electromagnetics. Tsitsos is a Member of the TCB (Technical Chamber of Greece), IEEE (Institute of Electrical and Electronics Engineers) and ARMMS (Automated RF and Microwave Measurement Society), UK.

An Accurate High-Speed Method for Mutual Inductance Calculations of Coplanar Disk Coils Using Generalized Hypergeometric Functions

Yao Luo

School of Electrical Engineering
Wuhan University, Wuhan, 430072, China
ostpreussen@qq.com

Abstract ─ Traditional method using integral of the Bessel and Struve functions is not suitable for calculating the mutual inductance between two coplanar disk coils. Considering the monotonicity of modified Bessel and Struve functions, an alternative method using these monotonic functions is applied to calculate the mutual inductance, and numerical evaluations can be accelerated considerably. Series solutions using the generalized hypergeometric functions are further obtained by solving the infinite integrations, and these series are compared with the aforementioned integral methods. The numerical results show that the series solutions are much more faster than the integral ones, and with the series method, results of very high accuracy can be obtained within a small fraction of one second in most cases. Furthermore, we point out and prove the existence of the decoupling positions at which the mutual inductance will vanish.

Index Terms ─ Disk coils, generalized hypergeometric function, modified Bessel functions, mutual inductance.

I. INTRODUCTION

Disk coils are broadly applied in the electrical instruments, especially in recently popular areas such as the wireless power transmission, in which the disk coils are essential components and the mutual inductance of the coils is very important for optimization of the efficiency of the power transmission [1-3]. However, mutual inductance calculations of the disk coils are relatively difficult compared with that of the long circular coils (*e.g.*, the thin-wall solenoids). For two coaxial thin-wall solenoids, the mutual inductance can be solved in closed-form by the complete elliptic integrals [4, 5], but for two coaxial disk coils, it seems unlikely to obtain accurate closed-form solution and so far the mutual inductance must be solved by the integral of inverse trigonometric functions [6] or that of Bessel and Struve functions [7, 8]. Only for the concentric coplanar disk coils closed-form expressions are obtained [9]. In the general non-coaxial case, the solution is given in [6] by integral of Bessel and Struve functions and it can be described as follows.

Two disk coils are located in the parallel planes with distance z_0, and their axes are separated by a distance r_0. One coil has N_1 turns and the inner and outer radii R_1, R_2, the other has corresponding parameters of N_2, R_3, R_4 (See Fig. 1), then the mutual inductance of them is given by:

$$M = \frac{\mu_0 \pi^3 N_1 N_2}{4(R_2 - R_1)(R_4 - R_3)} \int_0^\infty \left[w(R_2) - w(R_1) \right] \cdot \left[w(R_4) - w(R_3) \right] J_0(kr_0) e^{-kz_0} \frac{dk}{k^2}, \tag{1}$$

where

$$w(r) = r\left[J_1(kr)\mathbf{H}_0(kr) - J_0(kr)\mathbf{H}_1(kr) \right], \tag{2}$$

with special functions $J_n(x)$ and $\mathbf{H}_n(x)$ listed in Table 1.

Table 1: Special functions applied

Symbol	Special Function
$J_n(x)$	Bessel function of the first kind of order n
$I_n(x)$, $K_n(x)$	Modified Bessel functions of the first and second kind of order n
$\mathbf{H}_n(x)$	Struve function of order n
$\mathbf{L}_n(x)$	Modified Struve function of order n
${}_pF_q(\boldsymbol{a}; \boldsymbol{b}; x)$	Generalized hypergeometric function
$(x)_n$	Pochhammer symbol
$\Gamma(x)$	Gamma function

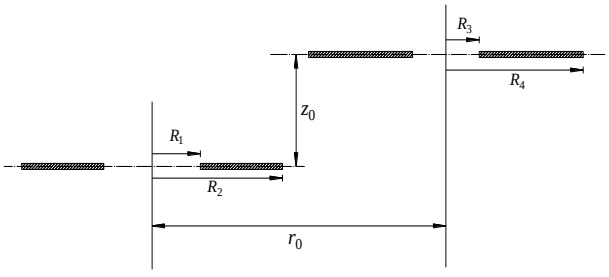

Fig. 1. Side view of two disk coils with parallel axes.

When z_0 is not too small, (1) is proper for the evaluation of the mutual inductance of disk coils since

Submitted On: October 14, 2013
Accepted On: March 17, 2016

the exponential factor will decrease rapidly in magnitude as $k\to\infty$. However, for small values of z_0 the numerical performance of (1) will become worse, especially for the coplanar case, the efficiency of (1) is in fact doubtful for the numerical evaluations. On the other hand, if we admit the transcendental nature of (1), we can then seek the series solutions of (1) rather than the closed-form ones and we will see that this consideration is achievable for (1) with z_0=0. In this work, for the non-coaxial coplanar disk coils the mutual inductance will be given in the form of series of generalized hypergeometric functions which will lead to a high speed and accuracy method for the numerical evaluations of the mutual inductance of these coils.

In addition, alternative representations of the mutual inductance using the modified Bessel and Struve functions will be introduced, which can be derived from the alternative forms of the eigenfunction expansion of the reciprocal distance [10-13] from which the proposed series expressions will be derived. The monotonic nature of the modified Bessel and Struve functions may be beneficial to numerical integration of the expressions of mutual inductance. Without these alternative methods, it will be nearly impossible to compare the proposed method of series type with that of integral type, since when z_0=0, the evaluation of (1) is extremely time-consuming and the results of high accuracy are very difficult to obtain.

II. FORMULATIONS OF MUTUAL INDUCTANCE

A. Mutual inductance of coplanar disk coils with $r_0 \geq R_2+R_4$

According to the Neumann formula, the mutual inductance of two coplanar disk coils with dimension parameters given in Section I is (See Fig. 2):

$$M=\frac{\mu_0 N_1 N_2}{4\pi(R_2-R_1)(R_4-R_3)}\int_{R_1}^{R_2} r_1 dr_1\cdot\int_{R_3}^{R_4} r_2 dr_2\int_0^{2\pi} d\varphi_2 \cdot\int_0^{2\pi}\frac{\cos(\varphi_1-\varphi_2)}{\sqrt{r_1^2+\rho^2-2r_1\rho\cos(\varphi_1-\varphi)}}d\varphi_1, \tag{3}$$

where

$$\rho^2=r_2^2+r_0^2-2r_2 r_0\cos(\varphi_2+\pi/2),$$

and

$$\rho\cos\varphi=r_2\cos\varphi_2.$$

Using the expansion of reciprocal distance in the cylindrical coordinate [10],

$$\frac{1}{\sqrt{r_1^2+\rho^2-2r_1\rho\cos(\varphi_1-\varphi)}}=\sum_{n=0}^{\infty}\varepsilon_n\cdot\cos n(\varphi_1-\varphi)\cdot f_n(r_1,\rho), \tag{4}$$

where

$$f_n(r_1,\rho)=\begin{cases}\dfrac{2}{\pi}\displaystyle\int_0^{\infty} I_n(kr_1)K_n(k\rho)dk, & \text{for } \rho\geq r_1,\\ \dfrac{2}{\pi}\displaystyle\int_0^{\infty} K_n(kr_1)I_n(k\rho)dk, & \text{for } r_1\geq\rho,\end{cases} \tag{5}$$

and

$$\varepsilon_n=\begin{cases}1, & n=0\\ 2, & n\neq 0\end{cases}, \tag{6}$$

is the Neumann's factor [14]; the following results of the mutual inductance can be obtained:

$$M=-\frac{\mu_0\pi^2 N_1 N_2}{2(R_2-R_1)(R_4-R_3)}\int_0^{\infty}\left[u(R_2)-u(R_1)\right]\cdot\left[u(R_4)-u(R_3)\right]K_0(kr_0)\frac{dk}{k^2}, \tag{7}$$

where $r_0\geq R_2+R_4$, and

$$M=\frac{\mu_0\pi^2 N_1 N_2}{2(R_2-R_1)(R_4-R_3)}\int_0^{\infty}\left[u(R_2)-u(R_1)\right]\cdot\left[v(R_4)-v(R_3)\right]I_0(kr_0)\frac{dk}{k^2}, \tag{8}$$

where $0\leq r_0\leq R_3-R_2$, with

$$u(r)=r\left[I_1(kr)\mathbf{L}_0(kr)-I_0(kr)\mathbf{L}_1(kr)\right], \tag{9}$$

and

$$v(r)=r\left[K_1(kr)\mathbf{L}_0(kr)+K_0(kr)\mathbf{L}_1(kr)\right]. \tag{10}$$

$I_n(x)$, $K_n(x)$ and $\mathbf{L}_n(x)$ are modified Bessel and Struve functions listed in Table 1. For the coplanar disk coils no overlap will occur.

In addition, using the same technique of (4)-(6) we can obtain the mutual inductance of two disk coils without radial overlap:

$$M=-\frac{\mu_0\pi^2 N_1 N_2}{2(R_2-R_1)(R_4-R_3)}\int_0^{\infty}\left[u(R_2)-u(R_1)\right]\cdot\left[u(R_4)-u(R_3)\right]K_0(kr_0)\cos(kz_0)\frac{dk}{k^2}, \tag{11}$$

where $r_0>R_2+R_4$, and

$$M=\frac{\mu_0\pi^2 N_1 N_2}{2(R_2-R_1)(R_4-R_3)}\int_0^{\infty}\left[u(R_2)-u(R_1)\right]\cdot\left[v(R_4)-v(R_3)\right]I_0(kr_0)\cos(kz_0)\frac{dk}{k^2}, \tag{12}$$

where $0\leq r_0<R_3-R_2$. Expressions (11) and (12) are suitable for the disk coils with small z_0 (the nearly coplanar coils), as the factor $\cos(kz_0)$ is slowly oscillatory in this case.

For $r_0\geq R_2+R_4$ we solve (7) to a series form. Applying the expression:

$$u(\alpha)-u(\beta)=\frac{2k}{\pi}\int_{\alpha}^{\beta} rI_1(kr)dr, \tag{13}$$

we have

$$S_1=\int_0^{\infty}\left[u(R_2)-u(R_1)\right]\left[u(R_4)-u(R_3)\right]K_0(kr_0)\frac{dk}{k^2} \tag{14}$$
$$=\frac{4}{\pi^2}\int_{R_1}^{R_2}r_1dr_1\int_{R_3}^{R_4}r_2dr_2\int_0^{\infty}I_1(kr_1)I_1(kr_2)K_0(kr_0)dk.$$

Solving the infinite integral in (14) [15] we obtain:

$$S_1=\frac{1}{2\pi r_0^3}\int_{R_1}^{R_2}r_1^2dr_1\cdot\int_{R_3}^{R_4}r_2^2F_4\left(\frac{3}{2},\frac{3}{2};2,2;\frac{r_1^2}{r_0^2},\frac{r_2^2}{r_0^2}\right)dr_2. \tag{15}$$

By writing the Appell function F_4 [16] as its power series and perform the remaining radial integrations term-by-term, we obtain:

$$S_1=\frac{1}{2\pi r_0^3}\sum_{m=0}^{\infty}\sum_{n=0}^{\infty}\frac{\left(R_1^{3+2m}-R_2^{3+2m}\right)}{r_0^{2(m+n)}(3+2m)(3+2n)} \tag{16}$$
$$\cdot\frac{\left(R_3^{3+2n}-R_4^{3+2n}\right)(3/2)_{m+n}^2}{m!n!(2)_m(2)_n}.$$

Then by solving the summation with respect to m we get:

$$S_1=\frac{1}{6\pi r_0^3}\sum_{n=0}^{\infty}\frac{\left(R_3^{3+2n}-R_4^{3+2n}\right)(3/2)_n^2}{r_0^{2n}(3+2n)n!(2)_n} \tag{17}$$
$$\cdot\left[R_1^3f_1\left(n,\frac{R_1}{r_0}\right)-R_2^3f_1\left(n,\frac{R_2}{r_0}\right)\right],$$

with

$$f_1(n,x)={}_3F_2\left(\frac{3}{2},n+\frac{3}{2},n+\frac{3}{2};2,\frac{5}{2};x^2\right). \tag{18}$$

Finally we have the mutual inductance for $r_0\geq R_2+R_4$:

$$M=-\frac{\mu_0\pi^2N_1N_2}{2(R_2-R_1)(R_4-R_3)}S_1$$
$$=-\frac{\mu_0\pi N_1N_2}{12r_0^3(R_2-R_1)(R_4-R_3)}\sum_{n=0}^{\infty}\frac{\left(R_3^{3+2n}-R_4^{3+2n}\right)(3/2)_n^2}{r_0^{2n}(3+2n)n!(2)_n} \tag{19}$$
$$\cdot\left[R_1^3f_1\left(n,\frac{R_1}{r_0}\right)-R_2^3f_1\left(n,\frac{R_2}{r_0}\right)\right],$$

with $f_1(n, x)$ given by (18).

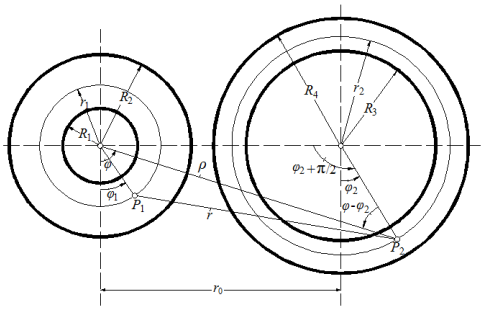

Fig. 2. Plan view of two coplanar disk coils.

B. Mutual inductance of coplanar disk coils with $0\leq r_0\leq R_3-R_2$

For the case of $0\leq r_0\leq R_3-R_2$, using (13) and the expression,

$$v(\alpha)-v(\beta)=\frac{2k}{\pi}\int_{\alpha}^{\beta}rK_1(kr)dr, \tag{20}$$

we have

$$S_2=\int_0^{\infty}\left[u(R_2)-u(R_1)\right]\left[v(R_4)-v(R_3)\right]I_0(kr_0)\frac{dk}{k^2}$$
$$=\frac{4}{\pi^2}\int_{R_1}^{R_2}r_1dr_1\int_{R_3}^{R_4}r_2dr_2\int_0^{\infty}I_1(kr_1)K_1(kr_2)I_0(kr_0)dk \tag{21}$$
$$=\frac{1}{\pi}\int_{R_1}^{R_2}r_1^2dr_1\cdot\int_{R_3}^{R_4}\frac{1}{r_2}F_4\left(\frac{3}{2},\frac{3}{2};1,2;\frac{r_0^2}{r_2^2},\frac{r_1^2}{r_2^2}\right)dr_2.$$

Then solve the remaining integrals in the similar manner we have:

$$S_2=\frac{1}{2\pi}\sum_{m=0}^{\infty}\sum_{n=0}^{\infty}C_{mn}$$
$$=\frac{1}{2\pi}\sum_{m=0}^{\infty}\sum_{n=0}^{\infty}\frac{r_0^{2m}(1/2)_{m+n}(3/2)_{m+n}}{(R_3R_4)^{2(m+n)}(3+2n)(m+n)}$$
$$\cdot\frac{\left(R_1^{3+2n}-R_2^{3+2n}\right)\left(R_3^{2(m+n)}-R_4^{2(m+n)}\right)}{m!n!(1)_m(2)_n}. \tag{22}$$

It should be noticed that the general term C_{mn} of (22) has the factor $m+n$ in the denominator, hence m and n cannot vanish simultaneously, for the summation with respect to m, the lower index of n must be set to be 1, *i.e.*,

$$\sum_{m=0}^{\infty}\sum_{n=1}^{\infty}C_{mn}=\sum_{n=1}^{\infty}\frac{(1/2)_n(3/2)_n\left(R_2^{3+2n}-R_1^{3+2n}\right)}{(R_3R_4)^{2n}n(3+2n)n!(2)_n} \tag{23}$$
$$\cdot\left[R_4^{2n}f_2\left(n,\frac{r_0}{R_3}\right)-R_3^{2n}f_2\left(n,\frac{r_0}{R_4}\right)\right],$$

with

$$f_2(n,x)={}_3F_2\left(n,n+\frac{1}{2},n+\frac{3}{2};1,n+1;x^2\right). \tag{24}$$

Then we consider the remaining terms C_{m0}. The term C_{00} is unusual and a limit process must be take:

$$C_{00}=\lim_{\substack{m\to0\\n\to0}}C_{mn}=\frac{2}{3}\left(R_1^3-R_2^3\right)\ln\frac{R_3}{R_4}. \tag{25}$$

The summation of the remaining terms C_{m0} with $m\geq1$ is:

$$\sum_{m=1}^{\infty}C_{m0}=\sum_{m=1}^{\infty}\frac{\left(R_1^3-R_2^3\right)\left(R_3^{2m}-R_4^{2m}\right)r_0^{2m}(1/2)_m(3/2)_m}{3(R_3R_4)^{2m}m(m!)^2}$$
$$=\frac{r_0^2\left(R_1^3-R_2^3\right)\left[R_3^2f_3\left(\frac{r_0}{R_4}\right)-R_4^2f_3\left(\frac{r_0}{R_3}\right)\right]}{4(R_3R_4)^2}, \tag{26}$$

with

$$f_3(x) = {}_4F_3\left(1,1,\frac{3}{2},\frac{5}{2};2,2,2;x^2\right). \tag{27}$$

Then combining (8) and (22)-(27) gives the mutual inductance for $0 \le r_0 \le R_3 - R_2$:

$$\begin{aligned} M &= \frac{\mu_0 \pi^2 N_1 N_2}{2(R_2-R_1)(R_4-R_3)} S_2 \\ &= \frac{\mu_0 \pi N_1 N_2}{4(R_2-R_1)(R_4-R_3)} \left(\sum_{m=0}^{\infty}\sum_{n=1}^{\infty} C_{mn} + \sum_{m=0}^{\infty} C_{m0} + C_{00} \right) \\ &= \frac{\mu_0 \pi N_1 N_2}{2(R_2-R_1)(R_4-R_3)} \left\{ \frac{1}{2} \sum_{n=1}^{\infty} \left\{ \left(R_2^{3+2n} - R_1^{3+2n}\right) \right.\right. \\ &\cdot \frac{(1/2)_n (3/2)_n}{(R_3R_4)^{2n}\, n(3+2n)n!(2)_n} \left[R_4^{2n} f_2\left(n, \frac{r_0}{R_3}\right) - R_3^{2n} f_2\left(n, \frac{r_0}{R_4}\right) \right] \Bigg\} \\ &\left. + \frac{r_0^2 \left(R_1^3 - R_2^3\right) \left[R_3^2 f_3\left(\frac{r_0}{R_4}\right) - R_4^2 f_3\left(\frac{r_0}{R_3}\right) \right]}{8(R_3R_4)^2} + \frac{1}{3}\left(R_1^3 - R_2^3\right) \ln \frac{R_3}{R_4} \right\}. \end{aligned} \tag{28}$$

Expression (28) may be a little complicated, and in fact a concise form can be found if we write (21) in another way. Using the formula [17]:

$$\begin{aligned} &\Gamma(\mu+1)\Gamma(\nu+1) I_\mu(ax) I_\nu(bx) = (ax/2)^\mu (bx/2)^\nu \\ &\cdot \sum_{n=0}^{\infty} \frac{(ax/2)^{2n}}{n!(\mu+1)_n} {}_2F_1\left(-n, -\mu-n; \nu+1; b^2/a^2\right), \end{aligned} \tag{29}$$

and

$$\int_0^{\infty} k^{2n+1} K_1(kr_2)\, dk = \frac{\pi}{2r_2^2} \left(\frac{2}{r_2}\right)^{2n} \left(\frac{1}{2}\right)_n \left(\frac{3}{2}\right)_n, \tag{30}$$

we have

$$\begin{aligned} S_2 &= \frac{1}{6\pi} \sum_{n=0}^{\infty} C_n \\ &= \frac{1}{6\pi} \sum_{n=0}^{\infty} \frac{\left(\frac{1}{2}\right)_n \left(\frac{3}{2}\right)_n r_0^{2n} (R_3R_4)^{-2n} \left(R_3^{2n} - R_4^{2n}\right)}{n(n!)^2} \\ &\cdot \left[R_1^3 f_4\left(n, \frac{R_1}{r_0}\right) - R_2^3 f_4\left(n, \frac{R_2}{r_0}\right) \right], \end{aligned} \tag{31}$$

where

$$f_4(n,x) = {}_3F_2\left(\frac{3}{2}, -n, -n; 2, \frac{5}{2}; x^2\right). \tag{32}$$

When n=0 the term C_n of (31) must be treated with a limit process as well:

$$C_0 = \lim_{n\to 0} C_n = 2\left(R_1^3 - R_2^3\right) \ln \frac{R_3}{R_4}. \tag{33}$$

Combining (8) and (31)-(33) gives an alternative form of the mutual inductance for $0 \le r_0 \le R_3 - R_2$:

$$\begin{aligned} M &= \frac{\mu_0 \pi}{6(R_2-R_1)(R_4-R_3)} \left\{ \sum_{n=1}^{\infty} \frac{\left(\frac{1}{2}\right)_n \left(\frac{3}{2}\right)_n r_0^{2n} \cdot \left(R_3^{2n} - R_4^{2n}\right)}{2n(n!)^2 (R_3R_4)^{2n}} \right. \\ &\left. \cdot \left[R_1^3 f_4\left(n, \frac{R_1}{r_0}\right) - R_2^3 f_4\left(n, \frac{R_2}{r_0}\right) \right] + \left(R_1^3 - R_2^3\right) \ln \frac{R_3}{R_4} \right\}. \end{aligned} \tag{34}$$

Expression (34) cannot be applied to the concentric case r_0=0 but it can converge faster than (28) especially when r_0 is very close to the value $R_3 - R_2$. Letting z_0=0 in (1) and performing the integrations in a similar manner of (14) or (21), (19) and (28) can also be obtained. Letting r_0=0 in (28), the term (26) will vanish and (23) can be solved to a closed-form of ${}_{q+1}F_q(\boldsymbol{a}; \boldsymbol{b}; x)$ and the result is:

$$\begin{aligned} M &= \frac{\mu_0 \pi N_1 N_2}{288(R_2-R_1)(R_4-R_3)} \\ &\cdot \left\{ 16 \left\{ R_1^3 \left[f_5\left(\frac{R_1}{R_3}\right) - f_5\left(\frac{R_1}{R_4}\right) \right] + R_2^3 \left[-f_5\left(\frac{R_2}{R_3}\right) + f_5\left(\frac{R_2}{R_4}\right) \right] \right\} \right. \\ &+ 9 \left\{ R_1^5 \left[-\frac{1}{R_3^2} f_6\left(\frac{R_1}{R_3}\right) + \frac{1}{R_4^2} f_6\left(\frac{R_1}{R_4}\right) \right] \right. \\ &\left. \left. + R_2^5 \left[\frac{1}{R_3^2} f_6\left(\frac{R_2}{R_3}\right) - \frac{1}{R_4^2} f_6\left(\frac{R_2}{R_4}\right) \right] \right\} + 48\left(R_1^3 - R_2^3\right) \ln\left(\frac{R_3}{R_4}\right) \right\}, \end{aligned} \tag{35}$$

with

$$f_5(x) = {}_3F_2\left(\frac{1}{2}, \frac{3}{2}, \frac{3}{2}; 2, \frac{5}{2}; x^2\right), \tag{36}$$

and

$$f_6(x) = {}_4F_3\left(1,1,\frac{3}{2},\frac{5}{2};2,2,3;x^2\right). \tag{37}$$

This result of concentric coplanar case coincides with that given in [9].

III. DECOUPLING POSITIONS OF DISK COILS WITH PARALLEL AXES

It is interesting to give some additional discussions for the contents described above. When $r_0 \ge R_2 + R_4$, from (7), (9) and (13) we have the mutual inductance of two coplanar disk coils:

$$\begin{aligned} M &= -\frac{2\mu_0 N_1 N_2}{(R_2-R_1)(R_4-R_3)} \int_0^{\infty} K_0(kr_0)\, dk \\ &\cdot \int_{R_1}^{R_2} r_1 I_1(kr_1)\, dr_1 \int_{R_3}^{R_4} r_2 I_1(kr_2)\, dr_2. \end{aligned} \tag{38}$$

Considering $K_0(x)$ and $I_1(x)$ are always positive throughout $0<x<\infty$, it can be concluded that (38) is always negative for any pair of disk coils. On the other side, for the general case of disk coils with $z_0\neq 0$, from (1) and,

$$w(\alpha)-w(\beta)=\frac{2k}{\pi}\int_{\alpha}^{\beta} rJ_1(kr)\,dr, \tag{39}$$

we have

$$M=\frac{\mu_0\pi N_1N_2}{(R_2-R_1)(R_4-R_3)}\int_{R_1}^{R_2} r_1dr_1\int_{R_3}^{R_4} r_2dr_2 \cdot\int_0^{\infty} J_1(kr_1)J_1(kr_2)J_0(kr_0)e^{-kz_0}dk. \tag{40}$$

For sufficient large z_0 the following asymptotic relation holds [18]:

$$\int_0^{\infty} J_1(kr_1)J_1(kr_2)J_0(kr_0)e^{-kz_0}dk\sim\sum_{s=0}^{\infty}\frac{q^{(s)}(0)}{z_0^{s+1}}, \tag{41}$$

where

$$q^{(s)}(0)=\lim_{k\to 0}q^{(s)}(k), \tag{42}$$

and

$$q(k)=J_1(kr_1)J_1(kr_2)J_0(kr_0). \tag{43}$$

Hence, for very large z_0 we have:

$$\int_0^{\infty} J_1(kr_1)J_1(kr_2)J_0(kr_0)e^{-kz_0}dk\sim\frac{r_1r_2}{2z_0^3}-\frac{3r_1r_2\left(r_0^2+r_1^2+r_2^2\right)}{4z_0^5} +\frac{15r_1r_2\left(3r_0^4+r_1^4+3r_1^2r_2^2+r_2^4+6r_0^2\left(r_1^2+r_2^2\right)\right)}{16z_0^7}-..., \tag{44}$$

by omitting the terms of infinitesimal of higher order we can write:

$$\int_0^{\infty} J_1(kr_1)J_1(kr_2)J_0(kr_0)e^{-kz_0}dk\sim\frac{r_1r_2}{2z_0^3}, \tag{45}$$

for $z_0\to+\infty$. Hence, for very large z_0, (45) is always positive. As a corollary, (40) must also be positive when $z_0\to+\infty$. Noticing the mutual inductance is the continuous function of z_0, the following assertion can be obtained immediately.

For any given pair of disk coils with parallel axes and $r_0\geq R_2+R_4$, there is at least one zero point of z_0, at which the mutual inductance M will vanish, *i.e.*, the disk coils will be decoupled magnetically in this decoupling position.

IV. NUMERICAL EVALUATIONS

A. Coplanar disk coils with $r_0\geq R_2+R_4$

In case of $r_0\geq R_2+R_4$, the numerical validation of (7) and (19) will be implemented by using the following dimension parameters of the disk coils: R_1=0.2 m, R_2=0.8 m, R_3=2 m, R_4=3.5 m. The turns of both coils are irrelevant, since the normalized value $M/(N_1N_2)$ will be calculated. The results are given in Table 2. t_a and t_b are the computation time of (7) and (19), respectively, to obtain the same values in the second column of Table 2. The calculations were coded in Mathematica and implemented on a personal computer with a 3.4-GHz processor. As r_0 increases, both t_a and t_b decrease, and this is just contrary to the nature of (1). As long as the computation time is less than 1ms (which is the default minimum time interval of the timing program), it will be omitted automatically by the program and we will record it as "t<0.001s". We can see that t_b is always less than 1 second except for the case of $r_0\leq$4.4 m. The superior performance of the series expression (19) can be proved sufficiently. When $r_0=R_2+R_4$=4.3 m, both (7) and (19) are not efficient enough and we just give a result of 4 significant figures evaluated by (7): $M/(N_1N_2)=-65.08$nH, with the computation time of 1228.929s, and that of 7 significant figures evaluated by (19): $M/(N_1N_2)=-65.08078$nH, with the computation time of 18.658s. In addition, the evaluations of (1) with z_0=0 is extremely time-consuming so the computation time of it is not included in Table 2, but we can give a example here: for r_0=4.8m, it takes about 1253s to get a result of 5 significant figures: $M/(N_1N_2)=-35.273$nH.

Table 2: Performance of the mutual inductance for coplanar disk coils of $r_0\geq R_2+R_4$ evaluated with (7) and (19)

r_0 (m)	$M/(N_1N_2)$ (nH)	t_a (s)	t_b (s)	t_a/t_b
4.4	−56.064144480280	1941.713	1.404	1382.986
4.5	−49.190311789750	402.061	0.608	661.285
4.6	−43.669129789264	265.592	0.234	1135.009
4.7	−39.109839095754	187.217	0.156	1200.109
4.8	−35.273252555243	5.803	0.109	53.239
5.2	−24.550774873203	5.772	0.062	93.097
5.5	−19.428031335091	4.181	0.047	88.957
5.7	−16.840560836502	4.009	0.047	85.298
6.0	−13.806335361406	3.947	0.031	127.323
6.5	−10.251166170897	3.869	0.031	124.806
7.0	−7.861716936199	3.838	0.016	239.875
8.0	−4.962362649715	2.418	0.016	151.125
9.0	−3.353222796361	2.168	<0.001	>2168
10.0	−2.380250924534	2.153	<0.001	>2153

B. Coplanar disk coils with $0\leq r_0\leq R_3-R_2$

In the case of $0\leq r_0\leq R_3-R_2$, the numerical validation of (8), (28) and (34) will be implemented by using the

same dimension parameters as before: R_1=0.2 m, R_2=0.8 m, R_3=2 m, R_4=3.5 m. The results of the normalized value $M/(N_1N_2)$ are also given in Table 3. t_a and t_b are the computation time of (8) and (34), respectively, to obtain the same values in the second column of Table 3 (t_b is the computation time of (28) when r_0=0). We can see that t_b is always less than 0.1s, and for most values of r_0 in Table 3, it needs only less than 50 terms of (34) to converge to the results of 15 significant figures. The superior performance of (34) can be proved sufficiently. In addition, the computation time of (28) is slightly slower than that of (34) but it is still less than 1s. When $r_0=R_3-R_2$=1.2 m, (8), (28) and (34) are all inefficient and we just give a result of 5 significant figures evaluated by (8): $M/(N_1N_2)$=0.26645mH, with the computation time of 812.172s, and a result of 7 significant figures evaluated by (34): $M/(N_1N_2)$=0.2664547mH, with the computation time of 0.452s. The convergence rate of (1) is still very slow and it will not be discussed further.

Table 3: Performance of the mutual inductance for coplanar disk coils of $0\le r_0\le R_3-R_2$ evaluated with (8), (28) and (34)

r_0 (m)	$M/(N_1N_2)$ (mH)	t_a (s)	t_b (s)	t_a/t_b
0	0.210962364718285	3.307	<0.001	>3307
0.01	0.210965011812987	3.229	<0.001	>3229
0.1	0.211227575213022	3.214	<0.001	>3214
0.2	0.212029338411955	6.412	<0.001	>6412
0.3	0.213386502485260	6.443	<0.001	>6443
0.4	0.215332068455948	6.599	<0.001	>6599
0.5	0.217915867666375	6.380	<0.001	>6380
0.6	0.221209010694124	6.365	<0.001	>6365
0.7	0.225311129537439	22.932	0.016	1433.250
0.8	0.230362442894204	40.014	0.016	2500.875
0.9	0.236565023271967	134.910	0.016	8431.875
1.0	0.244224093537914	502.261	0.031	16200.516
1.1	0.253843100876854	1505.862	0.094	16019.809

C. Decoupling positions

For the numerical validation of the existence of decoupling positions, we plot the curves of mutual inductance with respect to z_0 for given values of r_0 and vice versa, using these parameters of coils: R_1=1 m, R_2=2 m, R_3=3 m, R_4=4 m. The curves are shown in Figs. 3, 4, which illustrate the decoupling positions clearly. In Fig. 3, for r_0=7 m, r_0=8.5 and r_0=10 m, the corresponding decoupling positions are z_0=3.947 m, z_0=5.274 m, and z_0=6.408 m; in Fig. 4, for z_0=4.5 m, z_0=5.5 and z_0=6.5 m, the corresponding decoupling positions are r_0=7.639 m, r_0=8.852 m, and r_0=10.118 m, respectively.

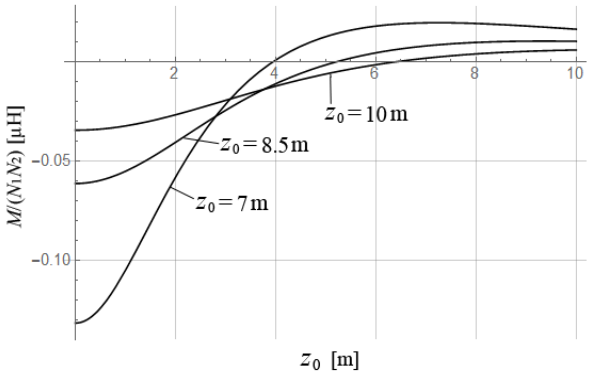

Fig. 3. The normalized mutual inductance of the disk coils with parallel axes, plotted with respect to z_0 for given r_0.

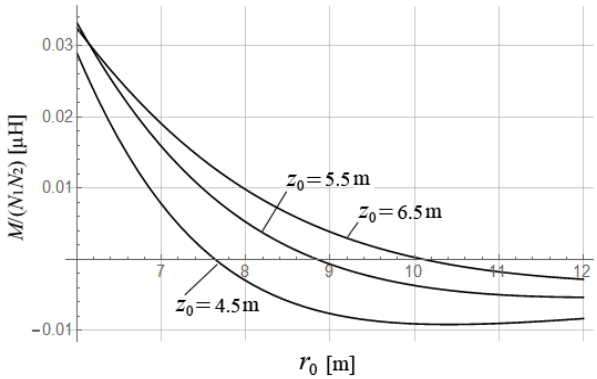

Fig. 4. The normalized mutual inductance of the disk coils with parallel axes, plotted with respect to r_0 for given z_0.

V. CONCLUSION

The integral expression using Bessel and Struve function is extremely time-consuming for the mutual inductance calculations of the coplanar disk coils. The method using modified Bessel and Struve functions is introduced to improve the numerical performance of the integral expressions, from which the series expressions using the generalized hypergeometric functions have been obtained and these expressions can be easily coded in the common mathematical packages such as Mathematica or Matlab. The numerical calculations show that the series expressions are much more faster than the expressions of integral type to get the results with the same accuracy. In most cases, it only takes less than 1 second to obtain a result of 15 significant figures by using the series expressions. In addition, the decoupling positions of the mutual inductance in the case of $r_0\ge R_2+R_4$ are noticed and we have proved

formally that these positions always exist for the disk coils with parallel axes.

REFERENCES

[1] S. Raju, R. Wu, M. Chan, and C. P. Yue, "Modeling of mutual coupling between planar inductors in wireless power applications," *IEEE Trans. Power Electr*., vol. 29, no. 1, pp. 481-490, Jan. 2014.

[2] J. Acero, C. Carretero, et al., "Analysis of the mutual inductance of planar-lumped inductive power transfer systems," *IEEE Trans. Ind. Electron.*, vol. 60, no. 1, pp. 410-419, Jan. 2013.

[3] Z. N. Low, R. A. Chinga, R. Tseng, and J. Lin, "Design and test of a high-power high-efficiency loosely coupled planar wireless power transfer system," *IEEE Trans. Ind. Electron.*, vol. 56, no. 5, pp. 1801-1812, May 2009.

[4] H. Haas, "Ein Beitrag zur Berechnung der Gegeninduktivität koaxialer Zylinderspulen," *Archiv für Elektrotechnik*, vol. 57, no. 1, pp. 21-26, Jan. 1975.

[5] S. Babic and C. Akyel, "Improvement in calculation of the self- and mutual-inductance of thin wall solenoids and disk coils," *IEEE Trans. Magn*., vol. 36, no. 4, pp. 1970-1975, Jul. 2000.

[6] S. Babic, S. Sheppard, and C. Akyel, "The mutual inductance of two thin coaxial disk coils in air," *IEEE Trans. Magn*., vol. 40, no. 2, pp. 822-825, Mar. 2004.

[7] J. T. Conway, "Inductance calculations for noncoaxial coils using Bessel functions," *IEEE Trans. Magn.*, vol. 43, no. 3, pp. 1023-1034, Mar. 2007.

[8] J. T. Conway, "Inductance calculations for circular coils of rectangular cross section and parallel axes using Bessel and Struve functions," *IEEE Trans. Magn*., vol. 46, no. 1, pp. 75-81, Jan. 2010.

[9] J. T. Conway, "Analytical solutions for the self- and mutual inductances of concentric coplanar disk coils," *IEEE Trans. Magn.*, vol. 49, no. 3, pp. 1135-1142, Mar. 2013.

[10] L. Hannakam, "Berechnung der Gegeninduktivität achsenparalleler Zylinderspulen," *Archiv für Elektrotechnik*, vol. 51, no. 5, pp. 141-154, May 1967.

[11] H. Buchholz, "Das elektromagnetische Feld eines in Seewasser parallel zum Spiegel verlegten, stromdurchflossenen, isolierten Drahtes mit blanken Enden in dem dreifach geschichteten Raum: Luft, Wasser, Erde: I. Der Gleichstromfall," *Archiv für Elektrotechnik*, vol. 47, no. 2, pp. 80-105, Mar. 1962.

[12] H. Buchholz, "Das elektromagnetische Feld eines in Seewasser parallel zum Spiegel verlegten, stromdurchflossenen, isolierten Drahtes mit blanken Enden in dem dreifach geschichteten Raum: Luft, Wasser, Erde: II. Der Wechselstromfall bei beliebigen Frequenzen," *Archiv für Elektrotechnik*, vol. 47, no. 3, pp. 80-105, May 1962.

[13] F. Oberhettinger, "Über ein Randwertproblem der Wellengleichung in Zylinderkoordinaten," *Annalen der Physik*, vol. 435, no. 1-2, pp. 136-160, 1943.

[14] G. N. Watson, *A Treatise on the Theory of Bessel Functions*, 2nd ed., Cambridge, U. K.: Univ. Press, 1944.

[15] A. P. Prudnikov, Y. A. Brychkov, and O. I. Marichev, *Integrals and Series*, vol. 2: Special Functions, New York: Gordon and Breach, 1992.

[16] P. W. Karlsson, "Inductance and hypergeometric functions," *J. Comput. Appl. Math.*, vol. 37, pp. 171-177, 1991.

[17] A. Erdelyi, W. Magnus, F. Oberhettinger, and F. G. Tricomi, *Bateman Manuscript Project: Higher Transcendental Functions*, vol. II, New York: McGraw-Hill, 1953.

[18] F. W. Olver, D. W. Lozier, R. F. Boisvert, et. al., *NIST Handbook of Mathematical Functions*, New York: Cambridge University Press, 2010.

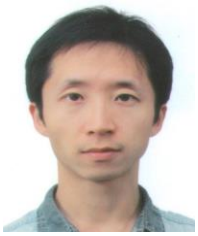

Yao Luo received the B.S. degree in Communication Engineering and the Ph.D. degree in Electrical Engineering from the Wuhan University (WHU), Wuhan, China, in 2006 and 2012, respectively.

From 2012 to 2013, he was a Lecturer in Electrical and Electronic Engineering, Hubei University of Technology. From 2013 to 2015, he was a Postdoctoral Researcher with Power and Mechanical Engineering, WHU. He is currently a Lecturer in Electrical Engineering, WHU. His current research interests include analytical calculation methods of electromagnetic fields, and the practical applications of the theory of special functions.

A New High Performance Hibiscus Petal Pattern Monopole Antenna for UWB Applications

M. Z. Mahmud [1], S. Kibria [1], M. Samsuzzaman [2], N. Misran [1], and M. T. Islam [1]

[1] Dept. of Electrical Electronic and Systems Engineering
Universiti Kebangsaan Malaysia
zulfikerm@siswa.ukm.edu.my, tariqul@ukm.edu.my

[2] Dept. of Computer and Communication Engineering
Patuakhali Science and Technology University

Abstract ─ A new ultra wideband (UWB) antenna is proposed that can be efficiently used for different wireless UWB applications. The antenna structure has a very simple patch with Hibiscus petal pattern. The antenna is designed on a 31×31 mm^2 Rogers RT/duroid 5870 substrate with permittivity 2.33, loss tangent 0.0012, 1.57 mm thickness and a 50 ohm impedance microstrip fed line. Different parts of antenna are analyzed to optimize the antenna properties. The novel patch of the antenna is modified to achieve the desired wide bandwidth behavior. The simulation results show that the antenna has an impedance bandwidth of 145% from 3.2 to 20 GHz with VSWR<2, a stable omnidirectional radiation pattern, an average gain of 5.1 dBi and the average radiation efficiency is 85%, which is ideal for use in UWB applications. The proposed antenna was successfully prototyped and the measured results are consistent with simulation.

Index Terms ─ Hibiscus petal pattern, monopole antenna, UWB, VSWR.

I. INTRODUCTION

In order to cope with rapid development of wireless communication technology, the demand of high performance antennas, which capable of operating at an extremely wider frequency band like ultra-wideband (UWB), are urgently needed. UWB communication technology has been regarded as one of the most promising technologies in the wireless communication industry because of their attractive features like high speed data rate, extremely low spectral power density, high precision ranging, simple and low cost designs, robustness to multi-path fading and very low interference, since the Federal Communications Commission (FCC) has allocated 7.5 GHz of the spectrum from 3.1 GHz to 10.6 GHz for UWB radio applications from February 2002 [1]. UWB also have wide applications in short range and high speed wireless systems, such as ground penetrating radars, medical imaging system, high data rate wireless local area networks (WLAN), communication systems for military and short pulse radars for automotive even or robotics [2-5].

Some of these UWB antennas can improve the properties by changing the shape of the radiator to circular, rectangular, elliptical, heart shape etc. Furthermore, reducing the ground plane dimensions can achieve wider bandwidth [6-9]. In the study by Gokmen et al. [10], a compact size UWB antenna with heart shape using triangular patches is proposed operating from 4 GHz to 19.1 GHz with dimensions of 25×26×0.5 mm^3. Liu and Yang [11] presented a hook-shaped UWB antenna operating from 3 GHz to 10.7 GHz with a dimension of 10×10×1.6 mm^3. Furthermore, Ojaroudi et al. [12] proposed an ultra-wideband monopole antenna with inverted T-shaped notch in the ground plane, operating from 3.12 GHz to 12.73 GHz, is presented with a compact size of 12×18 mm^2. A tapered slot antenna [13] with area of 22×24 mm^2 with operating frequencies from 3 GHz to 11.2 GHz is also presented in literature. In another study [14], a heart shaped monopole antenna over a defected ground plane was proposed and optimized for ultra-wide band applications. To improve the impedance bandwidth and reduce the return losses, three semi-circular slots in the ground plane were proposed. A heart-shaped monopole patch and two rectangular ground plane on the same side of a substrate can also achieve wide bandwidth [15]. The impedance bandwidth can be achieved from 2.1 to 11.5 GHz. Most antennas presented in literature suffer from low fractional bandwidth or large size.

In this paper, a new UWB Hibiscus Petal Pattern monopole antenna with enhanced impedance bandwidth is offered. This antenna consists of a trapezoidal shape partial ground plane on the opposite side of a patch with hibiscus petal shape. The outer edge of patch is partially etched away to increase the bandwidth. Simulation and measured results shows that the proposed antenna can

Submitted On: November 17, 2015
Accepted On: February 26, 2016

obtain the bandwidth from 3.2 to 20 GHz with evenly distributed current distribution and relatively stable omnidirectional radiation pattern and high radiation efficiency. It has a significant average peak gain. Simulated results for VSWR, gain, efficiency, radiation pattern, surface current distribution of different frequencies are presented along with the measured results. The simulation is carried out by using HFSS and CST software package.

II. ANTENNA DESIGN

The proposed Hibiscus Petal Pattern Monopole UWB antenna geometry layout is shown in Fig. 1, which is printed on a Rogers RT/duiroid 5870 substrate of thickness 1.57 mm, permittivity 2.33 and loss tangent 0.0012. The proposed antenna consists of a partial radiating patch on one side and ground plane on the other side of the substrate. Figure 1 (a) shows the front end of antenna where a hibiscus petal pattern patch is developed on the substrate. To achieve Hibiscus Petal Pattern, some parts of radiator has been etched away and a microstrip feed line printed on the same side of the substrate. The ground plane of the antenna is a trapezoidal shape as shown in Fig. 1 (b). The width of the microstrip feed line is tapered with base width of W_{f1} and upper edge width of W_{f2} with length L_f, as shown in Fig. 1. An SMA connector is soldered to the bottom of the microstrip feed line. The overall size of the antenna is W×L mm^2 and the ground plan has an area of $(W+W_g)/2\times L_1$ mm^2. The details of the optimized design parameter are summarized in Table 1.

Figure 2 shows the effect of ground plane length on the reflection coefficient of the proposed antenna. It is clearly seen that the proposed ground plane provides wider bandwidth than full ground plane (31 mm), half ground plane (16.5 mm) and a ground plane with 5 mm. For full ground plane, the reflection coefficient is much higher than that of operating bandwidth (-10 dB) and no resonant frequency is found over the entire bandwidth. For 16.5 mm a small bandwidth 9.4-9.7 GHz) is found where S11<-10 dB and first resonant frequency is found at 9.5 GHz. For 5 mm ground plane the first resonant is found at 2.7 GHz and its starting bandwidth is remarkable. But after 3 GHz reflection coefficient is starting to rise and no other band is found where S11<-10 dB. In Fig. 3, the reflection coefficient of the proposed antenna for different values of the gap between ground and the patch is shown. For the gap 0.78 mm, 0.53 mm, 0.72 mm and 0.42 mm, the starting bandwidth is higher than that of proposed bandwidth (1.58 mm). The lower frequency bandwidth is significantly affected when the gap is altered.

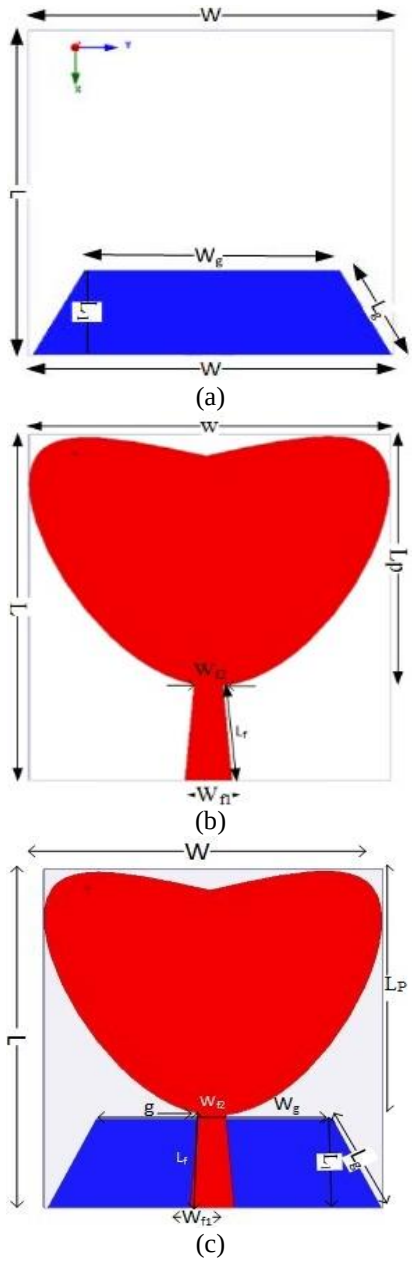

Fig. 1. The proposed antenna: (a) top layer, (b) bottom layer, and (c) both (all dimension are in mm).

Table 1: Optimized dimension of the prototype

Parameter	Value (mm)	Parameter	Value (mm)
W	31	L	31
Wf1	4	Lp	22.98
Wf2	2.43	L1	8
Lg	9.42	Lf	8.515
Wg	21.6		

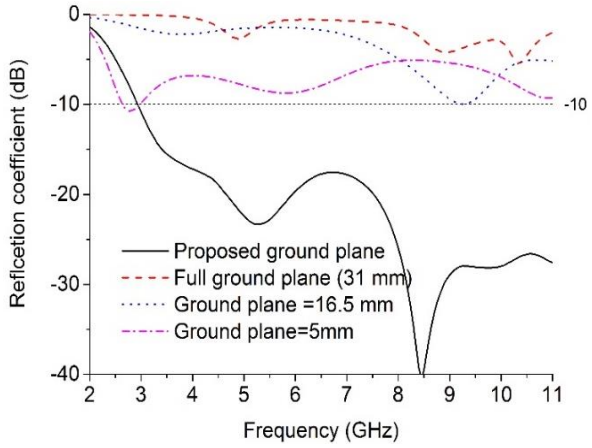

Fig. 2. Effect of ground plane length on S11 of the proposed antenna.

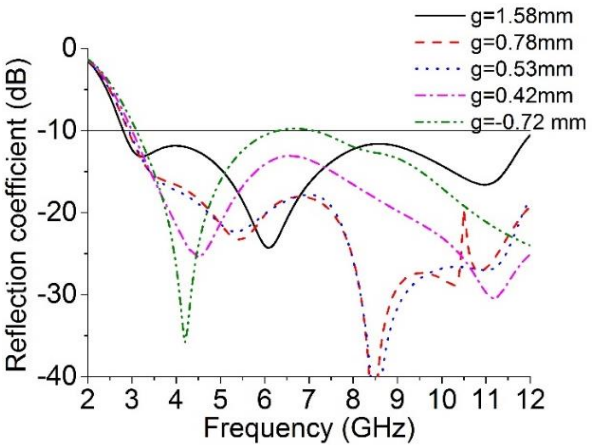

Fig. 3. Effect of gap between ground and patch on reflection coefficient.

III. RESULTS AND DISCUSSION

The photographs of the proposed antenna prototype (top and bottom view) are shown in Fig. 4. The performance of the proposed antenna has been analysed and optimized using the finite element method based high frequency 3D full-wave electromagnetic simulator Ansoft's HFSS and efficient computational 3D simulation software CST for electromagnetic design and analysis. The measured results were obtained using the Agilent E8362C vector network analyzer and Satimo near field anechoic chamber (UKM StarLab). Figure 5 illustrates the simulated and experimental voltage standing wave ratio (VSWR) of the antenna. The measured bandwidth for VSWR less than 2 ranges from 3.2 GHz to 20 GHz and in simulation using CST from 2.8 GHz to 20 GHz, whereas in HFSS from 3.2 to 20 GHz. The measured and simulated results show a good agreement. The minor discrepancies between simulated and measured results can be attributed to imperfect fabrication and the coaxial cable used during measurement. The cable is not considered in simulation. Although the size of proposed antenna is small, it achieves a much wider bandwidth compared with the designs published in literature. The proposed antenna easily covers the UWB band (3.1-10.6). The gain across the operational band, simulated (HFSS) and measured, are presented in Fig. 6. The gain varies between 1 to 8.3 dBi from 2 to 20 GHz. The peak is recoded at 6.4 GHz the average gain across the operational band is 5.1 dBi. In Fig. 7, the simulation (HFSS) and measured efficiencies of proposed antenna are presented. The average radiation efficiency is 85% over the bandwidth.

The surface current distribution on the antenna at 4, 8, 12 and 18 GHz are shown in Fig. 8 and the measured radiation pattern including the cross-polarization and co-polarization of the fabricated antenna for same frequency in three principle planes *xz-plane(φ=0)*, *yz-plane(φ=90)* and *xy-plane(φ=180)* are shown in Fig. 9. At the low frequency of 4 GHz, Fig. 6 (a) shows that the current is distributed evenly. With increasing frequency, the proposed design shows that the higher order current modes are starting to develop and current density is less evenly distributed on the radiator.

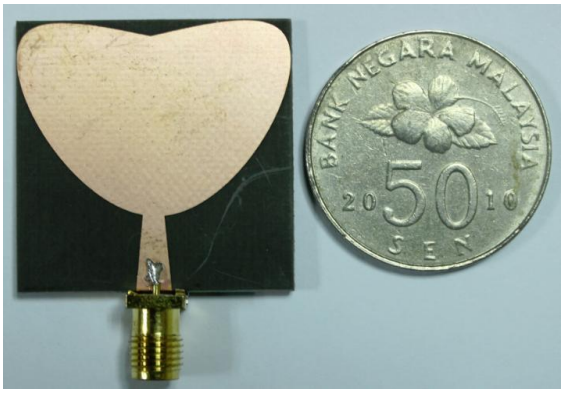

(a)

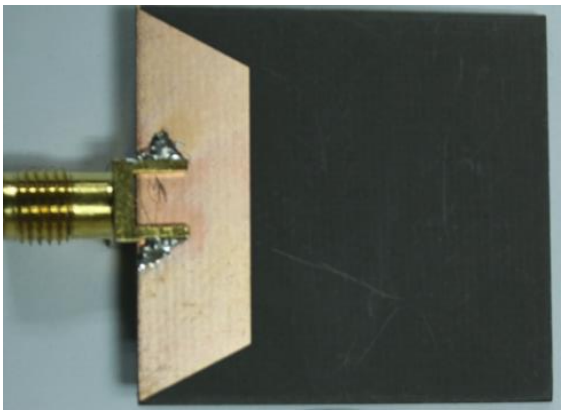

(b)

Fig. 4. Photographs of the fabricated antenna: (a) top layer and (b) bottom layer.

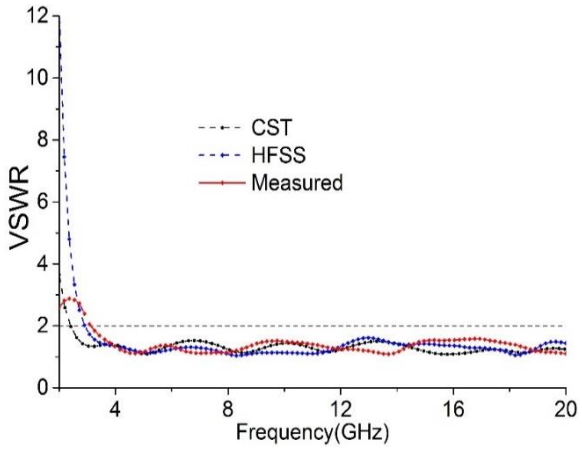

Fig. 5. Simulated and measured VSWR of the proposed antenna.

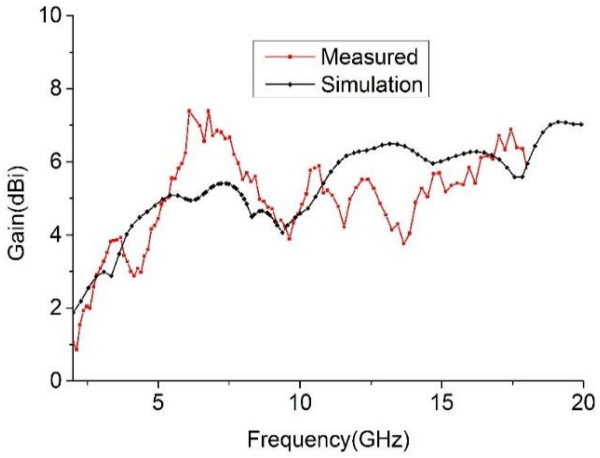

Fig. 6. Simulated and measured gain of the proposed antenna.

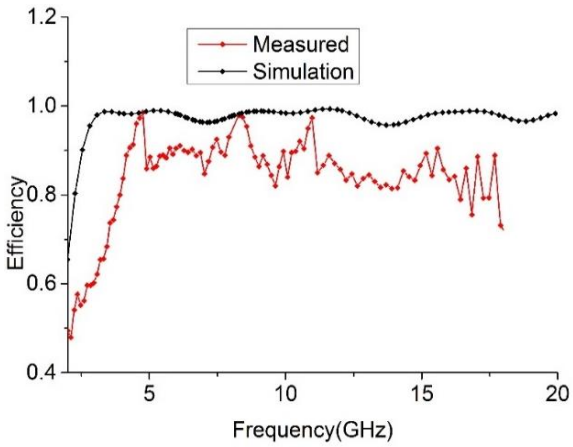

Fig. 7. Simulated and measured efficiency of the proposed antenna.

It can be seen that over the desired frequency band proposed antenna has stable radiation pattern characteristics. Based on these results of the radiation patterns of proposed antenna, it is evident that the proposed design is nearly omnidirectional for at lower frequencies. It is observed that with the increase of frequency produces undesirable cross-polarization due to the changing of surface current distribution. At higher frequency the radiation pattern become slightly directional. At the highest observed frequency in Fig. 8 (d) the higher order current modes are excited and current density is no longer distributed evenly. This results in the directional pattern seen in Fig. 9 (d). Furthermore, at higher frequencies, multiple nulls can be observed in the current distribution. This indicates that the radiating element is excited with higher order modes, which typically results in the directional radiation patterns.

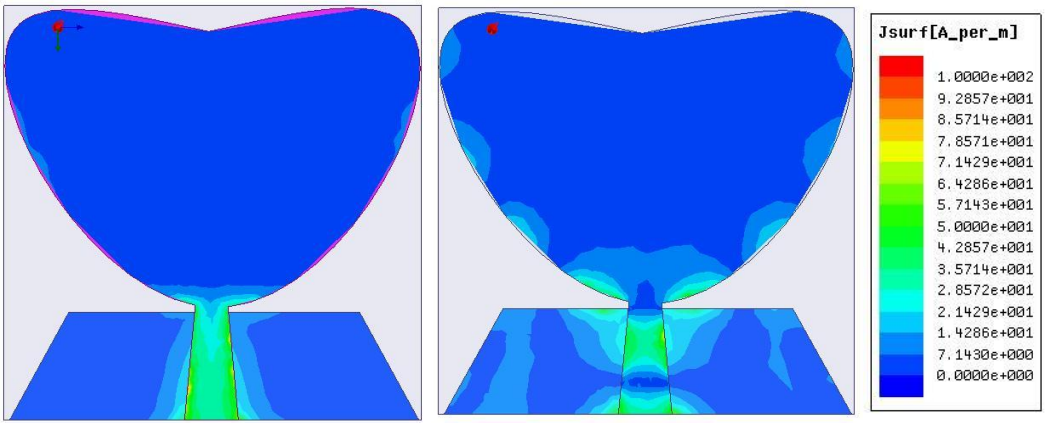

(a) (b)

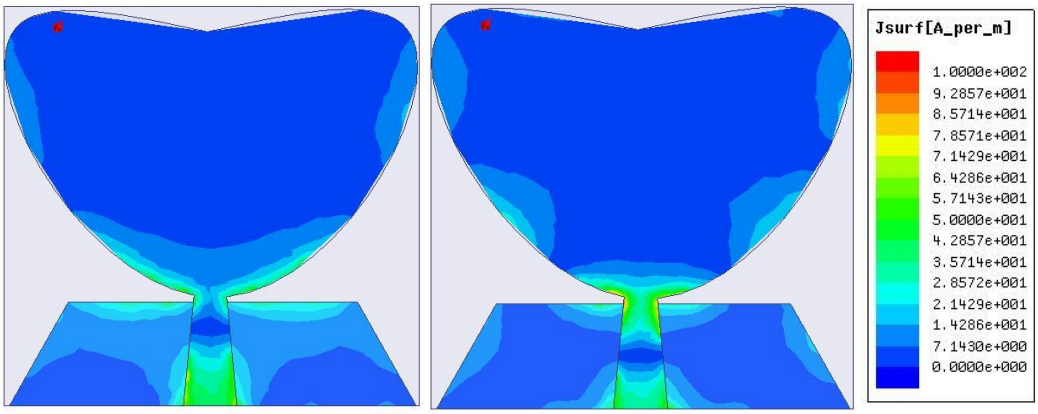

(c) (d)

Fig. 8. Surface current distribution of proposed antenna at: (a) 4, (b) 8, (c) 12, and (d) 18 GHz.

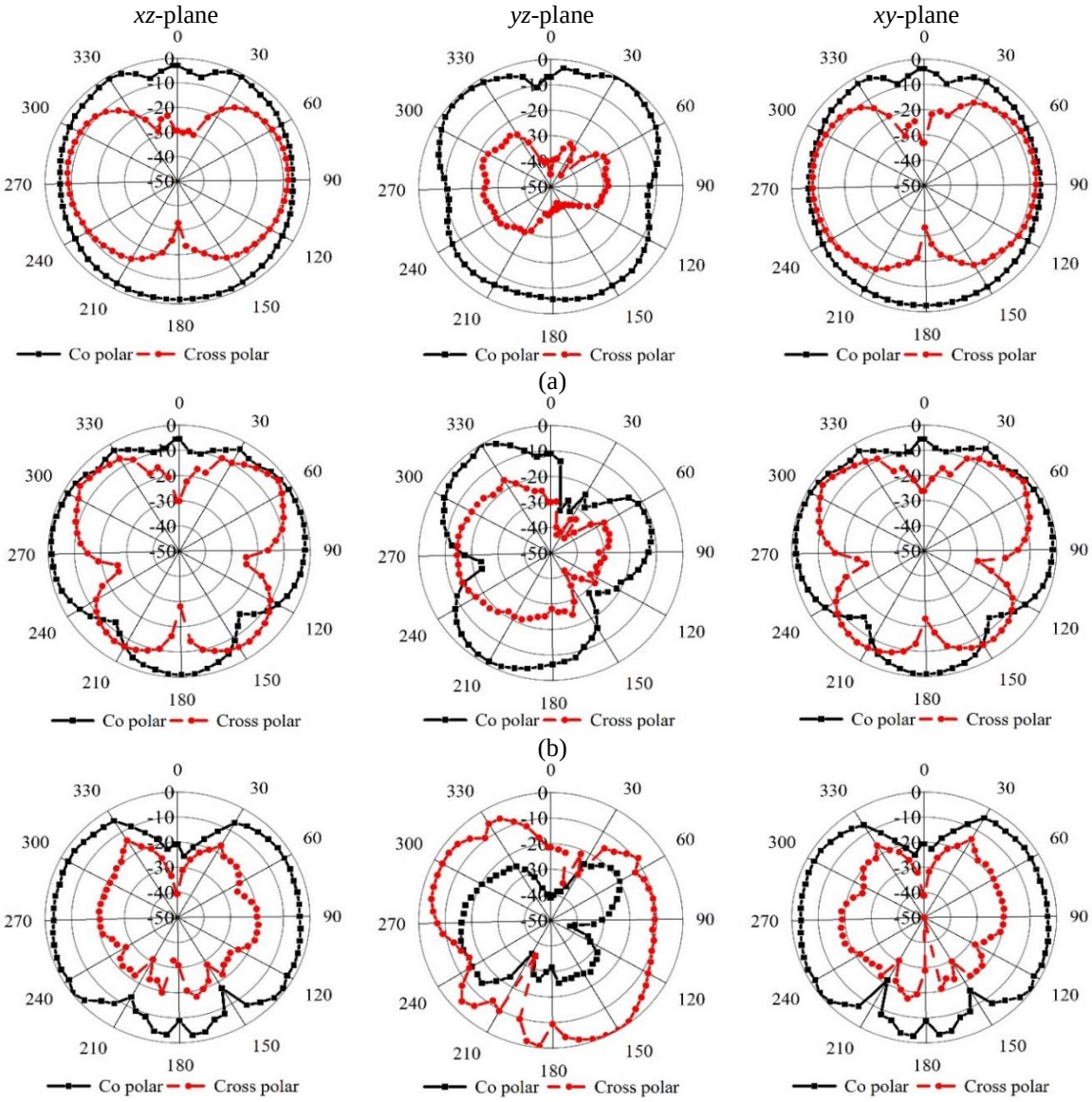

(a)

(b)

(c)

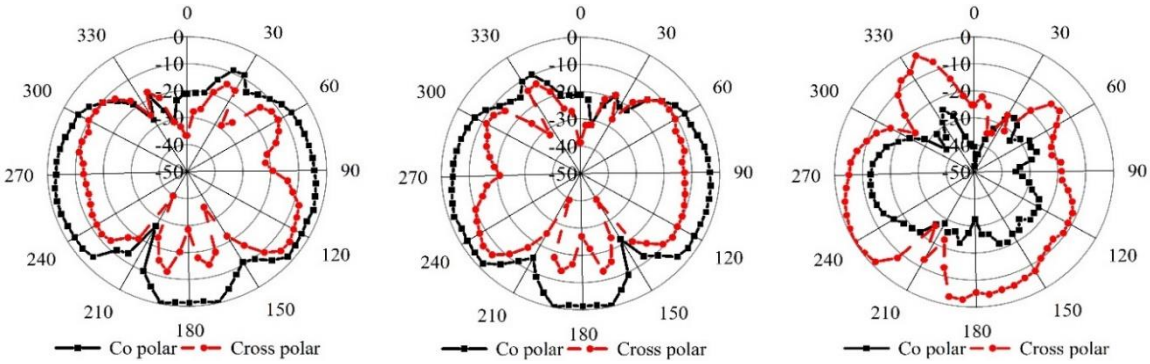

(d)

Fig. 9. Measured radiation pattern of cross-polarization and co-polarization of the proposed antenna at: (a) 4 GHz, (b) 8 GHz, (c) 12 GHz, and (d) 18 GHz.

Table 2 compares the proposed UWB antenna and existing antennas. The proposed antenna and the existing antennas (literature review) were also studied to conduct an impartial comparison where all reference antennas cover ultra-wideband spectrum. The performances parameters, such as applications, 10-dB bandwidth, dielectric constant, fractional bandwidth and gain are presented in Table 2. The proposed antenna's fractional bandwidth (FBW, 145%) is better than antennas presented in literature. Therefore, the proposed UWB metamaterial antenna can offer good compact characteristics while maintaining wide operational bandwidth.

Table 2: Bandwidth, dielectric constant, fractional bandwidth and gain comparison

Reference	Application	BW (S_{11}<-10dB)	Dielectric Constant	FBW (%)	Gain (dBi)
[4]	Near field imaging	3.4-9.9	4.8	97	Not reported
[5]	Breast cancer imaging	4.4-7.7	10.2	77	Not reported
[7]	UWB application	4-14	2.2	111	2.32-4.4
[8]	UWB application	3.1-15.2	4.4	132	2.5
[9]	UWB application	3.7-18	-	132	3.97
[10]	UWB application	4-19.1	3.50	130	>1
Proposed prototype	UWB application	3.2-20	2.33	145	5.1

VI. CONCLUSION

The design of a hibiscus petal pattern monopole antenna for UWB Applications with a size of 31×31 mm^2 has been presented in this paper. Measurement result shows that the antenna has an impedance bandwidth of about 145% from 3.2 to 20 GHz with VSWR<2, a stable omnidirectional radiation pattern, an average peak gain 5.1 dBi and the radiation efficiency is about 85% over the bandwidth. The design of the proposed antenna is very simple and can be used in microwave circuitry with low manufacturing cost, easy to integrate with portable devices. Experimental results show that the proposed antenna could be good candidate for various UWB applications.

REFERENCES

[1] F. C. Commission, "Revision of Part 15 of the Commission's Rules Regarding Ultra-Wideband Transmission Systems, First Report and Order, FCC 02," V48, April 2002.

[2] B. Allen, M. Dohler, E. Okon, W. Malik, A. Brown, and D. Edwards, *Ultra Wideband Antennas and Propagation for Communications, Radar and Imaging*, John Wiley & Sons, 2006.

[3] E. Fear and M. Stuchly, "Microwave detection of breast cancer," *Microwave Theory and Techniques, IEEE Transactions on*, vol. 48, pp. 1854-1863, 2000.

[4] M. T. Islam, M. Moniruzzaman, N. Misran, et al., "Curve fitting based particle swarm optimization for UWB patch antenna," *Journal Of Electromagnetic Waves And Applications*, vol. 23, iss. 17-18, pp. 2421-2432, 2009.

[5] M. N. Shakib, M. T. Islam, and N. Misran, "Stacked patch antenna with folded patch feed for ultra-wideband application," *IET Microwaves Antennas & Propagation*, vol. 4, iss. 10, pp. 1456-1461, 2010.

[6] M. Sharma and V. Shrivastava, "Printed fractal elliptical monopole antenna for UWB application," *in Recent Advances in Microwave Theory and Applications, 2008. Microwave 2008. International Conference on*, pp. 374-376, 2008.

[7] A. A. Shaalan and M. Ramadan, "Design of a compact hexagonal monopole antenna for ultra-wideband applications," *Journal of Infrared, Millimeter, and Terahertz Waves*, vol. 31, pp. 958-

968, 2010.
[8] Y. B. Yang, F. S. Zhang, F. Zhang, L. Zhang, and Y. C. Jiao, "A novel compact CPW-fed planar monopole antenna with modified stair-style ground for ultra-wideband applications," *Microwave and Optical Technology Letters*, vol. 52, pp. 2100-2104, 2010.
[9] L. Liu, S. Cheung, R. Azim, and M. T. Islam, "A compact circular-ring antenna for ultra-wideband applications," *Microwave and Optical Technology Letters*, vol. 53, pp. 2283-2288, 2011.
[10] G. Isik and S. Topaloglu, "A compact size 4–19.1 GHz heart shape UWB antenna with triangular patches," *International Journal of Antennas and Propagation*, vol. 2013, 2013.
[11] H.-W. Liu and C.-F. Yang, "Miniature hook-shaped monopole antenna for UWB applications," *Electronics Letters*, vol. 46, pp. 265-266, 2010.
[12] M. Ojaroudi, C. Ghobadi, and J. Nourinia, "Small square monopole antenna with inverted T-shaped notch in the ground plane for UWB application," *Antennas and Wireless Propagation Letters, IEEE*, vol. 8, pp. 728-731, 2009.
[13] R. Azim, M. T. Islam, and N. Misran, "Compact tapered-shape slot antenna for UWB applications," *Antennas and Wireless Propagation Letters, IEEE*, vol. 10, pp. 1190-1193, 2011.
[14] C. Figueroa Torres, J. Medina Monroy, H. Lobato Morales, R. Chavez Perez, and A. Calvillo Tellez, "Heart shaped monopole antenna with defected ground plane for UWB applications," *in Electrical Engineering, Computing Science and Automatic Control (CCE), 2014 11th International Conference on*, pp. 1-4, 2014.
[15] T. Yang and X. J. Tian, "A novel heart-shaped monopole antenna for UWB and RFID applications," *Microwave and Optical Technology Letters*, vol. 53, pp. 2288-2291, 2011.

Md. Zulfiker Mahmud is an Assistant Professor of AIS Department in Jagannath University Bangladesh. He received the B.Sc. and M.Sc. degree in Computer Science and Engineering from Islamic University Kushtia, Bangladesh. Currently he is working as a Ph.D. student in the Universiti Kebangsaan Malaysia (UKM), Malaysia. He has authored or co-authored a number referred journals and conference papers. He is currently a Graduate Research Assistant at the Department of Electrical, Electronic and Systems Engineering, UKM, Malaysia. His research interests include the microwave imaging, antenna design, satellite antennas, satellite communication and wireless communication.

Salehin Kibria was born in Dhaka, Bangladesh, in 1988. He received the B.Eng. (Hons.) degree in Electronics majoring in Telecommunications from Multimedia University (MMU), Malaysia. He is currently working toward the PhD. degree at the Universiti Kebangsaan Malaysia. He is also employed as a Research Assistant at the Institute of Space Science (ANGKASA) in a research project funded by the Malaysian government. His research interest focuses on RFID reader antenna designs, telecommunication, particle swarm optimization, etc.

Md. Samsuzzaman was born in Jhenaidah Bangladesh in 1982. He received B.Sc. and M.Sc. degree in Computer Science and Engineering from Islamic Univrsity Kushtia, Bangladesh in 2005 and 2007, respectively and the Ph.D. degree from the Universiti Kebangsaan Malaysia, Malaysia 2015. From February 2008 to February 2011, he worked as a Lecturer at Patuakhali Science and Technology University (PSTU), Bangladesh. From February 2011 till now, he is working as an Assistant Professor at the same university. He has authored or co-authored approximately 50 referred journals and conference papers. He is currently a Graduate Research Assistant at the Department of Electrical, Electronic and Systems Engineering, UKM, Malaysia. His research interests include the communication antenna design, satellite antennas, satellite communication, WSN and Semantic Web.

Norbahiah Misran received her B.Eng. in Electrical, Electronic & System Engineering from Universiti Kebangsaan Malaysia, UKM (1999). She completed her Ph.D. degree at the Queen's University of Belfast, Northern Ireland, UK (2004). She started her career as a Tutor in 1999. She later has been appointed as a Lecturer (2004) and an Associate Professor (2009). At present, she is a Professor at UKM. Her research interests include RF device design particularly in broadband microstrip antennas, reconfigurable antennas and reflectarray antennas. She is also conducting some researches in engineering education field.

Mohammad Tariqul Islam is a Professor at the Department of Electrical, Electronic and Systems Engineering of the Universiti Kebangsaan Malaysia (UKM). He is currently the Group Leader of the Radio Astronomy Informatics Group at UKM. He is the author of over 300 research journal articles, nearly 165 conference articles, and a few book chapters on various topics related to antennas, microwaves and electromagnetic radiation analysis with 11 inventory patents filed. Thus far, his publications have been cited 1990 times and his H-index is 25 (Source: Scopus). He is now handling many research projects from the Malaysian Ministry of Science, Technology and Innovation and Ministry of Education, and some international research grants from Japan. His research interests include communication antenna design, radio astronomy antennas, satellite antennas, and electromagnetic radiation analysis.

A Planar Monopole Antenna with Switchable Dual Band-Notched UWB/Dual-Band WLAN Applications

Mohammad M. Fakharian, Pejman Rezaei, and Vahid Sharbati

Department of Electrical and Computer Engineering
Semnan University, Semnan, 35131-19111, Iran
m_fakharian@semnan.ac.ir, prezaei@semnan.ac.ir, and v.sharbati@semnan.ac.ir

Abstract ─ In this paper, a planar monopole antenna in ultra-wide band (UWB) frequency range from 2.8 to 10.2 GHz with two notch band of 3.3–4.2 and 4.9–6 GHz is presented. The dual band-notched UWB antenna can be switched to dual wireless local area network (WLAN) frequency bands of 2.2–2.6 and 5–5.9 GHz. The proposed antenna has a simple structure and compact size of 15×15 mm^2. The antenna in the UWB function uses a circular radiator monopole with an embedded slot in the ground plane. Several stubs are etched on the radiator as rejecting elements. A parasitic element with an ideal switch is used in the backplane to achieve the dual-band WLAN function. In this mode, the stubs in the radiator are as resonating elements. The function of the antenna can be changed by switching states that make the various operating bands. The measurement and simulation results show that the antenna has good characteristics for cognitive radio application where the UWB antenna is required for spectrum sensing and the WLAN band antenna is used for reconfigurable operation.

Index Terms ─ Dual band-notched, dual-band WLAN, switchable, UWB antenna.

I. INTRODUCTION

One of the methods to develop switchable antennas in cognitive radio (CR) devices is to use the same antenna for both sensing and communication acts. It can performed by switching ultra-wide band (UWB) sensing antenna to communicate into multiple defined frequency bands [1]. Several designs of UWB antennas with reconfigurability options in frequency agility for CR systems have been implemented so far [2-7].

Recently, frequency switchable antennas that can support the UWB application and wireless local area network (WLAN) bands have been investigated [3, 8-10]. In [3], an incorporated planar UWB/reconfigurable slot antenna is proposed for CR applications. A slot resonator is embedded in the disc monopole radiator to obtain an individual narrowband antenna. A varactor diode is also deliberately inserted across the slot, providing a reconfigurable frequency function in the range of 5–6 GHz. In [8], an antenna is proposed that composed of four switches, a rectangular ring slot, a T-shaped stub, a coplanar waveguide feeding line, and two inverted S-shaped slots. By controlling the switches, the antenna is able to provide two operation modes whose operation bands can cover the dual-band WLAN bands and the single band-notched UWB bands. In [9], a rotatable reconfigurable antenna that can support the dual band-notch UWB application and the triple-band WLAN application is presented for CR systems. By controlling the rotational patch at different states, the antenna operates in two WLAN/mobile band and dual band-notched UWB complementary bands. However, these antennas have a complex structure and exhibit some defects in practical applications, require too much antenna space, and their center frequencies are difficult to control.

This paper presents a novel circular monopole antenna with switchable functions for UWB/WLAN applications. Several modified stubs in the radiation patch are used to realize the dual band-notch characteristic for the UWB antenna at worldwide interoperability for microwave access (WiMAX) band (3.3–3.7 GHz), C-band (3.7–4.2 GHz), and WLAN band (5.15–5.825 GHz). By embedding the cleaver-shaped parasitic element in backplane and using a switch between the ground plane and this parasitic element, the antenna is able to provide two operation cases which operation bands can cover the dual-band WLAN (2.4–2.48, 5.15–5.35, 5.725–5.825 GHz) and the dual band-notched UWB bands. Dimensions of the designed antenna are small, and its structure has less complexity and better usefulness. Additionally, novelty in comparison to previously presented antennas is another specification of this design, and with just one switch, two states are investigated.

II. ANTENNA DESIGN AND CONFIGURATION

The proposed monopole antenna fed by a 50-Ohm microstrip line is shown in Fig. 1, which is printed on

Submitted On: April 6, 2014
Accepted On: March 18, 2016

an FR4 substrate, with dimensions of 15×15×0.8 mm^3, permittivity 4.4, and loss tangent of 0.02. The antenna consists of a circular radiation patch with four stubs in up and down of it, a ground plane with rectangular-shaped of slot in it, and a cleaver-shaped parasitic element in backplane that contains a rectangular-shaped stub with a thin extruded stub from it. To achieve the desired frequency reconfigurability, one ideal switch is placed between the ground plane and parasitic element. In this study, the ideal switch for reconfigurability is metal bridge, which is achieved based on the proof of concept [9]. The presence of the metal bridge depicts that the switch state is ON; vice versa, the absence of the metal bridge depicts that the switch state is OFF in both simulation and fabrication. The dimension of the ideal switch is selected 0.7×0.2 mm^2 to be close to the actual dimension of a PIN diode switch. Signal transmission is mainly done by the means of an SMA connector attached to the monopole antenna.

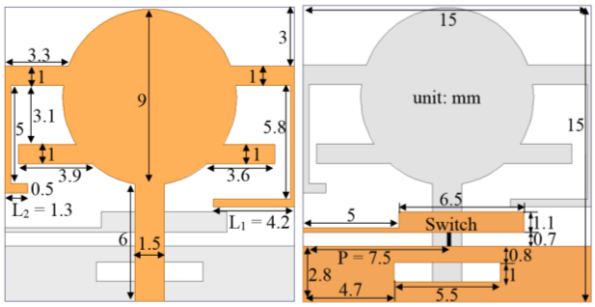

Fig. 1. Geometry of the proposed monopole antenna: (a) front view, and (b) bottom view.

By adjusting the total length of the bent stubs at the top of the patch to a half-wavelength of the rejecting bands, two notched bands with central frequencies of 3.7 and 5.5 GHz for WiMAX/C-band and WLAN can be obtained at UWB function, respectively. Widening bandwidth and operation band in the frequency range of 3.1–10.6 GHz for UWB system can be also achieved by tuning the lower stubs in the radiation patch and inserting a rectangular-shaped slot in the ground plane.

A dual band-notched UWB antenna to the dual-band function at the range of WLAN bands is introduced here by inserting an ideal switch between the ground plane and parasitic element in backplane. The position of the switch is determined somehow to create the desired frequency bands. When switch is ON, the proposed monopole antenna operates in dual-band WLAN mode. When switch is OFF, the antenna operates in dual band-notched UWB mode. When the proposed antenna works in dual-band WLAN mode, the two bent stubs at the top of the radiation patch provide the electrical current paths for producing the 2.4 and 5.5 GHz resonant frequency bands. The performance of the antenna is optimized and simulated with the Ansoft HFSS [11]. For this purpose, a wide parametric study is performed, and the final dimensions of the antenna are specified, as shown in Fig. 1. In addition, some important parameters of the proposed monopole antenna will be discussed in Section III in detail.

III. RESULTS AND DISCUSSION

A. Dual band-notched UWB antenna design

Figure 2 shows the schematic of the designed antenna in five steps used for dual band-notched UWB performance simulation studies. Comparisons among input reflection coefficients ($|S_{11}|$) for an ordinary circular monopole antenna [step 1], inserting a rectangular-shaped slot in the ground plane [step 2], attaching two rectangular-shaped stubs in the down of radiating patch [step 3], attaching a bent stub at the top of the radiating patch in the right [step 4], and the proposed antenna [step 5] are also respectively considered in Fig. 2. As shown in Fig. 2, the monopole antenna with slotted ground plane has wider impedance matching in comparison to the same antenna without slot in the ground plane. The current distribution on the slotted ground plane affects the impedance matching and the upper frequency bandwidth of the antenna. Also, it is found that by adding the stubs in the down of the radiating patch, the antenna can cover the full UWB band from 2.8-10.8 GHz. The first notched frequency (3.3–4.2 GHz) is achieved by the bent-shaped stub in the top right of the radiating patch, and eventually by using another bent-shaped stub in the top left of the radiating patch, a dual band-notch function is obtained that covers all the 5.2/5.8 GHz WLAN, 3.5/5.5 GHz WiMAX, and 4 GHz C-bands.

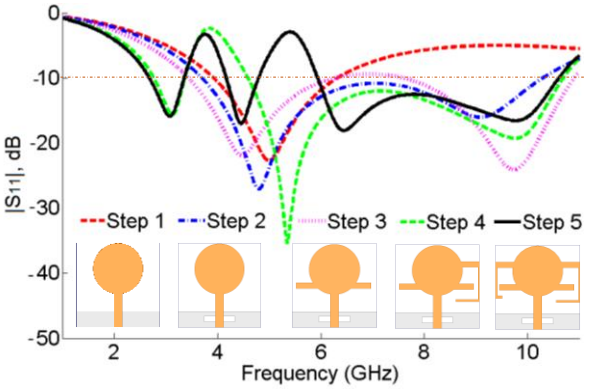

Fig. 2. Simulated $|S_{11}|$ of final design of the dual band-notched UWB antenna in five steps.

In order to understand the phenomenon behind the dual band-notch UWB performance, the simulated current distributions on the radiating patch at the

notched frequencies of 3.8 and 5.5 GHz are shown in Figs. 3 (a) and 3 (b), respectively. It can be observed in these figures that the current is concentrated at the edges of the U-shaped stub and the L-shaped stub and oppositely directed between the interior and exterior edges at 3.8 and 5.5 GHz, respectively. Therefore, the resultant radiation fields can be cancelled out, and high attenuation near the resonant frequency is achieved, thus the resulting notched band. By adjusting the dimensions of the U- and L-shaped stubs, the center frequencies of the lower and higher notched band can be independently controlled.

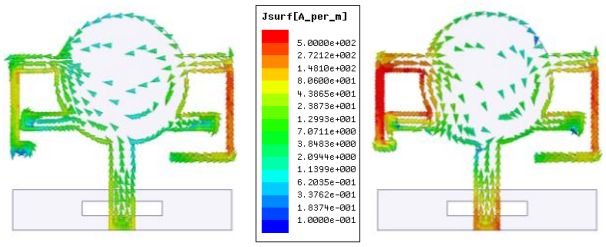

(a) (b)

Fig. 3. Simulated current distributions of the dual band-notched UWB antenna at the notch frequencies of: (a) 3.8 GHz and (b) 5.5 GHz.

Figure 4 shows the simulated $|S_{11}|$ of the dual band-notched UWB antenna for different dimensions of U- and L-shaped stubs. Figure 4 (a) presents the simulated $|S_{11}|$ curves of the antenna with the length L_1 = 3.2, 4.2, and 5.2 mm. It is found that with the increase of the length, the central frequency of the first notched band moves to a lower frequency, whereas the second notched band is slightly affected. Second, Fig. 4 (b) shows how the length of the L_2 affects the antenna performance. When the length of L_2 changes from 0.3 to 2.3 mm, the second notched band moves to the lower frequency, whereas the first notched band is not affected. As a result, we can adjust independently the notch frequencies by varying the length of L_1 and L_2.

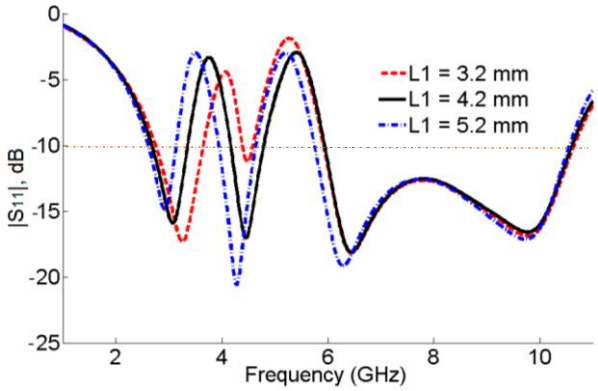

(a)

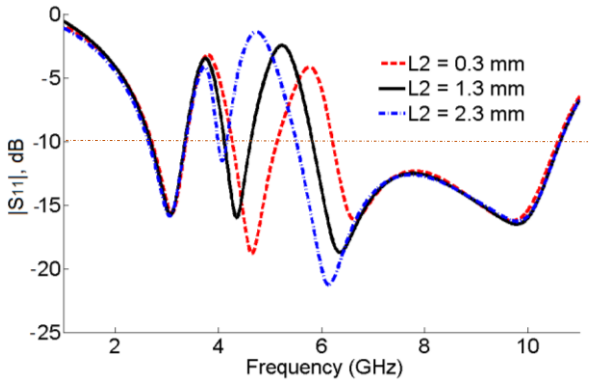

(b)

Fig. 4. Simulated $|S_{11}|$ of the dual band-notched UWB antenna with different values of: (a) L_1 and (b) L_2.

B. Switchable dual band-notched UWB/dual-band WLAN antenna design

The dual band-notched UWB antenna that was introduced in the Section A can be applied as a dual-band WLAN antenna using a parasitic element in the backplane and inserting a metal strip as ideal switch between the ground plane and it. Figure 5 shows the structure of the various antennas in three steps used for the dual-band performance simulation studies from the dual band-notched UWB antenna. $|S_{11}|$ for dual band-notched UWB antenna [step 1], with placing a cleaver-shaped parasitic element in the antenna backplane [step 2], and final design by placing a metal strip between parasitic element and ground planer [step 3] are also compared in Fig. 5. As shown in Fig. 5, the frequency bandwidth of the UWB antenna is not much affected by using the parasitic element in the steps 1 and 2, and the upper frequency just declined from 10.8 to 10.2 GHz. However, it is found that by inserting the metal strip, a dual-band function is achieved that covers all the 2.4/5.2/5.8 GHz WLAN bands. Therefore, the phenomenon of switching between the dual band-notched UWB and the dual-band WLAN performances is clarified here by the absence/presence of the metal strip for OFF/ON states in the steps 2/3, respectively.

To understand the operation theory of the antenna at the dual band-notch UWB with OFF switch and dual-band WLAN with ON switch, the current distributions of the two cases are shown in Fig. 6. As shown in Figs. 6 (a) and 6 (b), current flows are more dominant on the transmission line and are dispersed by the means of the stubs and concentrated around two sides of the rectangular slot in the ground plane in both frequency of 4.5 and 9.5 GHz. Also in Figs. 6 (a) and 6 (b), current flows on the feed line and the lower part of the patch have similar directions. In these structures, the central and top parts of the patch have current flows in rotational directions and electrically are neutralized. As

shown in Figs. 6 (a) and 6 (b), the current concentrated on the edges of the interior and exterior of the parasitic element in backplane at these frequencies. This figure shows that the electrical current does not change direction along the top edge of the ground plane. Therefore, the radiating power and bandwidth will not decrease significantly.

When the antenna works in the dual-band WLAN mode, the switch between the parasitic element and ground plane is ON. The parasitic element couples to the ground plane. In this case, for the 2.4 GHz excitation, clearly a larger surface current distribution is observed to flow along not only the feeding line, but also the stubs, especially the right side stub, as shown in Fig. 6 (c). This indicates that this stub does effectively provide the electrical current path for producing the 2.4 GHz resonant frequency band. However, for the 5.5 GHz excitation, the surface currents mainly flow along the left side stub, as shown in Fig. 6 (c). The difference between the two current distributions is because the proposed design can generate two various frequency bands that meet the demand of the dual-band WLAN application. The dual-band antenna has a slightly higher efficiency rather than dual band-notch UWB antenna in the 2.4 GHz radiating band, which is mainly owing to the electromagnetic coupling and the new resonant properties from the parasitic element which connected to the ground plane.

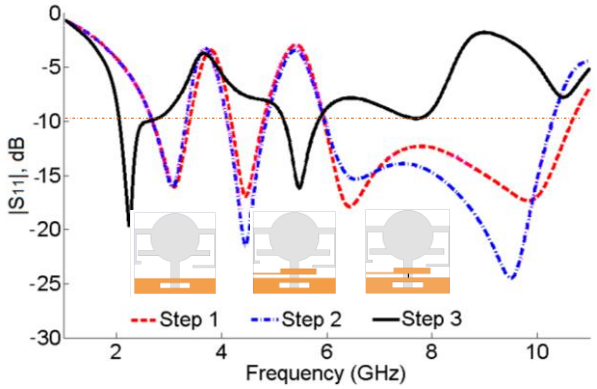

Fig. 5. Simulated $|S_{11}|$ of final design of the dual-band WLAN antenna in four steps.

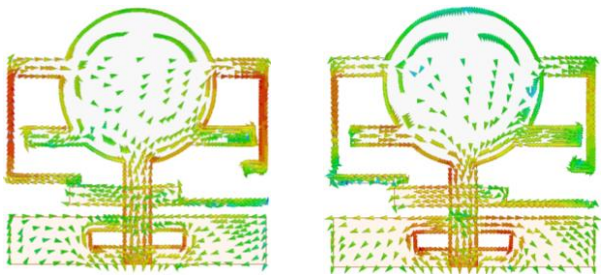

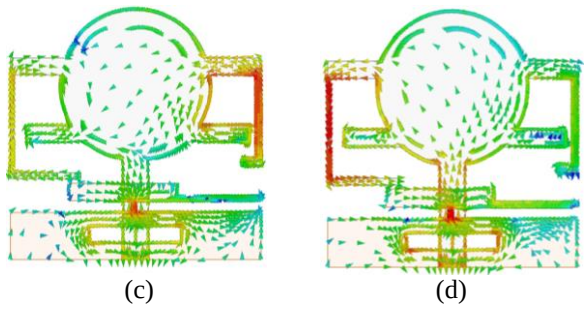

Fig. 6. Simulated current distributions of the antenna in the two cases; dual band-notched UWB mode at: (a) 4.5 GHz, (b) 9.5 GHz, and the dual-band WLAN mode at (c) 2.4 GHz, (d) 5.5 GHz.

To further investigate the design of the dual-band WLAN antenna, the influence of the position of the switch on the $|S_{11}|$ curves with various values of P is shown in Fig. 7. The position of switch is important in order to create desirable frequency bands in the WLAN mode. As shown in Fig. 7, the center frequencies of the lower and higher bands decrease with the decrease of P. Moreover, the bandwidth and impedance matching of the upper band can be controllable by changing the position of the switch.

To evaluate the performance of the proposed switchable antenna, the antennas with both switches ON/OFF are fabricated and measured. The prototype of the fabricated antenna is also shown in Fig. 8 (a). The simulated and measured $|S_{11}|$ of the switchable antenna with switch OFF/ON in the UWB/WLAN modes are shown in Fig. 8 (b). The discrepancy in the $|S_{11}|$ between the simulated and the measured may be mostly attributed to the effects of the SMA port, soldering, and manufacturing tolerance. In the dual-band WLAN mode, the switch is ON and the measured lower band for lower than -10 dB is from 2.2 to 2.6 GHz, and the measured higher band covers from 5 to 5.9 GHz. In the dual band-notched UWB mode, the switch is OFF and the antenna has a wideband performance of 2.8 to 10.2 GHz, covering the UWB frequency band with dual notched bands of 3.3–4.2 and 4.9–6 GHz for greater than -10 dB. Thereby, we can control the switches ON and OFF to allow the proposed antenna to work in underlay and overlay modes for CR communications. The proposed antennas can also be used for multimode wireless communication systems by controlling the switches at ON and OFF states.

The measured peak gain of the antenna versus frequency at the broadside direction is shown in Fig. 9. The antenna gain in the dual-band WLAN mode is more than 2.2 dB over the operating bands. Figure 9 also indicates that the gain of the dual band-notch UWB antenna is between 0–8 dB and has a comprehensive level during frequency bands except for two notched

bands at 3.8 and 5.5 GHz. The gains drop to -6.2 dB at lower notch band and -3.9 dB at the higher notch band.

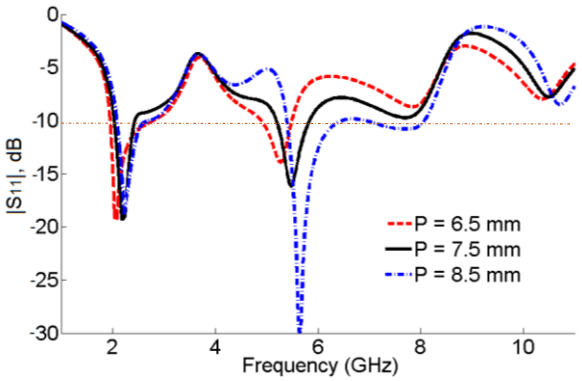

Fig. 7. Simulated $|S_{11}|$ of the dual-band WLAN antenna with different values of *P*.

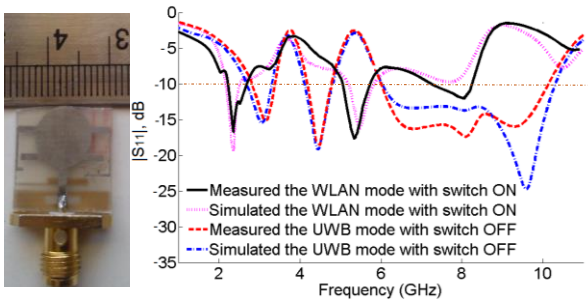

(a) (b)

Fig. 8. (a) Prototypes of the antennas in top view. (b) $|S_{11}|$ of the antennas in the UWB/WLAN modes.

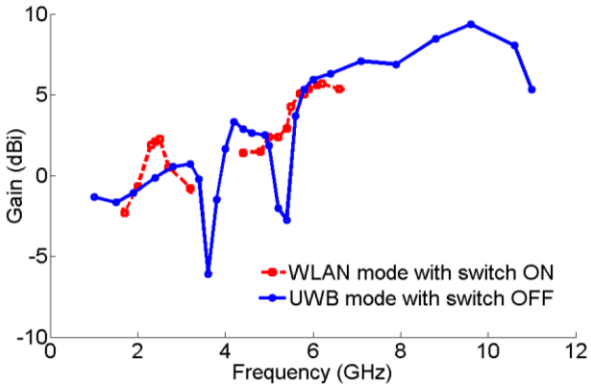

Fig. 9. Measured peak gain of the antenna in the UWB/WLAN modes.

The measured radiation patterns of two fabricated antennas in the two modes with switch ON/OFF are shown in Fig. 10. The antenna with switch ON/OFF can provide a nearly omnidirectional characteristic in H-plane and a dipole-like radiation characteristic in E-plane. Furthermore, the broadside directions of the two modes are almost identical. The rotation between low-frequency and high-frequency patterns results in the UWB mode is mostly due to the small ground plane effects and the change of excited surface current distributions on the system ground plane at high frequencies.

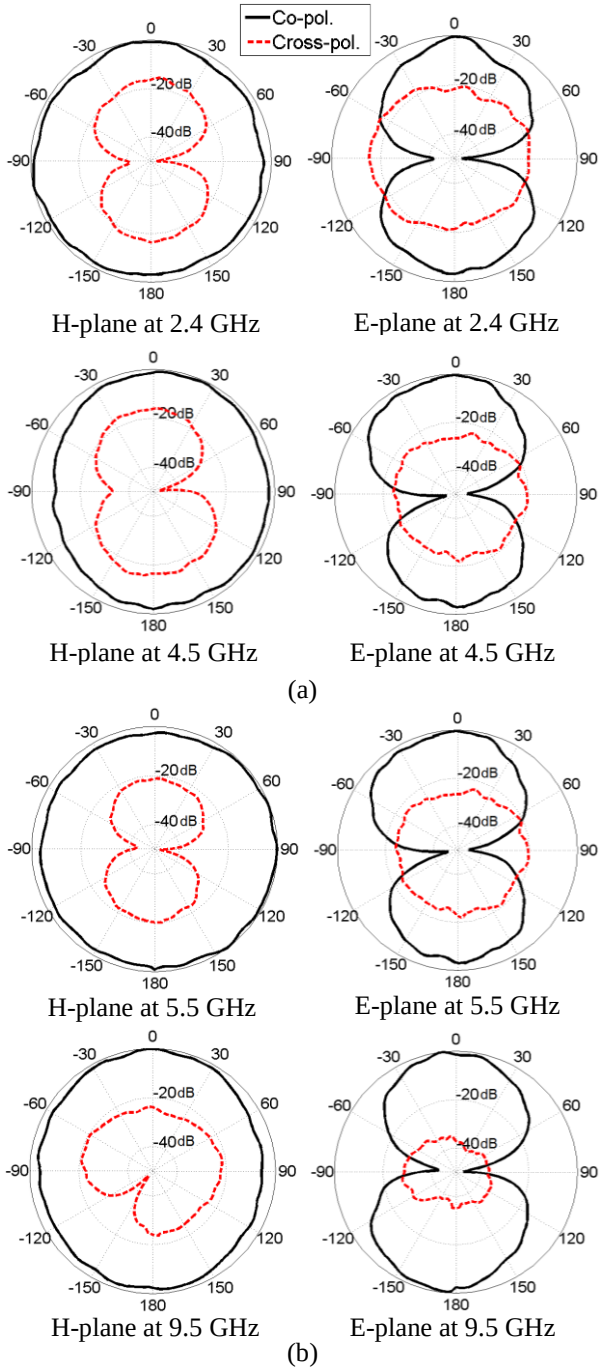

Fig. 10. Measured radiation patterns of the antenna in the two modes: (a) dual-band WLAN mode and (b) dual band-notched UWB mode.

IV. CONCLUSION

A planar monopole antenna with switchable frequency bands for dual band-notched UWB/dual-band WLAN applications has been introduced. It has been shown that using a rectangular slot in the ground plane with four stubs etched on the circular radiator patch can enhance bandwidth from 2.8 to 10.9 GHz with dual stop bands, which are exempt from interfaces with existing WiMAX band, C-band, and WLAN system. In addition, using a rectangular parasitic element in backplane and embedding an ideal switch in proper situations between the parasitic element and ground plane, the antenna can operate in two modes, namely, the dual band-notched UWB mode and the dual-band WLAN frequency mode. This antenna can offer sensing and communicating functions with a small size by controlling ideal switch that is either in the ON or the OFF position. The $|S_{11}|$ of the antenna was measured and agreed well with the simulation results. The measured radiation patterns and gain have been also demonstrated for different operating states of the antenna. The antenna is intended for use in multi radio wireless applications and future CR communications.

ACKNOWLEDGMENT

This work has been supported financially by the Office of Brilliant Talents at the Semnan University. The authors would like to thank all the members of the Antenna Laboratory at Iran Telecommunication Research Center (ITRC), especially Mr. Solat and Mr. Mirabdollahi, for their cooperation.

REFERENCES

[1] T. Aboufoul, A. Alomainy, and C. Parini, "Reconfiguring UWB monopole antenna for cognitive radio applications using GaAs FET switches," *IEEE Antennas Wireless Propag. Lett.*, vol. 11, pp. 392-394, 2012.

[2] M. M. Fakharian and P. Rezaei, "Very compact palmate leaf-shaped CPW-fed monopole antenna for UWB applications," *Microw. Optic. Tech. Lett.*, vol. 56, no. 7, pp. 1612-1616, 2014.

[3] E. Erfani, J. Nourinia, Ch. Ghobadi, M. Niroo-Jazi, and T. A. Denidni, "Design and implementation of an integrated UWB/reconfigurable-slot antenna for cognitive radio applications" *IEEE Antennas Wireless Propag. Lett.*, vol. 11, pp. 77-80, 2012.

[4] M. M. Fakharian, P. Rezaei, and A. A. Orouji, "A novel slot antenna with reconfigurable meander-slot DGS for cognitive radio applications," *Appl. Comput. Electromagn. Soc. J.*, vol. 30, no. 7, pp. 748-753, 2015.

[5] T. Wu, R. L. Li, S. Y. Eom, and S. S. Myoung, "Switchable quad-band antennas for cognitive radio base station applications," *IEEE Trans. Antennas Propag.*, vol. 58, no. 5, pp. 1468-1476, 2010.

[6] Y. Li, W. Li, and W. Yu, "A compact reconfigurable antenna using SIRs and switches for ultra wideband and multi-band wireless communication applications," *Appl. Comput. Electromagn. Soc. J.*, vol. 28, no. 5, pp. 427-440, 2013.

[7] M. M. Fakharian, P. Rezaei, and A. A. Orouji, "Reconfigurable multiband extended U-slot antenna with switchable polarization for wireless applications," *IEEE Antennas Propag. Mag.*, vol. 57, no. 2, pp. 194-202, 2015.

[8] P. Lotfi, M. Azarmanesh, and S. Soltani, "Rotatable dual band-notched UWB/triple-band WLAN reconfigurable antenna," *IEEE Antennas Wireless Propagat. Lett.*, vol. 12, pp. 104-107, 2013.

[9] B. Li, J. Hong, and B. Wang, "Switched band-notched UWB/dual-band WLAN slot antenna with inverted S-shaped slots," *IEEE Antennas Wireless Propagat. Lett.*, vol. 11, pp. 572-575, 2012.

[10] G. Zhang, J. S. Hong, B. Z. Wang, and G. Song, "Switched band-notched UWB/WLAN monopole antenna," *Appl. Comput. Electromagn. Soc. J.*, vol. 27, no. 3, 2012.

[11] Ansoft High Frequency Structure Simulator (HFSS), ver. 11, Ansoft Corp., Framingham, MA, 2010.

Mohammad M. Fakharian was born in Tehran, Iran, in 1987. He received the B.S. and M.S. degrees in Electrical Engineering from Semnan University, Semnan, Iran, in 2009 and 2012, respectively. Currently, he is working towards the Ph.D. degree in Communication Engineering from the Semnan University.

His research interests include low-profile antennas for wireless communication, reconfigurable antennas, and electromagnetic theory: numerical methods and optimization techniques.

Pejman Rezaei was born in Tehran, Iran, in 1977. He received the B.S. degree in Electrical-Communication Engineering from Communication Faculty, Tehran, Iran, in 2000, and the M.S. and Ph.D. degrees from Tarbiat Modarres University, Tehran, Iran,

in 2002 and 2007, respectively. Currently, he is Assistant Professor in the Semnan University, Semnan, Iran.

His current research interests are Electromagnetics theory, theory and design of antenna, metamaterial structure, and satellite communication.

Vahid Sharbati was born in Gorgan, Iran, in 1986. He received the B.S. degree in Electrical Engineering from Mazandaran University, Sari, Iran, in 2009. Currently, he is working towards the M.S. degree in Communication Engineering from the Semnan University. His current interest is in reconfigurable microstrip antennas.

Ultra-Wideband Planar Antenna with Notched Bands at 3.5/5.5 GHz

Rezaul Azim [1] and Mohammad T. Islam [2]

[1] Department of Physics
University of Chittagong, Chittagong 4331, Bangladesh
rezaulazim@yahoo.com

[2] Departemnt of Electrical, Electronic & Systems Engineering
Universiti Kebangsaan Malaysia, 43600 UKM Bangi, Malaysia
tariqul@ukm.edu.my

Abstract **—** In this paper, a microstrip planar antenna with notch bands at 3.5/5.5 GHz is proposed for ultra-wideband communication. An e-shape parasitic slit and an inverted C-shape slit are imprinted beneath the radiating patch to generate notch bands to suppress the interference from WiMAX and WLAN respectively. The experimental results confirmed that the fabricated prototype with a very small size has achieved an UWB operating band for VSWR ≤ 2 with two notched bands covering frequencies of 3.32 - 3.76 GHz and 5.2 - 5.92 GHz. The presented design achieved a good gain except at notched bands and exhibits stable omnidirectional radiation patterns. In this design, filter elements are embedded only on one side of the substrate without cutting any slot/s in the radiating element/ground plane and no modification of the patch or the ground plane is required which gives the proposed design an advantages over many designs reported for the same applications.

Index Terms **—** Dual notch band, parasitic slit, UWB, WiMAX, WLAN.

I. INTRODUCTION

The requirement for short distance wireless communication technologies has increased rapidly. ultra-wideband (UWB) has gained lot of attention as one of the most prodigious solutions for high speed wireless communications, imaging systems and high accuracy radars. Despite of high data rate, UWB system consumes low power compared to the other narrow band systems, resulting in not causing undesired interference to the existing communication systems. However, strong signals from IEEE 802.16 WiMAX (operating at 3.3 – 3.8 GHz) and IEEE 802.11a WLAN (covering 5.15 – 5.825 GHz band) narrow bands may degrade the UWB system's performance due to electromagnetic interference (EMI). In order to suppress these strong interfering signals, antennas that have filtering properties at their allocated frequencies are very important to UWB systems. At the same time, UWB antennas should possesses wide operating bandwidth, stable radiation patterns for omnidirectional communications and minimum distortion of the received waveform.

A good number of antennas have already been presented with band notched characteristics [1-17]. Despite UWB performance, some of the reported designs fail to achieve desired notched band/s and some designs use complex structures to generate notch band/s. For example, in [1], a band rejected UWB antenna is presented. The band notch performance at WiMAX and ITU band was realized by using two spiral resonators beside the feedline while a pair of complementary split ring resonators was etched on the ground plane to produce third stop band covering 4.92 - 6.1 GHz WLAN band. By properly choosing the position and size of the resonators, the reported design with an area of 36×60 mm^2 exhibits UWB characteristics with multiple stop bands. An UWB circular patch antenna with dual band filtering performances is reported in [2]. By introducing slots in the ground and etching two arc-shaped strips near the radiator, the designed antenna with a dimension of 35×39 mm^2 achieved dual notch bands to filter out WiMAX and WLAN bands. A 36×34 mm^2 size UWB microstrip patch antenna with multiple stop bands is reported in [3]. By inserting two hook-shaped slots in the ground plane, a stop band at 3.3 - 3.9 GHz was achieved while dual stop bands centered at 5.2 GHz and 5.8 GHz were realized by inserting a Ω-shaped slot in the radiator and a semi-octagonal-shaped resonator in the ground plane. In [4], a dual notch band monopole antenna was reported for UWB application. A rejected band centered at 3.5 GHz was realized by imprinting a U-shaped slot in the feedline while another notched band at 5.5 GHz was attained by cutting two L-shape slots in the ground plane. In [5], an UWB monopole antenna with dual notched band was reported. The 3.8 GHz notch band was attained by inserting a U-shaped slot in the ground structure while 5.8 GHz notch band was realized by etching an E-shaped

Submitted On: February 8, 2016
Accepted On: March 21, 2016

slot in the rectangular patch. A layout of an UWB antenna with notch band performance was proposed in [6]. To achieve band notch function for WiMAX, an arc H-shaped slot was inserted on the circular patch while to create a notched band for WLAN, two narrow slots were etched on the ground plane and the antenna occupies an area of 35.5×30 mm^2. In [7], a small planar antenna with band rejected performances has been presented. To produce a notch band at 3.25 - 3.85 GHz, a butterfly shaped backplane structure is inserted on the ground plane side while by imprinting a U-shaped slot in the radiator, a second notch band at 4.9 - 6.2 GHz is generated. An UWB antenna with multiple stop bands was reported in [8]. To achieved notch bands centered at 3.6 GHz, 7.5 GHz and 8.3 GHz three C-shaped slots have been inserted on the radiating patch while the notch bands for lower and upper WLAN are generated by etching C-shaped slots on the partial ground plane. In the design reported in [10], one capacitive loaded loop resonator has been attached to the radiator with an aim to reject the frequency band used by WLAN while one I-shape strip and one flip L-shape strip are added respectively to the lower and upper rectangular slots of the ground plane to filter out the frequency bands used by WiMAX and ITU band. In [16], a semicircular antenna with dual stop band performances is reported. To produce WLAN notch band of 5.2 - 5.9 GHz, a thin rectangular slot is etched in the radiating patch while by using two C-shaped circular slots in the defected ground structure, another notch band at 7.8 - 9.0 GHz is generated for C-band satellite communication. An UWB antenna with multiple stop band characteristics is reported in [17]. By inserting four modified bow-shaped slots in the radiator and a pair of rectangular-shaped slots in the ground plane, the designed antenna generates three notch bands covering frequencies of 3.3 - 4.2 GHz, 5.15 - 5.95 GHz and 7 - 8 GHz. All the above mentioned antennas exhibit wide operating band with required band notch characteristics. However to achieve dual/multiple notch bands, each of the above mentioned antennas uses slots, resonators and slits and they were etched simultaneously in both the ground plane and radiating patch which can create fabrication difficulties. Moreover, misplacement of the filter elements may also cause engineering problem resulting in the realization of undesired notched bands.

In this paper, a microstrip-line fed rectangular antenna that achieves compact planar profile is proposed for UWB communication. By etching two parasitic slits below the radiating element, the designed compact antenna realized UWB performance with two notched band at 3.5 GHz and 5.5 GHz. Unlike the antennas presented in [1-17], where the slit/s and slot/s were embedded on the radiating element as well as in the ground planes, the novelty of the proposed design is that it uses parasitic slits (filter element) on one side of the substrate without modifying or altering the shape, size of the patch and the ground plane.

II. ANTENNA DESIGN

The footprint of the proposed design is presented in Fig. 1. The microstrip line fed rectangular radiating patch of size 14.5×13.5 mm^2 is etched on the front side of a 1.6-mm thick FR4 dielectric material and the ground plane with side length 5.5 mm is imprinted on the rear side. The radiating patch is 0.5 mm away from the conducting partial ground plane. To achieve 50 **Ω** characteristic impedance, the feed line width and length are chosen as 2.75 mm and 6mm respectively. It is found that the radiating patch coupled strongly to the ground plane and designed antenna of overall volumetric size 29×20.5×1.6 mm^3 is able to achieve sufficient operating band to cover FCC defined ultra-wide frequency band as depicted in Fig. 4.

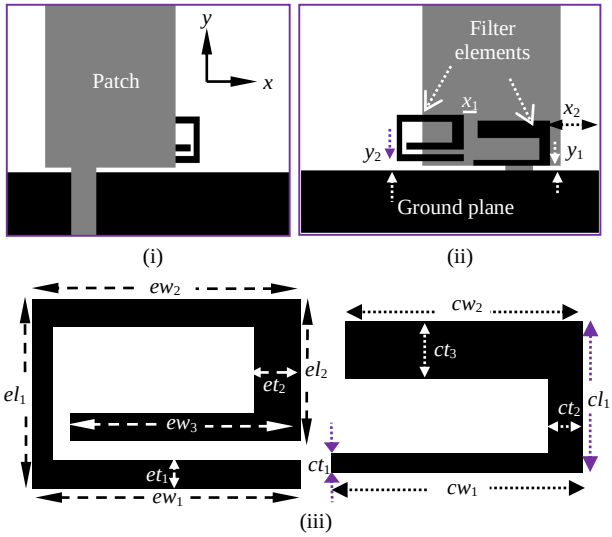

Fig. 1. Geometry of proposed antenna: (i) front view, (ii) rear view, and (iii) parasitic slits (filter element).

To generate a notch band at 3.5 GHz, an e-shape parasitic slit is etched systematically at a distance y_2 from the top edge of the ground plane. To produce second notch band at around 5.5 GHz, an inverted C-shape slit is embedded below the patch along with the e-shaped slit and it is at y_1 away from the ground plane. The distance between these two slits is x_1. The total length of each slit is about half of the guided wavelength (λg), which is given by [11]:

$$\lambda_g = \frac{\lambda}{\sqrt{\frac{\varepsilon_r + 1}{2}}}, \quad (1)$$

where ε_r is the dielectric constant of the substrate and λ is the wavelength of the respective notch band, i.e., centre frequency of the corresponding notch band. The detail dimensions of the different parameters of the

parasitic slits are depicted in Fig. 1 (iii).

The vector-current distribution at notch bands and pass bands frequencies are illustrated in Fig. 2 with an aim to understand the creation of notch bands. In the plot, the currents are strongly distributed as it approaches the areas marked red and concentration becomes denser. It can be seen in Fig. 2 (a) that at lower notch center frequency of 3.5 GHz, most of the surface current concentrated near the e-shaped slit while the currents in the rest part of the antenna is very weak. Figure 2 (b) displayed that at 5.5 GHz the surface currents at inverted C-shaped slit is stronger than the other part of the antenna. Therefore, the antenna impedance altered at these frequencies due to the insertion of parasitic slits. It is also revealed from Fig. 2 (a) and 2 (b) that, the currents in the symmetrical sides of the filter elements are reverse to each other resulting in weak radiation from the antenna at these frequencies. These current distributions implies that at the notch frequencies strong resonances are created and hence notch bands are produced at around 3.5 GHz and 5.5 GHz. Other than WiMAX and WLAN band, the currents in the parasitic slits are almost similar to that of the other parts of the antenna as displayed in Fig. 2 (c) and Fig. 2 (d). As a result, the parasitic slits (filter elements) act as a part of the radiating element and radiate effectively.

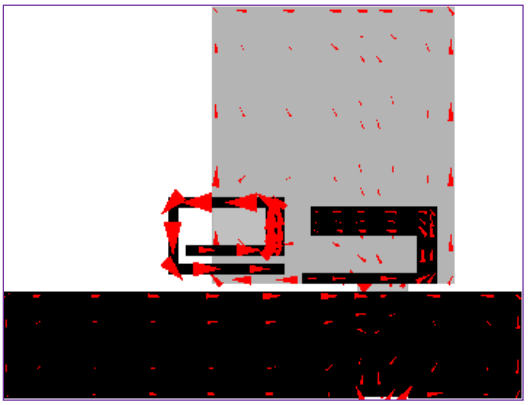

(a)

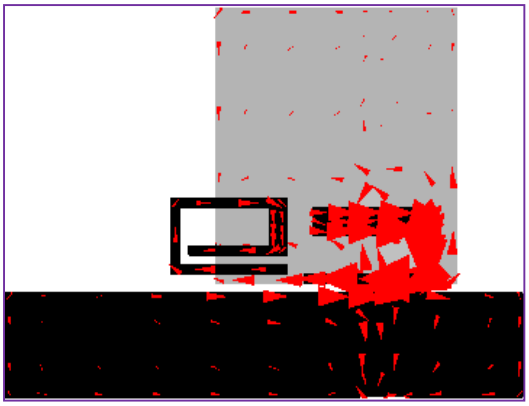

(b)

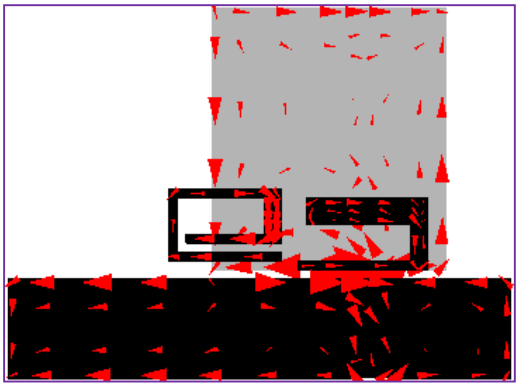

(c)

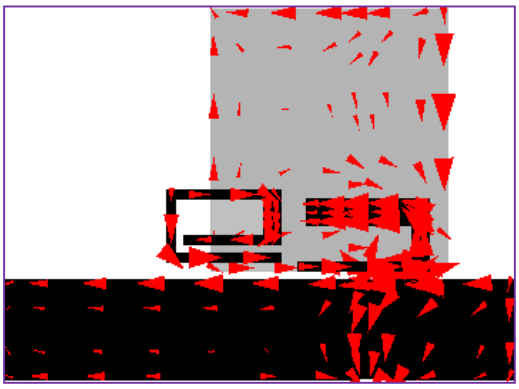

(d)

Fig. 2. Vector-current distribution at: (a) 3.5, (b) 5.5, (c) 6.2, and (d) 8.5 GHz.

The input impedance characteristic of the designed antenna, the antenna without filter structures (slits) and with single parasitic slit is displayed in Fig. 3. It is revealed from graph that for the antenna without notch bands, the input impedance is very much close to 50 Ω line and exhibits good impedance matching resulting in a UWB operating band.

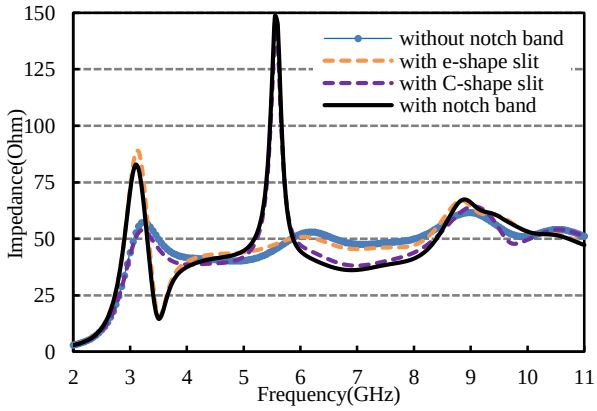

Fig. 3. Input impedances for without, with single and with double filter structure.

On the other hand, some parts of the impedance lines (at around 3.5 GHz and 5.5 GHz) of the antenna with notch bands are away from the 50 Ω characteristic impedance line and offers higher impedances resulting in poor matching. Due to this poor matching dual notch bands are created at around 3.5 GHz and 5.5 GHz. For embedment of single parasitic slit, high impedance is observed at the respective frequency band and hence single notch band at WiMAX and WLAN frequency spectrum are produced. Other than notched frequency band/s, the impedances are almost similar to that of antenna without notched bands.

III. SENSITIVITY ANALYSIS

As the notched bands are created by the parasitic slits, their size and location have a great impact on the notched band characteristics. A sensitivity test has been performed to examine the effects of different design parameters as well as to observe the performance of the proposed band notch design. All the simulations are done by using IE3D simulator from Zeland. Different VSWR curves are displayed in Fig. 4 by etching one slit (filter element) at a time while keeping the other slit absent. From Fig. 4 it can be seen that each slit stops a targeted frequency band. It is confirmed from Fig. 4 that e-shape slit reject 3.5 GHz WiMAX band while inverted C-shape slit notch WLAN band and insertion of both the e-shape and C-shape slits together can generate dual notch bands at 3.5 and 5.5 GHz. It is also revealed from the plot that the two slits can perform independently without any strong interference between them.

To explore the sensitivity of various design parameters of the parasitic slits on filtering performance, a parametric study is done. Since the parasitic slits are only the filter element in generating dual stop band, their width, length and thickness are chosen to do the sensitivity analysis. The effects of different design parameters such as ew_3, el_2, cl_1 and ct_2 on antenna performances are depicted in Fig. 5. Figures 5 (a) and 5 (b) respectively show the VSWR curves for different values of ew_3 and el_2 while the rest of the antenna dimension are remain fixed. As the width ew_3 varies from 3.5 to 5.5 mm, the WiMAX center frequency changes from 3.99 GHz to 3.52 GHz and the bandwidth of the this stop band is reduces with the increment of ew_3. However the second stop band for WLAN does not vary with the variation of ew_3. The simulated VSWR in Fig. 5 (b) shows that the resonance frequency of the WiMAX band as well as the bandwidth is strongly dependent on el_2 while it does not affect second stop band for WLAN. When the values of el_2 increases, the WiMAX center frequency goes to the lower frequency spectrum and its bandwidth is decreased with el_2. From these results, it may be commented that WiMAX center frequency as well as the bandwidth can be controlled by the ew_3 and el_2.

The simulated VSWR's with number of values of cl_1 is displayed in Fig. 5 (c). As the value of cl_1 varied from 3 mm to 5 mm, the WLAN center frequency is varied from 6.02 to 5.2 GHz and the operating band of this notch band is decreases. Figure 5 (d) indicates the VSWR characteristics for different ct_2. For ct_2 = 0.5, 1 and 1.5 mm with other dimensions remain fixed, the center frequency of the second notch band changes from 5.12 GHz to 6.08 GHz. It can be observed from the figure that ct_2 has significant effects on shifting the center frequency and operating band of the second notch band for WLAN.

The effects of all the parameters of the filter structures and their final values are summarized in the Table 1 from where it can be concluded that the bandwidth (BW) and center frequency (f_c) of the rejected band for WiMAX is completely controlled by the parameters of the e-shape slit, whereas the 5.5 GHz WLAN band can solely be generated and adjusted by the inverted C-shape slit, i.e., each notch band is not affected by the creation of others which give us an engineering advantages in the designing of band notch UWB antenna.

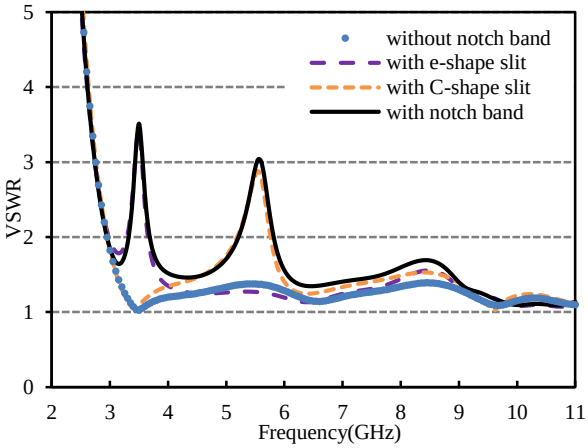

Fig. 4. VSWR curves for without and with parasitic slit/s.

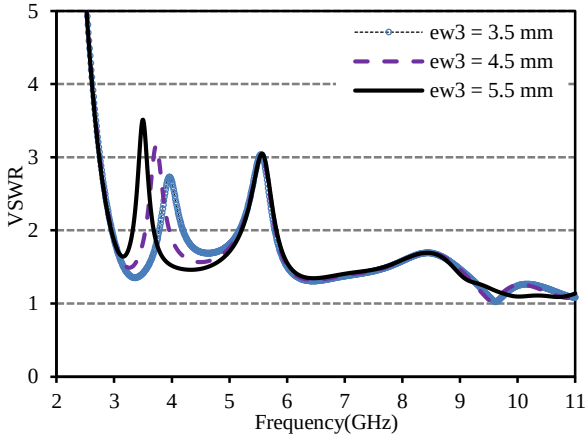

(a)

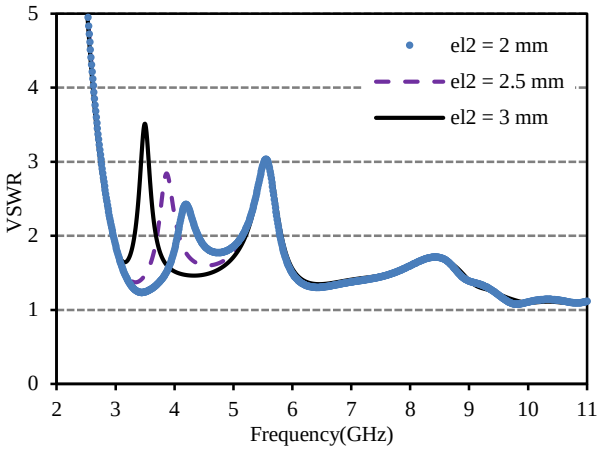

(b)

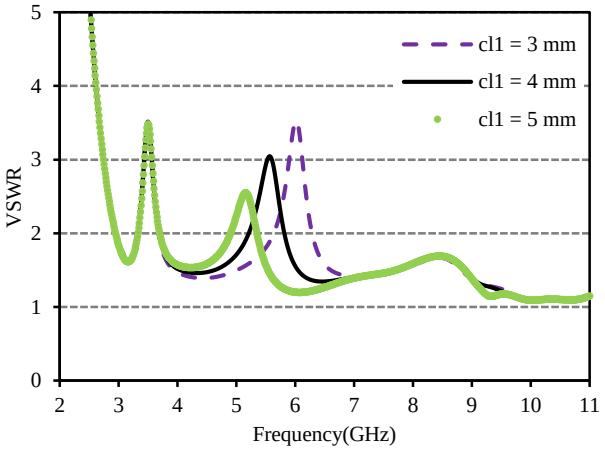

(c)

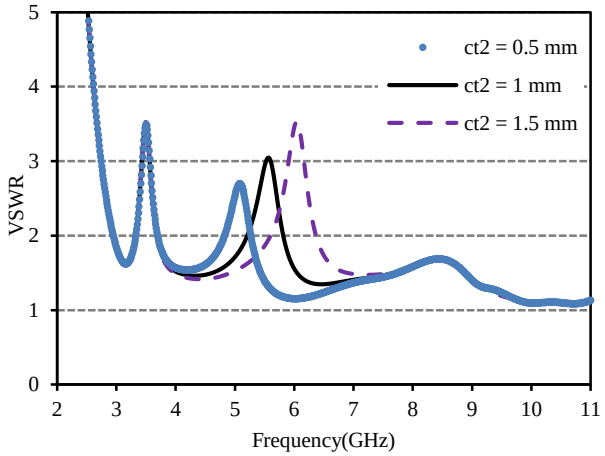

(d)

Fig. 5. Effects of: (a) ew_3, (b) el_2, (c) cl_1, and (d) ct_2 on antenna performance.

Table 1: Effects of different parameters on notch bands

Parameter	WiMAX Band		WLAN Band		Final Value (mm)
	BW	f_c	BW	f_c	
el_1▲	▲	Shifted to higher band	—	—	4
el_2▲	▼	Shifted to lower band	—	—	3
ew_1▲	—	Shifted to lower band	—	—	6.5
ew_2▲	▲	Shifted to lower band	—	—	6.5
ew_3▲	▼	Shifted to lower band	—	—	5.5
et_1▲	▼	Shifted to higher band	—	—	0.5
et_2▲	▲	Shifted to higher band	—	—	1
cl_1▲	—	—	▼	Shifted to lower band	4
cw_1▲	—	—	▼	Shifted to lower band	7.5
cw_2▲	—	—	▼	Shifted to lower band	7
ct_1▲	—	—	▼	Shifted to lower band	0.5
ct_2▲	—	—	▲	Shifted to higher band	1
ct_3▲	—	—	▲	Shifted to higher band	1.5
y_1▲	—	—	▼	Shifted to lower band	0.5
y_2▲	▲	Shifted to lower band	—	—	1
x_1▲	—	Shifted to lower band	—	—	1.5
x_2▲	▲	Shifted to lower band	▼	Shifted to higher band	4.75

** '▲' indicates increment '▼' indicates decrement and '—' unaffected.

IV. MEASURED RESULTS AND DISCUSSIONS

With the final design parameters displayed in Table 1, a pair of the proposed antenna was prototyped for experimental validation and is displayed in inset of Fig. 6. The VSWR characteristic was measured using E8362C PNA series VNA from Agilent. It can be revealed from the plot in Fig. 6 that the prototype of the proposed design exhibited a good impedance matching ranging from 3 to 10.72 GHz for VSWR ≤ 2. Two sharp notch bands centered at 3.5 GHz and 5.5 GHz have also been observed in the achieved UWB operating bands. The disagreement between experimental result and

predicted one especially at upper edge frequency is due to inaccuracies in fabrication, effect of feeding cable and higher loss tangent of inexpensive FR4 dielectric material. In spite of being compact in size than the antennas presented in [1-4, 6, 8, 11-13], the proposed design reveals UWB performances with two stop bands that may help to suppress the interference caused by WiMAX and WLAN.

The realized peak gain of the prototyped antenna is displayed in Fig. 7. It can be revealed from the figure that the proposed antenna achieved a good peak gain except at WiMAX and WLAN notched bands. At notched bands the gain decreases drastically, which indicate the effects of filter elements.

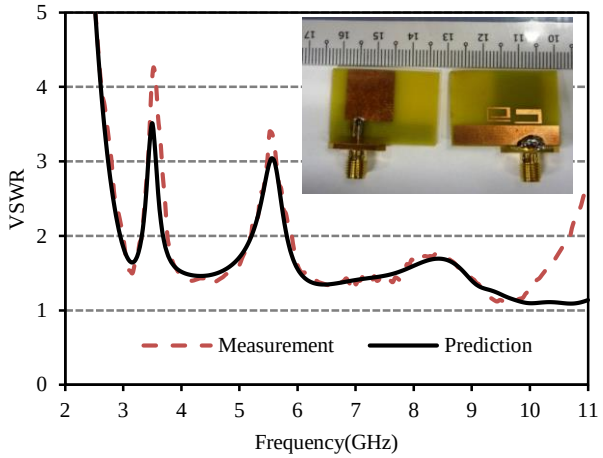

Fig. 6. Measured and predicted VSWR of the proposed antenna.

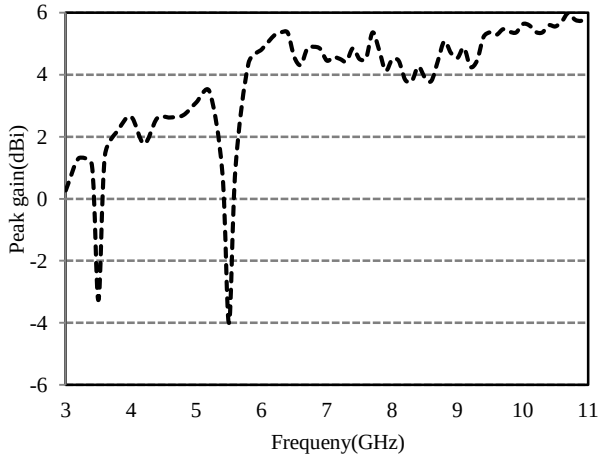

Fig. 7. Measured peak gain of the proposed antenna.

Figure 8 displayed the measured patterns of the radiation characteristics for *H*-plane (*xz*-plane) and *E*-plane (*yz*-plane). An omnidirectional radiation pattern has been exhibited by both *H*- & *E*-field plane of the designed antenna. As the frequency increases, nulls have been observed especially in the *E*-plane patterns which may be due to higher order harmonic and asymmetric radiating patch. Despite the nulls at higher frequencies, it can be commented that the realized antenna displays symmetric radiation characteristics all over the UWB spectrum.

The group delay that indicates the time delay of a signal is measured using a pair of identical prototypes at a distance 50 cm apart and is depicted in Fig. 9. Other than notched frequency bands, a fairly flat group delays with a variation of less than a nanosecond is observed. This property indicates that the proposed design could transmit the signal with minimum dispersion, which is a primary requisite for UWB applications.

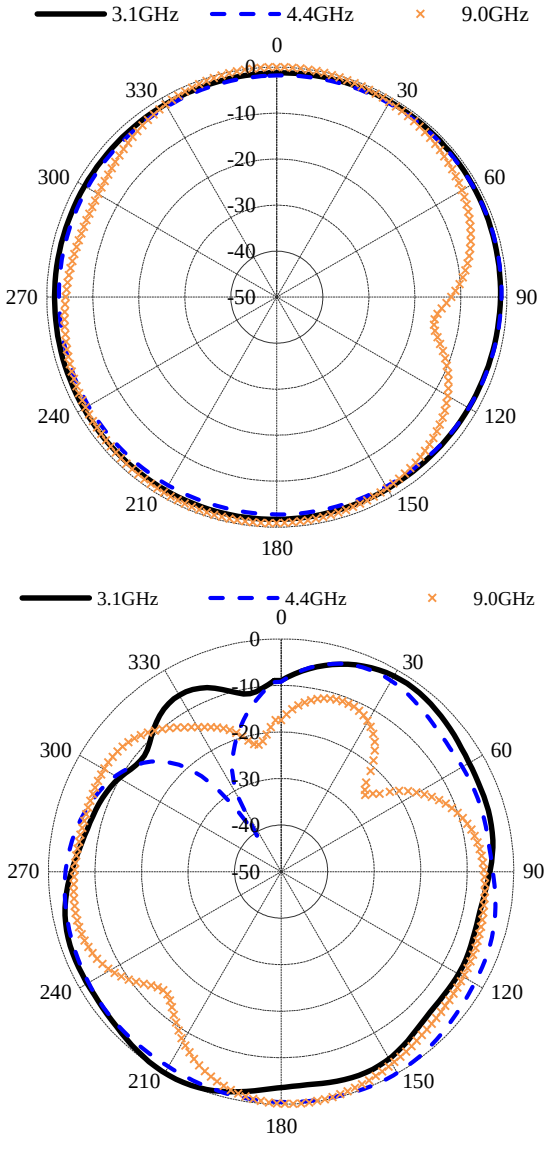

Fig. 8. Measured *H*-plane (top) and *E*-plane (bottom) patterns at different frequencies.

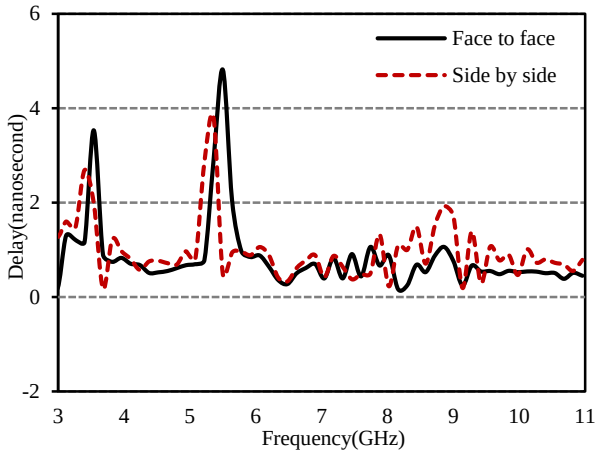

Fig. 9. Measured group delay of the proposed antenna.

V. CONCLUSION

A low profile planar antenna with two notch band is introduced for UWB application. To attain dual band notch performance, the designed antenna uses parasitic slits only on one side of the substrate without modifying or altering the patch or ground plane. It is found that by properly placing the slits, the prototype with optimized design parameters has been able to achieve UWB performance with two notch bands at 3.5 GHz and 5.5 GHz. These achieved notch bands will help to suppress the electromagnetic interference caused from WiMAX and WLAN respectively. Furthermore the fabricated prototype demonstrates stable radiation characteristics and achieved good gain except at notched bands.

REFERENCES

[1] J.-Y. Kim, N. Kim, S. Lee, and B.-C. Oh, "Triple band-notched UWB monopole antenna with two resonator structures," *Microw. Opt. Technol. Lett.*, vol. 55, no. 1, pp. 4-6, 2013.

[2] M. Yazdi and N. Komjani, "Planar UWB monopole antenna with dual band-notched characteristics for UWB applications," *Microw. Opt. Technol. Lett.*, vol. 55, no. 2, pp. 241-245, 2013.

[3] W. T. Li, X. W. Shi, and Y. Q. Hei, "Novel planar UWB monopole antenna with triple band-notched characteristics," *IEEE Antennas Wirel. Propag. Lett.*, vol. 8, pp. 1094-1098, 2009.

[4] J. Sun, X. Zhang, J. Chen, Z. Zhang, and L. Zhang, "Ultrawideband planar monopole antenna with dual band-notched characteristics," *Int. Symp. Signals Syst. Electron.*, Nanjing, China, pp. 1-3, September 2010.

[5] L. Luo, Z. Cui, J.-P. Xiong, X.-M. Zhang, and Y.-C. Jiao, "Compact printed ultra-wideband monopole antenna with dual band-notch characteristic," *Electron. Lett.*, vol. 44, no. 19, pp. 1106 1107, 2008.

[6] R. Shi, X. Xu, J. Dong, and Q. Luo, "Design and analysis of a novel dual band-notched UWB antenna," *Int. J. Antennas Propag.*, vol. 2014, Article ID: 531959, 10 pages, doi:10.1155/2014/531959, 2014.

[7] P. Beigi, J. Nourinia, B. Mohammadi, and A. Valizade, "Bandwidth enhancement of small square monopole antenna with dual band notch characteristics using U-shaped slot and butterfly shape parasitic element on backplane for UWB applications," *Appl. Comput. Electrom.*, vol. 30, no. 1, pp. 78-85, 2015.

[8] M. M. Islam, M. T. Islam, M. Samsuzzaman, and M. R. I. Faruque, "Five band-notched ultrawide band (UWB) antenna loaded with C-shaped slots," *Microw. Opt. Technol. Lett.*, vol. 57, no. 6, pp. 1470-1475, 2015.

[9] R. Azim, M. T. Islam, and A. T. Mobashsher, "Design of a dual band-notch UWB slot antenna by means of simple parasitic slits," *IEEE Antennas Wirel. Propag. Lett.*, vol. 12, pp. 1412-1415, 2013.

[10] M. Devi, A. K. Gautam, and B. K. Kanaujia, "A compact ultra wideband antenna with triple band-notch characteristics." *Int. J. Microw. Wirel. Technol.*, pp. 1-7, 2015. Doi: 10.1017/S1759078715000409.

[11] A. Subbarao and S. Rabhavan, "Compact CPW-fed UWB slot antenna with triple band-notched characteristics," *Microw. Opt. Technol. Lett.*, vol. 55, no. 9, pp. 2113-2117, 2013.

[12] H.-J. Zhou, B.-H. Sun, Q.-Zh. Liu, and J.-Y. Deng, "Implementation and investigation of U-shaped aperture UWB antenna with dual band-notched characteristics," *Electron. Lett.*, vol. 44 no. 24, pp. 1387-1388, 2008.

[13] M. Shokri, H. Shirzad, S. Movagharnia, B. Virdee, Z. Amiri, and S. Asiaban, "Planar monopole antenna with dual interference suppression functionality," *IEEE Antennas Wirel. Propag. Lett.*, vol. 12, pp. 1554-1557, 2013.

[14] P. Gao, L. Xiong, J. Dai, S. He, and Y. Zheng, "Compact printed wide-slot UWB antenna with 3.5/5.5-GHz dual band-notched characteristics," *IEEE Antennas Wirel. Propag. Lett.*, vol. 12, pp. 983-986, 2013.

[15] M. Akbari, "A new slot antenna with triple stop-band performance for UWB applications," *Microw. Opt. Technol. Lett.*, vol. 55, no. 10, pp. 2350-2354, 2013.

[16] M. Najafpur, J. Nourinia, and F. A. Jazi, "Design of a novel ultra-wideband semicircular printed antenna with dual-band notched characteristic," *Appl. Comput. Electrom.*, vol. 30, no. 3, pp. 345-350, 2015.

[17] A. Abdollahvand, A. Pirhadi, M. R. Hosseinnezhad, and H. Ebrahimian, "A compact UWB printed monopole antenna with triple-band notched

characteristics," *Appl. Comput. Electrom.*, vol. 30, no. 4, pp. 374-380, 2015.

Rezaul Azim received the B.Sc. and M.Sc. degree in Physics from University of Chittagong, Bangladesh and Ph.D. degree in Electrical, Electronic and Systems Engineering from the Universiti Kebangsaan Malaysia (The National University of Malaysia). In 2005, he joined the University of Chittagong, Bangladesh where currently he is an Associate Professor. From August 2009 to July 2014 he was with the Department of Electrical, Electronic & Systems Engineering and Institute of Space Science (ANGKASA), Universiti Kebangsaan Malaysia. He is a Member of Bangladesh Physical Society and Applied Computational Electromagnetic Society (ACES). He has authored and co-authored more than 50 articles in peer-reviewed journals and international conference proceedings, couple of book chapters. His articles have been cited more than 585 times and his *h*-index is 12 (Source: SCOPUS). His research interest concentrates on the enabling technology for RF & devices, antenna technology, electromagnetics.

Mohammad Tariqul Islam is a Professor at the Department of Electrical, Electronic and Systems Engineering of the Universiti Kebangsaan Malaysia (UKM). He is currently the Group Leader of the Group at UKM. He is the author of over 300 research journal articles, nearly 165 conference articles, 4 research level books and a few book chapters on various topics related to antennas, microwaves and electromagnetic radiation analysis with 11 inventory patents filed. Thus far, his publications have been cited 1990 times and his H-index is 26 (Source: Scopus). He is now handling many research projects from the Malaysian Ministry of Science, Technology and Innovation and Ministry of Education, and some international research grants from Japan. His research interests include communication antenna design, radio astronomy antennas, satellite antennas, and electromagnetic radiation analysis.

Islam currently serves as the Editor-in-Chief for the International Journal of Electronics and Informatics and Associate Editor for International Journal of Antenna and Propagation and Electronics Letter. He received several International Gold Medal awards, a Best Invention in Telecommunication Award, a Special Award from Vietnam for his Research and Innovation, and Best Researcher Awards in 2010 and 2011 at UKM. He also won the Best Innovation Award in 2011 and the Best Research Group in ICT niche in 2014 by UKM.

He was the recipient of Publication Award from Malaysian Space Agency in 2014, 2013, 2010, 2009 and the Best Paper Presentation Award in 2012 International Symposium on Antennas and Propagation, (ISAP 2012) at Nagoya, Japan and in 2015 in IconSpace. He is a Senior Member of the IEEE and Member of the Applied Computational Electromagnetic Society (ACES) and Institute of Electronics, Information and Communication Engineers (IEICE).

Design of a Compact Wideband Balun Bandpass Filter with High Selectivity

Hui Ma, Jiayuan Lu, Yuran Li, Lin Liu, and Jianpeng Wang

Nanjing University of Science and Technology, Nanjing 210094, China
hui644909@163.com, eejylu@njust.edu.cn, eeyuranli@163.com, eelinliu@163.com, eejpwang@gmail.com

Abstract ─ A new design method for compact wideband balun bandpass filter (BPF) with high selectivity is proposed in this paper. To achieve wide operation bandwidth, the first three resonant modes, i.e., one odd mode and two even modes, of a folded stepped-impedance multi-mode resonator are utilized and arranged inside the passband. Then, to realize good balance-to-unbalance performance, a microtrip to coplanar stripline transition structure is introduced in the design. Finally, a balun BPF characterized with both wide bandwidth and high selectivity has been eventually achieved through proper coupling topology. Besides, to further demonstrate the validity of our design concept, a practical microstrip wideband balun BPF with the fractional bandwidth (FBW) of 66% and two respective transmission zeros located at 1.4 GHz and 4.2 GHz is designed, fabricated, and measured. As expected, both the simulated and measured results exhibit good filtering and balun performance.

Index Terms ─ Balun Bandpass Filter (BPF), microstrip, multi-mode resonator, wide bandwidth.

I. INTRODUCTION

Recently, the rapid development of modern wireless communication system has put forward higher requirements on RF devices with low cost, high performance, as well as miniaturization, simultaneously. In order to accommodate to this tendency, the research on multiple function embedded component is meaningful. A typical work according to this tendency is the study on the balun BPF. The balun BPF is actually a balun embedded bandpass filter as it possesses both the functions of the balun and the bandpsss filter, which are both key components in RF front-end systems. Specifically, the balun BPF can not only provide a frequency selectivity of a bandpass filter, but also can maintain a function of balance-to-unbalanced conversion. Over the past few years, various balun BPFs with high performance have been explored in [1-9].

Based on the lumped-elements, baluns with significantly size reduction were proposed in [1]. However, it limits the application to higher frequency due to the inherent increased parasitic effect of the lumped elements. Meanwhile, the low temperature co-fired ceramic (LTCC) technology also shows its advantage on size reduction in the design of balun BPF due to its multi-layer structure [2]. In order to realize both the low cost and good phase balance performance, balun BPFs were proposed by Chen et al. in [3] and Shao et al. in [4], according to the inherent wideband out-of-phase property of the DSPSL structure. However, the spacing between the two layer PCB structures could significantly influence the phase balance performance. Besides, based on the electrical field distribution of the multi-mode resonator, various types of balun BPFs are designed with a variety of multi-mode resonators, such as the loop resonator in [5], the open loop resonator in [6]，the patch resonator in [7], the SIW resonator in [8], and the hybrid resonator in [9]. Although both characteristics of balun and bandpass filter can be realized, it is hard to realize the wideband performance as only the odd resonant modes can be utilized in the design according to this introduced method. Therefore, to the best knowledge, it is still a very challenging work to develop a compact balun BPF with both the performances of wide operation bandwidth and high selectivity.

The primary motivation of this paper is to design a compact balun BPF which can not only provide wideband response but also maintain high selectivity performance. For this purpose, a microstrip to coplanar stripline transition structure is proposed in order to realize the desired balance-to-unbalance conversion performance in the design initially. Then, the resonant properties of the employed folded stepped-impedance multi-mode resonator are studied. Afterwards, a wideband balun BPF with high selectivity has been successfully achieved through proper coupling topology. Finally, both simulated and measured results of the presented balun BPF are provided and good agreement between them is gained to demonstrate good experimental validation.

II. ANALYSIS AND DESIGNN OF THE PROPOSED BALUN BPF

A. Balun structure design

Figure 1 shows the top view and bottom view of

Submitted On: January 12, 2016
Accepted On: March 18, 2016

the proposed balun BPF respectively. As indicated in the Fig. 1, the proposed balun BPF is mainly composed of two sections, i.e., part A and part B. For part A in Fig. 1, it is constructed by the microstrip to coplanar stripline transition and plays the role of balun function. Specifically, the transition form is realized by connecting the ground plane of the microstrip line with one of the coplanar striplines (line S in Fig. 2) through shorting via-holes.

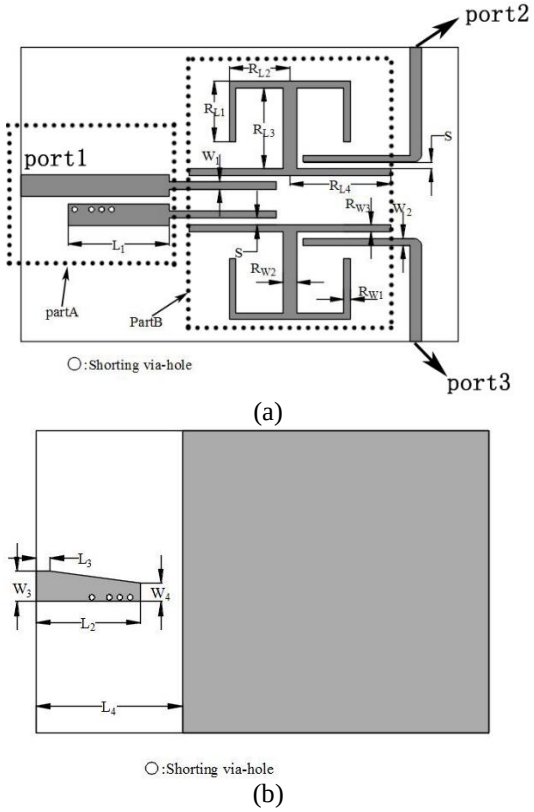

Fig. 1. Layout of the wideband balun BPF: (a) top view and (b) bottom view.

The coplanar stripline structure adopted here aims to achieve wideband phase and magnitude balance performance in the balun design. To illustrate the operation principle of the balun structure, electric field distributions referring to different cross-sections indicated in the transitions are displayed in Fig. 2.

As we can see from Fig. 2, when an unbalanced signal is initially fed into the microstrip line of the transition structure at the A-A' section, the electric fields are perpendicularly terminated at the ground of the substrate as depicted in Fig. 2 (b1). After the signal coming into the transition section, the electric fields at the section B-B' are displayed accordingly in Fig. 2 (b2). It shows that at the transition section B-B' the electric fields are terminated both at the back ground plane and one of the lines of the coplanar stripline which are bonding together by the introduced via holes. Owing to the transition structure, the unbalanced signal has successfully propagated along the coplanar stripline with the electric fields at the section C-C' displayed in Fig. 2 (b3). Finally, by introducing the back ground and decreasing the coupling between the coplanar stripline, the unbalanced signal transmits through the coplanar stripline will be eventually divided into a pair of balanced signals. As can be seen, the electric fields at the E-E' section in Fig. 2 (b4) for line M and line S are opposite, which means an 180° phase difference. Therefore, when an unbalanced signal is transmitted through the proposed transition circuit, a pair of balanced signals will be achieved at the two balanced outputs. Moreover, due to the inherent wideband property of the microstip-coplanar striplines transition, the proposed balun with wideband performance is promising.

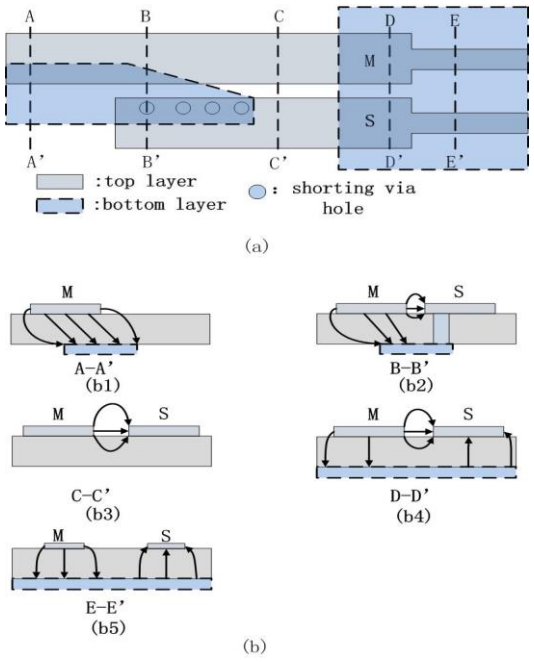

Fig. 2. Electrical field distributions on different cross-section: (a) sections in part A and (b) electric fields at different sections.

B. Filter part design

The filtering function is mainly achieved via the coupling between the balanced microstrip feed line and the presented multi-mode resonator shown in Part B of Fig. 1. As the bandwidth of the filter is mainly determined by the resonance of the multi-mode resonator, here, we will analyze it in detail. The configuration of proposed resonator is shown in Fig. 3. Since the resonator is symmetrical with respect to the symmetry plane, the well-known even- and odd-mode method is applied. Figure 3 also illustrates the equivalent

circuits of the resonator under the even- and odd-mode excitation. The input admittance can be derived as:

$$Y_{inodd} = Y_1 / (j \tan \theta_1), \quad (1)$$

$$Y_{ineven} = Y_1 \frac{Y_L + jY_1 \tan \theta_1}{Y_1 + jY_L \tan \theta_1}, \quad (2)$$

where

$$Y_L = \mathrm{j}\frac{Y_2}{2} \cdot \frac{(Y_2/2)\tan \theta_2 + Y_3 \tan \theta_3}{Y_2/2 - Y_3 \tan \theta_2 \tan \theta_3}. \quad (3)$$

For simplification, we set $Y_2=2Y_3$. Besides, $\tan\theta_1$, $\tan\theta_2$ and $\tan\theta_3$, approximately have the same value. Under the condition of resonance, it occurs when $Y_{ineven}=Y_{inodd}=0$. Thus, Equation (1) and (2) can be expressed as:

$$Y_1 / (\mathrm{j} \tan \theta_1) = 0, \quad (4)$$

$$\frac{Y_3}{Y_1} = \frac{\tan^2 \theta_2 - 1}{2}. \quad (5)$$

The above Equations (4) and (5) indicate that the odd- and even-mode resonant frequencies can be determined by θ_1 and the value of Y_3/Y_1. The first and the third resonant mode are even-mode, while the second mode is odd-mode. The even-mode resonant frequencies denoted by f_{r1} and f_{r2} are the first and second solutions of Equation (5). Therefore, the even-mode frequencies can be derived by a known R_{L3}. Figure 4 presents the influence of different Y_3/Y_1 on even-mode frequencies, which further reveals their relationship. By controlling the value of Y_3/Y_1, the bandwidth can be easily adjusted. As for the odd-mode resonance frequency f_{odd}, it is only determined by the electrical length of θ_1. Therefore, we can readily achieve a desired bandwidth by the values of Y_3/Y_1 and θ_1 properly selected.

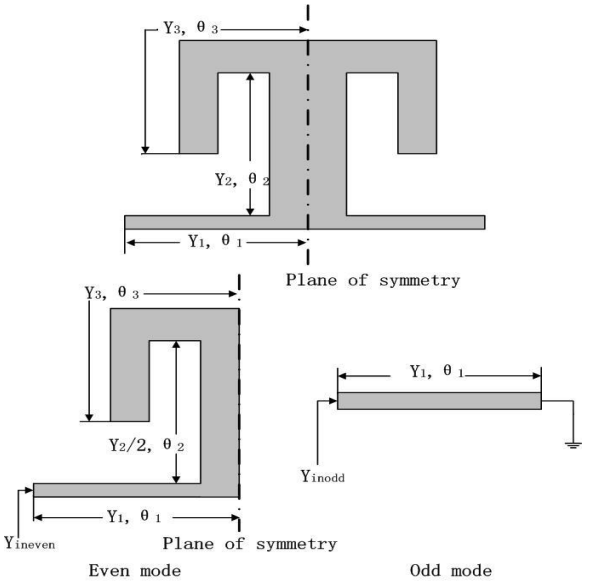

Fig. 3. Folded multi-mode resonator with it half bisections under odd- and even-mode excitation.

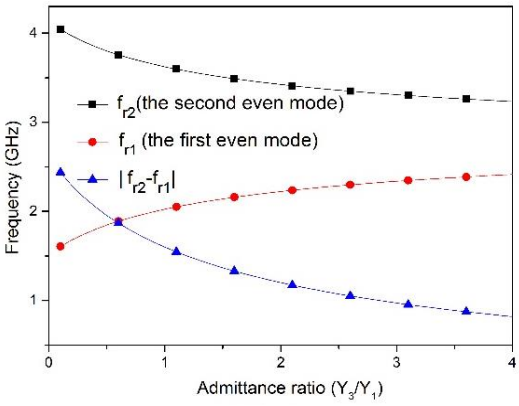

Fig. 4. Relationship between the admittance ratio and the even mode frequencies

III. SIMULATION AND MEASUREMENT RESULTS

To verify our design concept, one balun BPF sample is implemented by the method mentioned above. It is fabricated on a single layer substrate, i.e., Rogers RO4003C with a dielectric constant of 3.38, a loss tangent of 0.0027, and a thickness of 0.813 mm. The physical dimensions of the wideband balun BPF illustrated in Fig. 1 are as follows: L_1=18.5 mm, L_2=14 mm, L_3=4 mm, L_4=27.5 mm, W_1=0.6 mm, W_2=0.5 mm, W_3=3.6 mm, W_4=1.8 mm, R_{L1}=11.72 mm, R_{L2}=8.82 mm, R_{L3}=14.42 mm, R_{L4}=17.78 mm, R_{W1}=0.5 mm, R_{W2}=1.64 mm, R_{W3}=0.216 mm, S=0.1 mm.

The diameter of the via-hole is 0.8 mm. The photograph of the fabricated balun BPF is depicted in Fig. 5. Simulation was accomplished by the EM simulator HFSS 13.0 while the measurement was carried out on the Agilent N5244A.

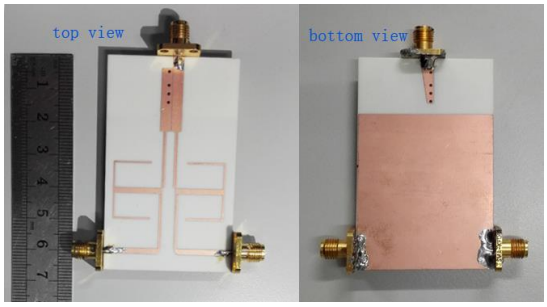

Fig. 5. Photograph of the wideband balun BPF.

The simulated and measured S-parameter parameters of the balun BPF are shown in Fig. 6. As indicated in the results, the designed balun BPF operates at the center frequency of 3.2 GHz with a fractional bandwidth (FBW) of 66%. Inside the whole passband, the insert loss is better than 1 dB and the return loss is better than 15 dB. Outside the passband,

two transmission zeros located at 1.4 GHz and 4.2 GHz can be clearly observed, which ensure the proposed balun BPF a better than 25 dB suppression. The phase imbalance and the magnitude imbalance are shown in Fig. 7. It can be seen that good balance performance is achieved with amplitude imbalance of less than 0.5 dB and phase imbalance of better than 5°. It should be mentioned that the small discrepancy between measured and simulated results are mainly due to the fabrication tolerance and the insert loss of SMA connector. To sum up, the presented balun BPF performs well in high selectivity and ideal balance performance.

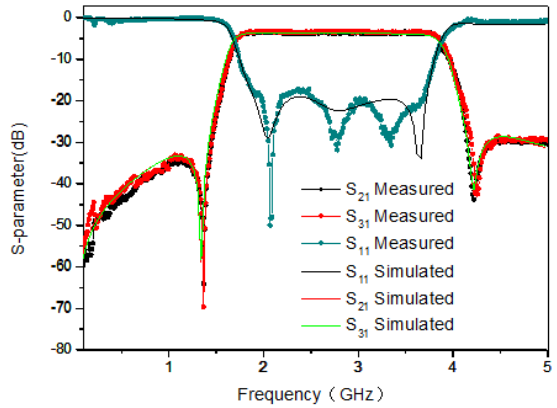

Fig. 6. Simulated and measured S-parameters of the proposed wideband balun BPF.

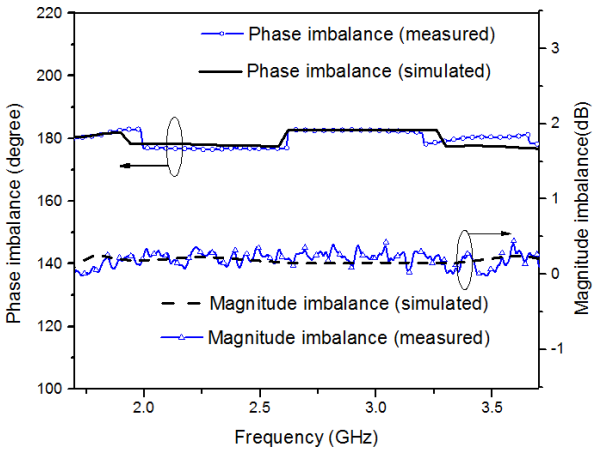

Fig. 7. Simulated and measured amplitude and phase imbalance in the passband.

IV. CONCLUSION

In this paper, a new method to design wideband balun BPF with high performance is proposed. To illustrate the design concept, both the operation principle of the balun circuit and the analysis of multi-mode resonator for the balun BPF are presented. One sample balun BPF is then designed and fabricated to validate the proposed design concept. As expected, the predicted results are well confirmed in experiment, thus validating that the presented wideband balun BPF is not only characterized by a good balance performance but also has high frequency selectivity. With these distinctive features, it is our belief that the developed balun BPF can be widely applied to modern advanced wideband wireless communication systems.

ACKNOWLEDGEMENT

This work was supported by the scientific research training fund (the BQW PLAN) of the Nanjing University of Science and Technology under Grant 201510288037.

REFERENCES

[1] V. G. Posadas, C. M. Pascual, J. L. J. Martín, and D. S. Vargas, “Lumped-element balun for UHF UWB printed balanced antennas,” *IEEE Trans. Microw. Theory Tech.*, vol. 56, no. 7, pp. 2102-2107, Jul. 2008.

[2] C. H. Tsai, H. C. Chen, and T. L. Wu, “A novel compact balun using a weakly coupled line with grounded resonator,” *IEEE Microw. Wireless Compon. Lett.*, vol. 24, no. 11, pp. 763-765, Feb. 2002.

[3] J. X. Chen, C. Y. Cheung, and Q. Xue, “Integrated bandpass filter balun based on double-sided parallel-strip line with an inserted conductor plane,” *APMC Microw. Conf.*, Thailand, pp. 1-4, Dec. 2007.

[4] J. Shao, R. G. Zhou, C. Chen, X. H. Wang, H. Kim, and H. L. Zhang, “Design of a wideband balun using parallel strips,” *IEEE Microw. Wireless Compon. Lett.*, vol. 23, no. 3, pp. 125-127, Mar. 2013.

[5] P. Cheong, T. S. Lv, W. W. Choi, and K. W. Tam, “A compact microstrip square-loop dual-mode balun-bandpass filter with simultaneous spurious response suppression and differential performance improvement,” *IEEE Microw. Wireless Compon. Lett.*, vol. 21, no. 2, pp. 77-79, Feb. 2011.

[6] Q. Xue, J. Shi, and J. X. Chen, “Unbalanced-to-balanced and balanced-to-unbalanced diplexer with high selectivity and common-mode suppression,” *IEEE Trans. Microw. Theory Tech.*, vol. 59, no. 11, pp. 2848-2855, Nov. 2011.

[7] S. Sun and W. Menzel, “Novel dual-mode balun bandpass filters using single cross-slotted patch resonator,” *IEEE Microw. Wireless Compon. Lett.*, vol. 21, no. 8, pp. 415-417, Aug. 2011

[8] H. Chu and J. X. Chen, “Dual-band substrate integrated waveguide balun bandpass filter with high selectivity,” *IEEE Microw. Wireless Compon. Lett.*, vol. 24, no. 6, pp. 379-381, June 2014.

[9] T. Yang, M. Tamura, and T. Itoh, "Compact hybrid resonator with series and shunt resonances used in miniaturized filters and balun filters," *IEEE Trans. Microw. Theory Tech.*, vol. 58, no. 2, pp. 390-402, Feb. 2010

Hui Ma is working towards the Bachelor degree at Nanjing University of Science and Technology. Her research interests include the high performance multi-function microwave components.

Jiayuan Lu received the B.S. degree in Electronics and Information Engineering from NJUST, Nangjing, China, in 2014. He is currently working toward the Ph.D. degree in Electromagnetic Field and Microwave Technology in NJUST. His research interest is the design of miniaturized high performance microwave/millimeter-wave passive device and numerical methods in electromagnetics.

Yuran Li is working towards the Bachelor degree at Nanjing University of Science and Technology. Her research interests include the high performance multi-function microwave components.

Lin Liu is working towards the Bachelor degree at Nanjing University of Science and Technology. Her research interests include the high performance multi-function microwave components.

Jianpeng Wang received the M.Sc. and Ph.D. degree from UESTC, Chengdu, China, in 2004, and 2007, respectively. Since Jan. 2008, he has been with the Ministerial Key Laboratory of JGMT, School of Electronic and Optical Engineering, NJUST. His research interests include the high performance microwave/millimeter-wave passive components, circuits and systems realized on PCB, LTCC, etc.

Novel Compact Branch-Line Coupler Using Non-Uniform Folded Transmission Line and Shunt Step Impedance Stub With Harmonics Suppressions

Sh. Nouri [1], J. Nourinia [1], N. Valizade [2], B. Mohammadi [1], and A. Valizade [3]

[1] Department of Electrical Engineering
Urmia University, Urmia, Iran
shalaleh.nouri@gmail.com, j.nourinia@urmia.ac.ir, b.mohammadi@urmia.ac.ir

[2] Department of Electrical Engineering
Iran University of Science and Technology, Tehran, Iran
Valizade@elec.iust.ac.ir

[3] Young Researchers and Elites Club
Qaemshahr Branch, Islamic Azad University, Qaemshahr, Iran
a.valizade@semnan.ac.ir

Abstract ─ In this paper, a novel compact branch-line coupler (BLC) using non-uniform folded transmission line (NUFTL) and shunt step impedance stubs (SSISs) with harmonics suppressions is presented and its design procedure is discussed. In the proposed structure, in order to reject the unwanted harmonic pass bands, a pair of SSISs is implemented along the ports of the coupler. To minimize the physical size of the coupler, NUFTL are used instead of uniform transmission lines in each arm of the branch-line. With the proposed approach, the size of the quarter-wavelength transmission line in the branch-line can be reduced greatly. The presented BLC has a compact size while showing good return loss and insertion loss characteristic in the frequency band of interest. Good agreement exists between the simulated and measured results.

Index Terms ─ Branch-line coupler (BLC), harmonics suppressions, non-uniform folded transmission line (NUFTL), shunt step impedance stub (SSIS).

I. INTRODUCTION

The compact BLC is an important sub-circuit in microwave integrated circuits and can be used as a power divider/combiner or a part of a mixer [1-5]. The conventional BLC was composed of four quarter-wavelength uniform transmission lines [1]. However, adopting the quarter wavelength transmission line to design the coupler takes too much space; therefore, larger circuit area may result in higher cost. The lumped-element approach [2], which uses spiral inductors and lumped capacitors, is one of the solutions to this problem. Nevertheless, using the lumped element in the circuit design requires an empirical model, such as an inductor model, attained via precise measurement. Mainly, two different approaches have been used to reduce the size of the conventional hybrids. One is to use transmission-line meandering to approximate quarter-wave transmission-line behavior over a certain bandwidth. The other is to use a distributed element approach for the same purpose [3-13]. Multiple shunted open stubs [5] or S-shaped structure loading [8] are well-known methods of miniaturization. The level of miniaturization is determined by the number of meander sections (shunt stubs) and the tightness of the meandering. However, each meander section adds some discontinuities. Moreover, tight meandering results in increased parasitic coupling between transmission-line sections [9-10].

In order to satisfy the compact requirement of the modern wireless systems, several miniaturized techniques [4-14] were proposed to miniaturize the circuit size of the BLC, such as using quasi-lumped elements approach with symmetrical or nonsymmetrical T-shaped structures [4], multiple shunted open stubs [5], compact ring BLC using nonuniform transmission line [6], and step impedance transmission lines (SITLs) [7-8]. A compact slow-wave microstrip BLC with four microstrip high-low impedance resonant cells which were periodically placed inside the BLC was introduced in [9-10]. Furthermore, the conventional coupler has spurious harmonics responses at the harmonics of the

Submitted On: March 31, 2015
Accepted On: February 24, 2016

fundamental frequency, which affects the circuit performance when used in microwave applications. Recently, several design techniques have been reported for size reduction and harmonics suppression [11-13]. In [11], transmission phase characteristic of the BLC is used to increase the bandwidth of inter-band attenuation between the two operating frequencies as well as to reduce the size. Planar artificial transmission line concept is another option to reduce the physical length of a transmission line. In this method, a transmission line incorporated with microstrip quasi-lumped elements is capable of synthesizing microstrip lines with reduced physical length, which can be used to reduce the size of BLC [12]. In [13], to realize multiband operations, a Pi-type-based multiband transmission line network with open- and short-ended stubs was employed. In [14], L-shaped conductor backed asymmetric coplanar stripline and U-shaped conductor backed coplanar waveguide BLC fed by microstrip transmission line have been used. In [15], wideband BLC with symmetrical four-strip is introduced.

This paper presents a novel compact BLC using NUFTL and SSISs with harmonics suppressions. In the proposed structure, in order to reject the unwanted harmonic pass bands, a pair of SSISs is implemented along the ports of the coupler. To minimize the physical size of the coupler, NUFTL are utilized instead of uniform transmission lines in each arm of branch-line. The occupied size of the proposed broadband BLC is merely 45.77% of the size of a conventional design. Simulated and measured results are presented to validate the usefulness of the proposed coupler structure for microwave integrated circuits applications. The proposed BLC structure and its design approach is discussed and illustrated in the following sections.

II. BLC DESIGN AND CONFIGURATION

The novel compact BLC with harmonics suppressions fed by a 50-Ω microstrip line is shown in Fig. 1, which is printed on a RO4003 substrate with permittivity of 3.55, thickness of 0.508 mm, and loss tangent of 0.0027. The basic BLC structure consists of NUFTL and SSISs. In this paper, miniaturization of the BLC is achieved by means of NUFTL located on the branch and through lines of the conventional coupler, and also four SSISs that placed inside the free area of a conventional BLC which are parallel with the conventional coupler's main transmission lines. The proposed BLC is connected to a 50 Ω SMA connector for signal transmission. The presented BLC operates over 2.06–2.81 GHz with S_{11} < -10 dB. The planar BLC with various design parameters was constructed, and the numerical and experimental results of the S-parameters and phase characteristics are presented and discussed. The parameters of the proposed BLC are studied by changing one parameter at a time while others were kept fixed. The simulated results are obtained using Ansoft simulation software high-frequency structure simulator (HFSS) [17]. In simulation studies the maximum number of passes and the maximum delta S were chosen 20 and 0.02 respectively. Increasing the mesh density will increase the accuracy at the cost of increased simulation time, but from certain limit it will not have a considerable effect on the accuracy. The final design parameters of the presented BLC are specified in Table 1.

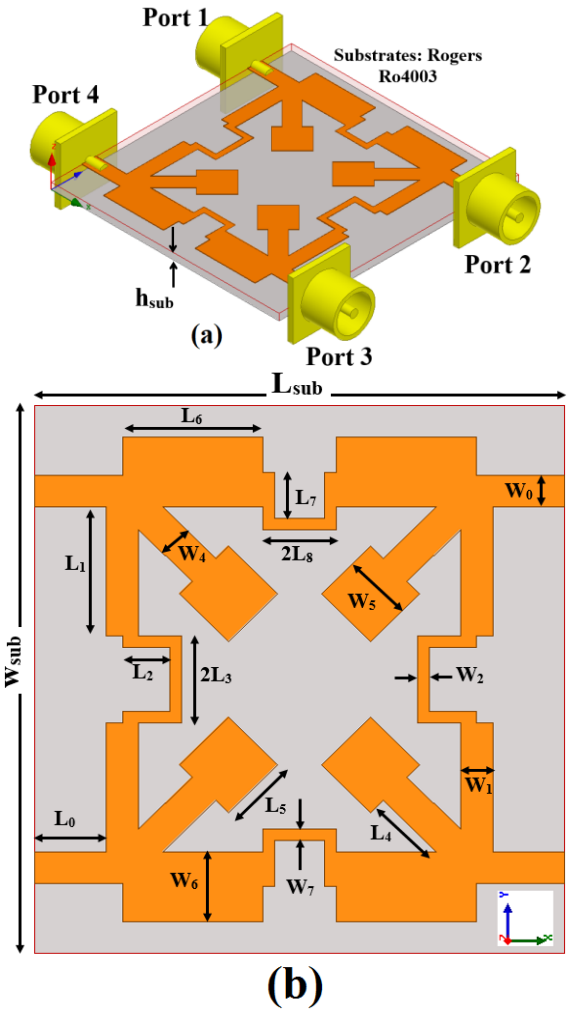

Fig. 1. The geometry of the proposed BLC using NUFTL and SSISs: (a) side view and (b) top view.

Table 1: The final dimensions of the designed BLC

Param.	mm	Param.	mm	Param.	mm
W_{sub}	19	W_6	2.4	L_3	1.5
W_0	1.1	W_7	0.4	L_4	2.5
W_1	1.1	L_{sub}	18	L_5	2.3
W_2	0.4	L_0	2.5	L_6	4.7
W_4	1.1	L_1	4.5	L_7	1.6
W_5	2.3	L_2	1.6	L_8	1.2

Figure 2 shows various BLC structures which were used for simulation studies. $|S_{11}|$ characteristics for conventional BLC (with four quarter-wavelength uniform transmission lines) (Fig. 2 (a)) and the BLC using SSISs (Fig. 2 (b)) are compared in Fig. 3. As shown in Fig. 3, for the proposed BLC configuration, in order to reject the unwanted harmonic pass bands, a pair of SSISs is implemented along the ports of the coupler. Moreover, the four SSISs that are placed inside the free area of conventional BLC play an important role in the miniaturization of the BLC.

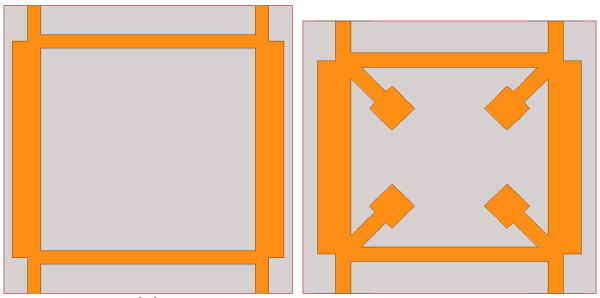

Fig. 2. The various BLC structures which were used in simulation studies: (a) the conventional BLC (with four quarter-wavelength uniform transmission lines), and (b) the BLC using SSISs.

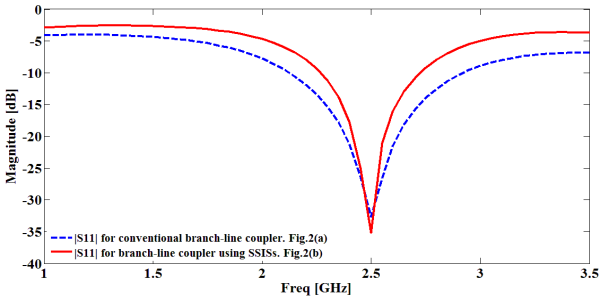

Fig. 3. The $|S_{11}|$ characteristics for BLC structures shown in Figs. 2 (a) and (b).

In general, the conventional BLC is composed of one pair of vertical Z_0 quarter-wavelength microstrip lines and one pair of horizontal 0.707 Z_0 quarter-wavelength microstrip lines, where Z_0 represents the 50 Ω characteristic impedance of the transmission line [1] as shown in Fig. 2 (a). When it is applied for variable attenuators and phase shifters, it would produce higher order harmonics [7-8]. In the design of a conventional BLC, these harmonics are unable to be suppressed. The total size of the conventional BLC is 23.8×20.2 mm^2, as shown in Fig. 2 (a). The conventional BLC, therefore, can hardly be realized due to its large size and because it is not easily implemented in system integration. Thus, the size of the conventional BLC must be reduced. This type of SSISs will introduce four step impedance stubs which are parallel with the conventional coupler's main transmission lines. As the inductances caused by the high-impedance lines of SSISs are only loaded at the sites connected to the ports and in a lumped form, we ignore its influence on the per unit length inductance of the main transmission lines between two adjacent ports. The capacitances caused by the low-impedance lines of SSISs are loaded parallel with the main transmission lines between two adjacent ports and in a distributed form [9-10]. This will increase the per unit length capacitance of the main transmission lines between two adjacent ports. Thus, this type of slow-wave loading here will mainly increase the shunt capacitance of the coupler. An increased propagation constant means that a shorter physical structure can be used to yield a required electrical length compared with a conventional transmission line [9-11]. The SSISs then act similar to a band stop filter at the second and third harmonics frequencies [7-8]. Therefore, the proposed compact BLC shows better microwave performance in case of harmonics rejection in comparison with the conventional BLC. The proposed miniaturization technique achieves 66.1% of size reduction compared to the conventional implementation, (19.6×16.2 mm^2), as shown in Fig. 2 (b).

The even and odd mode decomposition method can be used for a symmetrical four-port network analysis [16], [18-19]. Figure 6 shows the even and odd mode equivalent circuits of the proposed BLC [1]. Voltage (current) vanishes along the symmetrical plane at odd-mode (even-mode) excitation which leads to transmission line equivalent circuits which are depicted in Figs. 6 (a) and (b). In these figures, Y_i are the microstrip line characteristic admittances which are dependent on their corresponding microstrip line width in Fig. 1, and the θ_i are the electrical lengths which are dependent on their corresponding microstrip line length in Fig. 1. For odd-mode excitation the voltage distribution is null along the symmetrical plane and as a result the equivalent circuit in Fig. 6 (b) is applicable [18-19]. As shown in Fig. 6, these cascaded lines and stubs can be analyzed by the ABCD matrix method. In the four-port coupler, the following amplitude and phase conditions should be satisfied [16]:

$$|S_{21}| = |S_{31}|, \tag{1a}$$

$$S_{41} = 0, \tag{1b}$$

$$\angle S_{21} - \angle S_{31} = \pm 90^\circ. \tag{1c}$$

In the even and odd mode circuits, the ABCD matrix can be presented as follows [16]:

$$[ABCD]_o = T_{SC} T_S T_L T_S T_{SC}, \tag{2a}$$

$$[ABCD]_e = T_{OC} T_S T_L T_S T_{SC}, \tag{2b}$$

$$T_S = \begin{bmatrix} \cos\theta_4 & jY_4^{-1}\sin\theta_4 \\ jY_4\sin\theta_4 & \cos\theta_4 \end{bmatrix}\begin{bmatrix} 1 & 0 \\ jY_5\tan\theta_5 & 1 \end{bmatrix}, \quad (3a)$$

$$T_L = T_{L1}T_{L2}T_{L1}, \quad (3b)$$

$$T_{L1} = \begin{bmatrix} \cos\theta_6 & jY_6^{-1}\sin\theta_6 \\ jY_6\sin\theta_6 & \cos\theta_6 \end{bmatrix}, \quad (3c)$$

$$T_{L2} = \begin{bmatrix} \cos(2\theta_7+2\theta_8) & jY_7^{-1}\sin(2\theta_7+2\theta_8) \\ jY_7\sin(2\theta_7+2\theta_8) & \cos(2\theta_7+2\theta_8) \end{bmatrix}, \quad (3d)$$

$$T_{SC} = \begin{bmatrix} \cos\theta_1 & jY_1^{-1}\sin\theta_1 \\ jY_1\sin\theta_1 & \cos\theta_1 \end{bmatrix}\begin{bmatrix} 1 & 0 \\ -jY_2\cot(\theta_2+\theta_3) & 1 \end{bmatrix}, \quad (3e)$$

$$T_{OC} = \begin{bmatrix} \cos\theta_1 & jY_1^{-1}\sin\theta_1 \\ jY_1\sin\theta_1 & \cos\theta_1 \end{bmatrix}\begin{bmatrix} 1 & 0 \\ jY_2\tan(\theta_2+\theta_3) & 1 \end{bmatrix}. \quad (3f)$$

The subscripts e and o represent the even and odd mode, and also T_S, T_L, T_{SC}, T_{OC} represent the SSIS, NUFTL, short step impedance stub in odd mode and open step impedance stub in odd mode, respectively. From (2) and (3), we can obtain the reflection (Γ) and transmission coefficients (T) [1]:

$$\Gamma_{e,o} = \frac{A_{e,o}+B_{e,o}-C_{e,o}-D_{e,o}}{A_{e,o}+B_{e,o}+C_{e,o}+D_{e,o}}, \quad (4a)$$

$$\mathrm{T}_{e,o} = \frac{2}{A_{e,o}+B_{e,o}+C_{e,o}+D_{e,o}}. \quad (4b)$$

The magnitudes of S-parameter of the BLC at each port can be expressed as [1]:

$$S_{11} = \frac{1}{2}(\Gamma_e+\Gamma_o), \quad (5a)$$

$$S_{12} = \frac{1}{2}(\mathrm{T}_e+\mathrm{T}_o), \quad (5b)$$

$$S_{13} = \frac{1}{2}(\mathrm{T}_e-\mathrm{T}_o), \quad (5c)$$

$$S_{14} = \frac{1}{2}(\Gamma_e-\Gamma_o). \quad (5d)$$

Since the proposed BLC is symmetrical, the even-odd method is utilized. The voltage (current) is null along the symmetry plane which leads to the transmission line models depicted in Figs. 4 (a), (b) [3]. The presented coupler is analyzed theoretically based on Equations (2-5) and by means of MATLAB software. Because of the discontinuities in the microstrip lines (step discontinuities), associated fringe capacitance, and the changes in the frequency, the simulation and theoretical results differ from each other. The characteristic impedance (Z_i), and the effective permittivity of the transmission lines (ε_{eff}) must be determined in order to be used in theoretical calculations. The Equation (6) from [20] is used in order to determine these two parameters and the calculated (ε_{eff}, Z_i) for the Y_1, Y_2, Y_3, Y_4, Y_5, Y_6, Y_7 lines are (2.76, 50.56 Ω), (2.56, 82.25 Ω), (2.76, 50.56 Ω), (2.95, 30.69 Ω), (2.96, 29.74 Ω), (2.56, 85.25 Ω), respectively.

$$\varepsilon_e = \frac{\varepsilon_r+1}{2}+\frac{\varepsilon_r-1}{2}\left[\left(1+12\left(\frac{H}{W}\right)\right)^{-1/2}+0.04\left(1-\left(\frac{W}{H}\right)\right)^2\right] \quad when\left(\frac{W}{H}\right)<1, \quad (6a)$$

$$\varepsilon_e = \frac{\varepsilon_r+1}{2}+\frac{\varepsilon_r-1}{2}\left(1+12\left(\frac{H}{W}\right)\right)^{-1/2} \quad when\left(\frac{W}{H}\right)\geq 1, \quad (6b)$$

$$Z_0 = \frac{60}{\sqrt{\varepsilon_{eff}}}\ln\left(8\frac{H}{W}+0.25\frac{W}{H}\right)(ohms) \quad when\left(\frac{W}{H}\right)<1, \quad (6c)$$

$$Z_0 = \frac{120\pi}{\sqrt{\varepsilon_{eff}}\left[\frac{W}{H}+1.393+\frac{2}{3}\ln(\frac{W}{H}+1.44)\right]}(ohms) \; when\left(\frac{W}{H}\right)\geq 1. \quad (6d)$$

The frequency response of the equivalent BLC structures in Fig. 4 for the even and odd modes with the parameters values in the Table 1 is depicted in Fig. 5 (a). In these calculations the transmission matrix of the feed lines (W_0 and L_0) are applied to the Equation (2). As can be observed, the even and odd mode structures have different operating frequency bands. Figure 5 (a) shows the calculated frequency response for the BLC in Fig. 1 and based on Equation (5). The obtained results for the equivalent circuit can be used for determination of the frequency response of the structure and bandwidth effects. In other words, they are useful in order to calculate the effect of the parameters on the resonance frequency and the bandwidth. Also, a parametric study is done on the design parameters and the achieved results show that the W_1 and W_6 have the main effect on the operating frequency band while L_7 and L_8 have the least effect.

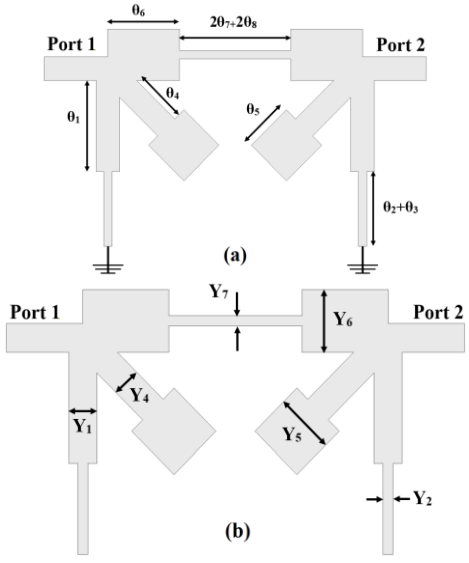

Fig. 4. Proposed BLC using NUFTL and SSISs: (a) odd-mode equivalent circuit, and (b) even-mode equivalent circuit.

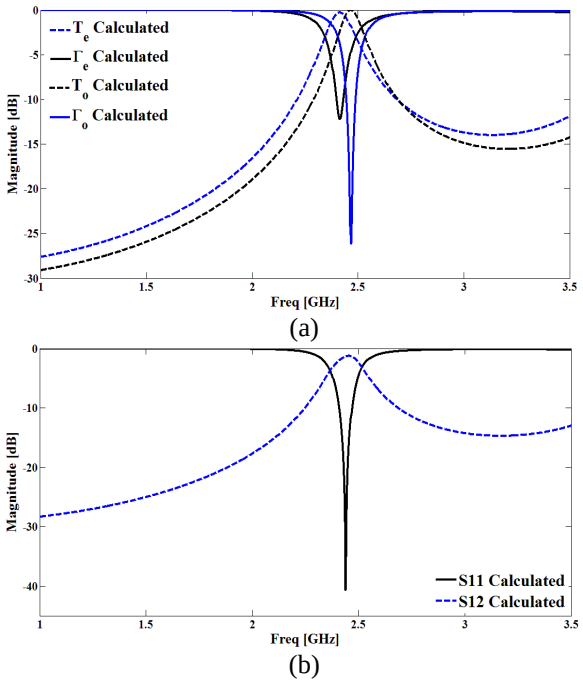

Fig. 5. Calculated frequency responses for BLC structures with MATLAB software: (a) odd mode and even mode responses for equivalent circuits in Fig. 4 with Equation (4), and (b) proposed BLC with Equation (5).

The transmission line (TL) equivalents for the odd and even modes are shown in Fig. 6 (a) and Fig. 6 (b), respectively. The voltage (current) is null along the symmetry plane in the odd mode (even mode) and as the result the TL equivalent in Fig. 6 (a) (Fig. 6 (b)) is obtained. The step discontinuities in the microstrip lines, the associated fringing capacitance, and also the frequency alteration are considered in simulation studies. The simulated results with HFSS software are depicted in Fig. 7 (a). The simulated results show that the proposed structure has high-pass characteristic at the odd mode and low-pass characteristic at the even mode. These effects lead to a proper out of band rejection which is desirable. The simulated results are similar with the results which were calculated based on the equations (1-5). In Fig. 7 (b), the simulated results for the proposed BLC are presented.

In order to modify the design parameters of the proposed BLC, a parametric study was performed. As examples of the aforementioned parametric study, the effect of two design parameters (W_5 and W_2) are presented and discussed here in Fig. 8 and Fig. 9.

Figure 8 shows the effect of variation in width of the low-impedance line of SSIS (W_5 in Fig. 1 (b)) on the frequency responses of the proposed BLC. It is found that by changing the width of the low-impedance line of SSIS, the position of the frequency band of interest can be adjusted properly. Figure 9 shows the effect of variation in finger width of the vertical arm of the NUFTL (W_2 in Fig. 1 (b)) on return loss characteristic of the proposed BLC for different cases. As it can be observed from this figure, the impedance bandwidth can be fine-tuned effectively by modifying this parameter. Another effective way to reduce the size of a BLC is the replacement of straight transmission lines segments by space-filling curve segments with the same electrical characteristics [5-6]. Moreover, nonuniform transmission line can be used instead of the quarter wavelength uniform transmission lines to reduce the size of BLC. In this method, the normalized width function of the nonuniform transmission lines is expanded in a truncated Fourier series and an optimization method applied to obtain the optimum values of the series coefficients. Generally, step impedance transmission line is a non-uniform transmission line, which can be used in microstrip circuits for size reduction, shift the spurious pass band to the higher frequency and even to suppress the multiple spurious pass bands [6-7].

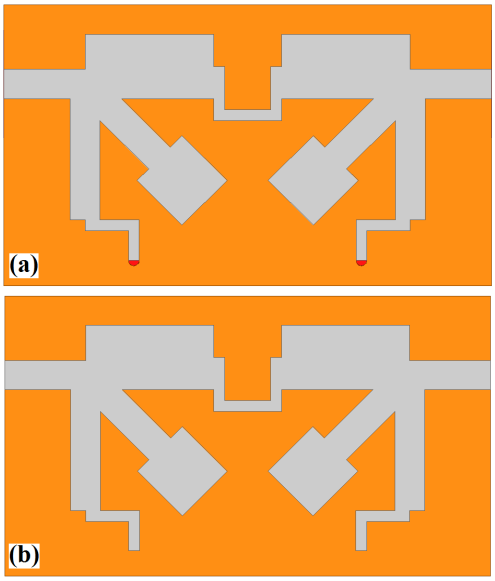

Fig. 6. Proposed BLC using NUFTL and SSISs: (a) odd-mode equivalent-TL, and (b) even-mode equivalent-TL.

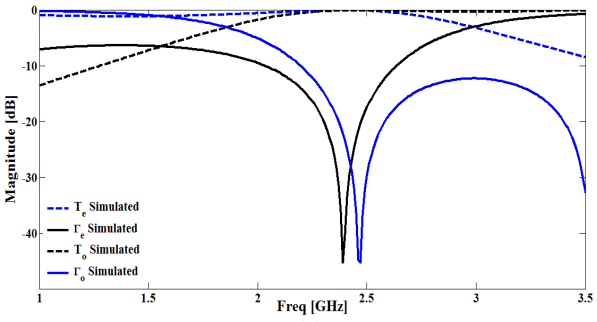

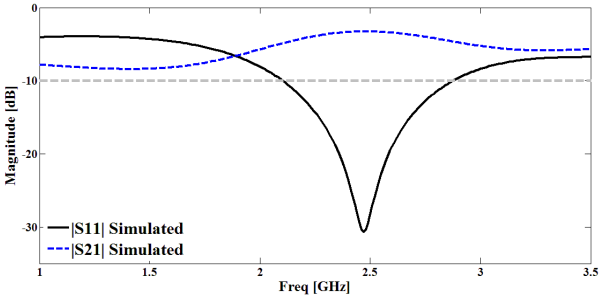

(b)

Fig. 7. Simulated frequency responses for BLC structures with HFSS software: (a) odd mode and even mode responses for equivalent-TL circuits in Fig. 6, and (b) proposed BLC in Fig. 1.

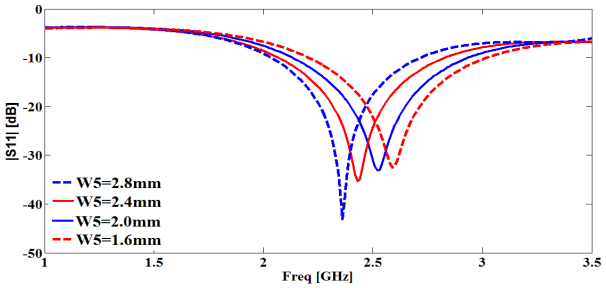

Fig. 8. The effect of variation in width of the low-impedance line of SSIS (W_5 in Fig. 1 (b)) on $|S_{11}|$.

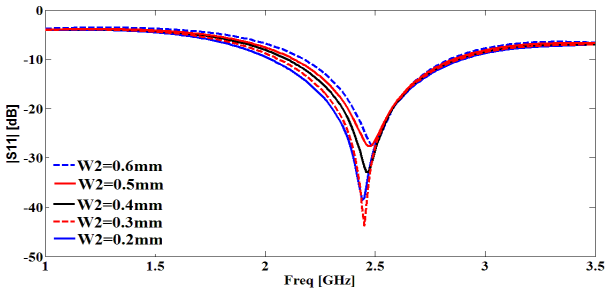

Fig. 9. The effect of variation in finger width of the vertical arm of the NUFTL (W_2 in Fig. 1 (b)) on $|S_{11}|$.

III. RESULTS AND DISCUSSIONS

The proposed BLC with final design parameters, as shown in Fig. 10, was fabricated and tested. All measured and simulated results of the fabricated BLC are shown in Fig. 11 and Fig. 12. From Fig. 11 (a), it can be confirmed that the proposed BLC has a wide bandwidth of 32% (2.06–2.81 GHz, centre frequency = 2.40 GHz) at the reference -10 dB reflection coefficient for all ports. In the operating bandwidth the isolation between port 1 and port 4 is more than 25 dB. The measured $|S_{21}|$ and $|S_{31}|$ at the center frequency are -3.3 dB and -3.4 dB, respectively. There exists good agreement between simulation and measurement results. Figure 12 shows the measured phase responses. There exists a discrepancy between the measured data and the simulated results. Simulated phase difference between port 2 and port 3 is 90° ± 2° at the operating bandwidth.

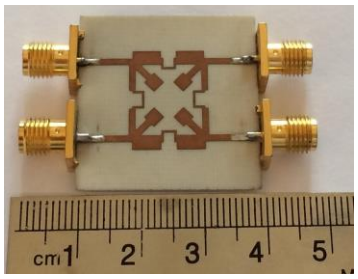

Fig. 10. Photograph of the fabricated BLC prototype with NUFTL and SSISs.

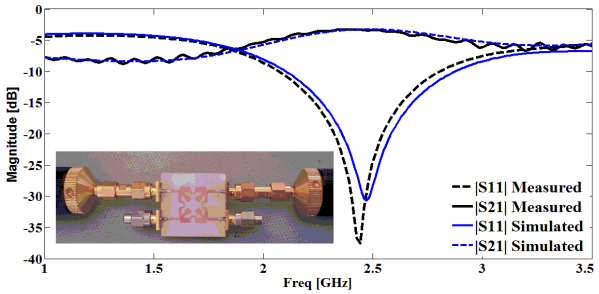

(a)

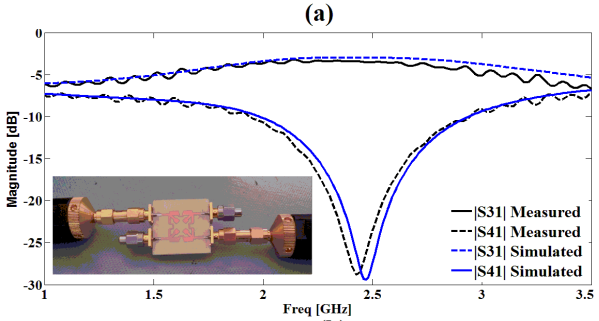

(b)

Fig. 11. Measured and simulated frequency responses of the fabricated BLC using NUFTL and SSISs shown in Fig. 1.

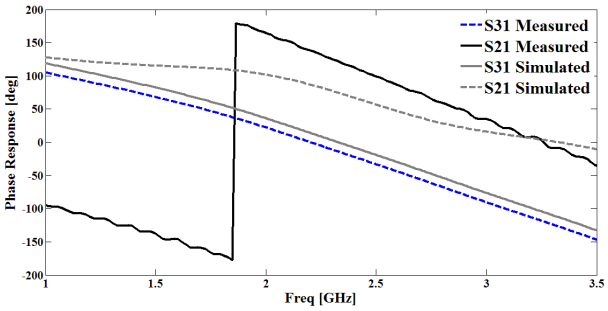

Fig. 12. Measured and simulated phase responses of the fabricated BLC using NUFTL and SSISs shown in Fig. 1.

As shown in measured results, there exists a discrepancy between the measured data and the simulated results. The discrepancy is mostly due to a number of parameters such as the fabricated BLC dimensions as well as the thickness and dielectric constant of the substrate, on which the BLC is fabricated. In order to confirm the accurate return loss characteristics for the designed BLC, it is recommended that the manufacturing and measurement processes need to be performed carefully; besides, SMA soldering accuracy and substrate quality need to be taken into consideration [21-22]. In summary, it can be said that a fine agreement between the measured and the simulated results is obtained in the frequency band of operation.

Finally, a comparison between the proposed BLC and other coupler structures with same characteristics which have been published in literature and used here as references is presented in Table 2. From this table, it can be concluded that the proposed BLC has improved in-band and out-of-band performances as well as size miniaturization. In comparison with [6] and [12], the proposed BLC has a smaller size, with respect to the operating frequency band. The presented BLC has a wider bandwidth in comparison with the BLCs in [4-7] and [9-10]. The out-of-band performance of the presented BLC is better than the ones in [4, 7, 10]. Moreover, the realization of the proposed BLC is simpler than the ones in [6, 7, 12, 14].

Table 2: A comparison among the proposed BLC using NUFTL and SSISs and the previous work

Ref.	f_0 (GHz)	FBW 10 dB(%)	ε_r/h (mm)	Size ($\lambda_0 \times \lambda_0$)
[3]	1	30	2.2/1.58	0.112×0.098
[4]	2.4	25	4.7 /0.80	0.074×0.095
[5]	2.4	22	4.3/0.80	0.117×0.087
[6]	2	25	2.2/0.508	0.272×0.128
[7]	1	28	3.55/0.76	0.233×0.257
[8]	5	40	4.4/0.80	0.087×0.091
[9]	2	10	2.1/0.508	0.130×0.130
[10]	0.836	12	4.2/1.02	0.221×0.207
[12]	2.4	33	3.38/0.813	0.159×0.192
[14]	2	26	10.2/1.27	0.092×0.090
This work	2.4	32	3.55/0.508	0.096×0.115

f_0: Centre frequency of operation band; ε_r: Substrate relative dielectric constant; h: Substrate thickness; λ_0: the free space wavelength of the operating frequency at the center of the pass-band (2.40 GHz).

IV. CONCLUSION

A novel compact BLC was presented and discussed. The presented BLC consists of a NUFTL and SSISs in order to obtain wideband characteristic, which is able to suppressing higher order harmonics of the BLC over a wideband. The BLC exhibits low insertion loss over the desired passband and sufficient isolation level at the frequency band of interest. Good agreement exists between the simulated and measured results.

ACKNOWLEDGMENT

The authors thank the Northwest Antenna and Microwave Research Laboratory (NAMRL) for their beneficial and professional help.

REFERENCES

[1] D. M. Pozar, *Microwave Engineering*, 4rd edition, New York: John Wiley & Sons, 2012.

[2] H. Oraizi and A. R. Sharifi, "Design and optimization of broadband asymmetrical multisection Wilkinson power divider," *IEEE Trans. Microw. Theory and Tech.*, vol. 54, no. 5, pp. 2220-2231, 2006.

[3] K. O. Sun, S. J. Ho, C. C. Yen, and D. van der Weide, "A compact branch-line coupler using discontinuous microstrip lines," *IEEE Microw. Wireless Compon. Lett.*, vol. 15, no. 8, pp. 519-520, Aug. 2005.

[4] S. S. Liao and J. T. Peng, "Compact planar microstrip branch-line couplers using the quasi-lumped elements approach with nonsymmetrical and symmetrical T-shaped structure," *IEEE Trans. Microw. Theory Tech.*, vol. 54, no. 9, pp. 3508-3514, Sep. 2006.

[5] C. W. Tang and M. G. Chen, "Synthesizing microstrip branch-line couplers with predetermined compact size and bandwidth," *IEEE Trans. Microw. Theory and Tech.*, vol. 55, no. 9, pp. 1926-1934, 2007.

[6] F. Hosseini, M. Hosseini, and M. Yazdany, "To compact ring branch-line coupler using nonuniform transmission line," *Microwave and Optical Technology Letters*, vol. 51, pp. 2679-2682, Nov. 2009.

[7] S. H. Sedighy and M. K. Amirhosseini, "Compact branch line coupler using step impedance transmission lines (SITLs)," *Applied Computational Electromagnetic Society (ACES) Journal*, vol. 28, no. 9, pp. 866-870, Sep. 2013.

[8] M. Maleki, J. Nourinia, Y. Zehforoosh, and V. Rafii, "A compact planar 90° branch line coupler using S-shaped structure loading for wideband application," *Applied Computational Electromagnetic Society (ACES) Journal*, vol. 28, no. 7, pp. 597-601, July 2013.

[9] J. Wang, B. Z. Wang, Y. X. Guo, L. C. Ong, and S. Xiao, "A compact slow-wave microstrip branch-line coupler with high performance," *IEEE Microw. Wireless Compon. Lett.*, vol. 17, no. 7, pp. 501-503, July 2007.

[10] K. Y. Tsai, H. S. Yang, J. H. Chen, and Y. J. E. Chen, "A miniaturized 3 dB branch-line hybrid coupler with harmonics suppression," *IEEE Microw. Wireless Compon. Lett.*, vol. 21, no. 10,

pp. 537-539, Oct. 2011.
[11] Z.-W. Lee and Y.-H. Pang, "Compact planar dual-band crossover using two-section branch-line coupler," *Electronics Letters*, vol. 48, no. 21, pp. 1348-1349, Oct. 2012.
[12] V. I. Nejad, A. A. L. Neyestanak, and A. Shahzadi, "Compact broadband quadrature hybrid coupler using planar artificial transmission line," *Electronics Letters*, vol. 48, no. 25, pp. 1602-1603, Dec. 2012.
[13] H. Ren, J. Shao, M. Zhou, B. Arigong, J. Ding, and H. Zhang, "Novel design of multiband branch-line coupler using multiband transmission lines," *Microwave and Optical Technology Letters*, vol. 56, pp. 2841-2845, Dec. 2014.
[14] C. Karpuz and P. Ozturk, "Design of branch line coupler loaded capacitively with interdigitated fingers by using microstrip fed coplanar structures (L-shaped conductor backed asymmetric cps and U-shaped conductor backed CPW)," *Microwave and Optical Technology Letters*, vol. 55, pp. 816-820, Apr. 2013.
[15] Y. B. Jung, "Wideband branch line coupler using symmetrical four-strip interdigitated coupler," *Electronics Letters*, vol. 50, no. 6, pp. 452-454, Mar. 2014.
[16] J. K. Lee, D. J. Jung, and K. Chang, "Dual-band branch-line coupler using double-sided parallel-strip line," *Microwave and Optical Technology Letters*, vol. 54, pp. 1898-1900, Aug. 2012.
[17] Ansoft High Frequency Structure Simulation (HFSS), ver. 15, Ansoft, Corporation, 2013.
[18] B. Mohammadi, A. Valizade, P. Rezaei, and J. Nourinia, "A new design of compact dual band-notch UWB BPF based on coupled wave canceller inverted T-shaped stubs," *IET Microwave and Antenna Propagation*, vol. 9, no. 1, pp. 64-72, Jan. 2015.
[19] B. Mohammadi, A. Valizade, J. Nourinia, and P. Rezaei, "Design of A compact dual-band-notch UWB bandpass filter based on wave cancellation method," *IET Microwave and Antenna Propagation*, vol. 9, no. 1, pp. 1-9, Jan. 2015.
[20] I. J. Bahl and D. K. Trivedi, "A designer's guide to microstrip line," *Microwaves*, vol. 16, pp. 174-182, May 1977.
[21] B. Mohammadi, J. Nourinia, C. Ghobadi, and A. Valizade, "Design and analysis of the stub and radial-stub loaded resonator bandpass filter with cross-shaped coupled feed-lines for UWB applications," *Applied Computational Electromagnetic Society (ACES) Journal*, vol. 28, no. 9, pp. 851-857, Sep. 2013.
[22] P. Beigi, J. Nourinia, B. Mohammadi, and A. Valizade, "Bandwidth enhancement of small square monopole antenna with dual band notch characteristics using U-shaped slot and butterfly shape parasitic element on backplane for UWB applications," *Applied Computational Electromagnetic Society (ACES) Journal*, vol. 30, no. 1, pp. 78-85, Jan. 2015.

Shalaleh Nouri received the B.S. degree in Electrical Engineering-Electronics from Azad University of Urmia, Iran, in 2012, and M.Sc. degrees in Electrical Engineering-Microwave, Antenna and Propagation from Urmia University, Urmia, Iran, in 2015, where she is currently working as a Research Assistant in the Northwest Antenna and Microwave Research Laboratory (NAMRL) in Urmia University, Urmia, Iran. His research interests include couplers, filters, and MIMO.

Javad Nourinia received his B.Sc. in Electrical and Electronic Engineering from Shiraz University and M.Sc. degree in Electrical and Telecommunication Engineering from Iran University of Science and Technology, and Ph.D. degree in Electrical and Telecommunication from University of Science and Technology, Tehran Iran in 2000. From 2000 he was an Assistant Professor and now he is a Professor in the Department of Electrical Engineering of Urmia University, Urmia, Iran. His primary research interests are in antenna design, numerical methods in electromagnetic, microwave circuits.

Nooshin Valizade received her B.Sc. degree in Electrical Engineering-Electronics from Shahid Beheshti University, Tehran, Iran, in 2013, and M.Sc. degrees in Electrical Engineering-Telecommunication from University of Science and Technology, Tehran, Iran, in 2016. Her primary research interests are in antenna design, reconfigurable structures, and MIMO systems.

Bahman Mohammadi received the B.S. degree in Electrical Engineering-Telecommunication from Tabriz University, Tabriz, Iran, in 2011 and M.Sc. degrees in Electrical Engineering-Microwave, Antenna and Propagation from Urmia University, Urmia, Iran, in 2013,

where he is currently working as a Research Assistant in the Northwest Antenna and Microwave Research Laboratory (NAMRL) in Urmia University, Urmia, Iran. His research interests include Periodic Structures (Reflectarray antenna, FSS), Microwave Components (filters, diplexers, couplers, crossovers, phase shifters, transitions, baluns, etc.), Optimization Methods (GA, NN, and NP), and MIMO.

Arash Valizade was born in Tehran, Iran 1986. He received his B.Sc. degree in Electrical Engineering-Electronics from Azad University of Sabzevar, Iran, in 2008 and M.Sc. degree in Electrical Engineering-Telecommunication from Urmia University, Urmia, Iran, in 2012, and Ph.D. degree in Electrical Engineering-Telecommunication from Semnan University, Semnan, Iran in 2016. His primary research interests are in numerical methods in electromagnetics, microstrip antenna design, microwave circuits, active integrated antenna design, and reconfigurable structures.

CPW Dependent Loss Analysis of Capacitive Shunt RF MEMS Switch

S. Suganthi [1], K. Murugesan [2], and S. Raghavan [3]

[1] Department of Electronics and Communication Engineering
K. Ramakrishnan College of Technology, Tiruchirappalli, Tamilnadu, India
tvssugi@gmail.com

[2] Department of Electronics and Communication Engineering
Sree Sastha Institute of Engineering and Technology, Chennai, India

[3] Department of Electronics and Communication Engineering
National Institute of Technology, Tiruchirappalli, India

Abstract ─ CPW (CoPlanar Waveguide) plays major role in design of RF MEMS switch to improve the performance in terms of losses and required bandwidth of operation. This paper proposes the analyses of the mechanical characteristics on the electrical performance of the Capacitive Shunt RF MEMS (CSRM) switch based on various CPW structures and contact area roughness of the switch using electromagnetic 2.5D ADS simulator. The result of momentum method was analyzed up to the K-band frequency of 100 GHz. The result shows that the CSRM switch with two conductor CPW coupler has a maximum isolation of -46 dB with operating bandwidth up to 90 GHz at the resonant frequency of 50 GHz. In order to validate the obtained result, Artificial Neural Network (ANN) has been trained using ADS result. Comparison shows good agreement between ADS and ANN results.

Index Terms ─ Artificial neural network, capacitive shunt switch, CPW, isolation loss, RF MEMS switch.

I. INTRODUCTION

Design of RF MEMS switches is one of the interesting research area that facilitates to design with great potential to improve the performance of communication circuit and systems. At microwave frequencies, the rapid development and use of micro electromechanical systems (MEMS) have proved tremendous advancement due to their high linearity and low losses [1] as well as low power consumption [2]. Among the various components of MEMS technology, MEMS switches are the basic building blocks replacing the conventional p-i-n diode and GaAs FET switches [3] in high frequency applications. Low cost MEMS switches are considered as prime category in MEMS technology due to their extremely low insertion loss (0.1 dB) [4] and very high isolation up to 100 GHz, near zero power consumption (10-200nJ/switching cycles) good isolation [5], lower insertion loss and low power consumption [3] properties. The analysis of MEMS switches from microwave to millimeter wave frequencies, have revealed superior performance than the diode based switches which offer poor performance in terms of losses [6], tuning linearity and intermodulation distortion. The excellent linearity [7] due to the mechanical passive nature [8] of the device and wide band width operation of MEMS switches make it ideal for several wireless applications, reconfigurable antennas, filters and tuners, low loss phase shifters and high Q passive devices and resonators [5].

MEMS switches are the devices which operate by the use of mechanical movement to achieve short or open circuit in RF circuits. The required force for mechanical movement can be obtained by different mechanisms for actuation like electrostatic and magneto static [5]. RF MEMS switches that are able to handle up to 20W and operating cycle of 10^{12} [1] have found applications in RADAR system, network analyzer, satellite communication system and in base stations [5].

MEMS switches can be designed in different configurations based on signal path (series or shunt), the actuation mechanism (electrostatic, thermal or magneto static), the type of contact (ohmic or capacitive) and the type of structure (cantilever or bridge) [9]. Extensive studies on various kinds of series and shunt MEMS switches are available in literature [10, 11]. The practical first capacitive shunt switch was presented by Raytheon based on fixed-fixed metal beam structure [11]. Later on, lot of research work has been carried out on capacitive shunt RF MEMS (CSRM) switches to achieve better performance [12].

In a CSRM switch, a thin metal membrane bridge is suspended over the center conductor of coplanar waveguide (CPW) [13] and fixed on the ground conductor

Submitted On: September 26, 2013
Accepted On: February 27, 2016

of CPW [14]. This configuration performs excellently for 10-100 GHz frequency range applications with a typical isolation of -17 dB at 10 GHz and -35 to -40 dB at 30-40 GHz for a capacitance of 4pF [7]. The electrical performance depends on the mechanical properties of structure, materials used for implementation and the method of fabrication [15]. The dependence of electrical performance of MEMS switches on mechanical properties can be studied by commercial simulation tools. Though RF MEMS switches are 3D structures, they can also be seen as 2.5D structure due to their high aspect ratio.

In this paper, the analyses of various losses of CSRM switch have been carried out using electromagnetic simulation for K-band (18-26.5 GHz) applications using 2.5D ADS–Momentum™ full wave EM software. The isolation analysis, bandwidth and frequency of operation are concentrated by considering various configurations of CPW.

II. CAPACITIVE SHUNT RF MEMS SWITCH

A. Selection of switch

As mentioned in Section I, there are several types of MEMS switches based on different design parameters. The major criteria for switch selection are its application and frequency of operation. Out of two types of switches based on contact, the shunt is preferred over series due to minimal parasitic involved and capable of handling more RF power. Shunt switches have the benefit of ease of fabrication and fewer parasitic due to continue t-line [9]. The capacitive MEMS switch has excellent performance up to 40 GHz [16] and life time in excess of 1 million cycles [17] under low power conditions.

B. Theory of capacitive shunt RF MEMS switch

The capacitive shunt MEMS switch taken for analysis is based on a fixed–fixed beam [18] design and is shown in Fig. 1 (a). The MEMS Bridge with the gap of g from the center conductor is connected to the CPW ground plane and the bridge is grounded. The center pull down electrode provides both the electrostatic actuation [5] and RF capacitance between the transmission line and ground. When the switch is down (off) state actuated, the capacitance to the ground provides good results in excellent short circuit and high isolation at microwave frequencies. The lumped element equivalent circuit model of CSRM switch is shown in Fig. 1 (b).

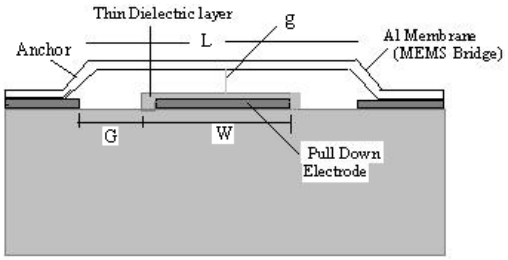

(a)

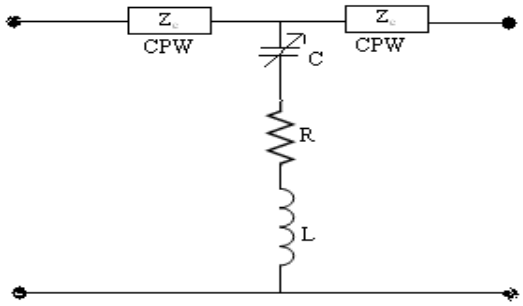

(b)

Fig. 1. Capacitive shunt RF MEMS switch: (a) cross section view and (b) equivalent circuit.

C. Structure of CPW

In the above mentioned lumped element model, the characteristic impedance (Z) of CPW plays a major role which is determined by G/W/G dimension. CPW is a planar transmission line (t-line) above which the shunt switch should be fabricated [5]. In this t-line, the signal and two ground lines are on the same plane [9]. There are various configuration of CPW like simple CPW, CPW with lower ground plane (CPWG), CPW with short open circuited stub (CPWSC), CPW with open circuited stub (CPWOC), CPW open end effect (CPWEF), CPW end gap (Cpwegp) and center conductor gap (Cpwcgp) and CPW coupler having two conductor connected (Cpwcpl2). The ADS symbols for the above mentioned CPWs are shown in Fig. 2.

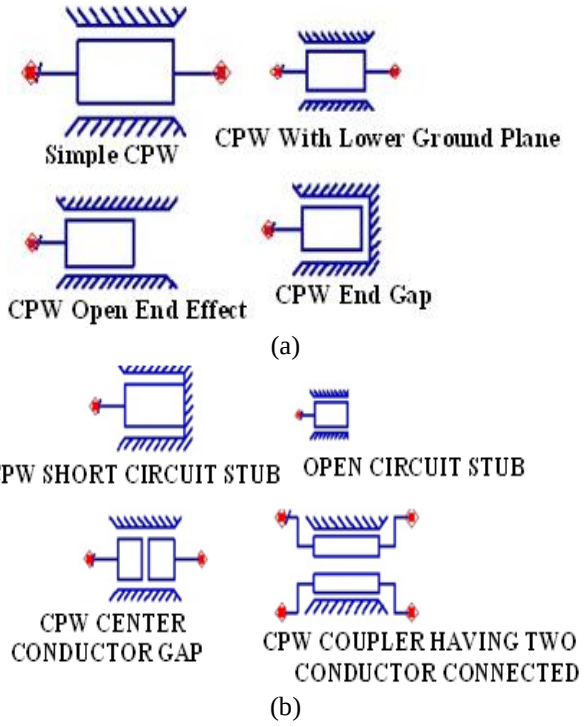

Fig. 2. Different configurations of coplanar waveguide.

The ADS illustration of simple CPW configuration used in this work is shown in Fig. 3. In this figure, CPWSUB is the substrate required for all coplanar waveguide components with W and L are the center conductor width and length respectively and G is the gap between center conductors. The fitted values of this parameter for getting better loss performance of the considered switch are given in Table 1.

Table 1: Typical parameters of CPW used for ADS

Name	Description	Value
H	Substrate thickness	675µm
Er	Relative dielectric constant	11.8
Mur	Relative permeability	1
Cond	Conductor conductivity	4.1e7
T	Conductor thickness	1µm
TanD	Dielectric loss tangent	0.01
Rough	Conductor surface roughness	0µm
W	Center conductor width	120µm
G	Gap between center conductor and ground plane	90µm
L	Center conductor length	300µm

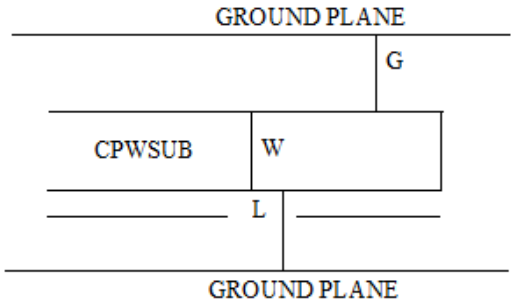

Fig. 3. Cross section of simple CPW.

D. Electromagnetic analysis of switch

The EM modeling of CSRM switch is proposed with 2.5D full wave EM ADS-Momentum software. Using this EM tool, this paper proposes the electrical modeling of capacitive switch taking into account of electrical performance on the mechanical properties. In the simulation, the isolation parameters are extracted in the frequency range up to 100 GHz for different CPW structures. The parameters of the lumped model are optimized to obtain the value of S-parameter which is closer to ideal.

E. Artificial neural network

ANNs are biologically inspired computer programs to simulate the way in which the human brain process information. Neural models can be much faster than original detailed EM/physics models, more accurate than polynomial and empirical models, allow more dimensions than table lookup models and are easier to develop when a new device/technology is introduced [19]. The power of computation in neural network is determined from connections in a network. Each neuron has weighted inputs, simulation function, transfer function and output. The weighted sum of inputs constitutes the activation function of the neurons. The activation signal is passed through a transfer function which introduces non-linearity and produces the output. Training a network consists of adjusting weights of the network using learning algorithms. During learning process, neural network adjusts the weights and thresholds so that the error between neural predicted output and sampled output is minimized. The learning algorithms used in this work are based on multilayer correction learning algorithm called back propagation [20]. During training process, the inter-unit connections are optimized until the error in prediction is minimized. Once the network is trained, new unseen input information is entered into the network to calculate the test output. The neural network architecture used in this paper is the MultiLayer Perceptron Neural Network (MLPNN), which is multilayer feed forward architecture composed of layers of computing nodes called neurons [21].

III. RESULTS AND DISCUSSION

Since the CPW has been used as the base for RF MEMS switches, we have taken various configuration of CPW to analyze the resonance frequency, bandwidth and isolation characteristics of capacitive shunt RF MEMS switch. Figure 4 shows the isolation of switch for different structures of CPW. It is clear that the resonance frequency obtained is above 15 GHz for all structures and the three structures (CPW coupler, CPW open end effect and CPW end gap) are able to work in two different resonant frequencies. The maximum operating frequency (90 GHz) can be obtained from CPW end gap and CPW open end effect structures with better isolation of nearly -75 dB.

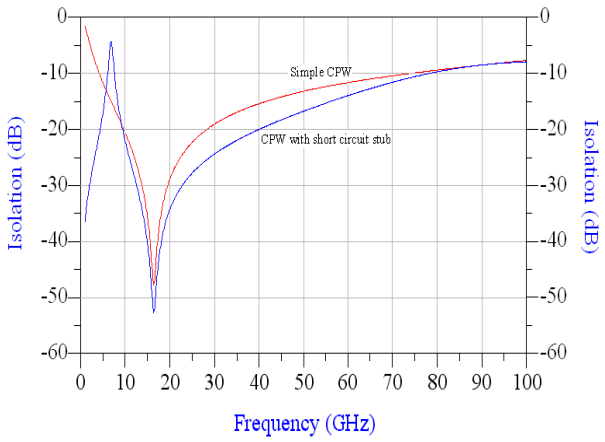

(a)

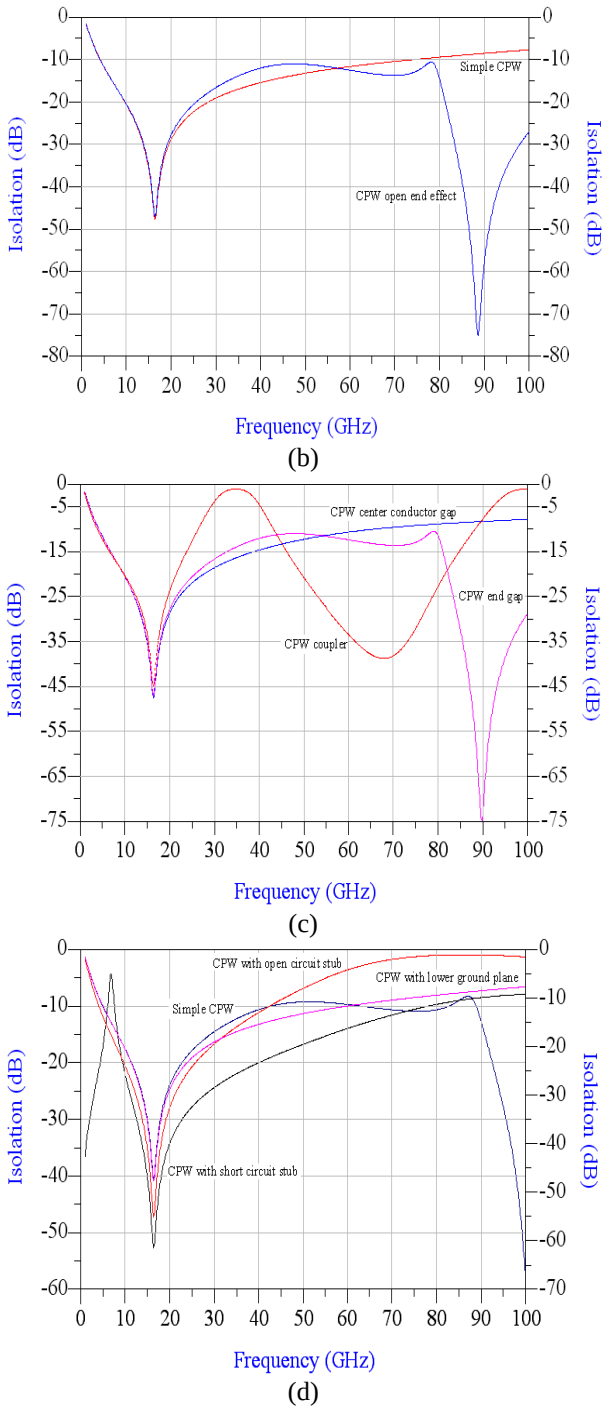

Fig. 4. Comparison result for isolation performance of CSRM switch with different CPW structures: (a) simple & short circuit stub, (b) simple and open end effect, (c) CPW center conductor gap, end gap and CPW coupler, and (d) CPW open, short circuit stub, lower ground plane and simple CPW.

Among all structures considered, the switch with CPW having lower ground plane differ in isolation loss characteristics by random variants of loss in operating frequency and maximum isolation of only -32 dB. All other switch structures can work with maximum isolation up to -45 dB at the resonance frequency of 15 GHz. The comparison of three parameters taken for analysis of CSRM switch for with various CPW structures is shown in Table 2. Since the resonant frequency of 15 GHz has been achieved in all CPW configuration of CSRM switch, these switches are much suitable for K-band satellite communications applications.

Table 2: Performance comparison of CSRM switch structures with simple CPW structure

CPW Type	Bandwidth Resonance (GHz)	Operating Frequency (GHz)	Isolation (dB)
SCPW	ENTIRE	16	-48
CPWG	ENTIRE	16	-41
CPWSC	5-80	16	-52
CPWOC	5-41	16	-48
CPWEF	5-90	16 & 88	-45 & -75
CPWEGP	5-90	16 & 90	-46 & -75
CPWCGP	5-70	16	-46
CPWCPL	5-25 & 45-90	16 & 68	-45 & -75

Based on the statistical obtained from comparison figures, it is obvious that the CSRM switch having CPW coupler with two conductors connected is having superior characteristics in terms of dual bandwidth with maximum operating bandwidth up to 90 GHz, higher isolation of -46 dB and resonant frequency of 67 GHz. The equivalent lumped circuit model of CSRM with simple CPW derived from ADS simulation is shown in Fig. 5. This switch topology is normally used in the integrated circuits where RF lines are DC grounded. In that condition, the membrane cannot be directly anchored to the CPW ground planes but a capacitive anchor is used for DC isolation.

The capacitive anchor of the membrane to the CPW ground planes has been considered as two shunt capacitors one for each anchor. The Fig. 6 (a) shows the comparison of isolation of the simple CPW CRSM switch with and without capacitive anchor. It is observed that the resonant frequency has been shifted to 30 GHz with the penalty of reduction in isolation loss of -7 dB with the addition of capacitive anchor for DC isolation when the switch is used for integrated circuits.

In the above lumped element model, the value of contact capacitance in the down state has the deviation in value which depends on the perfect roughness of the material between the membrane and the CPW center conductor. In order to validate the obtained result, the neural network comparison has been trained with the ADS result obtained for with and without capacitor anchor. After many trails, network (Fig. 6 (d)]) having

two hidden layers have been selected with dimensions of 4x14x10x2. This means that the numbers of neurons were 4 for input layer, 14 and 12 for first and second hidden layers respectively and 2 for output layer respectively.

The MLP network was trained with input and hidden layers having the hyperbolic tangent sigmoid activation function and output layer having linear activation function as the learning algorithms. Figure 7 shows the comparison between ADS and neural network result for simple CPW with and without capacitive anchor. The better agreement between the results from ADS and ANN training clears that the fitted circuit values in the lumped element model are optimized by simulation.

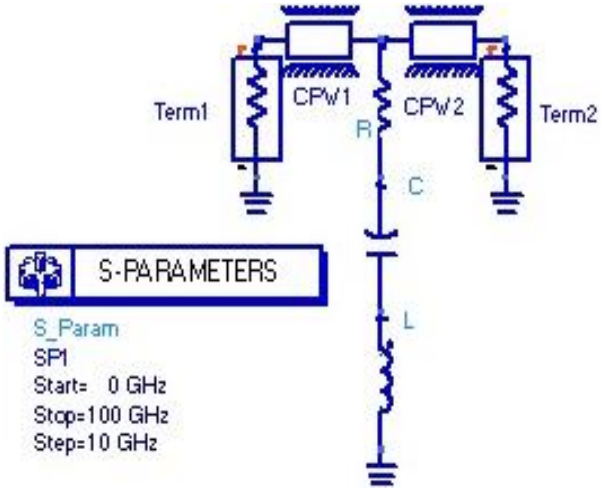

Fig. 5. ADS lumped element model of CSRM.

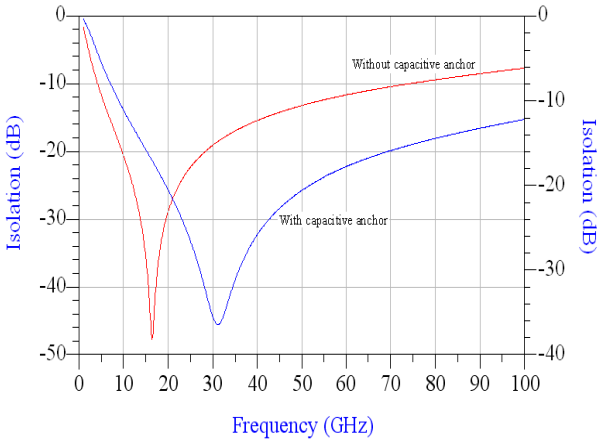

(a)

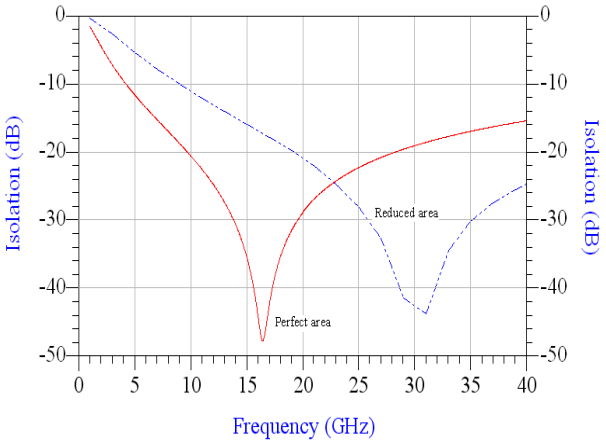

(b)

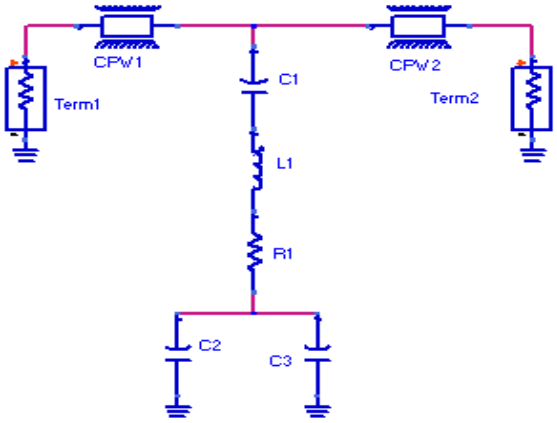

(c)

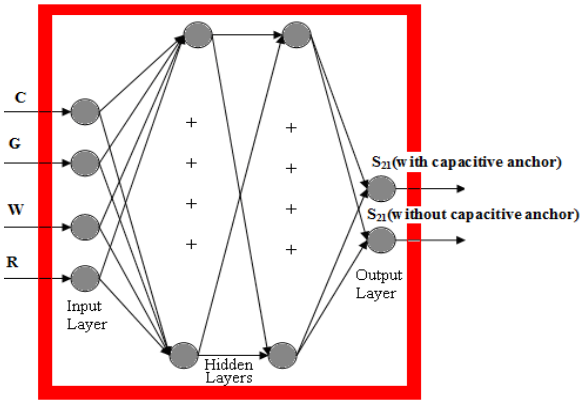

(d)

Fig. 6. Isolation performance comparison of CSRM: (a) with and without capacitive anchor, (b) with perfect and reduced contact area between membrane and center conductor, (c) lumped ADS circuit model of CSRM with shunt capacitor for DC isolation, and (d) ANN model.

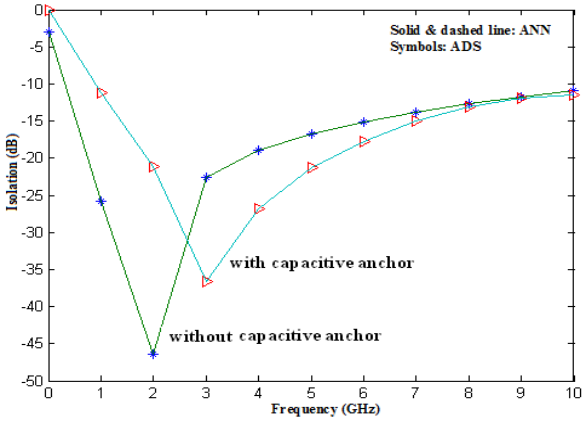

Fig. 7. Comparison of ADS and ANN trained values for isolation of CSRM switch with and without capacitive anchor.

VI. CONCLUSION

Different issues to analyze the mechanical properties on the electrical performance in terms of isolation and resonant frequency of capacitive shunt RF MEMS switch have been discussed for K-band satellite communication applications. The electromagnetic simulation results that the resonant frequency and the isolation performance of the proposed switch can be improved in two ways: by proper selection of CPW structures and the roughness of the contact between the membrane and CPW center conductor. From the analyses using different CPW structures, the better switching performance has been achieved from the switch with CPW coupler having two conductors connected. By reducing the contact area, the isolation increase of -4 dB and the resonant frequency up shift of about 15 GHz has been derived. The proposed switch performance can find applications with electronically scanned arrays (phase shifters), reconfigurable antennas and in tunable band-pass filters.

REFERENCES

[1] V. Markovic, L. Vietzorreck, Z. Marinkovic, and O. Pronic, "Modeling of RF MEMS switches for application in communication system," *Simpozijum o novim techologijama u postanskom I telecomunikacionom saobracaju-PosTel 2012*, Beograd, vol. 4, iss. 5, Dec. 2012.

[2] R. W. Herfst, P. G. Steeneken, and J. Schmitz, "Identifying degradation mechanisms in RF MEMS capacitive switches," *MEMS 2009*, Tucson, AZ, USA, Jan. 13-17, 2008.

[3] B. Pillans, J. Kleber, C. Goldsmith, and M. Eberly, "RF power handling of capacitive RF MEMS devices," *IEEE MTT-S*, pp. 329-332, 2002.

[4] S. Suganthi, K. Murugesan, and S. Raghavan, "ANN model of RF MEMS lateral SPDT switches for millimeter wave applications," *Journal of Microwaves, Optoelectronics and Electromagnetic Applications*, vol. 11, no. 1, pp. 130-143, 2011.

[5] Z. D. Milosavljevic, "RF MEMS switches," *Microwave Review*, pp. 1-8, June 2004.

[6] M. Fernndez Bolaos, J. Perruisseau Carrier, P. Dainesi, and A. M. Ionescu, "RF MEMS capacitive switch on semi-suspended CPW using low loss high resistivity silicon," *Microelectronics Engineering*, vol. 85, pp. 1039-1042, 2008.

[7] D. Verma and A. Kaushik, "Analysis of RF MEMS capacitive switch based on a fixed – fixed beam structure," *International Journal of Engineering Research and Applications*, vol. 2, iss. 5, pp. 391-394, Sep. 2012.

[8] S. Suganthi, K. Murugesan, and S. Raghavan, "RF MEMS switch beam position stabilization analysis using neural network," *International Journal of Microwave and Optical Technology*, vol. 7, no. 2, pp. 107-115, 2012.

[9] P. Verma and S. Singh, "Design and simulation of RF MEMS capacitive type shunt switch and its major applications," *IOSR Journal of Electronics and Communication Engineering*, vol. 4, iss. 5, pp. 60-68, Jan. 2013.

[10] C. M. Rebeiz and J. B. Muldavin, "RF MEMS switches and switch circuits," *IEEE Microwave Magazine*, Dec. 2001.

[11] J. J. Yao, "*Micro electromechanical RF switch*," United State Patent, Patent Assibnee: Rockwell International Corporation Patent No: 5578976, Nov. 1996.

[12] D. Peroulis, S. Pacheco, K. Saarbandi, and L. P. B. Katehi, "MEMS devices for high isolation switching and tunable filtering," *IEEE MTT-S Digest*, pp. 1217-1220, 2000.

[13] G. M. Rebeiz, *RF MEMS, Theory, Design and Technology*, John Wiley and Sons, Hoboken, 2003.

[14] J. Y. Qian, G. P. Li., and F. D. E. Flaviis, "A parametric model of low loss RF MEMS capacitive switches," *APMC Microwave Conference 2001*, Asia Pacific, vol. 3, pp. 1020-1023, 2001.

[15] M. A. Liamas, D. Girbau, E. Pausas, L. Pradell, S. Aouba, C. Villeneuve, V. Puyal, P. Pons, R. Plana, S. Colpa, and F. Giacomozzi, "Capacitive and resistive RF MEMS switches 2.5D and 3D electromagnetic and circuit modeling," *Proceeding of the 2009 Spanish Conference on Electron Devices*, Santiago de Compostela, Spain, Feb. 11-13, 2009.

[16] C. L. Golsmith, Z. Yao, S. Eshelman, and D. Denniston, "Performance of low loss RF MEMS capacitive switches," *IEEE Microwave and Guided Wave Letters*, vol. 8, no. 8, Aug. 1998.

[17] C. Goldsmith, J. Ehmke, A. Malczewski, B. Pillans, S. Eshelman, Z. Yae, J. Brank, and M.

Eberly, "Lifetime characteristics of capacitive RF MEMS switches," *IEEE International Microwave Symposium*, vol. 1, May 2001.

[18] J. Y. Park, G. H. Kim, K. W. Chung, and J. U. Bu, "Fully integrated micromachined capacitive switches For RF applications," *IEEE MTT-S International Microwave Symposium Digest*, Boston, Massachusetts, USA, pp. 283-286, June 2000.

[19] Y. Lee and D. S. Filipovic, "ANN based electromagnetic models for the design of RF MEMS switches," *IEEE Microwave and Wireless Components Letters*, vol. 15, no. 11, pp. 823-825, 2005.

[20] S. Haykin, *Neural Networks: A Comprehensive Foundation*, Macmillan College Publishing Comp., 1994.

[21] G. L. Creech, B. J. Paul, C. D. Lesniak, T. J. Jenkins, and M. C. Calcatera, "Artificial neural networks for fast and accurate EM-CAD of microwave circuits," *IEEE Trans. Microwave Theory Tech*., vol. 45, no. 5, pp. 1794-802, 1997.

Dual Band and Dual Mode Microstrip Antenna for Body Centric Wireless Communication

Seiran Khaledian and Zahra Atlasbaf

Department of Computer and Electrical Engineering
Tarbiat Modares University, Tehran, Iran
Seiran.kh@gmail.com, atlasbaf@modares.ac.ir

Abstract ─ A compact dual band and dual mode microstrip patch antenna, suitable for body centric wireless communication (BCWC) network is presented. The BCWC network works in two on-body and off-body modes. The proposed antenna has an outward radiation pattern for the off-body mode, which is suitable to communicate from on-body devices to off-body unite. Moreover, the antenna has an end-fire radiation pattern for the on-body mode, to communicate with other co-located worn devices from which data can be easily gathered. The proposed antenna resonances at 2.44 GHz (IEEE 802.11b/g) with 7.1 dB gain and linear polarization for the off-body mode and also at 5.43 GHz (IEEE 802.11a) with 6.6 dB gain and circular polarization for the on-body mode. Free space and on-body simulated and measured performances of the proposed antenna are shown. Specific absorption rate (SAR) value is also studied. The results show that the maximum averaged 10gr SAR is 0.26W/Kg for on-body mode when the antenna is placed on the chest of the human body model.

Index Terms ─ BCWC network, dual band, dual mode, microstrip patches antenna, miniaturization, on-body/off-body antenna.

I. INTRODUCTION

Advances in wireless technology have led to the development of wireless body area network (WBAN), where a set of communication devices is deployed in close proximity and around the human body. There are two main channels of interest for wireless body area network: off-body and on-body. The off-body channel is concerned for communication between a device on the body and a remote location. Some typical applications include short range communication between two soldiers on a battlefield or transmission of medical data from a wireless sensor body area network to a remote network access point. On-body channel is necessary for communication between devices located on the surface of a user's body; e.g., in telemedicine applications where wireless biosensors are distributed across the body, a controller rode is often located on the body to act as a relay between the biosensors and a non-local station several meters or more away from the user. In such applications, it is clear that both propagation modes (on the body and off-body) are required [1, 2]. Antennas used in this kind of applications require a low profile, tolerable power consumption, low manufacturing cost and must have little effects on the human body. In this regard, microstrip patch antennas are good candidates due to their low cost, physical size (low profile), higher power efficiency and their ability to provide proper radiation parameters. Radiation pattern in off-body link needs to have a good boresight (normal to the body surface) directivity and must propagate through a tangential creeping wave in the on-body link.

The antennas already designed for WLAN applications fall into two main groups: the first group includes antennas which can only run in the on-body or the off-body modes, separately [2-4]. On the contrary, a second group exists where simultaneous on or off-body modes can be expected [5, 9]. In [5], a dual band, dual mode and dual feed compact antenna is discussed where coaxial cables are used. In addition, a dual band and dual pattern antenna with two radiate elements and coaxial cable as the feed is introduced in [6-8]. To properly design, develop and apply these antennas on the human body model, the associated electrical characteristics must be first determined to explore the human body effects on the antenna propagation and vice versa. Antenna performance around the human body has already been carried out by a number of researches, most of whom have used simplified rectangular cube with electrical parameters of human muscle, representing the human body. In this paper, a compact square microstrip antenna with a single microstrip feed line and a single radiating element is proposed for dual band and dual mode WLAN operation. The gain of the antenna is increased compared to [5, 9] at both frequency bands. Moreover the proposed antenna is fed with a single probe at its edge which provides more practical device in order to implant on body surfaces, in comparison with antennas

Submitted On: January 17, 2014
Accepted On: February 20, 2016

which are fed by coax cable or multi probes. The antenna is simulated, fabricated and tested. Moreover, a human body model designed in CST microwave studio is used to investigate radiation characteristics of the antenna and SAR measurement.

II. ANTENNA DESIGN

Figure 1 shows the geometry of the proposed antenna. It consist of a square patch of dimensions 28×28 mm^2 etched on a two-layer stratified substrate (70×70 mm^2) of RO4003 with εr=3.55, tanδ=0.0027 and a thickness of 2.43 mm. In order to avoid coaxial feed and thereby making the antenna conformal to the body, a strip feed line is designed. It is etched on a 70×70 mm^2 substrate of RO4003 of thickness 0.813 mm.

The feed line excites the patch using a copper post of radius 0.6 mm that extends from the feed line to the patch. The substrate supporting the patch has a height of 1.623 mm with a dimension of 70×65 mm^2. The upper and lower substrates are different in dimension to implant SMA, feeding the strip line and also to provide a better impedance matching. Table 1 summarizes the dimensions of the antenna components designed.

The antenna is about to have a microstrip patch with a single radiating element to operate at two frequency bands of 2.4-2.484 GHz and 5.15-5.815 GHz for IEEE 802.11b/g and IEEE 802.11a, respectively. The antenna is considered to operate as a relay between sensors located on the body and non-local station so it's an advantage for the antenna to be able to have tangential radiation over the body surface in the on-body mode and a boresight pattern in the off-body mode at the frequency bands of 802.11a and 802.11b/g, respectively.

A corner truncated square patch with eight embedded slots in its structure is used to set the resonant frequency for IEEE 802.11 b/g without enlarging the whole patch dimensions. By means of cutting two long slots across the diagonal slots, with a length of l2, the TM10 current path will be prolonged but still not long enough to be fixed at our lower band, consequently by using two other shorter parallel slots (l3), the resonant frequency band is decreased to 2.44 GHz as required. At this frequency band (fundamental mode), the antenna's main beam is at boresight. To generate this monopole-like radiation pattern, various antenna types have been proposed. A compact patch antenna with a vertical ground wall and a shorting wall was proposed in [9]. A planar inverted antenna using a shorting wall on a two-third muscle equivalent arm phantom was published in [10]. Inspired by the design in [9], a higher mode (TM21) microstrip patch antenna (HMMPA) was introduced in [1], [11].

In this paper, in order to have a tangential pattern over the body surface at the upper band, shorting posts are used in the antenna structure. This shorting post acts as short-circuit to the capacitance of the antenna constituted by the upper plane above the ground plane. In a first approximation, we can consider that the inductance due to the shorting post(s) is set in parallel with the antenna capacitance, and so constitutes an anti-resonating circuit which explains the presence of the parallel resonance phenomenon [9]. Two grounding (shorting) posts offset from the fed are used to force nulls in the electric field between the ground plane and the patch element, exciting the higher order resonant mode (TM_{21}), [1].

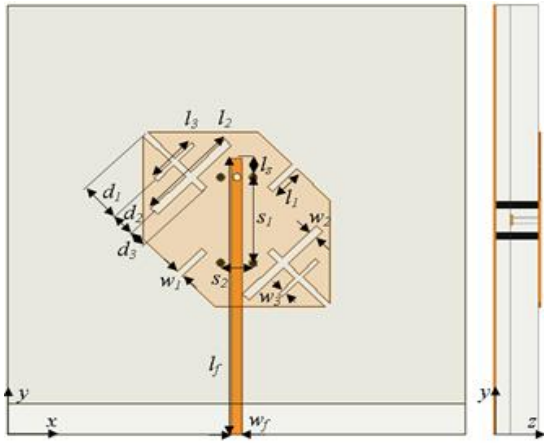

(a)

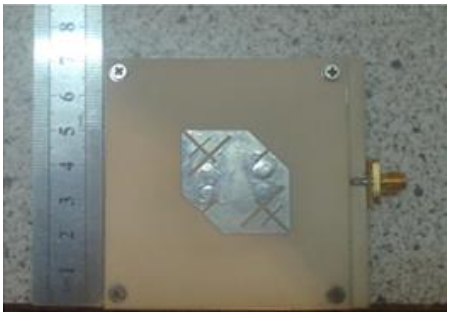

(b)

Fig. 1. (a) Configuration of the proposed antenna, and (b) the fabricated antenna.

Table 1: Design parameters

Component	Unit	Component	Unit
w_f	1.7 mm	l_2	16.8 mm
l_f	45 mm	l_3	5.84 mm
l_s	3 mm	d_1	3.3 mm
w_1	1 mm	d_2	2.54 mm
w_2	1.35 mm	d_3	2.07 mm
w_3	0.75 mm	s_1	14 mm
l_1	5.21 mm	s_2	2.5 mm

The radiation characteristics of the antenna are controlled by the dimension of the feed line, grounding posts' location and number of them, length and location

of the slots, and also by the height of the substrate and permittivity.

III. PARAMETER ANALYSIS

With the dimensions given in Table 1, the proposed antenna was simulated and tested in, first free space, then in close proximity of the human body are also investigated. We developed a human body. The human body model was developed in the CST Microwave Studio. It is an adult male of mass 100 kg, height 180 cm and chest circumference of 115 cm, including muscle, skeleton and brain with human tissue. The electrical properties were defined at the frequency band of 2-6 GHz with resolution of 100 MHz, [9]. Figure 2 shows the placement of the antennas on the model. The antenna is placed 0 mm, 2.5 mm and 10 mm apart from the chest of the model. The free space and on body simulated and measured S_{11} of the proposed antenna are illustrated in Fig. 3. In free space simulation, the antenna bandwidth is 28 MHz for the lower band and 116 MHz for the upper band while in measurement 35 MHz and 130 MHz bandwidths are achieved for lower and upper bands, respectively. Nevertheless, bandwidths of 80 MHz and 25 MHz for the upper and lower bands are achieved when the antenna is placed on the human model.

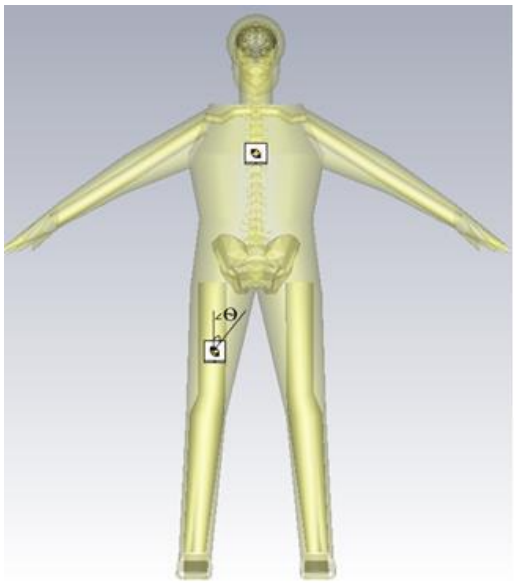

Fig. 2. The proposed antenna placed on the chest and right leg of the human body model.

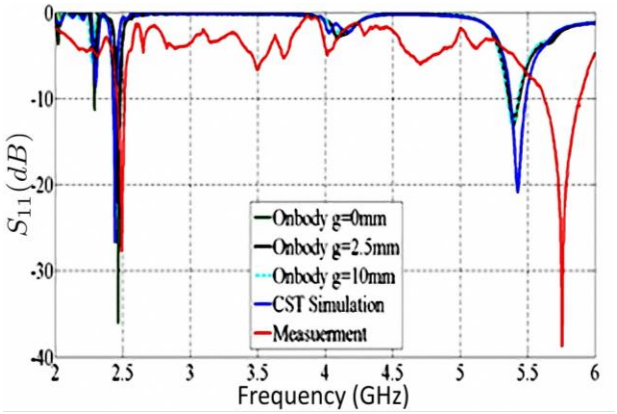

Fig. 3. Simulated, measured and on body S_{11} of the proposed antenna.

Figure 4 depicts the simulated and measured radiation patterns of the proposed antenna. The simulated results show that the maximum gain is about 7.1 dB at 2.44 GHz and 6.6 dB at 5.4 GHz. These are about 6.4 dB and 6.51 dB at 2.49 GHz and 5.56 GHz in measurement, respectively. The simulation shows 75% efficiency at 2.44 GHz and 82% at the upper band (5.4 GHz). It is observed that at the lower frequency band, the radiation pattern is directed towards the body, Figs. 4 (a, b), (it should be mentioned that the mismatch of the back-lob gains is because of measurement tolerance) and at the upper band it is tangential over the body surface, Figs. 4 (c, d). The results also show that when the antenna is placed on the human body model, the maximum gain decreases 0.2 dB at the lower band and increases to 1.35 dB at the upper band compared to the free space simulation. To investigate the antenna performance in the on-body communication mode, two antennas were placed on the chest and left leg of the human body model making an angle of Θ=0, 15, -30, -40 degrees to each other (Fig. 2). Antenna coupling (|S21| path gain) at the on body frequency (5.4 GHz) is shown in Fig. 5. As it can be noticed from Fig. 5, the best path gain is obtained as -33 dB when the antennas are placed in Θ=15.

Generally, the simulation results are in good agreement with those of measurement; though a frequency detuning is observed at the upper band. This may be explained by the manufacturing difficulties. The comparison between this work and related works can be found in Table 2.

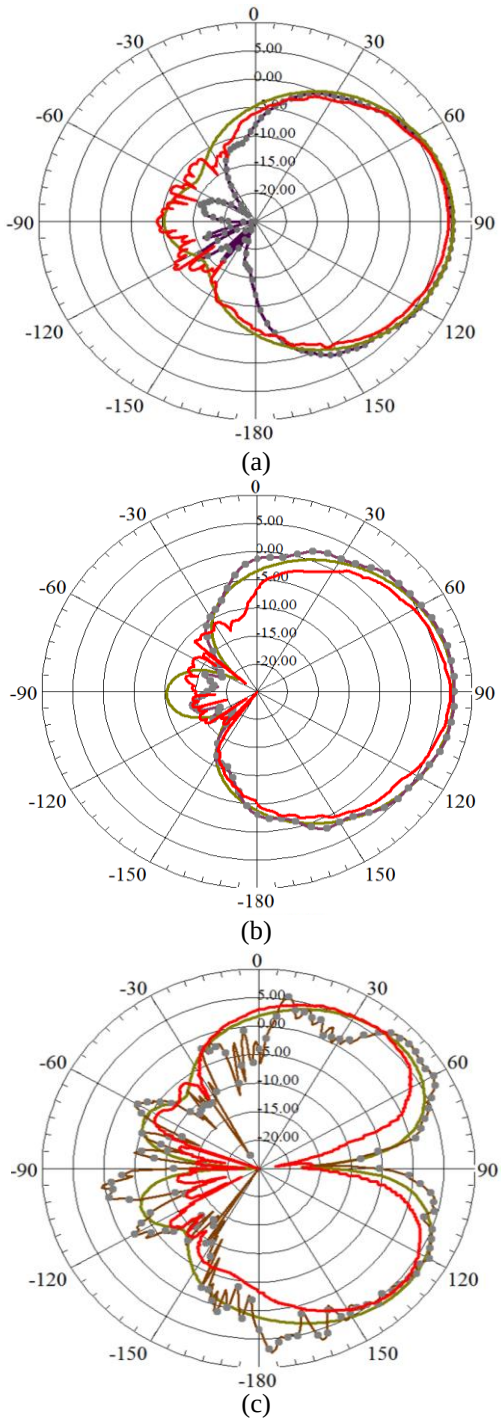

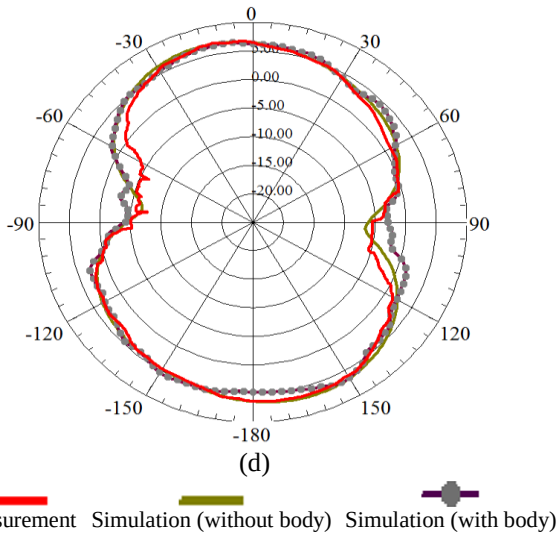

Fig. 4. Simulated and measured radiation pattern of the proposed antenna: (a) the radiation pattern in the *yz* plane, f_0=2.44 GHz; (b) the radiation pattern in the *xz* plane, f_0=2.44 GHz; (c) the radiation pattern in the *xz* plane, f_0=5.43 GHz; (d) the radiation pattern in the *xy* plane (θ=45°), f_0=5.43 GHz.

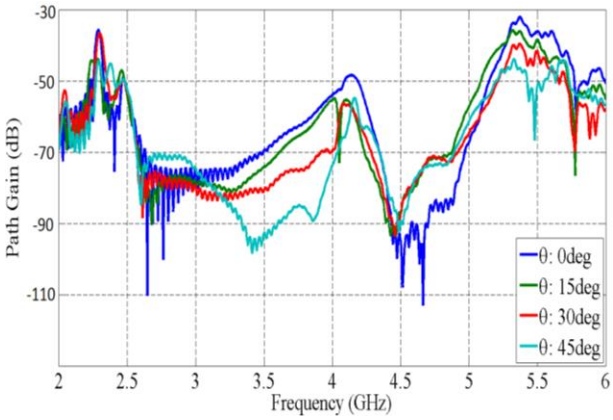

Fig. 5. S21 path gain of proposed antenna placed on the human body model for Θ=0, 15, 30, 45 degree.

Table 2: Comparison of this work with similar works

Parameter	Size LWh (mm)	Matching BW %	Gain (dBi)
Hertlee et al. [4]	50*46*3.94	3.4% @ 2.45 GHz	6.9
Tak et al. [11]	15.5*28*10.5	4.5% @ 2.45 GHz 7.2% @ 5.8 GHz	1.5 @ 2.45 GHz 1.27 @ 5.8 GHz
Conway et al. [1]	18*18*9.5 HMMPa 10 22*22*4.75 HMMPA5	6.7% HMMPA5 8.6% HMMPA10	1.2 HMMPA5 1.5 HMMPA10
Our work	28*28*2.439	3.4% @ 2.45 GHz 12% @ 5.43 GHz	7.1 @ 2.45 GHz 6.6 @ 5.43 GHz

IV. SAR MODELLING

Having investigated the electromagnetic characteristics of the proposed antenna and the effects of the human body, we now turn our focus on the rate of energy absorption as defined by the specific absorption rate (SAR). Table 3 summarizes the absorbed power, maximum SAR point and 1 gr and 10 gr averaged SAR for the proposed antenna. As it is shown in Table 3, maximum 1 gr SAR of the proposed antenna is 1.2 W/Kg which is 0.4 W/Kg less than the restriction of the USA [13].

Table 3: SAR simulation results SAR simulation results

Antenna Mode (f_0)	Off-Body (2.468 GHz)	On-Body (5.4 GHz)
Accepted power [W] (rms)	0.496953W	0.469259W
Absorbed power (tissue power absorbed)	0.0747296W (0.033708W)	0.112307W (0.0718987)
Total SAR (rms) [W/kg]	0.000226889 W/Kg	0.000483952 W/Kg
Max. point SAR (rms) [W/kg]	9.20803 W/Kg	20.5825 W/Kg
Max. SAR (rms, 1 g) [W/Kg]	0.507495 W/Kg	1.21299 W/Kg U.S & AU limit: 1.6 W/Kg
Max. SAR (rms, 10 g) [W/Kg]	0.266098 W/Kg	0.417621 W/Kg Europe limit: 2 W/Kg

V. CONCLUSION

An efficient dual band and dual pattern square patch antenna with strip line feed is proposed for on-body and off-body communication modes. The proposed antenna presents much improved gain with one truncated square radiating element than the previous works of the compact dual band and dual mode antennas. Simulated and measured performances of the antenna in free space were shown and the effects of presence a human around the antenna on the radiation characteristics were also investigated by modeling a human body. The antenna showed a horizontal pattern over the body surface at 5.4 GHz for the on-body mode with 7.2 dB gain and a directive radiation pattern at 2.468 GHz for the off-body mode with 6 dB gain at the presence of the human model. The results show that this antenna does not experience significant frequency detuning from the free space resonance at both frequency bands when simulated on the human body model due to shielding provided by the ground plane.

Simulations indicate that localized SAR values of 1 gr are 0.5 W/Kg for lower band and 1.21 W/Kg for the upper band being compatible with the basic restrictions for the general public.

ACKNOWLEDGMENT

The authors wish to thank ITRC (Iran Tele-communication Research Canter) for supporting this work.

REFERENCES

[1] G. A. Conway and W. G. Scanlon, "Antennas for over-body-surface communication at 2.45 GHz," in *Antennas and Propagation, IEEE Transactions on*, vol. 57, no. 4, pp. 844-855, Apr. 2009.

[2] A. R. Chandran, G. A. Conway, and W. G. Scanlon, "Compact low-profile patch antenna for medical body area networks at 868 MHz," in *Antennas and Propagation Society International Symposium, 2008. AP-S 2008. IEEE*, pp. 1-4, 5-11 July 2008.

[3] G. A. Conway, W. G. Scanlon, and D. Linton, "Low-profile microstrip patch antenna for over-body surface communication at 2.45 GHz," in *Vehicular Technology Conference, 2007. VTC2007-Spring. IEEE 65th*, pp. 392-396, 22-25 Apr. 2007.

[4] C. Hertleer, H. Rogier, L. Vallozzi, and L. Van Langenhove, "A textile antenna for off-body communication integrated into protective clothing for firefighters," in *Antennas and Propagation, IEEE Transactions on*, vol. 57, no. 4, pp. 919-925, Apr. 2009.

[5] D. Ma and W. X. Zhang, "A dual-band dual-polarized antenna for body area network," in *Antennas and Propagation (EuCAP), 2010 Proceedings of the Fourth European Conference on*, pp. 1-5, 12-16 Apr. 2010.

[6] M. M. Khan, Q. H. Abbasi, A. Alomainy, C. Parini, Y. Hao, "Dual band and dual mode antenna for power efficient body-centric wireless communications," in *Antennas and Propagation (APSURSI), 2011 IEEE International Symposium on*, pp. 396-399, 3-8 July 2011.

[7] S. Rezvani, Z. Atlasbaf, and K. Forooraghi, "A new compact reconfigurable patch antenna for polarization and frequency diversity," *Electromagnetics*, vol. 32, pp. 287-293, 2012.

[8] S. Rezvani, Z. Atlasbaf, and K. Forooraghi, "A movel miniaturized reconfigurable slotted microstrip patch antenna with DGS," *Journal of Electromagnetics*, vol. 31, pp. 349-354, 2011.

[9] C. Delaveaud, P. Leveque, and B. Jecko, "New kind of microstrip antenna: the monopolar wire-patch antenna," in *Electronics Letters*, vol. 30, no. 1, pp. 1-2, 6 Jan. 1994.

[10] L. Chia-Hsien, K. Saito, M. Takahashi, and K. Ito, "A compact planar inverted-F antenna for 2.45 GHz on-body communications," in *Antennas and*

Propagation, IEEE Transactions on, vol. 60, no. 9, pp. 4422-4426, Sept. 2012.

[11] J. Choi, D.-G. Kang, J. Tak, and K. Kwon, "Dual-mode antennas for WBAN applications," in *Electromagnetics (iWEM), 2014 IEEE International Workshop on*, pp. 264-264, 4-6 Aug. 2014.

[12] C. A. Balanis, *Advanced Engineering Electromagnetic*, Canada: John Wiley & Sons, ch. 8, 1989.

[13] "Specific Absorption Rate (SAR)," Internet: www.fcc.gov/encyclopedia/specific-absorption-rate-sar-cellular-telephones, Oct. 2013.

Seiran Khaledian received the B.S. degree in Electrical Engineering from Khaje Nasir University of Technology and M.S degree in Communication Engineering from Tarbiat Modares University, Tehran, Iran, respectively. She is currently a Ph.D. student at University of Illinois at Chicago (UIC). Her research interests include the design of antennas, Microwave and RF circuits.

Zahra Atlasbaf received the B.S. degree in Electrical Engineering from the University of Tehran, Iran, in 1993, and the and Ph.D. degrees in Electrical Engineering from the University of Tarbiat Modares, Tehran, Iran, in 1996 and 2002, respectively. She currently is an Associate Professor with the Faculty of Electrical and Computer Engineering, Tarbiat Modares University. Her research interests include numerical methods in electromagnetics, theory and applications of metamaterials, and microwave and antenna design.

A Novel Coupling Structure for Changing the Coupling Nature Between $TE_{01\delta}$-mode Dielectric Resonator and Combline Resonator

Bin Yu, Bao-Fu Jia, and Zhao-Jun Zhu

School of Physical Electronics
University of Electronic Science and Technology of China, Cheng Du, Si chuan, China
yuzhoumanyouzhe@yeah.net, bfjia@uestc.edu.cn, uestc98@163.com

Abstract ─ In this paper, a novel coupling structure is presented, which could easily change the coupling nature between combline resonator (CR) and dielectric resonator (DR). This coupling structure is based on electric field orientation of DR operating in $TE_{01\delta}$-mode, through altering the direction of copper sheet in the DR, the excited orientation of electric field would be changed along with the coupling nature between two resonators. To prove this method, two filters using cascaded triplet (CT) coupling relation are designed, fabricated and measured, showing the controllable coupling nature between CR and DR. Measured results confirmed the predicted performance.

Index Terms ─ Bandpass filter, combline resonator, coupling nature, dielectric resonator.

I. INTRODUCTION

With the rapid development of wireless communication, the frequency spectrum becomes more and more crowed. To utilize the frequency spectrum more efficiently, the bandpass filter in the wireless communication system should have steeper selectivity. Increasing the filter order is a conventional way to improve the selectivity of a bandpass filter, but deteriorate the insertion loss. A better way is introducing transmission zeros by cross-coupling. But, it will make a negative impact on the passband edge performance. Therefore, high *Q* resonator was employed to improve the passband performance in cross-coupling filters. In 2006, a novel approach to design bandpass filter based on resonators with non-uniform quality factors (*Q*) was firstly reported [1]. More flat passband can be achieved using this method. Then, this method was verified in [2] again, high *Q* and low *Q* path were connected in parallel to achieve good improvement of passband performance. In [3], a six-order series filter with non-uniform *Q* distribution was proposed to show how to select the most critical resonators which should be set high *Q*-factor in the series circuit. Compared with other filters consisting of resonators with uniform *Q*-factor, the application of the non-uniform *Q* with first and last resonators with lower *Q*-factor value than the rest of the cavities revealed that there is impact only in the absolute losses.

In practical engineering applications, due to the high *Q* value of dielectric resonator, the DR filters have good in-band performance. Many researches on DRs have been done so far [4-10]. However, spurious bands of DR filters are too closed to be accepted in practical applications. CR filters have good design flexibility, however, the employ of the cross-coupling will sacrifice the passband edge performance [11]. Therefore, in order to achieve steep selectivity and good in-band performance without sacrificing the dimension, CR and DR are both used to design a bandpass filter. Through circuit simulation, the most critical resonator in determining the passband edge performance could be found easily, which means in real model, this resonator should be high Q-factor so that the largest improvement of the passband edge insertion loss can be achieved. And a DR is always used here due to its high-Q characteristic [12]. In this way, the filter could have better out-band performance than dielectric filters and better passband edge performance than combline filters.

In [13], due to the coupling between the feeding probe and second DR cavity, the transmission zero was obtained, and rotating the angle of the feeding position, the transmission zero was shifted to the lower or upper stopband. In the previous designs, the coupling between CR and DR is achieved through the coupling channel which only coupling strength can be adjusted. Therefore, in this letter, a novel coupling structure is proposed to change the coupling nature between $TE_{01\delta}$-mode DR and CR. When the EM-field is coupling from CR to DR, through changing the rotating direction of the coupling structure in DR cavity, the coupling nature between two resonators would be changed. This is the first time that the coupling between CR and DR has been discussed.

II. COUPLING BETWEEN DR AND CR

Figure 1 shows the EM field distributions of a $TE_{01\delta}$-mode DR cavity and a CR cavity. The $TE_{01\delta}$-mode

Submitted On: January 2, 2016
Accepted On: March 21, 2016

DR cavity has a loop electric field distribution and the magnetic field distributes alone the axis of the DR disk and at a sufficient distance outside the disk. The CR cavity has a radial electric field distribution outside the metal cylinder which surrounded by the magnetic field. Figure 2 demonstrates the proposed coupling structure. The coupling structure contains three parts, two copper cylinders and one copper sheet. The copper sheet is grounded at both ends (CSGE) by the copper cylinders, which could help fasten the copper sheet and make it stay at the strong EM field area.

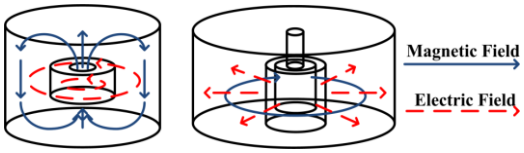

Fig. 1. EM field distributions of a $TE_{01\delta}$-mode DR cavity (left side) and a CR cavity (right side).

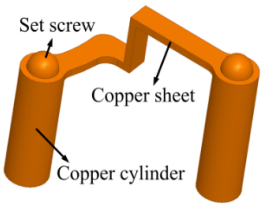

Fig. 2. The proposed coupling structure.

Figure 3 and Fig. 4 demonstrate the proposed model of the CT-based bandpass filter. Their input and output structures are constructed by CR while the main difference is the rotating direction of the coupling structure in cavity II. When a filter is working at its center frequency, according to the electromagnetic field theory shown below:

$$\nabla \times \vec{H} = \frac{\partial \vec{D}}{\partial t} + \vec{J} = \mu_0 \frac{\partial \vec{E}}{\partial t} + \vec{J}.$$

The coupling current and the electric field are in the same direction. As shown in Fig. 3 and Fig. 4, when electromagnetic field is coupling from cavity I (CR) to cavity II (DR), the radial electric field of the CR will lead to the coupling current flowing from cavity I to cavity II through the CSGE. Then the direction of the coupling current determines the clockwise rotating direction of the $TE_{01\delta}$-mode electric field in DR. Comparing Fig. 3 (b) with Fig. 4 (b), due to the different rotating direction of the CSGE between cavity II and cavity III, the induced coupling current had different flow directions. Therefore, the phase of the coupling current is changed by the type of the rotating direction, which results in different coupling nature between CR and DR.

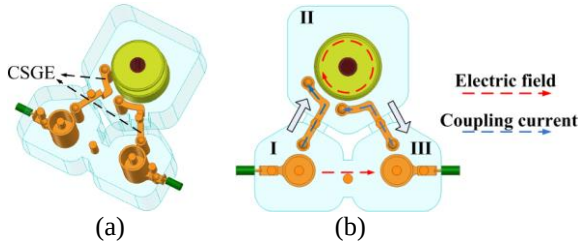

Fig. 3. The proposed CT-based bandpass filter with the same rotating direction of two CSGEs between DR and two CRs: (a) 3-D view and (b) top view.

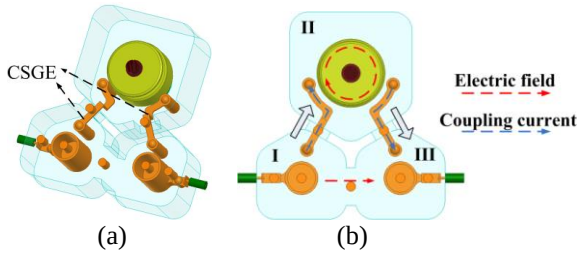

Fig. 4. The proposed CT-based bandpass filter with the opposite rotating direction of two CSGEs between DR and two CRs: (a) 3-D view and (b) top view.

The coupling coefficient between CR and DR is calculated by the Y-matrix method [14]. The EM-field is changed through changing the insertion depth of the tuning screws alone with the self- and mutual-coupling coefficient, which results in the controllable filter function. Figure 5 shows how to set the lumped port in CR and DR cavity when calculating the coupling coefficient between them. The port impedance should be studied before calculating the coupling strength. Figure 6 shows the computed coupling coefficients between CR and DR with different rotating angle θ of the CSGE in the DR cavity. The coupling coefficient increases along with the rotating angle θ of the CSGE in the DR cavity.

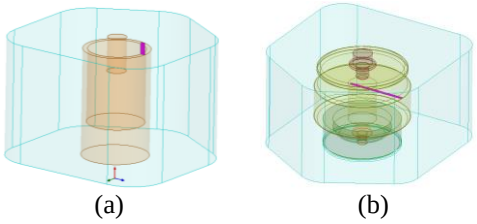

Fig. 5. The way to set the lumped port in the CR and DR cavity when using the Y-matrix method: (a) CR cavity and (b) DR cavity.

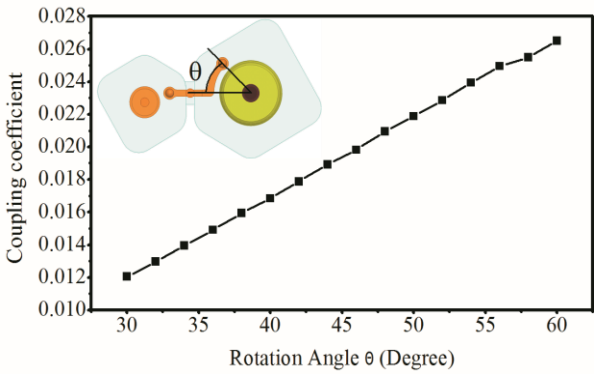

Fig. 6. Computed coupling coefficients between CR and DR when the CSGE rotating clockwise in DR from the top view.

III. FILTERS DESIGN

To verify the approach above, two CT-based bandpass filters [15] contain two CRs and one DR have been simulated, fabricated and measured. Two CRs were employed to build the input and output (I/O) structure of the two CT-based bandpass filter. The DR used in this design has a dielectric constant of 46. The details of the single DR cavity structure are shown in Fig. 7, where *DIE_D*=28.6 mm, *H1_D*=8.6 mm, *DIE_H*=2 mm, *DR_H*=11.5 mm, *DR_H1*=8 mm, *DR_D*=23.5 mm, *H_D*=17.5 mm. As shown in Fig. 7 (b), the cavity is pentagonal from the top view. The distance from the edge to the center point of the cavity is 26 mm (*CAV_DIS*), and the height is 30 mm. Besides, the details of the single CR cavity structure are shown in Fig. 8, where *CAV_a*=38 mm, *CAV_h*=25 mm, *COM_D1*=14 mm, *COM_D2*=12 mm, *COM_hin*=16 mm, *COM_hout*=22.5 mm. The cavity is also pentagonal from the top view. The distance from the edge to the center point of the cavity is 19 mm (*CAV_DIS*). The type of the tuning screw is M4.

The coaxial connectors were associated with the first and last CR through two sheet metals. Two tuning screws were introduced to control the external quality factor Q_{ex} after fabrication. Figure 9 shows the computed external quality factor Q_{ex} of different screw insertion depths and various heights of the linked metal block.

Both of the proposed Chebyshev three-pole filters have a passband ripple of 0.0694 dB, a center frequency at 1.772 GHz and a bandwidth of 45 MHz. One of them has a transmission zero located at 1.68 GHz, thus the inter-resonator coupling value K_{12}=-K_{23}=0.024, K_{13}=0.0057, and external quality factor Q_{ex}=37.29 were required [16]. The other one had a transmission zero located at 1.84 GHz, which resulted in the inter-resonator coupling value K_{12}=K_{23}=0.023, K_{13}=0.0089, and the external quality factor Q_{ex}=37.28.

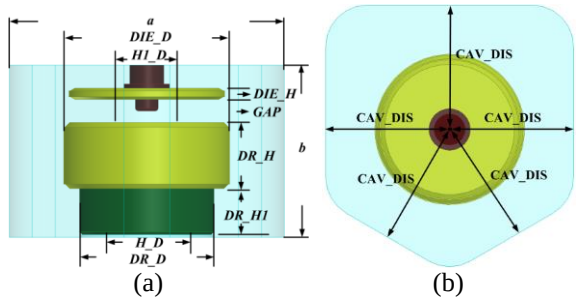

Fig. 7. Single DR cavity with tuning dielectric disk: (a) side view and (b) top view.

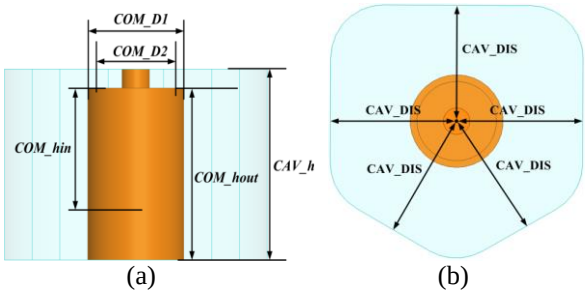

Fig. 8. Single CR cavity with tuning dielectric disk: (a) side view and (b) top view.

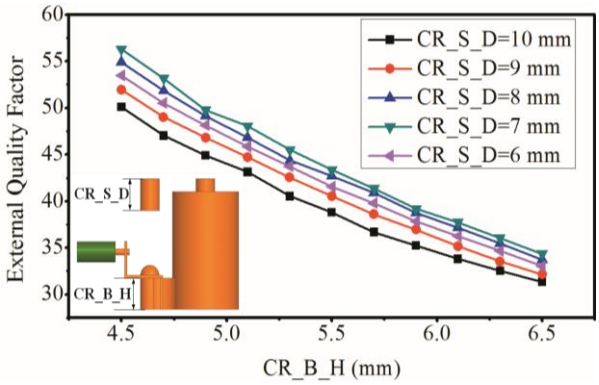

Fig. 9. Q_{ex} of different screw insertion depths as a function of the heights of the linked metal block.

The photographs of two fabricated three-pole bandpass filters are given in Fig. 10. The housings of two filters are constructed from aluminum. Figure 11 shows the E-M simulated and measured result of the proposed CT-based bandpass filters. In Fig. 11 (a), the two CSGEs in DR rotate in the same direction, which means that the coupling natures between two CRs and DR are the same. Therefore, the transmission zero (TZ1) appears at the upper stopband. However, in Fig. 11 (b), the rotating directions of two CSGEs in the DR are different. It means that the coupling natures between

DR and two CRs are different, which results in that the transmission zero (TZ1) appears at the lower stopband. Moreover, as shown in Fig. 11, the extra transmission zero appears at the upper stopband (TZ2) are caused by the CSGEs. The reason is that the CSGE serves as not only a coupling structure but also a half-wavelength resonator with two shorted ends.

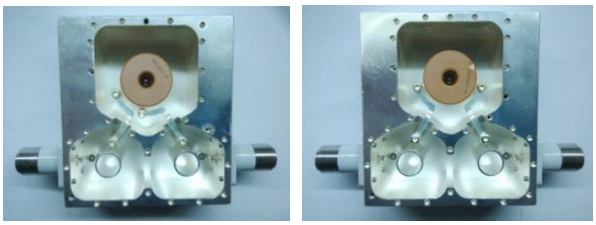

(a) (b)

Fig. 10. Photograph of two fabricated three-pole bandpass filter: (a) filter 1 and (b) filter 2.

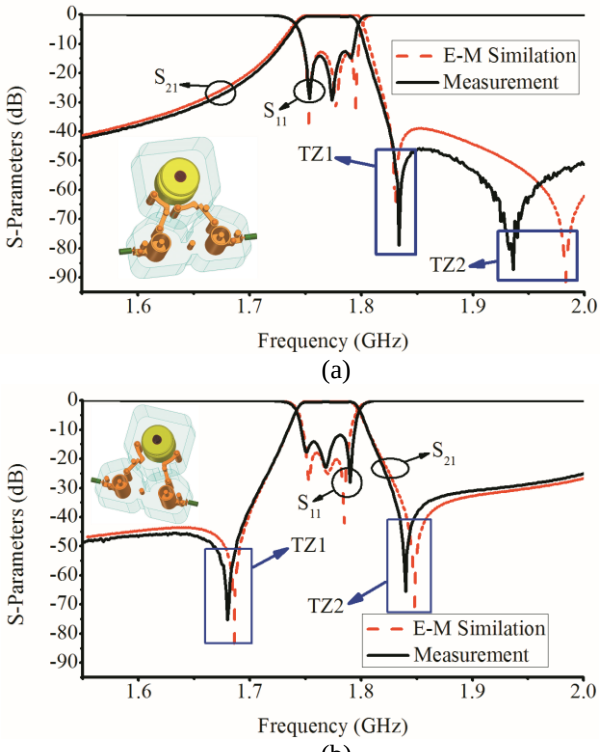

Fig. 11. E-M Simulated and measured result of the proposed CT-based bandpass filter: (a) response of fabricated filter shown in Fig. 10 (a), and (b) response of fabricated filter shown in Fig. 10 (b).

IV. CONCLUSION

A novel structure to change the coupling nature between $TE_{01\delta}$-mode DR and CR was proposed in this letter. Different coupling nature between DR and CR has been achieved through altering the rotating direction of the coupling structure in $TE_{01\delta}$-mode DR. The coupling strength was enhanced due to the employ of the copper cylinders located at both sides of the copper sheet. Tuning screws were introduced to achieve the adjustability of the coupling coefficients. In order to verify the proposed method, two CT-based bandpass filters contain CR and DR were designed, fabricated and measured, respectively. The simulated and measured results prove the effectiveness of the proposed method.

ACKNOWLEDGMENT

This work is supported by National Natural Science Foundation of China (Grant 61101042) and The Fundamental Research Funds for the Central Universities (Grant ZYGX2009J043).

REFERENCES

[1] A. C. Guyette, I. C. Hunter, and R. D. Pollard, "The design of microwave bandpass filters using resonators with non-uniform *Q*," *IEEE Trans. Micro. Theory Techn.*, vol. 54, no. 11, pp. 3914-3922, November 2006.

[2] M. Meng and I. C. Hunter, "The design of parallel connected filter networks with non-uniform *Q* resonators," *IEEE Trans. Micro. Theory Techn.*, vol. 61, no. 1, pp. 372-381, January 2013.

[3] P. M. Iglesias and I. C. Hunter, "Non-uniform *Q* factor distribution in microwave filters," *Microwave Integrated Circuit Conference (EUMIC)*, Amsterdam, pp. 802-805, October 2012.

[4] S. B. Cohn, "Microwave bandpass filters containing high-*Q* dielectric resonators," *IEEE Trans. Micro. Theory Techn.*, vol. 16, no. 4, pp. 218-227, April 1968.

[5] J. K. Plourde and C.-L. Ren, "Application of dielectric resonators in microwave component," *IEEE Trans. Micro. Theory Techn.*, vol. 29, no. 8, pp. 754-769, August 1981.

[6] C. Wang, K. A. Zaki, A. E. Atia, et al., "Dielectric combline resonators and filters," *IEEE Trans. Micro. Theory Techn.*, vol. 46, no. 12, pp. 2501-250, December 1998.

[7] J.-F. Liang and W. D. Blair, "High-*Q* TE_{01} mode DR filters for PCS wireless base stations," *IEEE Trans. Micro. Theory Techn.*, vol. 46, no. 12, pp. 2493-2500, December 1998.

[8] R. Zhang and R. R. Mansour, "Low-cost dielectric-resonator filters with improved spurious performance," *IEEE Trans. Micro. Theory Techn.*, vol. 55, no. 10, pp. 2168-2175, October 2007.

[9] R. R. Mansour, "High *Q* tunable dielectric resonator filters," *IEEE Microwave Magazine*, vol. 10, no. 6, pp. 84-98, October 2009.

[10] X. Wang and K.-L. Wu, "A TM_{01} mode monoblock dielectric filter," *IEEE Trans. Micro. Theory Techn.*, vol. 62, no. 2, pp. 275-281, February 2014.

[11] H.-W. Yao and A. E. Atia, "Temperature characteristics of combline resonators and filters," *IEEE MTT-S Int. Microwave Symp. Dig.*, Phoenix, USA, vol. 1, pp. 1475-1478, May 2001.
[12] C. Wang and K. A. Zaki, "Dielectric resonators and filters," *IEEE Microwave Magazine*, vol. 8, no. 5, pp. 115-127, October 2007.
[13] Q.-X. Chu, X. Quyang, H. Wang, et al., "$TE_{01\delta}$-mode dielectric-resonator filters with controllable transmission zeros," *IEEE Trans. Micro. Theory Techn.*, vol. 61, no. 3, pp. 1086-1094, March 2013.
[14] S. Otto, A. Lauer, J. Kassner, et al., "Full wave coupled resonator filter optimization using a multi-port admittance-matrix," *Asia-Pacific Microw. Conf.*, Yokohama, Japan, pp. 777-780, December 2006.
[15] N. Yildirim, M. Karaaslan, Y. Sen, et al., "Cascaded triplet filter design using cascade synthesis approach," *IEEE MTT-S Int. Microwave Symp. Dig.*, Anaheim, CA, USA, pp. 903-906, June 1999.
[16] R. J. Cameron, "General coupling matrix synthesis methods for Chebychev filtering funtions," *IEEE Trans. Microw. Theory Tech.*, vol. 47, no. 4, pp. 433-442, April 1999.

Bin Yu was born in Fujian, China, on September 12, 1988. He received the B.S. degree in Electronic Information Science and Technology from the University of Electronic Science and Technology of China, Chengdu, China, in 2011, and is working toward the Ph.D. degree in Radio Physics at the University of Electronic Science and Technology of China, Chengdu, China. He was currently involved with the research of various microwave filters and equalizers.

Bao-Fu Jia was born in Hebei Province, China, in 1952. He received the B.S. degree and M.D. degree in Microwave Electronics from the University of Electronic Science and Technology of China, Chengdu, in 1977 and 1982 respectively, and the Ph.D. degree in Electromagnetic Field and Microwave Technology from the University of Electronic Science and Technology of China, Chengdu, in 1989. Since 2004, he has been a Professor with the University of Electronic Science and Technology of China, Chengdu. His research interests include the simulation technology of microwave circuits and system.

Zhao-Jun Zhu was born in Sichuan, China, on November 8, 1978. He received the B.S. degree in Physical Electronics from the University of Electronic Science and Technology of China, Chengdu, in 2002, and the Ph.D. degree in Physical Electronics from the University of Electronic Science and Technology of China, Chengdu, in 2007. Since 2012, he has been an Associate Professor with the University of Electronic Science and Technology of China, Chengdu. His research interests include the analysis and design of microwave and millimeter-wave circuits.

The Substrate Integrated Waveguide T-junction Power Divider with Arbitrary Power Dividing Ratio

Asrin Piroutiniya and Pejman Mohammadi

Department of Electrical Engineering
Urmia Branch, Islamic Azad University, Urmia, Iran
tear_ap@yahoo.com, p.mohammadi@iaurmia.ac.ir

Abstract ─ An X-band H-plane wideband substrate-integrated waveguide (SIW) T-junction power divider with unequal-power-division ratio is presented. Several inductive posts are used to have arbitrary power dividing ratio and also to control the phase difference. The position and diameter of these posts tune the power-split ratio and the phase difference in whole bandwidth. Parametric studies have been done to choose the best positions and diameters to get better results. Two different prototypes have been verified the proposed technique. They are designed and fabricated at a center frequency of 11 GHz. The measured input impedance bandwidths are 54% for Δ_{out} =3 dB and 45% for Δ_{out} =6 dB respectively.

Index Terms ─ Arbitrary power, dividing ratio, power divider, SIW.

I. INTRODUCTION

Rectangular waveguide components are one of the essential parts in microwave and millimeter wave systems. Although metallic rectangular waveguides have been utilized wildly, they are less practical, due to their weight, bulky shape and size and difficult integration with planar circuits. SIW is an alternative technology that overcomes all mentioned problems [1-5]. SIW technology is common because of its easy integration, high quality factor, small dimension, planar structure and easy fabrication. A lot of applications using substrate-integrated-waveguide technology have been reported [1-8], [12].

Power dividers are one of the most fundamental and crucial components of microwave circuits and networks. They are one of the important parts of feeding networks and circuits. Arbitrary power dividing ratio over a wide bandwidth is required for feeding systems which are used in various applications such as phased-array antennas and SIW slot array antennas. In order to reach this goal, some studies have been carried out on investigating of H-Plane T-junction power dividers and lots of articles have been reported [1-7], [9]. In [10], multiple posts are used to demonstrate the flexibility and usefulness of designing SIW power divider. Three inductive posts resulted in a good matching at input port and output ports and also equal power division ratio at two output ports. In [11], unequal power dividing ratio over a broadband is provided by corner structure and three inductive posts. Adjusting the position and diameter of the inductive posts gives an arbitrary power-split ratio. In this article, a novel design of H-plane broadband substrate-integrated waveguide (SIW) T-junction power divider with unequal-power-division is proposed. By using multiple posts technique, the power-split ratio is tuned and the phase difference is controlled in whole bandwidth. The position and diameter of multiple posts adjust the output power-division ratio (Δ_{out}) and phase difference.

II. DESIGN PROCEDURE

A typical structure of T-junction SIW power divider which covers the X-band frequency range (8-12 GHz) is shown in Fig. 1. T-junction SIW power divider consists of three SIW transmission lines and three SIW to microstrip line transitions and an inductive post. In order to have impedance and mode matching transition from SIW to 50 Ω microstrip line is required.

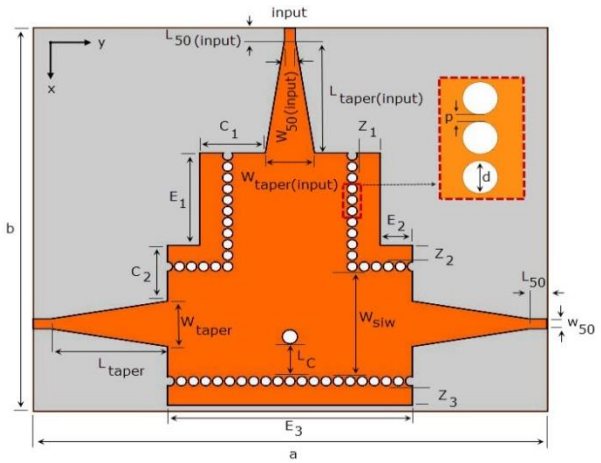

Fig. 1. Geometry of equal output SIW power divider.

Submitted On: November 9, 2015
Accepted On: March 18, 2016

The mode of microstrip line is quasi-TEM and the mode of SIW is TE_{10}, the transition part matches these two different modes. Thus, the transition is an essential part of the project and plays an important role in designing. The design parameters of the equal power divider which are optimized are given in Table 1. The input width of the microstrip line is designed by considering its impedance equal to 50 Ω. The dimension of the SIW parts are calculated based on the equivalent waveguide circuit [3] and the frequency of operation and cut off frequency. Then matching the SIW to microstrip line is defined W_{taper}. All of these parameters have been optimized by HFSS.

Table 1: The parameters of equal power divider

Parameter	Value	Parameter	Value
W_{50}	1.1 mm	$W_{50(input)}$	1.1 mm
L_{50}	2.61 mm	$L_{50(input)}$	1.38 mm
W_{taper}	4.56 mm	$L_{taper\ (input)}$	12.11 mm
L_{taper}	10.78 mm	$W_{taper\ (input)}$	5.2 mm
W_{SIW}	11.4 mm	L_c	3.75 mm
d	1 mm	P	0.2 mm
C_1	6.4 mm	a	51.2 mm
C_2	6.2 mm	b	41.5 mm
E_1	10 mm	Z_1	2.4 mm
E_2	3.2 mm	Z_2	1.8 mm
E_3	24.4 mm	Z3	2.14 mm

The inductive post reduces reflection in input port and optimizes the S_{11} in a wide frequency band. The important and decisive parameters of this via hole are the diameter and the location. The post is situated at the center of this power divider. The equivalent circuit of inductive post is a parallel susceptance. Altering the diameter and the place of this post resulted in adjusting the reflecting signals, the power division ratio and the phase difference.

The proposed unequal SIW power divider is illustrated in Fig. 2. According to Fig. 2, three inductive posts are used to obtain a different power division ratio at output ports.

As mentioned in [10], placing posts 1 and 2 at the end of input arm in symmetrical way lead to having equal outputs and improving the amount of coupling between the input port and the output ports which reduce S_{11}. So changing the position of one of these posts leads to unequal power-split ratio because in this way most of the power goes to output 1 and the rest goes to the other port. In fact, these posts affect current which has direct relation with H-field, which is shown in Fig. 2 (b). The distance between two posts and the radius of posts are helped to have adjustable power-split ratio. In fact, these posts make a bend which lead the most of power to output 1. In the printed circuit board technology the posts are realized with metallic via. The dimension and location of these two posts, that are located in input arm, specify the various levels of outputs. Post 3, which is situated in output 1, optimize S_{11} and affects the reflection coefficient. In addition, by changing the position of this post, phase difference is tunable.

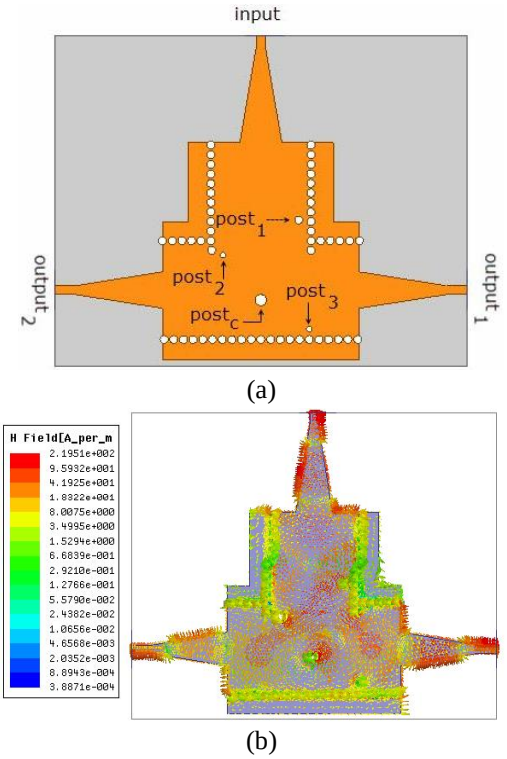

Fig. 2. (a) The SIW power divider with Δ_{out} = 3dB, and (b) the H-field of proposed structure.

As mentioned, the position and diameter of multiple posts adjust the outputs power-division ratio and phase difference. In the following, the effects of changing the position (x, y) and the diameter of posts on return loss have been investigated. As the Fig. 3 shows, 0.5 mm changes in placement of post 1 just affects S_{11} and does not have much effect on Δ_{out}. So x=23.2 mm is chosen in order to have better bandwidth and S11.

Figure 4 depicts that 0.5 mm changes in the y position of post 1 has a great effect on return loss on whole frequency band especially from 8 GHz to 9.5 GHz. Preferred y position is y=30.3 mm, because deeper return loss and wider bandwidth are achieved in this position. Second important parameter to design unequal power divider is the diameter of the inductive posts. Figure 5 demonstrates that the diameter of post 1 change S_{11} and does not affect the outputs.

Based on Fig. 6, the position of inductive post 2 does not have the same result of Δ_{out} in all frequencies. According to Fig. 7, the y position of post 2 play an important role in setting the Δ_{out} and having an arbitrary

power division ratio. In addition, it has a great impact on return loss. Choosing the right position is completely crucial. It can be understood from Fig. 8 that, the diameter of post 2, which modify S-parameters, does not have steady effect on whole frequency band. It mostly shows its influence from 8.5 GHz to 9.5 GHz.

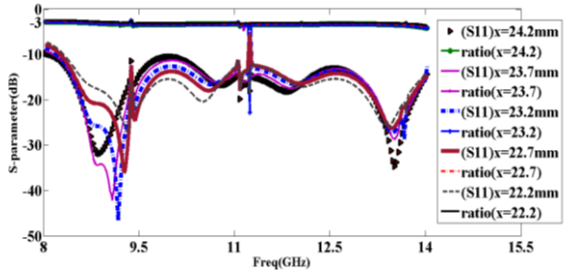

Fig. 3. The effect of changing the x (position) of post 1.

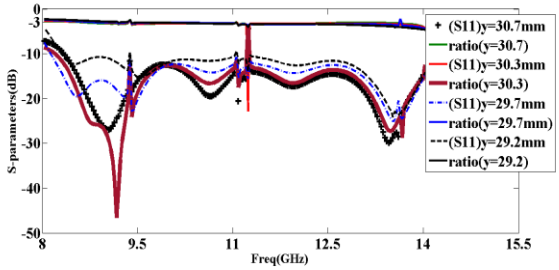

Fig. 4. The effect of changing the y (position) of post 1.

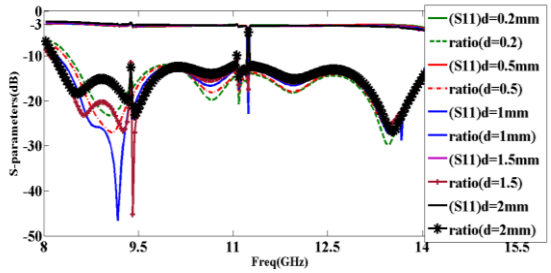

Fig. 5. The effect of changing the d (diameter) of post 1.

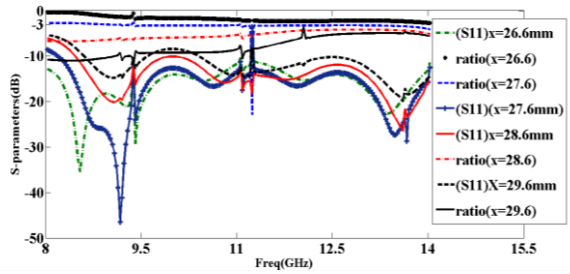

Fig. 6. The effect of changing x (position) of post 2.

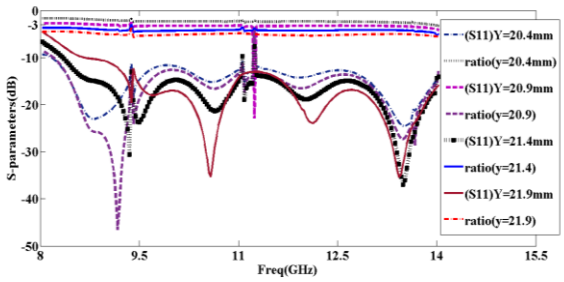

Fig. 7. The effect of changing the y (position) of post 2.

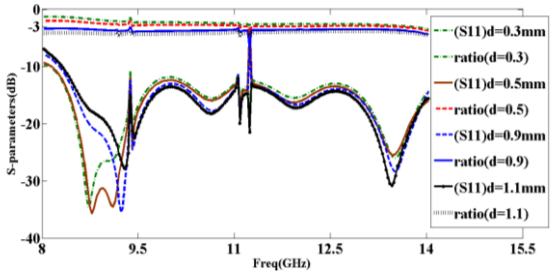

Fig. 8. The effect of changing the d (diameter) of post 2.

Figures 9, 10 and 11 indicate that changing the x position and diameter of post C affect return loss and do not change the power division ratio so much. On the other hand, y position has a challenging effect on Δ_{out}, however the effect is not stable over the whole bandwidth. It has been illustrated in Figs. 12 and 13 that the x position of post 3 is more crucial than the y position and moving the post in the x direction lead to considerable changes in return loss and power division ratio specially from 8 GHz to 10 GHz, which is not steady in whole bandwidth. Little change from 8 GHz to 14 GHz is resulted from altering the y position. The result of modifying the diameter of post 3 is shown in Fig. 14, which indicates that in comparison with the changing the x and y position, it does not affect return loss and Δ_{out} very much.

Post 1 affects the return loss and bandwidth. The best result of the bandwidth depends on choosing the right y position. Although post 1 affects S_{11}, it does not change the Δ_{out}. Any change in the position or the radius of post 2 affects bandwidth, S_{11} and also power-split ratio. The important factor is the y position of this post which leads to steady change of Δ_{out}. The x position of post 3 is really crucial. Altering it results in different S_{11}, bandwidth and unsteady Δ_{out}. Also, by changing the x position of this post the phase difference can be tuned. Post C mostly affects bandwidth and return loss. Choosing the best y position for this post is really important. Finally, it can be seen that post 2 is more effective than post 1 and is the main factor to determine

the power division ratio. The most effective parameter is the diameter of post 2 which has a relatively steady change in whole bandwidth. Also, moving post C and post 3 toward y axial lead to significant change. So the position and diameter of these posts are the determinant factors of designing the unequal power dividers.

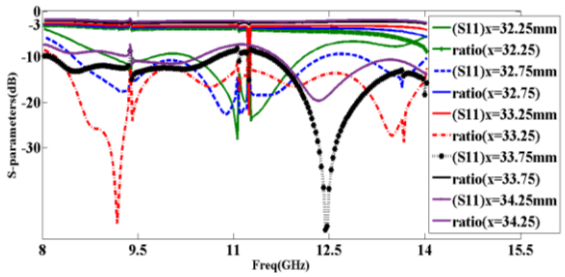

Fig. 9. The effect of changing x (position) of post C.

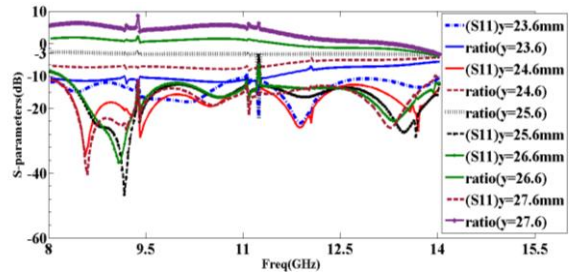

Fig. 10. The effect of changing the y (position) of post C.

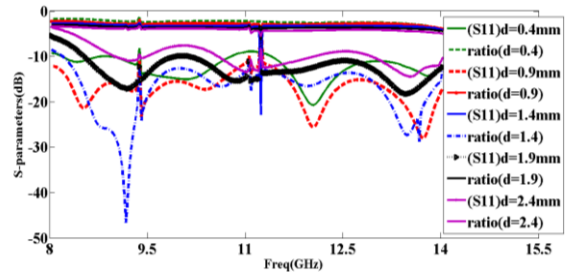

Fig. 11. The effect of changing the d (diameter) of post C.

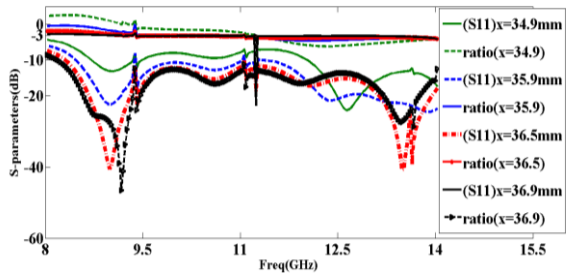

Fig. 12. The effect of changing x (position) of post 3.

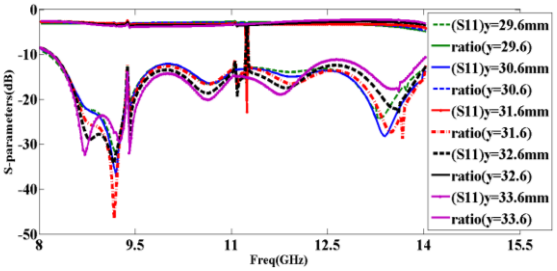

Fig. 13. The effect of changing the y (position) of post 3.

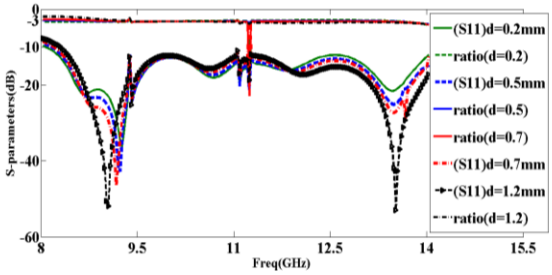

Fig. 14. The effect of changing the d (diameter) of post 3.

The two examples of power dividers with unequal outputs and different power dividing ratio were simulated by Ansoft HFSS. Two prototypes are fabricated on Rog4003 substrate of thickness 0.508 mm and tanδ=0.0027 and dielectric constant is 3.55. Fabricated structures are shown in Fig. 15. The first structure which is designed, has Δ_{out} =3 dB and the Δ_{out} of the second one is 6 dB. The positions of the inductive posts are given in Tables 2 and 3. The simulation results of the presented structures are verified by Network Analyzer and there is a good agreement between simulation results and measured results.

Figures 16 and 17 present the comparison of measured and simulated results. Measured results show that Δ_{out} of the first sample is about 3 dB over the whole bandwidth from 8.2 GHz to 14.3 GHz, that is 54% of the bandwidth. In addition, return loss is better than 13 dB. The phase difference is about 0 degree.

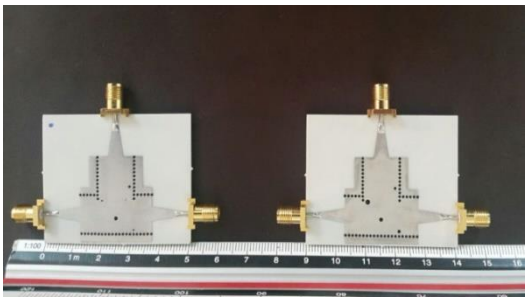

Fig. 15. The proposed power dividers.

Table 2: The position of posts in power divider with Δ_{out} =3 dB

	Position	Diameter
Post 1	(23.2,30.3)	1 mm
Post 2	(27.6,20.9)	0.7 mm
Post 3	(36.9,31.6)	0.7 mm
Post c	(33.25,25.6)	1.4 mm

Table 3: The position of posts in power divider with Δ_{out}= 6dB

	Position	Diameter
Post 1	(23.2,30.3)	1 mm
Post 2	(27.6,21.1)	1.7 mm
Post 3	(36.7,31.6)	1.2 mm
Post c	(33.1,25.6)	1.4 mm

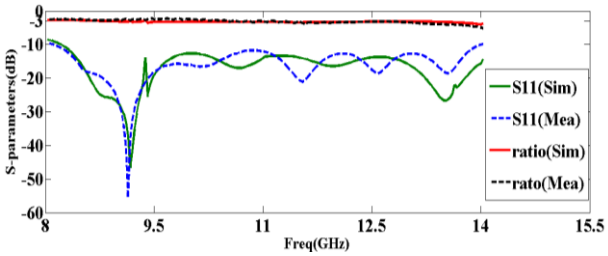

Fig. 16. The S parameters of power divider with Δ_{out} =3 dB.

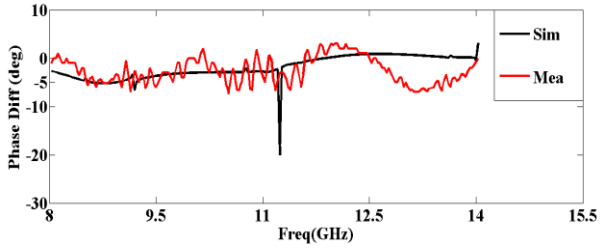

Fig. 17. The phase difference of power divider with Δ_{out} =3 dB ports.

The other power divider with a power division ratio 1:4 has about 45% bandwidth of 8.8 GHz to14.5 GHz (Fig. 18). The S_{11} is about -12 dB over the whole bandwidth. Δ_{phase} is about 180 deg. (shown in Fig. 19). It can be observed that the phase is steady from 8.8 GHz to 14 GHz, which is depicted in Fig. 20. Designing an unequal SIW T-junction with an arbitrary output ratio over a wideband is flexible and effective.

The designs when compared to the previous power dividers with arbitrary power division ratio in Table 4 show significantly better fractional bandwidth and also selectable power-split ratio and phase difference. Phase difference can be near zero or about 180˚.

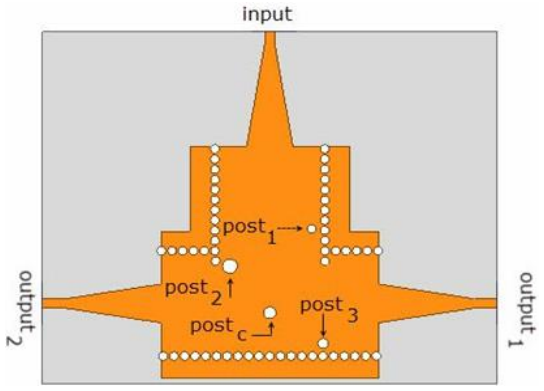

Fig. 18. The SIW power divider with Δ_{out} =6 dB.

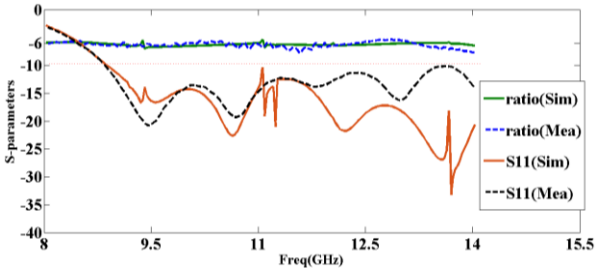

Fig. 19. The S parameters of power divider with Δ_{out} =6 dB.

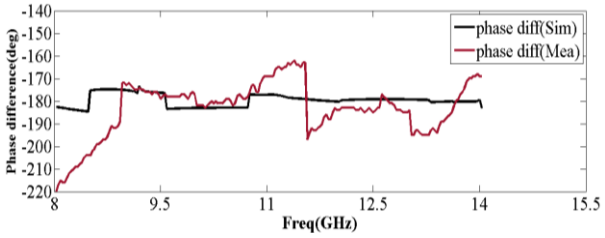

Fig. 20. The phase difference of the power divider with Δ_{out} =6 dB.

Table 4: Comparison between this structure and some reported work

Reference	Δ_{out} (dB)	Center Frequency	Fractional Bandwidth	Adjusted Phase Difference
[10]	3.4	10 GHz	40%	No
[13]	6	23 GHz	12%	No
[14]	6	32.5 GHz	44.06%	No
This work	3	11 GHz	54%	Yes
This work	6	11 GHz	45%	Yes

III. CONCLUSION

In this article, a new design for adjusting the output power level of the SIW T-junction power divider at X-

band has been introduced. Using multiple posts in the power divider resulted in flexible and suitable design over a broadband. The position and diameter of post 2, 3 and C are really challenging. In this article the power division ratio is controlled by the diameter and the positions of the posts 1 and 2. In addition, return loss is optimized by using post 3 and post C. The easily modifying of the output level with post's positions and diameters show that this power divider could have an important role in millimeter wave systems.

REFRENCES

[1] Z. He, J. Cai, Z. Shao, X. Li, and Y. Huang, "Novel power divider integrated with SIW and DGS technology," *Progress In Electromagnetics Research*, vol. 139, pp. 289-301, 2013.

[2] P. Mohammadi and S. Demir, "Loss reduction in substrate integrated waveguide structure," *Progress In Electromagnetics Research*, vol. 46, pp. 125-133, 2014.

[3] B. Rahali and M. Feham, "Substrate integrated waveguide power divider circulator and coupler in 10-15 GHz band," *International Journal of Information Sciences and Techniques (IJLST)*, 4, no. 1/2, Mar. 2014.

[4] Y. Songnan and A. E. Fathy, "Synthesis of an arbitrary power split ratio divider using substrate integrated waveguides," *IEEE MTT-S Int. Microwave Symp. Dig. (IEEE MTT-S)*, Honolulu, HI, USA, pp. 427-430, Jun. 2007.

[5] G.-L. Huang, S.-G. Zhou, T.-H. Chio, and T.-S. Yeo, "Design of a symmetric rectangular waveguide T-junction with in-phase and unequal-power split characteristics," *In IEEE International Symposium on Antennas and Propagation*, Orlando, FL, pp. 2119-2120, 2013.

[6] D. Deslandes and K. Wu, "Accurate modeling, wave mechanisms, and design considerations of a substrate integrated waveguide," *IEEE Trans. Microwave Theory & Tech*., vol. 54, no. 6, pp. 2516-2526, Jun. 2006.

[7] F. Wenjie, C. Wenquan, and D. Kuan, "Compact planar magic-T using E-plane substrate integrated waveguide (SIW) power divider and slotline transition," *IEEE Microwave and Wireless Components Letters*, vol. 20, pp. 331-333, 2010.

[8] K. Wu, D. Deslands, and Y. Cassivi, "The substrate integrated circuits - A new concept for high-frequency electronics and optoelectronics," *Microwave Review*, Dec. 2003.

[9] G. L. Huang, T. H. Chio, H. T. Hui, and T. S. Yeo, "Physically symmetric wideband waveguide T-junction with equal-phase and unequal power division," *Microwave and Optical Technology Letters*, vol. 57, pp. 1216-1219, May 2015.

[10] A. R. Akbarzade and Z. X. Shen, "Waveguide power dividers using multiple posts," *Microwave and Optical Technology Letters*, vol. 50, pp. 981-984, Apr. 2008.

[11] T. Li and W. Don, "Broadband substrate-integrated waveguide T-junction with arbitrary power-dividing ratio," *Electronics Letters*, 5th, vol. 51, pp. 259-260, Feb. 2015.

[12] P. Mohammadi and S. Demir, "Multi-layer substrate integrated waveguide E-plane power divider," *Progress In Electromagnetics Research C*, vol. 30, pp. 159-172, 2012.

[13] S. Contreras and A. Peden, "Graphical design method for unequal power dividers based on phase-balanced SIW tee junctions," *Int. J. Microw. Wirel. Technol*., 5, pp. 603-610, 2013.

[14] T. Li, W. Dou, and H. Weng, "Broadband power dividers based on waveguide T-junctions at Ka-band," *IEIEC Electronics Express*, pp. 1-7, Jan. 2016.

Asrin Piroutiniya was born in 1983 in Urmia, Iran. She received her B.Sc. degree in Electrical Engineering from Azad University, Naein Branch and M.Sc. degree in Electrical Engineering from Department of Electrical Engineering, Science and Research Branch, Islamic Azad University, West Azerbaijan, Iran. Her research interests include substrate integrated waveguide technology, power divider and feeding networks for array antenna and antennas.

Pejman Mohammadi was born in 1973 in Tehran, Iran. He received the Ph.D. in Electrical Engineering from Middle East Technical University Turkey. Since 2001, he has been with the Department of Electrical Engineering, Islamic Azad University of Urmia, where he is currently a Lecturer. His research interests include microwave component SIW, microstrip antennas, small antennas for wireless communications and reconfigurable structure.

Small Wearable Meta Materials Antennas for Medical Systems

Albert Sabban

Department of Electrical Engineering
Ort Braude College, Karmiel, 2161002, Israel
sabban@netvision.net.il

Abstract ─ Communication industry is in rapid growth in the last years. Efficient small antennas are crucial in the development of medical systems. Low efficiency is the major disadvantage of small antennas. Meta material technology is used to improve the efficiency of small antennas. Design tradeoffs, computed and measured results of wearable meta-materials antennas with high efficiency are presented in this paper. All antennas were analyzed by using 3D full-wave software, ADS. The antennas electrical parameters on the human body are presented. The gain and directivity of the patch antenna with split-ring resonators, SRR, is higher by 2.5 dB than the patch antenna without SRR. The resonant frequency of the antennas with SRR is lower by 5% to 10% than the antennas without SRR. The resonant frequency of the antenna with SRR on human body is shifted by 3%.

Index Terms ─ Metamaterial antennas, printed antennas.

I. INTRODUCTION

Printed antennas are widely used in communication systems. Features of microstrip antennas such as low profile, flexible, light weight, compact and low production cost are crucial for wireless systems. Compact printed antennas are presented in journals and books, as referred in [1]-[4]. However, small printed antennas suffer from low efficiency. Meta material technology is used to design small printed antennas with high efficiency. Printed wearable antennas were presented in [5]. Artificial media with negative dielectric permittivity were presented in [6]. Periodic SRR and metallic posts structures may be used to design materials with dielectric constant and permeability less than 1 as presented in [6]-[14]. In this paper, meta-material technology is used to develop small antennas with high efficiency. Electrical properties of human tissues have been investigated in several papers such as [15-16]. Wearable antennas have been presented in papers in the last years as referred in [17-23]. The computed and measured bandwidth of the antenna with SRR and metallic strips is around 50% for VSWR of 2.3:1.

II. ANTENNAS WITH SRR

A microstrip printed antenna with SRR is shown in Fig. 1. The microstrip loaded dipole antenna with SRR in Fig. 1 provides horizontal polarization. The slot antenna provides vertical polarization. The resonant frequency of the antenna with SRR is 400 MHz. The resonant frequency of the antenna without SRR is 10% higher. The antennas shown in Fig. 1 consist of two layers. The dipole feed network is printed on the first layer. The radiating dipole with SRR is printed on the second layer. The thickness of each layer is 0.8 mm. The dipole and the slot antenna create dual polarized antenna. The computed S11 and antenna gain are presented in Fig. 2. The length of the antenna shown in Fig. 1 is 19.8 cm.

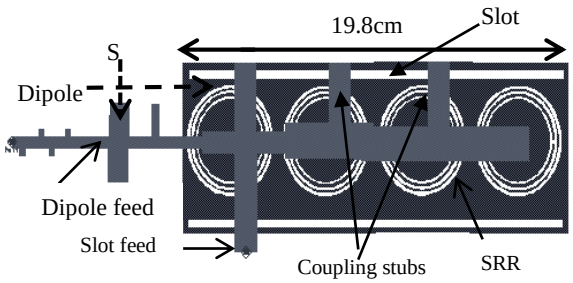

Fig. 1. Printed antenna with split ring resonators.

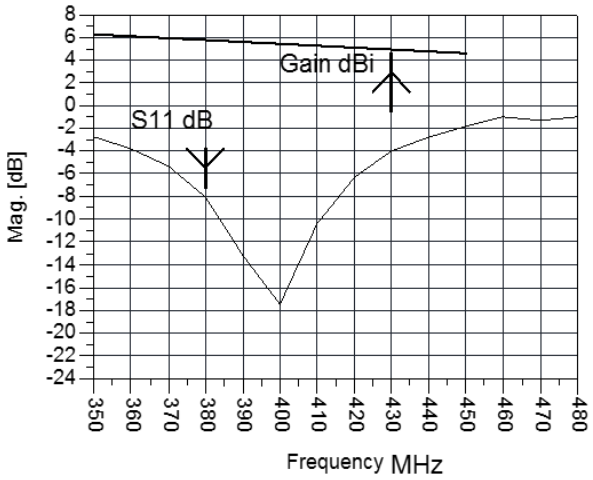

Fig. 2. Antenna with SRR, computed S11.

Submitted On: November 6, 2014
Accepted On: February 20, 2016

The length of the antenna without SRR is 21 cm as presented in [5]. The ring width is 1.4 mm the spacing between the rings is 1.4 mm. The antennas was designed by using ADS software. Directivity and gain of the antenna with SRR is around 5.5 dBi. Location and dimensions of the matching stubs was tuned to get the best VSWR results for the antennas presented in Fig. 1 and Fig. 3. The length of the stub S is 10 mm. The antenna axial ratio may be varied from 0 dB to 30 dB by optimizing the locations and the number of the coupling stubs. The number of coupling stubs in Fig 1 is three. Moreover, the antenna axial ratio value may be tuned by varying the position of the slot feed line. The measured bandwidth of the antenna without SRR is around 10% for VSWR better than 2:1. The antenna beam width is 100º. The antenna gain is around 2d Bi to 3 dBi. There is a good agreement between measured and computed results. The antenna presented in Fig. 1 has been modified as shown in Fig. 3. The location and the dimension of the coupling stubs have been modified to get wider bandwidth as shown in Fig. 4. The location and the dimension of the coupling stubs in Fig. 1 were optimized, as shown in Fig. 5, to get two resonant frequencies.

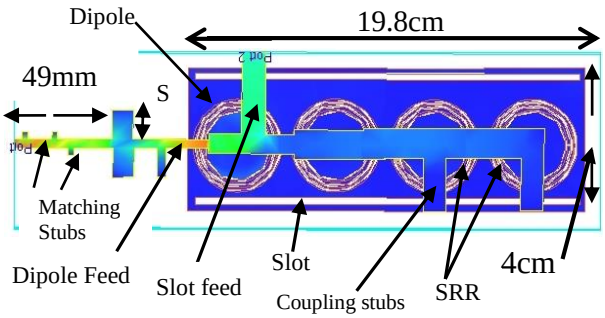

Fig. 3. Current distribution of the modified antenna.

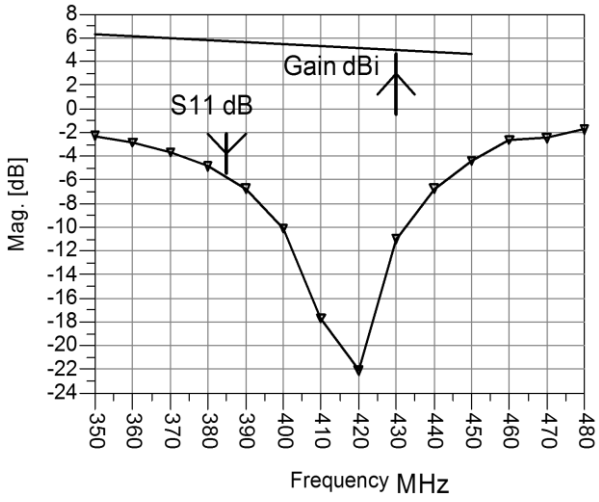

Fig. 4. Measured S11of the antenna without SRR.

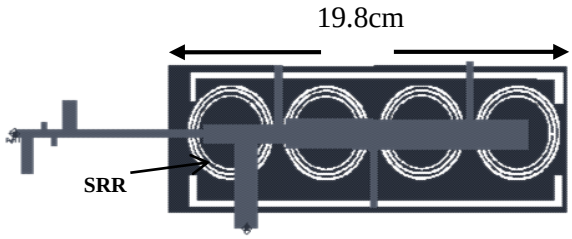

Fig. 5. Antenna with SRR with two resonant frequencies.

The first resonant frequency is 370 MHz, as shown in Fig. 6. Metallic strips have been added to the antenna with SRR as presented in Fig. 7. The antenna gain and computed S11 of the antenna with metallic strips is presented in Fig. 8. The antenna bandwidth is around 40% for VSWR better than 2.5:1. The 3D computed radiation pattern is shown in Fig. 9. Directivity and gain of the antenna with SRR is around 5.5dBi as shown in Fig. 10. The length of the antennas with SRR is smaller by 5% than the antennas without SRR. Moreover, the resonant frequency of the antennas with SRR is lower by 5% to 10%. The feed network of the antenna in Fig. 7 was optimized to yield VSWR better than 2:1 in frequency range of 250 MHz to 420 MHz as shown in Fig. 11. Optimization of the number of the coupling stubs and the distance between the coupling stubs may be used to tune the antenna resonant frequency. The current distribution along the antenna with SRR and two coupling stubs is shown in Fig. 12. The SRR have an important role in the radiation characteristics of the antenna. The antenna with two coupling stubs has two resonant frequencies. The first resonant frequency is 370 MHz and the second resonant frequency is 420 MHz.

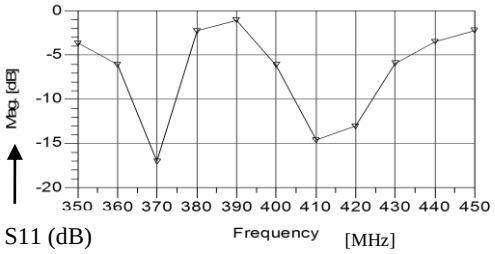

Fig. 6. S11 for antenna with two resonant frequencies.

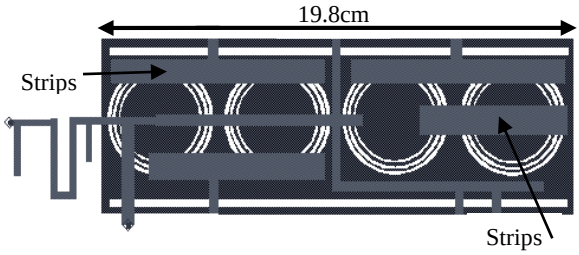

Fig. 7. Antenna with SRR and metallic strips.

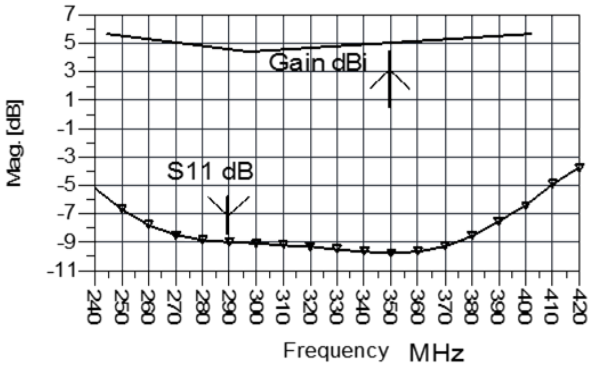

Fig. 8. S11 for antenna with SRR and metallic strips.

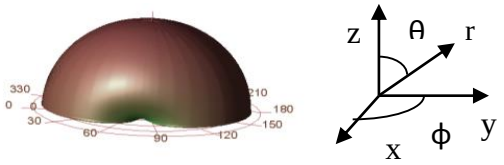

Fig. 9. 3D radiation pattern for antenna with SRR.

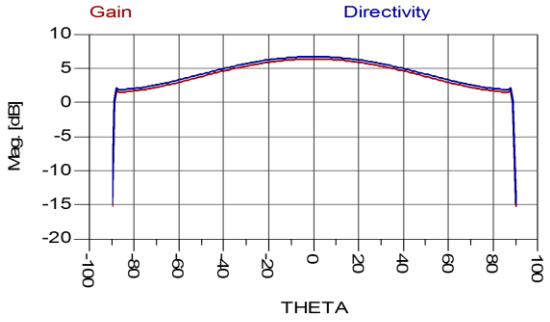

Fig. 10. Directivity of the antenna with SRR.

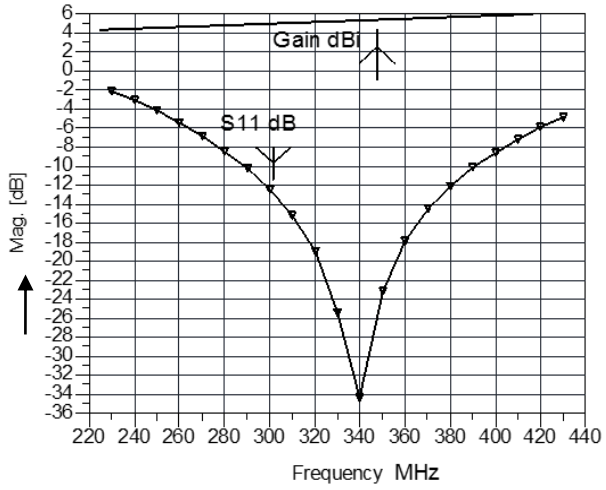

Fig. 11. S11 and gain for antenna with metallic strips.

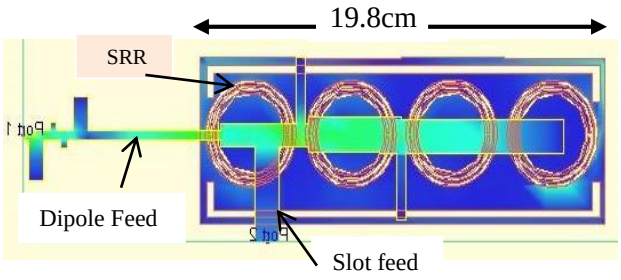

Fig. 12. Antenna with SRR with two coupling stubs.

The computed S11 parameter of the antenna with two coupling stubs is presented in Fig. 13. The 3D radiation pattern for antenna with two coupling stubs is shown in Fig. 14. The antenna with metallic strips was optimized to yield wider bandwidth as shown in Fig. 15. The S11 parameter of the modified antenna with metallic strips is presented in Fig. 16. The antenna bandwidth is around 50% for VSWR better than 2.3:1. Comparison between antennas with and without SRR is given in Table 1. The measured results agrees with the computed results.

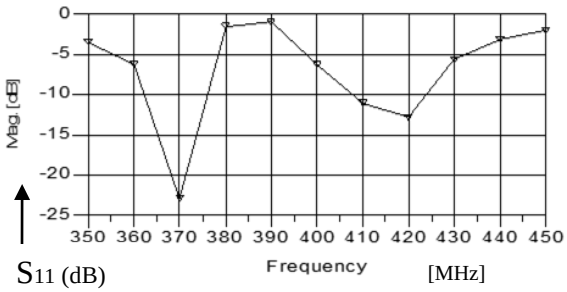

Fig. 13. S11 for antenna with two coupling stubs.

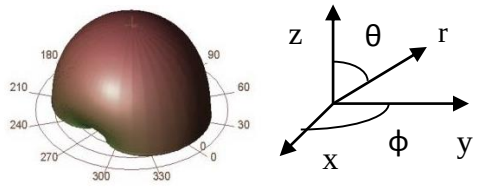

Fig. 14. 3D radiation pattern for antenna with SRR.

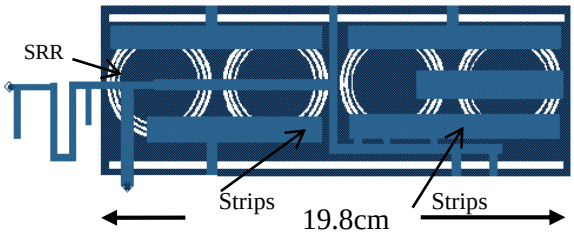

Fig. 15. Wideband antenna with SRR and metallic strips.

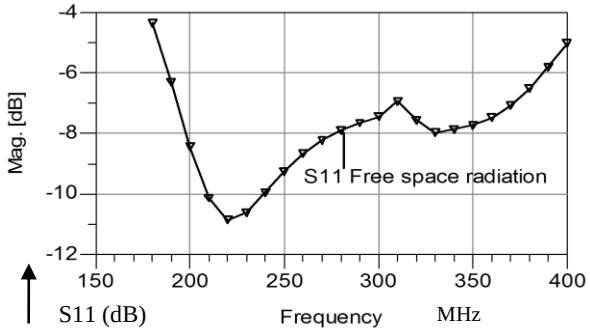

Fig. 16. S11 for antenna with SRR and metallic strips.

Table 1: Comparison between antennas with SRR

Antenna	Freq. (MHz)	VSWR %	Gain (dBi)	Length (cm)
With SRR	434	10	5.5	19.8
Without SRR	400	10	2.5	21
SRR and Strips	300	50	5.5	19.8

III. FOLDED DIPOLE META-MATERIAL ANTENNA WITH SRR

The length of the antenna shown in Fig. 1 may be reduced from 20 cm to 7 cm by folding the printed dipole as shown in Fig. 17. The antenna bandwidth is around 10% for VSWR better than 2:1. The antenna beam width is around 100º. The antenna gain is around 2 to 3 dBi. The size of the antenna with SRR shown in Fig. 1 may be reduced by folding the printed dipole as shown in Fig. 18. The dimensions of the folded dual polarized antenna with SRR presented in Fig. 18 are 11x11x0.16 cm. Figure 19 presents the antenna computed S11 parameters. The antenna bandwidth is 10% for VSWR better than 2:1. The computed radiation pattern of the folded antenna with SRR is shown in Fig. 20.

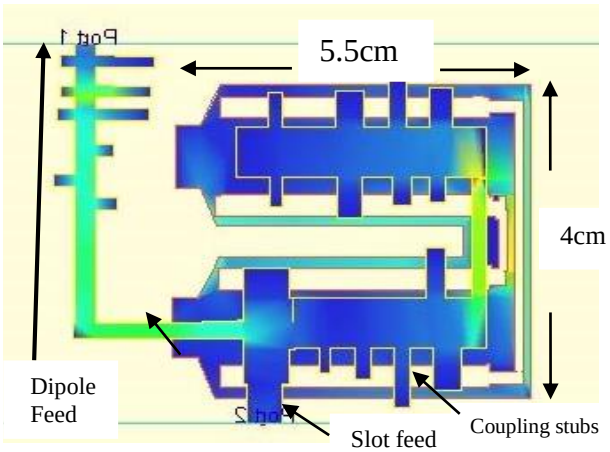

Fig. 17. Current distribution of the folded dipole.

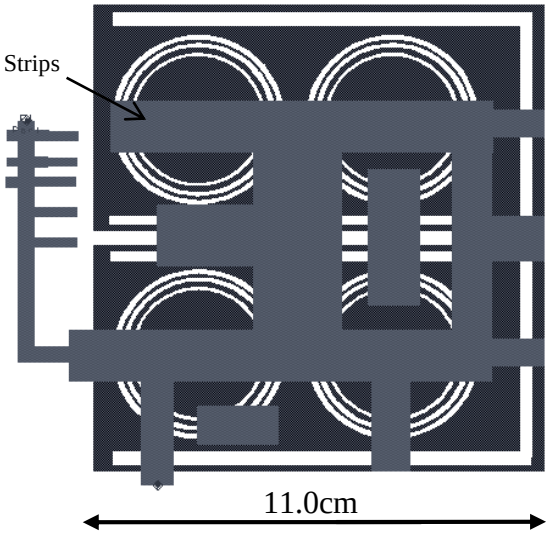

Fig. 18. Folded dual polarized antenna with SRR.

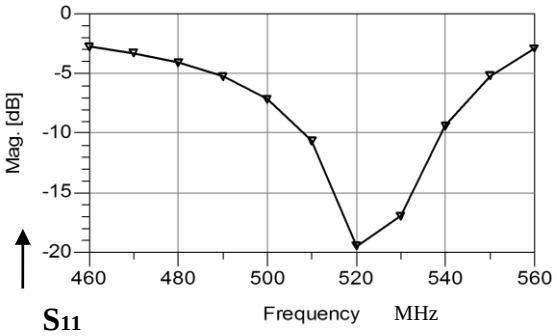

Fig. 19. Folded antenna with SRR, computed S11.

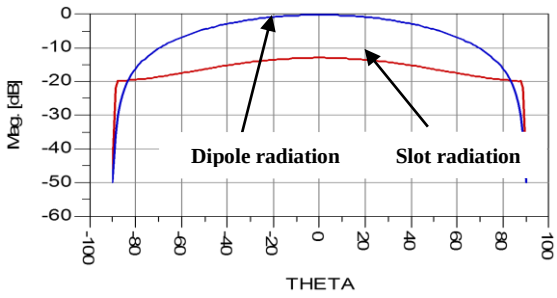

Fig. 20. Radiation pattern of the folded antenna with SRR.

IV. STACKED PATCH ANTENNA WITH SRR

At first a stacked patch antenna [1-3] has been designed. The second step was to design a patch antenna with SRR. The antenna consists of two layers. The first layer consists of FR4 substrate with dielectric constant

of 4. The second layer consists of RT-Duroid 5880 with dielectric constant of 2.2. The dimensions of the antenna shown in Fig. 21 are 33x20x3.2 mm. The antenna bandwidth is around 5% for VSWR better than 2.5:1. The antenna beam width is 72º.

The antenna gain is 7 dBi. The computed S11 parameters are presented in Fig. 22. Radiation pattern of the stacked patch is shown in Fig. 23. The antenna with SRR is shown in Fig. 24. This antenna has the same structure as the antenna shown in Fig. 21. The ring width is 0.2 mm the spacing between the rings is 0.25 mm. Twenty eight SRR are placed on the radiating element. There is a good agreement between measured and computed results. The measured S11 parameters of the antenna with SRR are presented in Fig. 25. The antenna bandwidth is around 12% for VSWR better than 2.5:1. By adding an air space of 4 mm between the antenna layers the VSWR was improved to 2:1. The antenna gain is around 9 to 10 dBi. The antenna computed radiation pattern is shown in Fig. 26. The antenna beam width is around 70º. The gain and directivity of the stacked patch antenna with SRR is higher by 2 dB to 3 dB than patch the antenna without SRR.

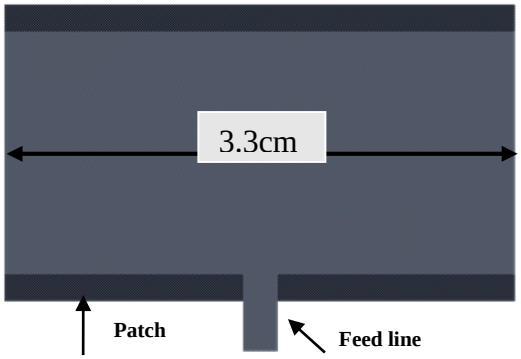

Fig. 21. A microstrip stacked patch antenna.

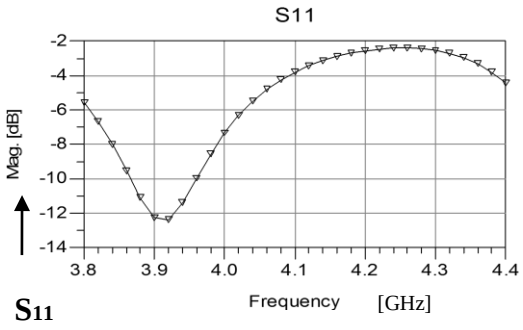

Fig. 22. Computed S11 of the microstrip stacked patch.

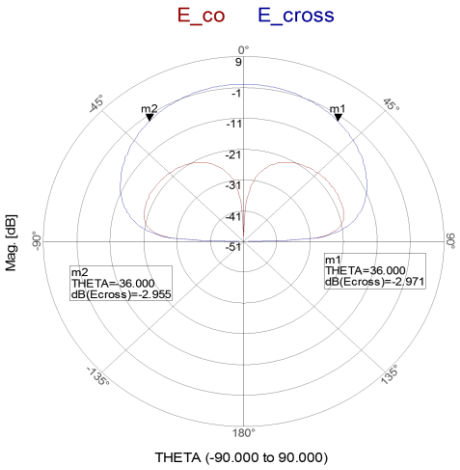

Fig. 23. Radiation pattern of the microstrip stacked patch.

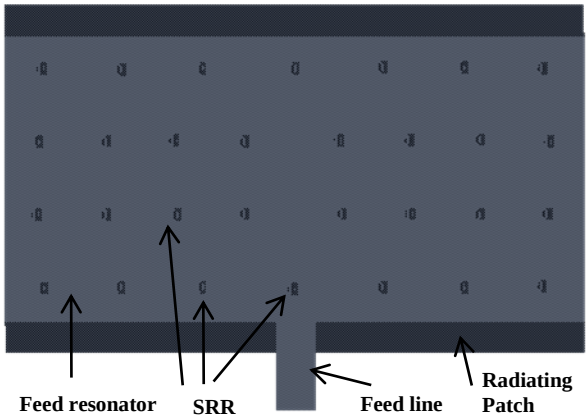

Fig. 24. Printed antenna with split ring resonators.

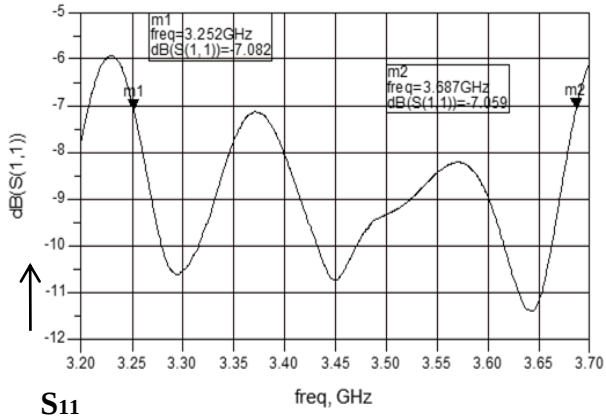

Fig. 25. Patch with split ring resonators, measured S11.

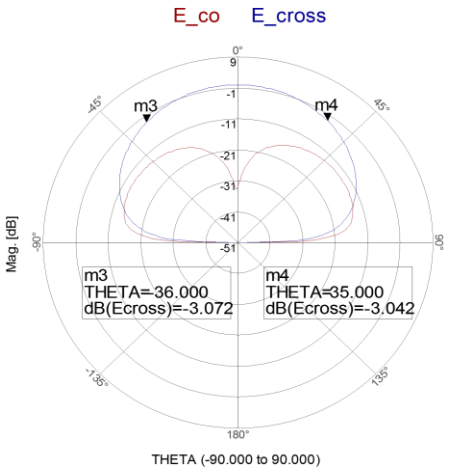

Fig. 26. Radiation pattern for patch with SRR.

V. PATCH ANTENNA LOADED WITH SRR

A patch antenna with split ring resonators has been designed. The antenna is printed on RT- DUROID 5880 dielectric substrate with dielectric constant of 2.2 and 1.6 mm thick. The dimensions of the microstrip patch antenna shown in Fig 27 are 33x16.6x3.2 mm. The antenna bandwidth is around 14% for S11 lower than -7.5 dB. The antenna bandwidth is 16% for VSWR better than 3:1. The antenna beam width is around 72º. The antenna gain is around 8 dBi. The computed S11 results are presented in Fig. 28. The gain and directivity of the antenna with SRR is higher by 3 dB than the patch antenna without SRR.

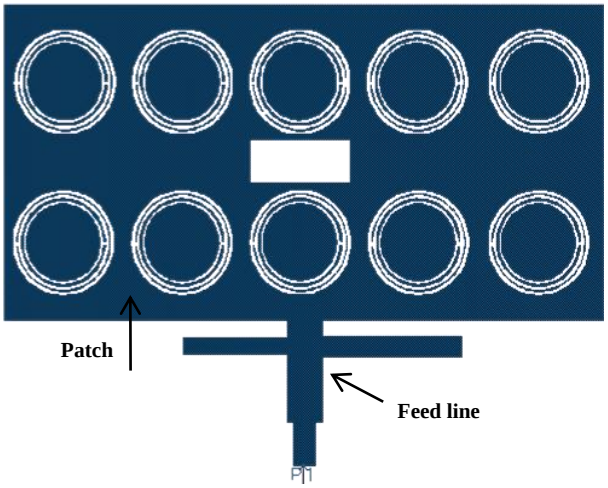

Fig. 27. Patch antenna with split ring resonators.

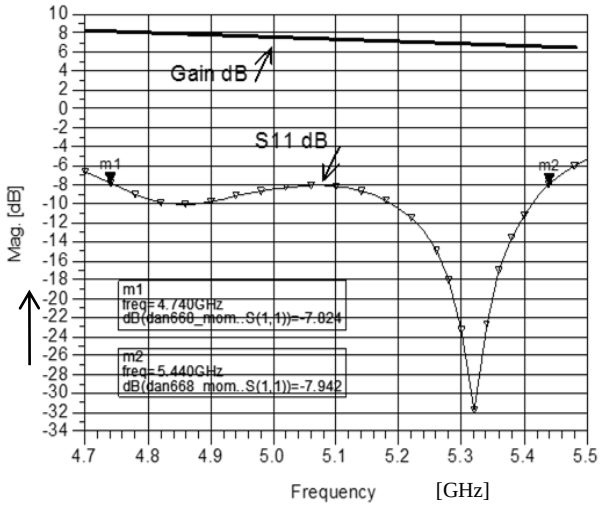

Fig. 28. Patch with SRR, computed S11.

VI. METAMATERIAL ANTENNAS IN VICINITY TO THE HUMAN BODY

The meta-materials antennas S11 variation in vicinity of the human body were computed by using the structure presented in Fig. 29 (a). Electrical properties of human body tissues are given in Table 2, see [15]. The antenna location on the human body is taken into account by computing S11 for different dielectric constant of the body tissues. The variation of the dielectric constant of the body from 43 at the stomach to 63 at the colon zone shifts the antenna resonant frequency by to 2%. The antenna was placed inside a belt with thickness between 1 to 4mm as shown in Fig. 29 (b). The belt dielectric constant was varied from 2 to 4. The antennas impedance was computed and measured for air spacing of 0 mm to 8 mm, between the patient shirt and the antennas. The dielectric constant of the patient shirt was varied from 2 to 4. Figure 30 presents S11 results of the antenna with SRR shown in Fig. 12 on the human body. The antenna resonant frequency is shifted by 3%. Figure 31 presents S11 results of the antenna with SRR and metallic strips, shown in Fig. 15. The antenna resonant frequency is shifted by 1%. Results presented in Fig. 31 indicate that the antenna has V.S.W.R better than 2.3:1 for 50% bandwidth. The radiation pattern of the antenna with SRR and metallic strips on human body is presented in Fig. 32. Figure 33 presents S11 results for different belt thickness, shirt thickness and air spacing between the antennas and human body for the antenna without SRR. One may conclude from results shown in Fig. 33 that, the antenna has S11 better than -9.5 dB for air spacing up to

8 mm between the antennas and the human body. Tunable wearable antenna may be used to control the antenna resonant frequency at different positions on the human body, see [24]. Figure 34 presents S11 results of the folded antenna with SRR, shown in Fig. 18, on the patient body. The antenna resonant frequency is shifted by 2%. The radiation pattern of the folded antenna with SRR on human body is presented in Fig. 35.

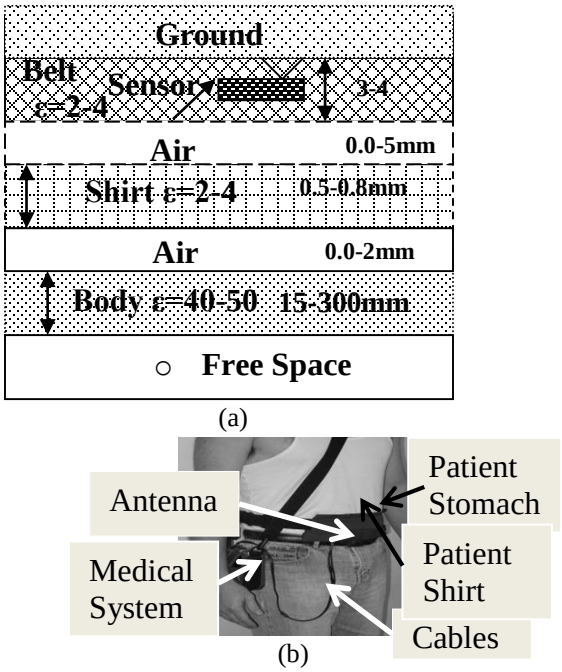

Fig. 29. (a) Antenna environment and (b) patient.

Table 2: Electrical properties of human body tissues

Tissue	Property	434 MHz	1200 MHz
Stomach	σ	0.67	0.97
	ε	42.9	39.06
Colon, muscle	σ	0.98	1.43
	ε	63.6	59.41
Fat	σ	0.045	0.056
	ε	5.02	4.58

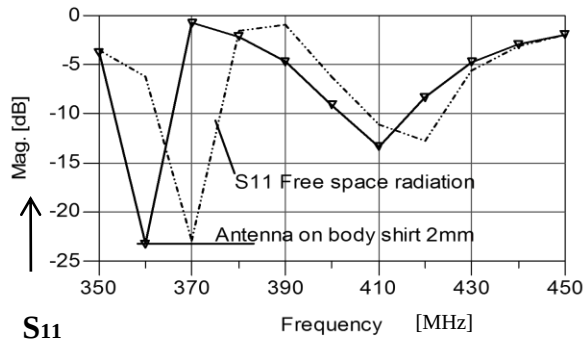

Fig. 30. S11 of the antenna with SRR on the human body.

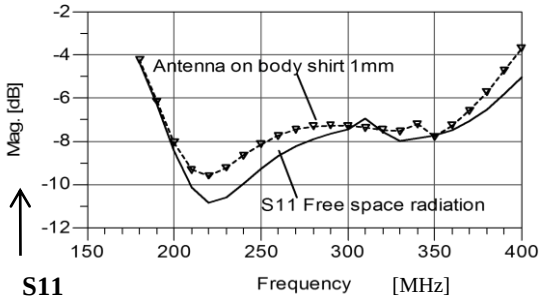

Fig. 31. Antenna with SRR S11 results on a patient.

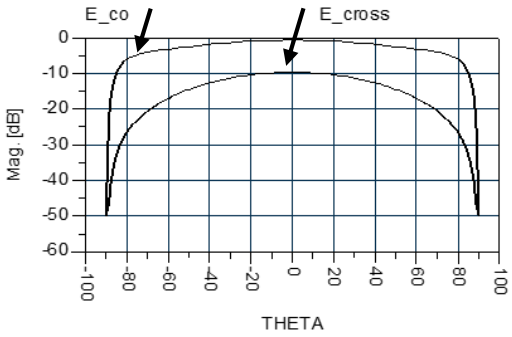

Fig. 32. Radiation pattern for antenna with SRR shown in Fig. 16 on the human body.

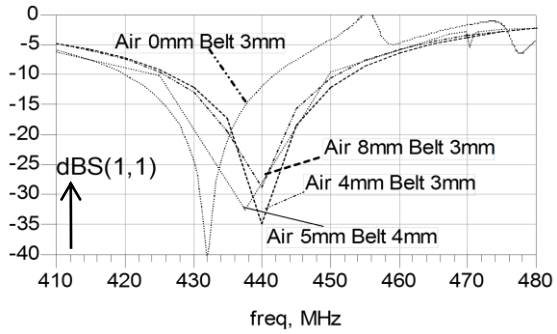

Fig. 33. S11 results for different locations relative to the human body for the antenna without SRR.

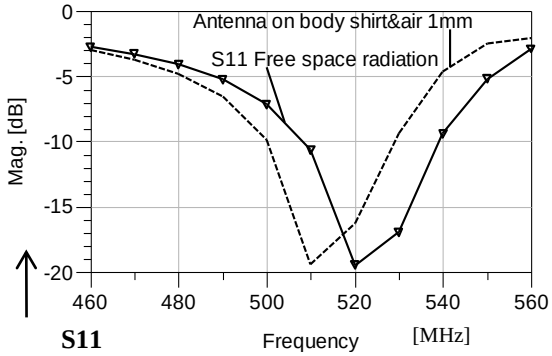

Fig. 34. Folded antenna with SRR, S11 on the body.

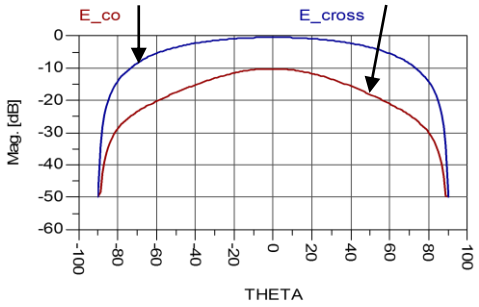

Fig. 35. Radiation pattern of the folded antenna with SRR on human body.

VII. METAMATERIAL WEARABLE ANTENNAS

The proposed meta-materials antennas may be placed on the patient body as shown in Fig. 36 (a). The patient in Fig. 36 (b) is wearing a wearable antenna. The antennas belt is attached to the patient front or back body. The cable from each antenna is connected to the medical system. The received signals are transferred via a SP8T switch to the receiver. The medical system selects the signal with the highest power. Usually the received signal during medical test with fat Persons is higher than the received signal during medical test with thin persons. The explanation is that the dielectric constant and conductivity of fat is much lower than the dielectric constant and conductivity of muscle and bone. The antennas electrical characteristics on human body have been measured by using a phantom that represents the human body electrical properties as presented in [5]. In several wearable systems the distance separating the transmitting and receiving antennas is in the near field zone. In the near-field area the antennas are magnetically coupled and only near field effects should be considered.

In the age of wireless products the proposed antennas are critical in developing efficient wearable systems. A photo of meta-material patch antenna with SRR is shown in Fig. 37.

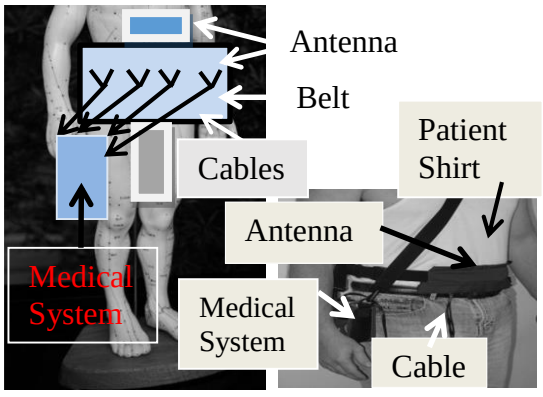

Fig. 36. (a) Medical system with wearable antennas, and (b) patient with printed wearable antenna.

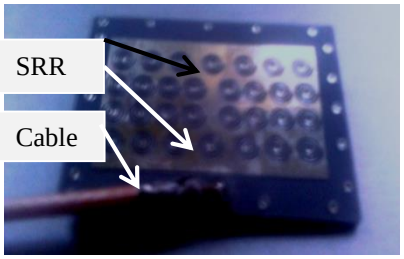

Fig. 37. Meta-material patch antenna with SRR.

VIII. ANALYSIS OF WEARABLE ANTENNAS

The major issue in the design of wearable antennas is the interaction between RF transmission and the human body. Electrical properties of human body tissues should be considered in the design of wearable antennas.

The dielectric constant and conductivity of human body tissues may be used to calculate the attenuation α of RF transmission through the human body. Figure 38 presents attenuation values of human tissues. Stomach tissue attenuation at 500 MHz is around 1.6 dB/cm. In Table 3 advantages of patch antennas with SRR is listed.

Results presented in Tables 1 and 3 show that antennas with SRR are more efficient, smaller and have a wider bandwidth than similar antennas without SRR. There is a good agreement between measured and computed results.

Table 3: Advantages of patch antennas with SRR

Patch\Value	Freq. (GHz)	Dimensions (mm)	VSWR 3:1	Gain dBi
Patch	3.9.5	36x20x3.2	2%	4.5
Patch with SRR	3.75	33x20x3.2	10%	7.5
Patch with SRR	5.1	33x16.6x3.2	14%	7.5
Stacked Patch	3.9	33x20x3.2	6%	7
Stacked Patch - SRR	3.5	33x20x3.2	12%	9.5

$$\gamma = \sqrt{j\omega\mu(\sigma + j\omega\varepsilon)} = \alpha + j\beta, \quad (1)$$

$$\alpha = Re(\gamma). \quad (2)$$

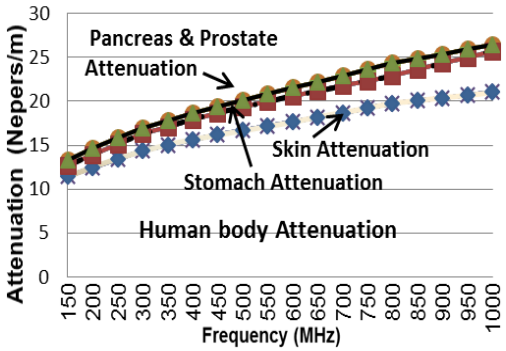

Fig. 38. Attenuation of human body tissues.

IX. CONCLUSION

Meta material technology is used to develop small antennas with high efficiency for medical systems. A new class of printed meta-materials antennas with high efficiency is presented. The bandwidth of the antenna with SRR and metallic strips is around 50% for VSWR better than 2.3:1. Optimization of the feed network, number of the coupling stubs and the length of the coupling stubs may be used to tune the antenna resonant frequency, radiation characteristics and the number of resonant frequencies. The length of the antennas with SRR is smaller by 5% than the antennas without SRR. Moreover, the resonant frequency of the antennas with SRR is lower by 5% to 10% than the antennas without SRR. The gain and directivity of the patch antenna with SRR is higher by 2 to 3 dB than the patch antenna without SRR. Measured results agrees with computed results.

REFERENCES

[1] J. R. James, P. S. Hall, and C. Wood, *Microstrip Antenna Theory and Design*, IEE, London, 1981.

[2] A. Sabban and K. C. Gupta, "Characterization of radiation loss from microstrip discontinuities using a multiport network modeling approach," *IEEE Trans. on M.T.T*, vol. 39, no. 4 , pp. 705-712, Apr. 1991.

[3] A. Sabban, "A new wideband stacked microstrip antenna," *IEEE Antenna and Propagation Symp*., Houston, Texas, U.S.A, June 1983.

[4] A. Sabban, *Microstrip Antenna Arrays, Microstrip Antennas*, Nasimuddin (Ed.), ISBN: 978-953-ISBN: 978-953-307-247-0, InTech, pp. 361-384, 2011.

[5] A. Sabban, "New wideband printed antennas for medical applications," *IEEE Journal, Trans. on Antennas and Propagation*, vol. 61, no. 1, pp. 84-91, Jan. 2013.

[6] J. B. Pendry, A. J. Holden, et al., "Extremely low frequency plasmons in metallic mesostructures," *Phys. Rev. Lett*., vol. 76, pp. 4773-4776, 1996.

[7] J. B. Pendry, A. J. Holden, et al., "Magnetism from conductors and enhanced nonlinear phenomena," *IEEE Trans. MTT*, vol. 47, pp. 2075-2084, 1999.

[8] R. Marque´s, F. Mesa, et al., "Comparative analysis of edge and broadside coupled split ring resonators for metamaterial design: Theory and experiment," *IEEE Trans. Antennas Propag*., vol. 51, pp. 2572-2581, 2003.

[9] R. Marque´s, J. D. Baena, et al., "Novel small resonant waveguides electromagnetic particles for metamaterial and filter design," *Phys. Rev. Lett*., vol. 89, Proc. ICEAA, pp. 439-442, Torino, Italy, 2003.

[10] R. Marque´s, J. Martel, et al., "Left-handed-media simulation and transmission of EM waves in sub wavelength split-ring-resonator loaded metallic waveguides," *Phys. Rev. Lett*., vol. 89, 2002.

[11] J. D. Baena, R. Marque´s, et al., "Experimental results on metamaterial simulation using SRR-loaded waveguides," I*EEE-AP/S Int. Symposium on, Antennas and Propagation Proc*., pp. 106-109, 2003.

[12] R. Marque´s, J. Martel, et al., "A new 2-D isotropic left-handed metamaterial design: Theory and experiment," *Microwave Opt. Tech. Lett*., vol. 35, pp. 405-408, 2002.

[13] R. A. Shelby, D. R. Smith, et al., "Microwave transmission through a two dimensional, left-handed meta-material," *Appl. Phys. Letters*, vol. 78, pp. 489-491, 2001.

[14] J. Zhu and G. V. Eleftheriades, "A compact transmission line metamaterial antenna with extended bandwidth," *IEEE Antennas and Wireless Propagation Wireless Propagation Letters*, vol. 8, 2009.

[15] L. C. Chirwa, et all., "Electromagnetic radiation from ingested sources in the human intestine between 150 MHz and 1.2 GHz," *IEEE Transaction on Biomedical Eng*., vol. 50, no. 4, pp. 484-492, Apr. 2003.

[16] D. Werber, A. Schwentner, and E. M. Biebl, "Investigation of RF transmission properties of human tissues," *Adv. Radio Sci*., 4, pp. 357-360, 2006.

[17] B. Gupta, S. Sankaralingam, et al., "Development of wearable and implantable antennas in the last decade," *Microwave Symposium (MMS), 2010*, Mediterranean, pp. 251-267, 2010.

[18] T. T. Z. Popovic, et al., "Investigation and design of a multi-band wearable antenna," *3rd European Conference on Antennas and Propagation, EuCAP 2009*, pp. 462-465, 2009.

[19] P. Salonen, Y. Rahmat-Samii, et al., "Wearable antennas in the vicinity of human body," *IEEE Antennas and Propagation Symp.*, vol. 1 pp. 467-470, July 2004.

[20] A. Sabban, "Wideband printed antennas for medical applications," *APMC Conference*, Singapore, Dec. 2009.

[21] A. Alomainy, A. Sani, et al., "Transient characteristics of wearable antennas and radio propagation channels for ultra-wideband body wireless communication," *IEEE Trans. on Antennas and Propagation*, vol. 57, no. 4, pp. 875-884, Apr. 2009.

[22] M. Klemm and G. Troester, "Textile UWB antenna for wireless body area networks," *IEEE Trans. on Antennas and Propagation*, vol. 54, no. 11, pp. 3192-3197, Nov. 2006.

[23] P. M. Izdebski, H. Rajagoplan, et al., "Conformal ingestible capsule antenna: A novel chandelier

meandered design," *IEEE Trans. on Antennas and Propagation*, vol. 57, no. 4, pp. 900-909, Apr. 2009.

[24] A. Sabban, "Wideband tunable printed antennas for medical applications," *IEEE Antenna and Propagation Symp*., Chicago, IL, USA, July 2012.

A. Sabban (M'87-SM'94) received the B.Sc. degree and M.Sc. degree Magna Cum Laude in Electrical Engineering from Tel Aviv University, Israel in 1976 and 1986 respectively. He received the Ph.D. degree in Electrical Engineering from Colorado University at Boulder, USA, in 1991. Sabban reasearch interests are microwave and antenna engineering. In 1976 he joined the armament development authority RAFAEL in Israel. In RAFAEL he worked as a Senior Researcher, Group Leader and Project Leader in the Electromagnetic Department till 2007. In 2007 he retired from RAFAEL. From 2008 to 2010 he worked as an RF Specialist and Project Leader in Hitech Companies. From 2010 to date he is a Senior Lecturer and Researcher in Ort Braude College in Israel in the Electrical Engineering Department. He published over 60 research papers and hold a patent in the antenna area. Sabban wrote two books on Low Visibilty Antennas and a book on Electrmagnetics and Microwave Theory for graduate students. He also wrote two chapters in books on Microstrip Antennas.

A Hybrid Explicit-Implicit Scheme for Spectral-Element Time-Domain Analysis of Multiscale Simulation

H. Xu, D. Z. Ding, and R. S. Chen

Department of Communication Engineering
Nanjing University of Science and Technology, Nanjing, 210094, China
dzding@njust.edu.cn

Abstract ─ The multiscale simulation usually leads to dense meshes discretization for fine structures, thus making time step size of the spectral-element time-domain (SETD) method extremely small to ensure stability for explicit scheme. In this paper, a hybrid explicit-implicit scheme for SETD is proposed to deal with the simulation of multiscale electromagnetic problems. The central-difference is applied for the coarse region with large cells and the Newmark-Beta scheme is for the fine region with small cells. Then a large size of time step can be selected in the whole domain instead of the one limited by the smallest cell. When solving the matrix equation formed by the implicit scheme, two approaches are employed. One uses the sparse matrix solver UMFPACK directly and the other involves an explicit and iterative scheme. Numerical results show that the hybrid method is an efficient alternative to conventional SETD method for multiscale simulation.

Index Terms ─ Explicit-implicit, iterative Newmark-Beta, multiscale, spectral-element time-domain (SETD) method.

I. INTRODUCTION

When handling the multiscale electromagnetic simulations, traditional techniques face great challenges as some small grids may appear in very fine structures, which will result in a very small size of time step for the whole domains to obtain a stable solution [1]. Therefore, it will waste a lot of time because in other coarse domains a larger size of time step can be used. Unconditionally stable methods are often employed for the fine features as the time step size can be chosen in spite of the restriction between the time step size and the space step to guarantee stability [2]. However, most of the existing unconditionally stable techniques are implicit, which generally need a matrix solution. FDTD (finite-difference time-domain) is a very useful and simple time domain method [3]-[6], and some implicit methods are proposed based on FDTD such as the CN (Crank-Nicolson)-FDTD [5], ADI (alternating direction implicit)-FDTD [6]. Meanwhile, some FETD (finite-element time-domain) based methods [7]-[10] are also developed to reach unconditional stability such as the CN (Crank-Nicolson)-FETD [8], ADI (alternating direction implicit)-FETD [9], the Newmark-Beta scheme [10] and so on. If the implicit method is adopted for the whole domain, it will lead to a very large matrix, which is computationally expensive. Some hybrid time-stepping techniques are studied to improve the efficiency of the methods [11], [12]. Discontinuous Galerkin time-domain methods are very popular to deal with the multiscale simulations. The whole region is separated into a few subregions and different time-stepping scheme can be applied in these subregions [11]. However, the derivation is troublesome and additional cost is required on the interface for communicating fields among different subregions.

Here, a hybrid explicit-implicit scheme for spectral-element time-domain method is proposed and it is relatively simple and easy to implement. The spectral-element time-domain method makes use of Gauss-Lobatto-Legendre (GLL) polynomials and the mass matrix is diagonal or block-diagonal [13], so the inverse of the mass matrix can be easily obtained. One advantage of the proposed hybrid algorithm is that it is not derived with the help of the discontinuous Galerkin technique. As a result, the algorithm is easy to implement on the existing program without extra procedure for the interfaces of different subdomains. The simple central-difference is applied for the large elements region and the Newmark-Beta scheme is applied for the small elements region. Consequently, in the coarse region conditionally stability is realized and in the fine region unconditionally stability is realized. So the size of time step in the fine region could be chosen as large as the one in the coarse region instead of the one limited by the smallest mesh. Two approaches are used for the matrix solution in the fine region. The first one directly uses the sparse matrix solver UMFPACK [15] to solve the matrix equation. For the other, an iterative and explicit scheme is developed. Computational cost is also compared in the

Submitted On: March 8, 2016
Accepted On: March 24, 2016

demonstrated example.

This paper is organized as follows. In Section II, the basic theory and formulations of explicit-implicit scheme for SETD are presented. Stability analysis is given in Section III and numerical results are given to demonstrate the validity of the proposed method in Section IV. Conclusions are summarized in Section V.

II. THEORY AND FORMULATIONS

To deal with the multiscale problem, we start from the vector wave equation:

$$\nabla\times\nabla\times\mathbf{E}+\mu\varepsilon\frac{\partial^2\mathbf{E}}{\partial t^2}=0\,. \tag{1}$$

The GLL element discretization is applied in SETD method, which can achieve the spectral accuracy. The Nth-order GLL basis function in a one-dimensional reference unit $\xi\in[-1,1]$ is defined by [13]:

$$\phi_j^{(N)}(\xi)=\frac{-1}{N(N+1)L_N(\xi_j)}\frac{(1-\xi^2)L_N'(\xi)}{\xi-\xi_j}. \tag{2}$$

Consequently, when applying the 3-D standard reference unit, the basis functions are described as:

$$\begin{aligned}\mathbf{\Phi}_{rst}^{\xi}&=\hat{\xi}\phi_r^{(N_\xi)}(\xi)\phi_s^{(N_\eta)}(\eta)\phi_t^{(N_\zeta)}(\zeta)\\ \mathbf{\Phi}_{rst}^{\eta}&=\hat{\eta}\phi_r^{(N_\xi)}(\xi)\phi_s^{(N_\eta)}(\eta)\phi_t^{(N_\zeta)}(\zeta)\,.\\ \mathbf{\Phi}_{rst}^{\zeta}&=\hat{\zeta}\phi_r^{(N_\xi)}(\xi)\phi_s^{(N_\eta)}(\eta)\phi_t^{(N_\zeta)}(\zeta)\end{aligned} \tag{3}$$

Therefore, the electric field can be expanded by the basis functions:

$$\mathbf{E}(\xi,\eta,\zeta)=\sum_{j=1}^{N}e_j\mathbf{\Phi}_j\,. \tag{4}$$

Then the Galerkin's test is used and we have a discretized system of equations:

$$\begin{aligned}&[S]e+[T]\frac{d^2e}{dt^2}=0\\ &S_{ij}=\frac{1}{\mu}\iiint_{V^e}\nabla\times\tilde{\mathbf{\Phi}}_i\cdot\nabla\times\tilde{\mathbf{\Phi}}_j dV\,.\\ &T_{ij}=\varepsilon\iiint_{V^e}\tilde{\mathbf{\Phi}}_i\cdot\tilde{\mathbf{\Phi}}_j dV\end{aligned} \tag{5}$$

Where $\tilde{\mathbf{\Phi}}$ represents the basis function in the physical domain and has the following mapping relationship with the basis function $\mathbf{\Phi}$ in the reference domain [14]:

$$\begin{aligned}\tilde{\mathbf{\Phi}}&=J^{-1}\mathbf{\Phi}\\ \nabla\times\tilde{\mathbf{\Phi}}&=\frac{1}{|J|}J^T\nabla\times\mathbf{\Phi}\end{aligned}\,. \tag{6}$$

In the conventional SETD method, the derivative in Equation (5) is substituted via the central-difference in the entire computation domain:

$$[T]e^{n+1}=\left(2[T]-\Delta t^2[S]\right)e^n-[T]e^{n-1}\,. \tag{7}$$

As the basis functions have the property of orthogonality and the GLL quadrature is used [16], the mass matrix [T] is diagonal or block-diagonal. Therefore, the inverse can be directly obtained. It could be a great advantage of the SETD method over the conventional FETD method whose mass matrix doesn't have the block-diagonal characteristic.

When handling some complicated electromagnetic problems such as the multiscale simulation, very small meshes usually appear in the fine features. Moreover, it is the same to other complex materials or structures because the curved hexahedrons are used and extremely small size meshes are unavoidably produced sometimes. Since the size of time step is limited by the spatial discretization of the simulation domain according to the CFL condition, the time step size may become very small because of small cells. It will result in a large number of simulation steps and the efficiency is low.

Here, a novel hybrid explicit-implicit spectral-element time-domain method is proposed to deal with this kind of problem. The fine structures can be wrapped by a proper box and treated as the fine region, the rest is treated as the coarse region. In the coarse region with large elements, the traditional central-difference is employed, which is displayed in Equation (7). In the fine region with very small elements, the Newmark-Beta scheme is used to guarantee unconditional stability with a large size of time step, which is the same as the one used in the coarse domain:

$$S\left(\beta e^{n+1}+(1-2\beta)e^n+\beta e^{n-1}\right)+T\frac{e^{n+1}-2e^n+e^{n-1}}{\Delta t^2}=0\,. \tag{8}$$

Navsariwala and Gedney [10] have demonstrated that when the parameter is chosen to be $\beta\geq 0.25$, the unconditional stability can be ensured. So the size of time step could be selected in spite of the stability condition:

$$\begin{aligned}\left([T]+\Delta t^2\beta[S]\right)e^{n+1}=&\left(2[T]-\Delta t^2(1-2\beta)[S]\right)e^n\\ &-\left([T]+\Delta t^2\beta[S]\right)e^{n-1}\end{aligned}\,. \tag{9}$$

As far as Equation (7) is concerned, the unknowns related to one node will form a block in the mass matrix, which is the characteristic of the spectral-element time-domain method. So each node in an element can be solved independently in one time step. In Fig. 1, assuming there are two elements, the nodes in the red dashed box are marked as the coarse region while the rest nodes are marked as fine region. The two different regions do not have overlapped nodes, so no extra procedure for the interfaces of different regions is needed. In the coarse region, Equation (7) is solved explicitly. In the fine region, because the mass matrix in the left-hand side of (9) does not have the characteristic of block-diagonal, a solver is required to solve the matrix equation. The first approach uses the sparse

matrix solver UMFPACK [15], [17] with the solving process illustrated in Fig. 1. When computing Equation (9), the electric field e^{n+1} in the adjacent large cells is needed as a known quantity. As a result, in each time step, Equation (7) is solved ahead of Equation (9).

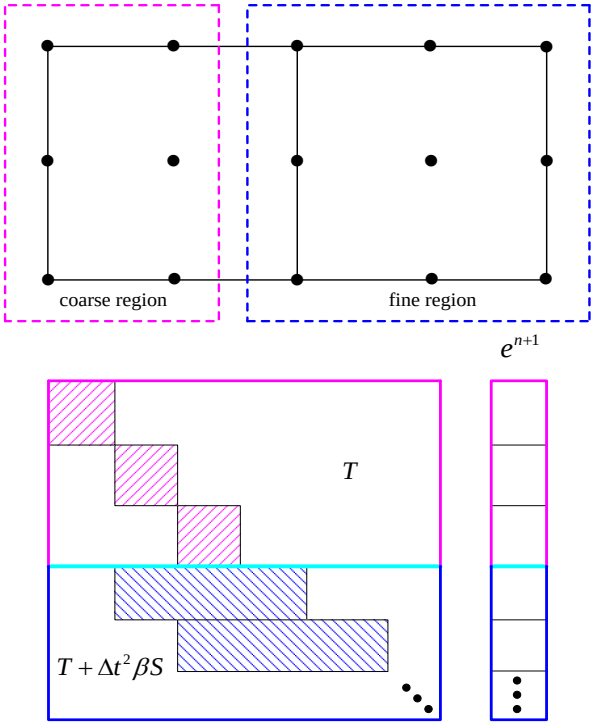

Fig. 1. Schematic diagram of the explicit-implicit scheme.

When dealing with a large problem, using the UMFPACK solver is quite time-consuming. Moreover, the solver costs additional memory because of the LU factorization. In the second scheme, a new splitting scheme is proposed, where [S] can be split into two parts, one is a block-diagonal matrix the same as [T] and is merged with [T] to form a new matrix marked as [T'], the rest is marked as [S'] and it is moved to the right-hand side of the equation:

$$\left[T'\right]e^{n+1}=\left(2\left[T\right]-\Delta t^2\left(1-2\beta\right)\left[S\right]\right)e^n-\left(\left[T\right]+\Delta t^2\beta\left[S\right]\right)e^{n-1}-\Delta t^2\beta\left[S'\right]e^{n+1}. \quad (10)$$

As the [T'] is block-diagonal, it possesses the advantage of the SETD method whose equations can be solved explicitly. Moreover, the linear system of (10) will be solved iteratively:

$$\left[T'\right]e_{k+1}^{n+1}=\left(2\left[T\right]-\Delta t^2\left(1-2\beta\right)\left[S\right]\right)e^n-\left(\left[T\right]+\Delta t^2\beta\left[S\right]\right)e^{n-1}-\Delta t^2\beta\left[S'\right]e_k^{n+1}. \quad (11)$$

Where the subscript k represents the kth iteration. Firstly, the initial value of e^{n+1} in the right-hand side of the equation is set to be the previous time step value e^n, after a few iterations for the solution e_{k+1}^{n+1}, the error is acceptable and it will then go to the next time step.

III. STABILITY ANALYSIS

The stability analysis of the system is divided into two parts. As for the coarse region, after applying the z-transform of Equation (7), we obtain:

$$\left(z-1\right)^2e\left(z\right)+\Delta t^2\mathbf{T}^{-1}\mathbf{S}ze\left(z\right)=0. \quad (12)$$

To make the scheme stable, z should be inside the unit circle of the complex z plane, which means the magnitude of z should be bounded by one. Further analysis results in the following equation:

$$\left(z-1\right)^2+\Delta t^2\lambda z=0, \quad (13)$$

where λ is the eigenvalue of $\mathbf{T}^{-1}\mathbf{S}$ and the eigenvalues are non-negative and real.

To make z in (13) bounded by 1, we can find that the time step should satisfy the condition:

$$\Delta t\le\frac{2}{\sqrt{\rho\left(\mathbf{T}^{-1}\mathbf{S}\right)}}, \quad (14)$$

where $\rho\left(\cdot\right)$ represents the spectral radius of matrix $\left(\cdot\right)$.

As for the fine region, when using the Newmark-Beta scheme, the system is unconditionally stable [10]. Convergence analysis is needed for the iterative Newmark-Beta method. If we describe the exact solution of Equation (9) as u^{n+1}, then the error of the kth iteration is [18]:

$$err_k^{n+1}=u^{n+1}-e_k^{n+1}. \quad (15)$$

From (10), we can get:

$$u^{n+1}=\Delta t^2\beta\mathbf{T}'^{-1}\mathbf{S}'u^{n+1}+b, \quad (16)$$

and from (11):

$$e_{k+1}^{n+1}=\Delta t^2\beta\mathbf{T}'^{-1}\mathbf{S}'e_k^{n+1}+b, \quad (17)$$

where

$$b=\left(2\mathbf{T}'\mathbf{T}-\Delta t^2\left(1-2\beta\right)\mathbf{T}'^{-1}\mathbf{S}\right)e^n-\left(\mathbf{T}'\mathbf{T}+\Delta t^2\beta\mathbf{T}'^{-1}\mathbf{S}\right)e^{n-1}. \quad (18)$$

Substitute (16) and (17) into (15):

$$err_{k+1}^{n+1}=\Delta t^2\beta\mathbf{T}'^{-1}\mathbf{S}'err_k^{n+1}. \quad (19)$$

As a result,

$$\left\|err_{k+1}^{n+1}\right\|=\rho\left(\Delta t^2\beta\mathbf{T}'^{-1}\mathbf{S}'\right)^{k+1}\left\|err_0^{n+1}\right\|. \quad (20)$$

We can find that only when the $\rho\left(\Delta t^2\beta\mathbf{T}'^{-1}\mathbf{S}'\right)$ is smaller than one, the iterative method can be a convergent solver.

When Δt is chosen,

$$\Delta t<\frac{2}{\sqrt{\rho\left(\mathbf{T}'^{-1}\mathbf{S}'\right)}}, \quad (21)$$

and $\beta=0.25$, we can finally get:

$$\rho\left(\Delta t^2\beta\mathbf{T}'^{-1}\mathbf{S}'\right)=\Delta t^2\beta\rho\left(\mathbf{T}'^{-1}\mathbf{S}'\right)<1. \quad (22)$$

IV. NUMERICAL RESULTS

To verify the performance of the proposed method, we carried out the simulation of a cavity as shown in Fig. 2. It is a PEC cavity and there is a dielectric ring inside. The dielectric constant of the ring was 2.06. Because the thickness of the ring was very thin, it leaded to a multiscale problem with very small cells in the ring. The hybrid method, together with the traditional SETD were employed to do the simulation and compute the resonate frequencies of the cavity. The number of the total discretized hexahedron was 10440 with 240 for the fine domain and 10200 for the coarse domain. Unstructured hexahedron mesh grids are demonstrated in Fig. 3.

To simulate the example, the traditional SETD required a time step of 1ps and 25000 steps while the explicit-implicit SETD using the UMFPACK was able to use 3730 steps to finish the simulation with a time step as large as 6.7ps. As for the explicit-implicit SETD using the iterative Newmark-Beta scheme, time step was chosen to be 3.3ps and it needed 7575 steps. It can be seen from Fig. 4 that the electric field waveform in time domain of one observation point inside the cavity agrees well with each other among the three methods. After the Fourier transform, the frequency spectrums of the electric field were shown in Fig. 5.

Excellent agreements can also be observed. Finally, the computational costs of the three methods were listed in Table 1.

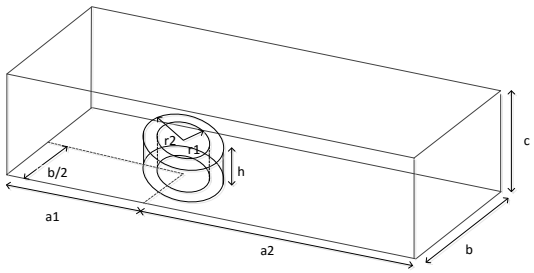

Fig. 2. A rectangular PEC cavity loaded with a dielectric ring: a1 = 207.25 mm, a2 = 440.75 mm, b = 242 mm, c = 43 mm, r1 = 9.5 mm, r2 = 10.0 mm, h=14.0 mm.

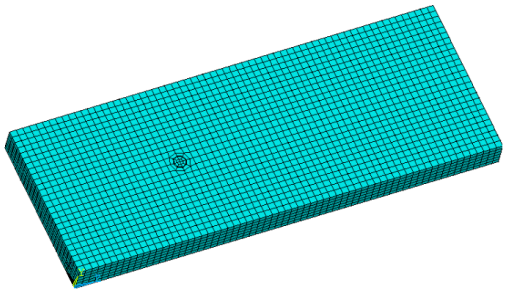

Fig. 3. Mesh grids used to model the cavity.

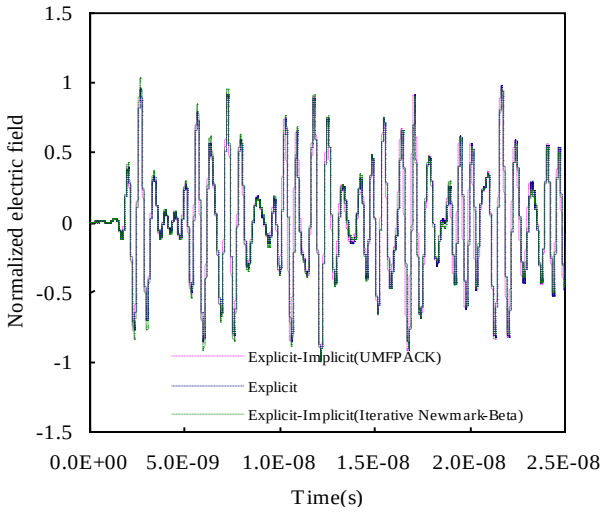

Fig. 4. Electric field in time domain calculated by three methods.

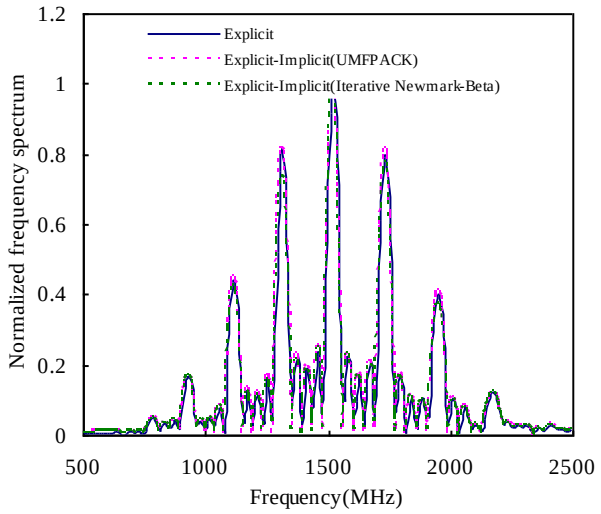

Fig. 5. Normalized frequency spectrum of the electric field.

Table 1: Comparison of the computational cost among the hybrid explicit-implicit SETD method and the traditional SETD method

	Time Step (ps)	CPU Time (min)	Memory (MB)
Explicit	1	67	1156
Explicit-Implicit (UMFPACK)	6.7	23	1639
Explicit-Implicit (Iterative Newmark-Beta)	3.3	25	1264

We can clearly find out that the proposed methods are more efficient in terms of the simulation time. The

explicit-implicit SETD with the UMFPACK solver cost approximate 1/3 simulation time of the traditional method while sacrificed more memory. The iterative Newmark-Beta scheme required a little more CPU time than the UMFPACK method as the time step couldn't be selected too large to ensure the convergence. In this example, the iterative number of the Equation is 8.

V. CONCLUSION

In this paper, we have proposed an explicit-implicit spectral-element time-domain method for the multiscale simulation. Explicit scheme is used in the coarse domain while implicit scheme is used in the fine domain. Explicit scheme can avoid solving the matrix equation. To solve the matrix equation generated by the implicit method, two schemes are developed. The first employs the UMFPACK and the second involves an iterative and explicit method. Comparisons have been made among different methods. The numerical results verify the correctness of the algorithm and demonstrate that the simulation time could be saved as the size of time step is much larger than the one chosen by conventional method. In addition, the method is very efficient when the unknowns of the fine domain are much smaller than those of the coarse domain. Because the discontinuous Galerkin technique is not involved in the proposed methods, conformal mesh grids must be ensured on the interface of different subdomains. How to use the nonconformal grids to make the methods more flexible will be our research topic in the future.

ACKNOWLEDGMENT

We would like to thank the support of Natural Science Foundation of 61431006, 61522108, Natural Science Foundation of 61271076, 61371037, Ph.D. Programs Foundation of Ministry of Education of China of 20123219110018.

REFERENCES

[1] J. Chen and Q. H. Liu, "A hybrid spectral-element/finite-element method with the explicit-implicit Runge-Kutta time stepping scheme for multiscale computation," *IEEE Antennas and Propagation Society International Symposium*, pp. 1-4, July 2010.

[2] Q. He, H. Gan, and D. Jiao, "Explicit time-domain finite-element method stabilized for an arbitrarily large time step," *IEEE Trans. Antennas Propagat*., vol. 60, no. 11, pp. 5240-5250, 2012.

[3] K. S. Yee, "Numerical solution of initial boundary value problems involving Maxwell's equations in isotropic media," *IEEE Trans. Antennas Propagat*., vol. AP-14, no. 5, pp. 302-307, May 1966.

[4] A. Taflove and S. C. Hagness, *Computational Electrodynamics: The Finite-Difference Time-Domain Method*, Boston, MA, USA: Artech House, 2000.

[5] G. Sun and C. W. Trueman, "Accuracy of three unconditionally-stable FDTD schemes for solving Maxwell's equations," *Applied Computational Electromagn. Soc. J.*, vol. 18, pp. 41-47, Nov. 2003.

[6] Y. Yang, R. S. Chen, W. C. Tang, K. Sha, and E. K. N. Yung, "Analysis of planar circuits using unconditionally stable three-dimensional ADI-FDTD method," *Microwave and Optical Technology Letters*, vol. 46, no. 2, pp. 175-179, July 2005.

[7] J. Jin, *The Finite Element Method in Electromagnetics*, New York: Wiley, 1993.

[8] R. S. Chen, L. Du, Z. B. Ye, and Y. Yang, "An efficient algorithm for implementing the Crank-Nicolson scheme in the mixed finite-element time-domain method," *IEEE Trans. Antennas Propagat*., vol. 57, no. 10, pp. 3216-3222, Oct. 2009.

[9] L. Du, R. S. Chen, Z. B. Ye, and Y. Yang, "A further study on the use of the alternating-direction implicit scheme for the finite-element time-domain method," *IEEE Antennas and Wireless Propagation Letters*, vol. 8, pp. 775-778, 2009.

[10] S. D. Gedney and U. Navsariwala, "An unconditionally stable finite-element time-domain solution of the vector wave equation," *IEEE Microw. Guided Wave Lett.*, vol. 5, no. 5, pp. 332-334, May 1995.

[11] J. Chen and Q. H. Liu, "Discontinuous Galerkin time domain methods for multiscale electromagnetic simulations: A review," *Proc. IEEE*, pp. 242-254, 2013.

[12] J. Chen and J. Wang, "Numerical simulation using HIE-FDTD method to estimate various antennas with fine scale structures," *IEEE Trans. Antennas Propagat.*, vol. 55, no. 12, pp. 3603-3612, Dec. 2007.

[13] J.-H. Lee and Q. H. Liu, "A 3-D spectral element time-domain method for electromagnetic simulation," *IEEE Trans. Microw. Theory Tech*., vol. 55, no. 5, pp. 983-991, May 2007.

[14] J.-H. Lee, T. Xiao, and Q. H. Liu, "A 3-D spectral-element method using mixed-order curl conforming vector basis functions for electromagnetic fields," *IEEE Transactions on Microwave Theory and Techniques*, vol. 54, no. 1, pp. 437-444, Jan. 2006.

[15] UMFPACK Version 5.1 User Guide, [Online]. Available: http://www.cise.ufl.edu/research/sparse/umfpack/

[16] W. H. Press, B. P. Flannery, S. A. Teukolsky, and

W. T. Vetterling, *Numerical Recipes*, New York: Cambridge Univ. Press, 1989.

[17] H. Xu and R. S. Chen, "A hybrid unconditionally/ conditionally stable parallel spectral-element time-domain algorithm for multi-scale computation," *IEEE International Conference on Computational Electromagnetics (ICCEM)*, pp. 169-171, 2015.

[18] S. M. Wang and J. Chen, "A performance study of the iterative ADI-FDTD method," *IEEE Trans. Antennas Propag*., vol. 53, no. 10, pp. 3413-3417, Oct. 2005.

Hao Xu received the B.Sc. degree in Electronic Information Engineering from the School of Electrical Engineering and Optical Technique, Nanjing University of Science and Technology, Nanjing, China, in 2010. He is currently working towards the Ph.D. degree in Electromagnetic Fields and Microwave Technology at the School of Electrical Engineering and Optical technique, Nanjing University of Science and Technology. His research interests include semiconductor simulation, RF-integrated circuits, and computational electromagnetics.

Dazhi Ding was born in Jiangsu, China, in 1979. He received the B.S. and Ph.D. degrees in Electromagnetic Field and Microwave Technique from Nanjing University of Science and Technology (NUST), Nanjing, China, in 2002 and 2007, respectively.

During 2005, he was with the Center of Wireless Communication in the City University of Hong Kong, Kowloon, as a Research Assistant. He is currently an Associate Professor with the Electronic Engineering of NJUST. He is the author or co-author of over 30 technical papers. His current research interests include computational electromagnetics, electromagnetic scattering, and radiation.

Rushan Chen (M'01) was born in Jiangsu, China. He received the B.Sc. and M.Sc. degrees from the Department of Radio Engineering, Southeast University, China, in 1987 and 1990, respectively, and the Ph.D. degree from the Department of Electronic Engineering, City University of Hong Kong, in 2001.

He joined the Department of Electrical Engineering, Nanjing University of Science and Technology (NJUST), China, where he became a Teaching Assistant in 1990 and a Lecturer in 1992. Since September 1996, he has been a Visiting Scholar with the Department of Electronic Engineering, City University of Hong Kong, first as Research Associate, then as a Senior Research Associate in July 1997, a Research Fellow in April 1998, and a Senior Research Fellow in 1999. From June to September 1999, he was also a Visiting Scholar at Montreal University, Canada. In September 1999, he was promoted to Full Professor and Associate Director of the Microwave and Communication Research Center in NJUST, and in 2007, he was appointed Head of the Department of Communication Engineering, NJUST. He was appointed as the Dean in the School of Communication and Information Engineering, Nanjing Post and Communications University in 2009. And in 2011 he was appointed as Vice Dean of the School of Electrical Engineering and Optical Technique, Nanjing University of Science and Technology. His research interests mainly include microwave millimeter-wave systems, measurements, antenna, RF-integrated circuits, and computational electromagnetics. He has authored or co-authored more than 200 papers, including over 140 papers in international journals.

Chen received the Science and Technology Advance Prize several times given by the National Military Industry Department of China, the National Education Committee of China, and Jiangsu Province. He is the recipient of the Foundation for China Distinguished Young Investigators presented by the National Science Foundation (NSF) of China in 2003. In 2008, he became a Chang-Jiang Professor under the Cheung Kong Scholar Program awarded by the Ministry of Education, China. Besides, he was selected as a Member of Electronic Science and Technology Group by Academic Degree Commission of the State Council in 2009. Chen is a Fellow of the Chinese Institute of Electronics (CIE), Vice-Presidents of Microwave Society of CIE and IEEE MTT/APS/EMC Nanjing Chapter. He serves as the Reviewer for many technical journals such as IEEE Trans. on AP and MTT, Chinese Physics etc., and now serves as an Associate Editor for the International Journal of Electronics.

Broadband CRLH Beam Scanning Leaky-Wave Antenna Designed on Dual-Layer SIW

Mohsen Niayesh [1] and Zahra Atlasbaf [2]

[1] Department of Electrical and Computer Engineering
University of Tehran, Iran
mohsenniayesh@ut.ac.ir

[2] Faculty of Electrical and Computer Engineering
University of Tarbiat modares, Iran
atlasbaf@modares.ac.ir

Abstract ─ This paper presents a broadband Composite Right/Left Handed (CRLH) leaky-wave antenna operating above the cutoff frequency based on the substrate integrated waveguide (SIW) is introduced. The proposed antenna consists of two dielectric layers, as the host of the structure, an interdigital capacitor radiation slot and a pair of twisted inductive post. The beam scanning capability of the leaky wave antennas will be achieved using CRLH, which allows radiation both in RH and LH regions. The design procedure begins with designing a unit-cell and evaluated with dispersion diagram. Based on the proposed unit-cell, the antenna structure consists of 10 units-cells, is developed at the X-band. The bandwidth of 66% has been obtained beside 105° of the beam steering angle both in the RH and LH regions, while the frequencies change from 6.5 GHz up to 9.5 GHz. The proposed antenna could be used in radar and imaging systems.

Index Terms ─ Beam scanning, Composite Right/Left Handed (CRLH), leaky-wave antenna, metamaterial, Substrate Integrated Waveguide (SIW).

I. INTRODUCTION

Many researchers have been interested in the concept of composite right left handed based antenna due to posing outstanding features beside the fabrication process in the comparison with other metamaterial structures introduced yet, which makes such structures more practical. By using CRLH, backward waves could be obtained based on its left hand properties [1]. Using the CRLH in the leaky-wave antennas, which are categorized in traveling wave antennas, could enhance the performance of these antennas including the beam steering capability [2], [3].

Many approaches are available to design balanced CRLH above the cutoff frequency and appropriate to be used as an antenna, but the most common way, is using the advantages of rectangular waveguide. Many researchers have been through the concept of CRLH based on the rectangular waveguide like [4-6]. Although these structures provide high power capability, but such structures are bulky and costly. Also, non-negligible losses will be imposed due to the nature of the waveguide. However, the proposed antenna in [4] could scan 76°, but since the proposed structure uses short stub to provide the negative permeability and consists of 20 unit-cells in rectangular waveguide structure, it becomes so massive, which makes it unable to be applicable structure.

With emerging the substrate integrated waveguide (SIW) technology, a new horizon in the microwave and antenna engineering has been evolved [7]. These structures synthesized on a planar dielectric with periodic arrays of metallic vias. This technology has desirable features such as low profile, low cost, and easily integrated with planar circuits maintaining the advantageous characteristics of conventional rectangular waveguide. Using the concept of substrate integrated waveguide (SIW) technique gives us the ability to overcome some of the limitations we are dealing with in the microwave and antenna engineering, such as high price and heavy constructed structure with waveguide technology, which is the reason why it becomes popular in recent years.

Leaky-wave antennas (LWA) uses traveling waves that radiates along a guiding structure in order to produce radiation. One of the features of LWA is the ability to beam scanning. With particular development in the recent years being directed toward planar LWAs, which have the advantage of being low profile an easy to fabricate, which has been facilitated with SIW technology.

In [8], benefiting from the concept of CRLH and

Submitted On: November 8, 2015
Accepted On: February 26, 2016

LWA, a prototype antenna is reported, which provides the bandwidth of 4.3 GHz with 15 unit-cells. Although a beam steering angle of 130° has been achieved during the frequency scan, but the radiation parameters, i.e., SLL has been dramatically changed, hence a poor performance for the practical application has been achieved.

In this paper the proposed antenna possesses the advantages of low-profile, low-cost and wideband, besides the radiation properties of the antenna will not affect the performance of the antenna. A comparison between the proposed structure with the most recent relevant aforementioned has been summarized in Table 1.

Table 1: Comparison between the reported antenna designs in literature and the proposed antenna

Ref.	Bandwidth (GHz)	Beam Scans (°)	Backward Radiation
[3]	2.9	76	No
[9]	-	40	No
[8]	4.2	130	Yes
This design	6	105	Yes

II. DESIGN PROCEDURE

A low profile antenna is proposed with a wide coverage at the X-band frequencies and also the ability to change the direction of the main lobe, which yields to have a beam scanning antenna. The proposed structure consists of three major sections, which are discussed more in details in the following. It is worthwhile to mention that the main lobe radiation angle of a leaky-wave antenna is straightforwardly determined by Equation (1). Due to the dispersion diagram of a CRLH leaky-wave antenna, such antenna theatrically could scan from the backfire (θ = -90) to endfire (θ = +90), and broadside radiation (θ = 0) is also possible and the stop band problem does not occur in such structure [10]. Figure 1 indicates the radiation angle of the main lobe when port 1 is excited and port two is terminated to the matched load which is the measurement scenario.

$$\theta(\omega) = \arcsin\left(\frac{\beta_0(\omega)}{k_0}\right). \quad (1)$$

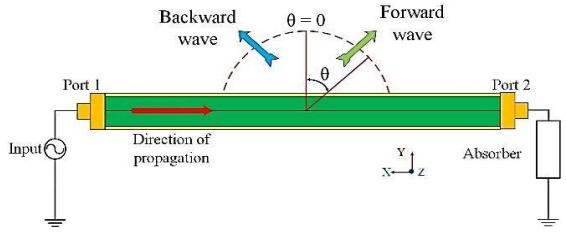

Fig. 1. The measurement, obtaining scenario for the radiation angle of the main lobe. Showing side view of the antenna including the SMA connectors.

A. SIW

In order to reduce the undesirable losses and miniaturizing the structure, the advantages of SIW technology are used in the proposed structure. The Equation (2) is used to calculate the width of the SIW [11]:

$$a_{SIW} = a_{eq} + \frac{d^2}{0.95h}. \quad (2)$$

In the Equation (2), a_{eq} is the equivalent waveguide width which is chosen as 12.13 mm with respect to the substrate of Rogers 4003c with ε_r = 3.55 and height of 0.813 mm for X-band, and d indicates the diameter of the metallic vias of the SIW. The SIW design parameters of the unit-cell with respect to Fig. 2 and Fig. 3, can be found in Table 2.

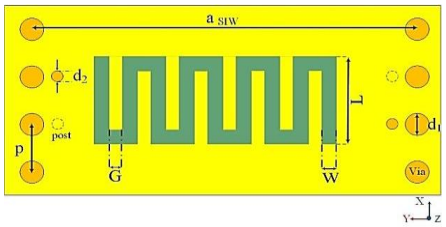

Fig. 2. Top view aspect of the proposed unit-cell structure.

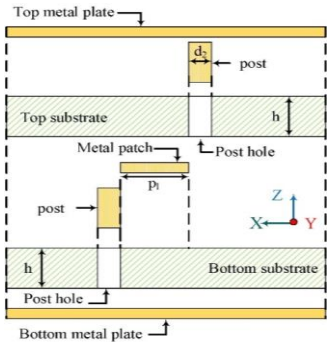

Fig. 3. Side view of the proposed unit-cell which shows the twisted post configuration.

Table 2: Design parameters of the proposed unit-cell

Quantity	Value (mm)	Description
a_{SIW}	12.736	Width of SIW
p	8.00	Adjacent via center-to-center space
d_1	0.80	Via diameter
d_2	0.50	Post diameter
Pl	0.80	Patch length
Pw	0.50	Patch width
L	3.00	IDC length
W	0.50	IDC width
G	0.50	Width of finger
h	0.813	Substrate high

B. Radiation slot

Since we are dealing with a leaky-wave antenna, and in this type of antennas the propagation occurs while the wave inside the structure travelling from the excited port to the terminated one, thus it is in need of some radiation aperture to form the leaked power. It should be noticed that the parameters of the interdigital capacitor (IDC) slots is not independent with the SIW host and the inductive posts. The schematic of the radiation slot with the design parameters are shown in Fig. 2. Using the IDC as radiation slots not only give us the controllability of the leaked power but also the balanced frequency. By increasing the length of the IDC slots (L), the provided capacitance was increased, thus the balanced frequency would be decreased. On the other hand, this capacitance decreases as the slot is widened, by increasing the W.

C. Post

Increasing the total inductance of the structure is a way to tackle the existence of band gap at the operational bandwidth of the antenna. In this way the balanced conditions will be satisfied in a higher frequency, so the left handed region will be extended. Using inductive elements to increase the inductance of the structure much more than what is provided by the nature of waveguide, is obtained with a twisted post which is realized with two metallic vias in the top and bottom substrate and are connected with each other using a metal patch etched to the top surface of the bottom substrate. Figure 3 illustrates the metallic posts and the metal patch in order to obtain the twisted post. It should be noticed that in Fig. 3 the side wall vias of the SIW are not shown for the better view of the post.

The equivalent circuit model for the proposed unit-cell could be found at Fig. 4. This circuit model consists of a series inductor (L_R) and shunt capacitor (C_R) which dictate the properties of the dielectric including the permeability and permittivity respectively. The right handed capacitor (C_R) which was used in conventional right handed circuits, is now parallel with the capacitance of the twisted post and forms a total capacitance of (C') as (3). The same procedure has been applied to the shunt inductance of the left handed inductor (L_L) and makes (L') as (4).

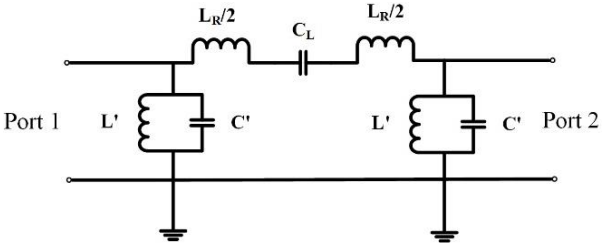

Fig. 4. Equivalent circuit model for the proposed unit-cell.

$$C' = \frac{C_R}{2} + \frac{C_P}{2} = \frac{C_R + C_P}{2}, \tag{3}$$

$$L' = \frac{L_L + L_P}{2L_L L_P}. \tag{4}$$

III. SIMULATED AND MEASURED RESULTS

The proposed structure is simulated using finite element method in a full wave simulation, to obtain the dispersion diagram of the unit-cell and also the scattering parameters of the antenna.

The dispersion diagram of the proposed unit-cell calculated and depicted as Fig. 5. The balanced condition satisfied at 6.8 GHz. The band below this frequency would be named as the left handed area. Another band which is above the balanced frequency named as Right Handed (RH) band indicated in Fig. 5. Also the airline is separated the operating region into the two separate bands, which are radiating and guiding region. The region, above the airline is the radiation region, which is ideal for antenna applications. On the other hand, the region below the airline indicates the guiding region which is used for the guiding applications. Figure 5 clarifies that the proposed unit-cell is appropriate to the antenna application.

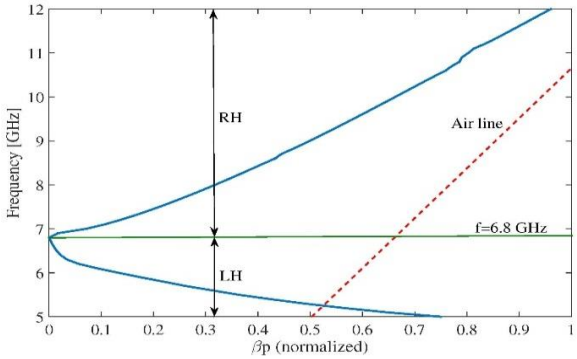

Fig. 5. Dispersion diagram of proposed the unit-cell.

Base on the unit-cell, which is discussed above, the antenna consists of 10 units-cells, is designed. The scattering parameters of the antenna are depicted in Fig. 6. Since the antenna is a leaky-wave antenna based on the mechanism of the operation, while the S_{11} is less than -10 dB and also the S_{21} is kept above -3 dB, are the ideal cases for operating the LWA. The proposed antenna provides 66% as the fractional bandwidth, based on the measurement data.

A wide variety of techniques are available to feed SIW structures, one of the popular and easiest way to design the feeding, is using the tapering transition from microstrip to SIW structure technique. Figure 7 shows the schematic of the designed tapering transition used in

the proposed antenna. The dimensions used to design the tapering transition are as: l_1=5.1 mm, l_2=5 mm, w_1=7 mm, w_2=3 mm.

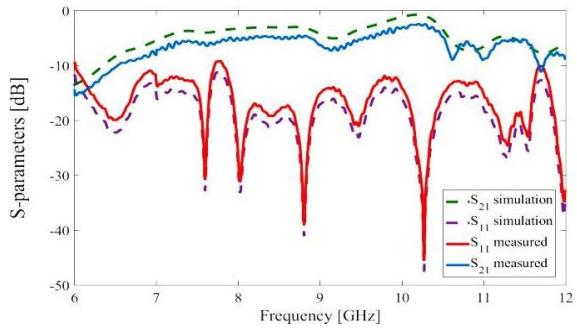

Fig. 6. Simulated and measured scattering parameters of the proposed antenna containing 10 unit-cells.

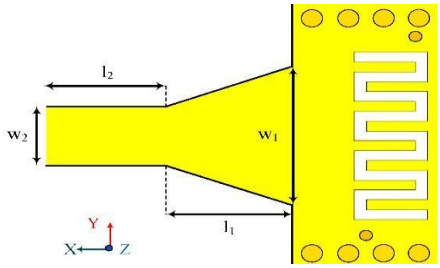

Fig. 7. Microstrip to SIW transition for feed the proposed antenna.

One of the dominant features of proposed antenna beside the wide coverage in the X-band frequency, is the ability to do the beam sweep while changing the operating frequency. The radiation pattern of the proposed antenna contains 10 unit-cells, for the simulation and measurement are depicted in Fig. 8 and Fig. 9 respectively. As it is observed, the proposed antenna can change the direction of the main lobe from -34° up to +72° angle including the broadside obtained from measurement.

On the other hand, other parameters of the antenna will be changed when the operating frequency changes and exactly this is where a tradeoff between bandwidth and the gain of the antenna should be taken into the account. The other parameters of the proposed antenna including the realized gain and side lobe level of the antenna at different frequencies could be found in Table 3. It is worthwhile to mention that another feature of the proposed structure which made it distinguishable from other similar works is the low sensitivity of the radiation parameters with respect to changing the operating frequency, that they are not affected, as it is obvious in Table 3.

The antenna is fabricated using the substrate of Rogers 4003c with ε_r = 3.55 and height of 0.813 mm. The total physical dimension of the antenna is 100.2 mm×13.53 mm×1.69 mm. The fabricated antenna can be found in Fig. 10.

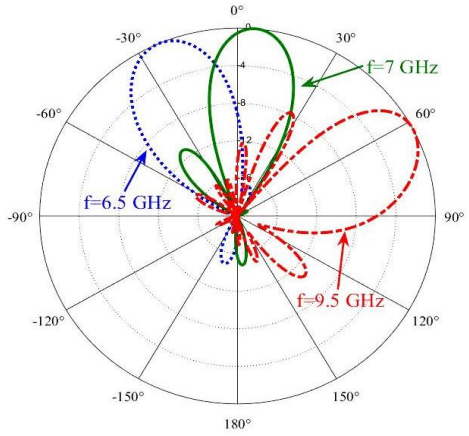

Fig. 8. The Simulated normalized radiation pattern.

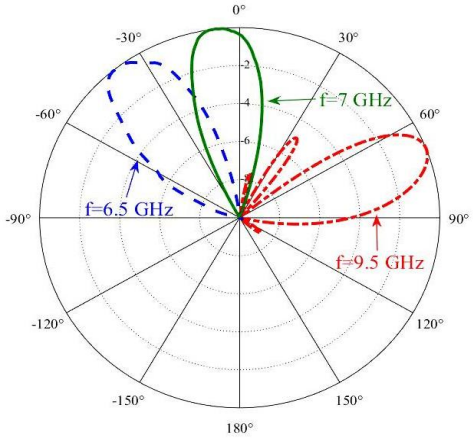

Fig. 9. Normalized radiation pattern. The radiation pattern is measured at the frequencies 6.5, 7, 9.5 GHz.

Table 3: The obtained CRLH LWA antenna radiation properties

Quantity/Freq. (GHz)	6.5	7	8	9	9.5
Simulated Gain (dB)	14.37	15.47	10.1	13.15	12.41
Measured Gain (dB)	14.18	15.28	9.95	12.72	11.18
Simulated SLL (dB)	-12.1	-13.5	-10	-11	-6.1
Measured SLL (dB)	-10.26	-11.41	-8	-9.15	-5.5
Simulated HPBW (°)	28	25.9	25.11	24.6	26.3
Measured HPBW (°)	31.79	28.2	27	26.8	28.2

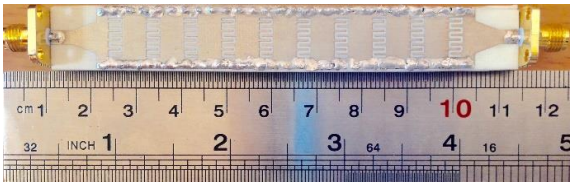

Fig. 10. Fabricated CRLH leaky-wave antenna based on SIW containing 10-unit-cells.

IV. CONCLUSION

A CRLH leaky-wave benefiting from the SIW technology, which operates above the cutoff frequency was presented. The proposed unit-cell for the antenna consists of two inductive twisted posts and an interdigital capacitor (IDC) radiation slot. The unit-cell has been evaluated with the dispersion diagram and then a 10 unit-cell antenna has been designed. The antenna has the ability to change the direction of its' main lobe continuously from -34° up to +72° besides obtaining the bandwidth of 66% according to the measurement, and there is a decent agreement between the simulation and measured results.

REFERENCES

[1] A. Grbic and G. V Eleftheriades, "Experimental verification of backward-wave radiation from a negative refractive index metamaterial," *J. Appl. Phys.*, vol. 92, no. 10, 2002.

[2] C. Caloz and T. Itoh, *Electromagnic Metamaterials: Transmission Line Theory and Microwave, The Engineering Approach*., Wiley-IEEE Press, 2005.

[3] K. Hosseini and Z. Atlasbaf, "Analysis and synthesis of singly-curved microstrip structures utilizing modified Schwarz-Christoffel transformation," *IEEE Trans. Antennas Propag*., vol. 61, no. 12, pp. 5940-5947, 2013.

[4] D.-J. Kim and J.-H. Lee, "Beam scanning leaky-wave slot antenna using balanced CRLH waveguide operating above the cutoff frequency," *IEEE Trans. Antenna Propag.*, vol. 61, no. 5, pp. 2432-2440, 2013.

[5] D.-J. Kim and J.-H. Lee, "Broadband left-handed rectangular waveguide using a shorted stub and twisted E-plane posts," *Microw. Opt. Technol. Lett.*, vol. 55, no. 4, pp. 835-840, 2013.

[6] T. Ikeda, K. Sakakibara, T. Matsui, N. Kikuma, and H. Hirayama, "Beam-scanning performance of leaky-wave slot-array antenna on variable stub-loaded left-handed waveguide," *Antennas Propagation, IEEE Trans.*, vol. 56, no. 12, pp. 3611-3618, 2008.

[7] D. Deslandes and W. Ke, "Integrated microstrip and rectangular waveguide in planar form," *Microw. Wirel. Components Lett. IEEE*, vol. 11, no. 2, pp. 68-70, 2001.

[8] D. Yuandan and T. Itoh, "Composite right/left-handed substrate integrated waveguide and half mode substrate integrated waveguide leaky-wave structures," *Antennas Propagation, IEEE Trans.*, vol. 59, no. 3, pp. 767-775, 2011.

[9] J. Tanabe, "Dual-band Composite Right/Left Hand Substrate Integrated Waveguide Leaky Wave Antenna Phased Array Design," *Ph.D.*, UCLA: Electrical Engineering, 2013.

[10] D. Yuandan and T. Itoh, "Substrate integrated composite right-/left-handed leaky-wave structure for polarization-flexible antenna application," *Antennas Propagation, IEEE Trans.*, vol. 60, no. 2, pp. 760-771, 2012.

[11] D. Deslandes and W. Ke, "Design consideration and performance analysis of substrate integrated waveguide components," in *Microwave Conference, 2002, 32nd European*, pp. 1-4, 2002.

Mohsen Niayesh was born in Tehran, Iran in Jan. 1989. He received the Bachelor's degree in Electrical Engineering specialized in Communication Engineering from the Islamic Azad University, Tehran, Iran in May 2012 and the Master's degree in Electrical Engineering major in Communication Engineering from the University of Tehran, Tehran, Iran, in Feb. 2015.

His main areas of interest in research are Metamaterial, Microstrip antenna, Radio wave propagation, Radar, On-body communication, Microwave circuits and Mobile communication.

Since early 2014 he has been with the University of Tehran as Research Assistance.

Zahra Atlasbaf (M'08) received the B.S. degree in Electrical Engineering from the University of Tehran, Tehran, Iran, in 1993, and the M.S. and Ph.D. degrees in Electrical Engineering from the University of Tarbiat Modares, Tehran, Iran, in 1996 and 2002, respectively.

She is currently an Associate Professor with the Faculty of Electrical and Computer Engineering, Tarbiat Modares University. Her research interests include numerical methods in electromagnetics, theory and applications of metamaterials, radar, mobile communications, microwave and antenna design.

Evaluation of E-Field Distribution and Human Exposure for a LTE Femtocell in an Office

Hsing-Yi Chen and Shu-Huan Wen

Department of Communications Engineering
Yuan Ze University, Chung-Li, Taoyuan, 32003, Taiwan
eehychen@saturn.yzu.edu.tw, s1034835@mail.yzu.edu.tw

Abstract ─ Firstly, the finite-difference time-domain (FDTD) method was used to calculate electric fields emitted from a long-term evolution (LTE) femtocell placed at the left-hand side of an empty office at frequencies of 700, 860, 1990, and 2600 MHz. After validating the accuracy of the FDTD method, the FDTD method was used to calculate electric field distributions inside the office, with and without the presence of 20 people and furniture for the LTE femtocell placed near the center of a horizontal plane with a distance of 1.0 m from the ceiling and transmitting a power of 10 dBm. Simulated electric fields at most of the locations on the horizontal plane with a height of 1.0 m above the floor for the office with and without the presence of 20 people and furniture are found in the range of -10 to -30 dBV/m, which means a good signal will be picked up in the office. The maximum power density emitted from the LTE inside the office and maximum localized SAR induced in a standing person are far below the ANSI/IEEE safety standard for public exposure in uncontrolled environments.

Index Terms ─ Electric field, femtocell, LTE, RF exposure, SAR.

I. INTRODUCTION

Recently, indoor wireless networks have increased interest in LTE [1-3] femtocell developments. Through self-optimized configuration and backhaul costs, a LTE femtocell can considerably lower the delivery cost per bit and make it more cost effective for operators to invest in LTE wireless networks. In the near future, LTE femtocells will play a key role in enterprise and metro deployment areas for indoor wireless communications. With the increasing use of indoor wireless networks, there is a challenge to provide a better coverage, higher cell capacity, and higher data rates for mobile applications in the initial design and planning. Therefore, EM field distribution and variability, wave propagation, and path loss of LTE femtocells in different indoor-environments such as offices, airports, railway stations, etc. should be well studied in order to ensure an adequate coverage and good performance for indoor wireless communications. Indoor wave propagation and path loss have been extensively studied, leading to improved coverage and capacity within office buildings [4-11]. The study of indoor EM field distribution and variability for indoor LTE planning and design is not available. EM field strengths at users' locations inside an office should be guaranteed above a threshold level in order to meet the best radio frequency (RF) condition where it is free from interference.

On the other hand, people are great concerned about the potential health hazards due to RF exposure from femtocells in everyday life inside indoor environments such as offices, schools, laboratories, and homes. The biological effect of long-term exposure to RF propagation is simply not known yet with certainty. Additionally, it is impossible to say that exposure to RF radiation, even at levels below safety standards and exposure guidelines, is totally without potential health risks. The potential health hazards resulting from biological effects may include cancers, neurological disorders, allergies, fatigue, sleep disturbance, dizziness, loss of mental attention, headaches, grogginess, memory problems, ringing in the ears (tinnitus), etc. Therefore, the study of long-term exposure due to RF field emission is especially important, since people spend most of their life-time in indoor environments. To access the potential health hazards due to RF fields, the specific absorption rate (SAR) in human bodies in close proximity to LTE femtocells is an important parameter for assessment. Some safety standards and exposure guidelines for human exposure at RF frequencies have been recommended by several national and international organizations such as the National Council on Radiation Protection and Measurements (NCRP) [12], the American National Standards Institute/Institute of Electrical and Electronics Engineers (ANSI/IEEE) [13], and the International Commissions on Non-Ionizing Radiation Protection (ICNIRP) [14]. These safety standards and guidelines define basic restriction and reference levels for human exposure at different frequencies. In the last few years, a few studies have focused on RF exposures in outdoor environments. Some reports about RF

Submitted On: October 12, 2015
Accepted On: February 25, 2016

exposure in outdoor environments are available in the literature [15-19]. A few reports about exposure to RF fields emitted from femtocell in indoor environments are also available in the literature [20-24].

Therefore, it is an important trade-off issue for RF engineers to design a safe indoor environment with LTE femtocells and also to keep RF field intensities above a threshold level for good indoor wireless communications. In this paper, the FDTD method [25] was first used to calculate electric fields emitted from a LTE femtocell placed at a fixed location inside an empty office. The validity of the FDTD method was checked by comparing numerical results of electric field distributions with measurement data obtained using a Narda Model NBM-3006 high frequency selective radiation meter [26]. After validating the accuracy of the FDTD method, the FDTD method was used to calculate electric field distributions for the LTE femtocell placed at the center of a horizontal plane with a distance of 1.0 m from the ceiling inside the office with and without the presence of 20 people and furniture. Localized SARs induced in 20 people were also calculated for the 20 people standing up and sitting on 20 metallic chairs in front of 20 wooden desks inside the office. Numerical results of localized SARs were used to verify whether the office complies with safety standards and guidelines for human exposure to RF fields at frequencies of 700, 860, 1990, and 2600 MHz.

II. THE FDTD MODEL

The FDTD method [25] is a direct solution for Maxwell's time-dependent curl equations. It is based on space-time mesh sampling of the unknown electromagnetic (EM) fields within and surrounding the object of interest. Due to its accuracy and simplicity, the FDTD method has been widely applied in antenna design, electromagnetic interference (EMI), EM wave propagation and scattering problems, design of microwave circuits, photonic device design, bioelectromagnetics, and many electromagnetic problems. In the FDTD solution procedure, the coupled Maxwell's equations in differential form are solved for various points of the scatter as well as the surrounding in a time-stepping manner until converged solutions are obtained. Following Yee's notation and using centered difference approximation on both the time and space first-order partial differentiations, six finite-difference equations for six unique field components within a unit cell are obtained. In these six finite-difference equations, electric fields are assigned to half-integer (n+1/2) time steps and magnetic fields are assigned to integer (n) time steps for the temporal discretization of fields. To ensure numerical stability, the time step δ_t is set to $\delta/(2C_o)$, where δ and C_o are the cell size and the speed of light, respectively. The center difference approximation ensures that the spatial and temporal discretizations have second-order accuracy, where errors are proportional to the square of the cell size and time increment [25]. An important problem encountered in solving the time-domain electromagnetic-field equation, by the FDTD method, is the absorbing boundary conditions. Several absorbing boundary conditions (ABC) have been proposed in the FDTD method such as second-order Mur [27], and Liao [28], and perfectly matched layer (PML) [29]. Liao's ABC and PML require a lot of memory. Second-order Mur absorbing boundary conditions are among the most frequently cited, and work in many cases. In our formulation, the second-order Mur approximation of absorbing boundary conditions [27] is used for the near-field irradiation problems. The second-order Mur absorbing boundaries are employed because they do not require much memory and have a reasonable accuracy. In this study, the external absorbing boundaries are placed at a distance of 8 δ on all sides of the scattering object as shown in Fig. 1, where δ is the cell size.

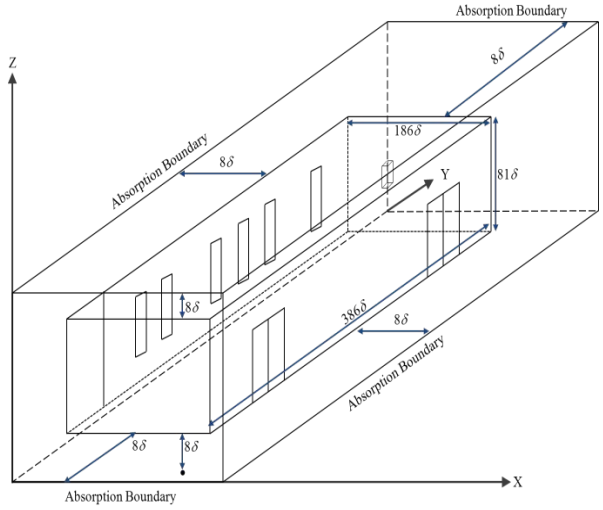

Fig. 1. FDTD model with 202×402×97=7876788 cubic cells. The cell size is 5 cm.

III. DESCRIPTION OF THE OFFICE AND LTE FEMTOCELL

Research work was conducted in an office on the tenth floor of building 7 at Yuan Ze University as shown in Fig. 2. The office has a dimension of 19×9×3.65 m and consists of two reinforced concrete slabs (ceiling and floor) with a thickness of 20 cm, two reinforced concrete walls with a thickness of 15 cm, two concrete block walls with a thickness of 15 cm, two wooden doors with a thickness of 5 cm, seven glass windows with a thickness of 1 cm, and four square reinforced concrete columns with a side length of 80 cm. The floor plan and detail dimensions of the empty office are shown in Fig. 2 (b). Relative dielectric constants and conductivities of various materials used for constructing the office at frequencies of 700, 860, 1990, and 2600 MHz [30-35] are listed in Table 1. Figure 3 (a) shows a LTE femtocell

consisting of four larger and four smaller dipole radiators designed for operating at frequencies of 698~960 and 1710~2700 MHz, respectively. The larger and the smaller radiators have dimensions of 11×3 and 4×1.5 cm respectively. The larger and smaller radiators are mounted on two different metallic plates with heights of 10 and 5 cm, respectively. Metallic plates are designed to increase the electric field strength in air. The larger and smaller metallic plates have dimensions of 30×30 and 15×15 cm, respectively. Two large radiators are opposite each other and are separated by a distance of 18 cm, and two small radiators, also opposite each other, have a distance of 8.2 cm between them. The LTE femtocell is designed to have radiation patterns normal to metallic plates with a gain of 6.1~9.8 dBi in frequency bands of 698~960 and 1710~2700 MHz.

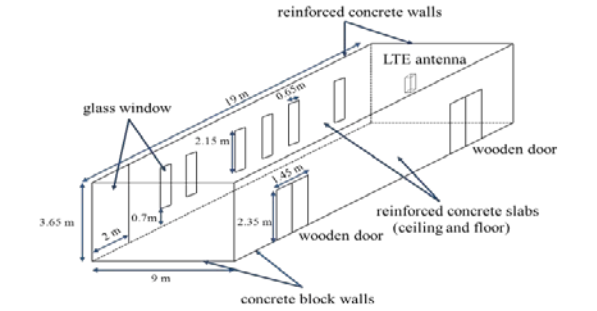

(a) Illustration of the office

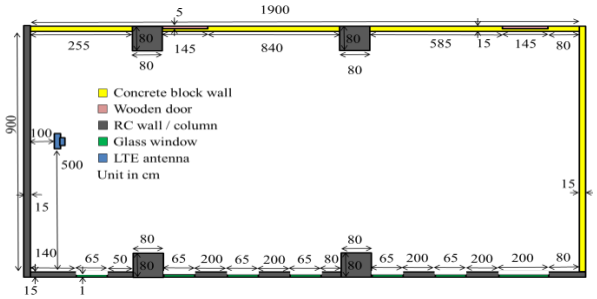

(b) Floor plan of the office with indication of the LTE femtocell

Fig. 2. The office and dimensions of walls, windows, doors, columns, and slabs.

IV. SIMULATION AND MEASUREMENT

Measurements of electric fields emitted from the LTE femtocell, placed at a height of 1.0 m above the floor on the left-hand side of the empty office as shown in Fig. 2 (b), were made at 700, 860, 1990, and 2600 MHz. The LTE femtocell was fed with a continuous sine wave generated from a signal generator Anritsu MG3694B at frequencies of 700, 860, 1990, and 2600 MHz. The emitting power of the LTE femtocell was set to be 10 dBm. Electric fields on a horizontal plane with a height of 1 m above the floor inside the empty office were measured by using a Narda Model NBM-3006 high frequency selective radiation meter. The Narda Model NRM-3006, having an isotropic E-field probe with three axis antennas, is designed to measure RF and microwave fields over the frequency range from 27 MHz to 6.0 GHz. The Narda Model NBM-3006 has an ultra-wide dynamic range from 50 V/m to 200 V/m for the frequency range of 27 MHz-6.0 GHz. Before starting measurements, a fast frequency scanning had been performed to ensure that background signals were excluded and measured frequencies were clean. In measurement, any two adjacent test points were kept at a distance of 50 cm and the Narda Model NRM-3006 was set by a very narrow-band of 1 kHz for each measured frequency. Maximum-hold measurements of all present signals were executed for about 3 minutes at each measured location. It took about 32 hours to measure electric fields at 684 grid points in the empty office for each frequency.

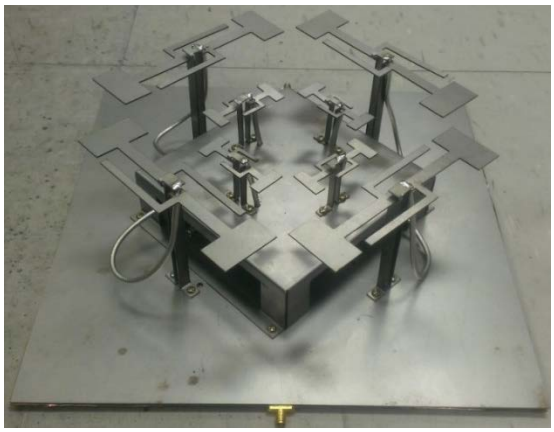

(a) The LTE femtocell

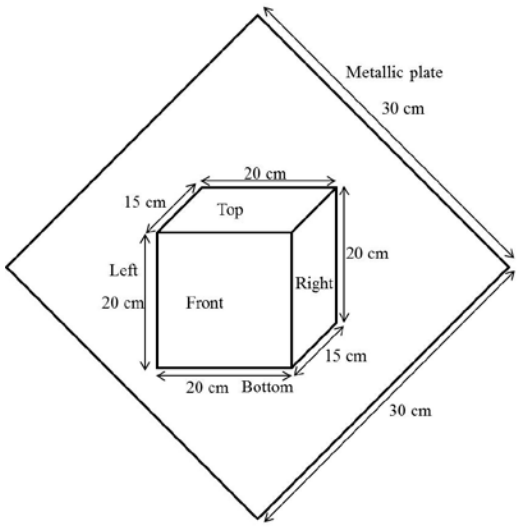

(b) Measurement locations of source fields at front, left, right, top, and bottom surfaces

Fig. 3. Picture of the LTE femtocell and locations of source fields.

In order to model the entire problem space with a uniform cell size of 5 cm, the spaces occupied by the LTE femtocell and the glass window were replaced by two different equivalent materials with many uniform cells. The equivalent material is obtained by the effective material property technique [36]. The formula of the effective material property technique is described as following:

$$\varepsilon_{eq}^{*} = \varepsilon_{air} + \frac{3V_f \times \varepsilon_{air}(\varepsilon_{m/g}^{*} - \varepsilon_{air})/(\varepsilon_{m/g}^{*} + 2\varepsilon_{air})}{1 - V_f(\varepsilon_{m/g}^{*} - \varepsilon_{air})/(\varepsilon_{m/g}^{*} + 2\varepsilon_{air})} = \varepsilon_{eq}^{'} - j\varepsilon_{eq}^{''}, \quad (1)$$

where ε_{air} and V_f are the relative dielectric constant of air and volume fraction occupied by the metallic material or the glass in a unit volume, $\varepsilon_{eq}^{'}$ and $\varepsilon_{eq}^{''}$ are the real and imaginary parts of the equivalent complex relative permittivity ε_{eq}^{*}, and $\varepsilon_{m/g}^{*}$ is the complex relative permittivity of the metallic material or the glass, respectively. It should be noted that, the imaginary part of ε_{eq}^{*} can be expressed by $\varepsilon_{eq}^{''} = \frac{\sigma_{eq}}{\omega\varepsilon_0}$, where σ_{eq} is the conductivity of an equivalent material, ω is the angular frequency, ε_0 is the dielectric constant of air, respectively. Equivalent materials in the spaces occupied by the LTE femtocell and the glass window were obtained by assuming volume fractions of 0.023 and 0.20 for the copper and the glass, respectively. Relative dielectric constants and conductivities of the equivalent materials in the spaces occupied by the LTE femtocell and the glass window are listed in Table 1. The office model has 202×402×97=7876788 cubic cells with cell size of 5 cm. For FDTD simulations, the measurement results of electric fields in the vicinity of the LTE femtocell were used as the initial sinusoidal time varying electric fields (source fields) in the FDTD model. The measurement locations of source fields at front, left, right, top, and bottom surfaces are shown in Fig. 3 (b). The measured electric fields in the vicinity of the LTE femtocell in x-, y-, and z-axis at various frequencies are listed in Table 2. In FDTD simulations, all materials were assumed to be non-magnetic (μ_r = 1.0). Simulation and measurement results of electric field distributions on a horizontal plane with a height of 1 m above the floor inside the empty office at 700, 860, 1990, and 2600 MHz are shown in Figs. 4-7. It took about 2-4 hours to run a FDTD simulation with 7876788 cubic cells in a HP work station depending on the frequency to be simulated. From Figs. 4-7, it is shown that measurement data make a good agreement with simulation results. It is also found that the field strength near the LTE femtocell has a maximum value of about 15 dBV/m and decays rapidly to about -30 dBV/m as the separation distance from the LTE femtocell increases from 0 to 19 m.

Table 1: Relative dielectric constants and conductivities of various materials

Frequency	700 MHz		860 MHz		1990 MHz		2600 MHz	
Materials	ε_r	$\sigma(S/m)$	ε_r	$\sigma(S/m)$	ε_r	$\sigma(S/m)$	ε_r	$\sigma(S/m)$
Glass	5.22	5.71×10^{-4}	5.21	7.04×10^{-4}	5.19	1.90×10^{-3}	5.17	2.93×10^{-3}
Space occupied by glass	1.40	2.53×10^{-5}	1.40	3.12×10^{-5}	1.39	8.48×10^{-5}	1.39	1.31×10^{-4}
Wood	2.99	8.51×10^{-3}	2.98	1.10×10^{-2}	2.96	2.26×10^{-2}	2.95	3.14×10^{-2}
Concrete block	4.75	9.73×10^{-3}	4.62	1.31×10^{-2}	4.53	2.70×10^{-2}	4.42	4.02×10^{-2}
RC wall/ Slab/Column	6.25	1.16×10^{-2}	6.13	3.25×10^{-2}	5.98	6.51×10^{-2}	5.90	1.02×10^{-1}
Iron	1.00	1.07×10^{7}	1.00	1.07×10^{7}	1.00	1.07×10^{7}	1.00	1.07×10^{7}
Copper	1.00	5.80×10^{7}	1.00	5.80×10^{7}	1.00	5.80×10^{7}	1.00	5.80×10^{7}
Space occupied by femtocell	1.07	5.67×10^{-12}	1.07	8.56×10^{-12}	1.07	4.58×10^{-11}	1.07	7.82×10^{-11}
Muscle	55.8	0.88	55.2	0.93	53.3	1.59	52.49	1.83
Computer case	1.00	1.07×10^{7}	1.00	1.07×10^{7}	1.00	1.07×10^{7}	1.00	1.07×10^{7}
Epoxy resin substrate	4.15	3.12×10^{-3}	4.13	3.71×10^{-3}	4.04	8.06×10^{-3}	3.99	1.02×10^{-2}
Plastics	2.54	3.32×10^{-5}	2.51	3.96×10^{-5}	2.35	8.58×10^{-5}	2.25	1.09×10^{-4}
Equivalent material of computer case	1.06	2.66×10^{-11}	1.06	4.01×10^{-11}	1.06	2.15×10^{-10}	1.06	3.66×10^{-10}
Interior of computer	1.47	1.53×10^{-4}	1.46	1.83×10^{-4}	1.46	4.10×10^{-4}	1.45	5.28×10^{-4}
Monitor	1.72	8.16×10^{-6}	1.71	9.85×10^{-6}	1.66	2.26×10^{-5}	1.63	2.99×10^{-5}

After checking the accuracy of the FDTD method, the FDTD method was used to study electric field distributions on a horizontal plane with a height of 1.0 m above the floor of the office with and without the presence of 20 people and furniture. In the study, a homogeneous model having a height of 180 cm and constructed with 808 cubical cells was used to model a standing or sitting person as shown in Fig. 8. To ensure an exposure minimization and to provide a more homogeneous field strength distribution (better signal coverage) in the office, the LTE femtocell was placed near the center of a horizontal plane having a distance of 1.0 m from the ceiling. The 20 people were simultaneously assumed to stand up or sit on 20 metallic chairs in front of 20 wooden desks as shown in Fig. 9. Figure 10 shows a computer model consisting of a mainframe and one monitor used for FDTD simulations. Equivalent electric properties of the interior of the mainframe are obtained from the effective material property technique [36] by assuming volume fractions of 0.1, 0.4, and 0.5 for the copper, epoxy resin substrates, and air located inside the interior of the mainframe, respectively. Equivalent electric properties of the computer case are obtained by assuming volume fractions of 0.02 and 0.98 for the iron and air, respectively. Equivalent electric properties of the monitor are obtained by assuming volume fractions of 0.05, 0.35, and 0.6 for the copper, plastics, and air occupied in the monitor, respectively. Relative dielectric constants and conductivities of various equivalent materials used for constructing the computer at frequencies of 700, 860, 1990, and 2600 MHz [30-35] are listed in Table 1. Figures 11-14 show the comparison of electric field distributions on a horizontal plane with a height of 1.0 m above the floor for the office with and without the presence of 20 people and furniture at 700, 860, 1990, and 2600 MHz, respectively. It is clear that the presence of 20 people and furniture affects distribution of the electric field strengths inside the office. The electric field strengths in the vicinity of 20 wooden desks have 5-10 dBV/m drops due to the impact of shadowing effect of the 20 people and furniture as shown in Figs. 11-14. It is also found that the electric field strength in the back of a metallic chair has a very low value of about -100 dBV/m. From Figs. 11-14, electric field strengths at most locations on the horizontal plane with a height of 1.0 m above the floor for the office with and without the presence of 20 people and furniture are found in the range of -10 to -30 dBV/m at 700, 860, 1990, and 2600 MHz. Since the basic sensitivity requirement for a user terminal is -83.61 dBV/m (based on -110 dBm which is corresponding to a power density of 5.8×10^{-12} W/m^2 [33]), the minimum electric field strength of -30 dBV/m obtained inside the office means a good signal will be picked up in the office. According to ANSI/IEEE standards for public exposure in uncontrolled environments, the maximum permissible exposure at frequencies of 700-2600 MHz should be below 4.6-17.3 W/m^2. It is clear that the maximum power density emitted from the LTE femtocell is about 1.326×10^{-4} W/m^2 (converted from -10 dBV/m) which is far below the ANSI/IEEE standard for public exposure.

Table 2: Measured electric fields in the vicinity of the femtocell in x-, y-, z-axis at frequencies of 700, 860, 1990, and 2600 MHz. Locations of E-field sources related to the x, y, and z coordinates are front surface (92~95, 360, 24~28) δ, left surface (92, 361~362, 24~28) δ, right surface (95, 361~362, 24~28) δ, top surface (92~95, 360~362, 29) δ, and bottom surface (92~95, 360~362, 23) δ. The cell size δ is 5 cm

	700 MHz					860 MHz				
E-field (V/m)	Front	Left	Right	Top	Bottom	Front	Left	Right	Top	Bottom
E_x	4.17	1.23	1.77	1.80	2.67	5.92	0.48	2.72	1.27	1.95
E_y	1.82	1.41	1.69	0.67	1.31	3.88	1.22	2.12	1.67	1.39
E_z	1.70	0.43	0.84	2.09	1.19	4.65	0.20	0.97	0.75	2.13
	1990 MHz					2600 MHz				
E-field (V/m)	Front	Left	Right	Top	Bottom	Front	Left	Right	Top	Bottom
E_x	5.01	0.41	0.94	0.43	1.00	6.17	0.69	1.66	0.50	1.31
E_y	2.43	0.10	0.55	0.39	0.49	5.63	0.41	0.76	1.09	0.50
E_z	4.40	0.12	0.13	0.73	1.09	4.35	0.61	0.56	0.58	1.68

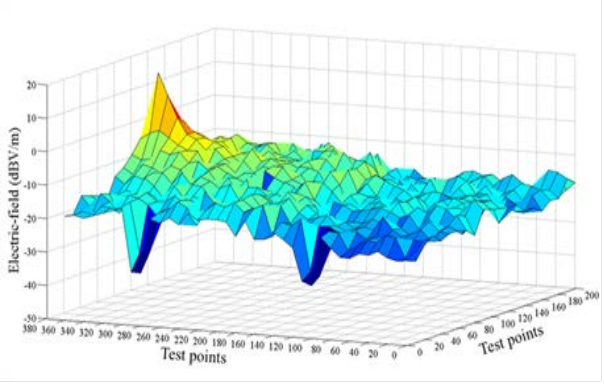

(a) Measurement

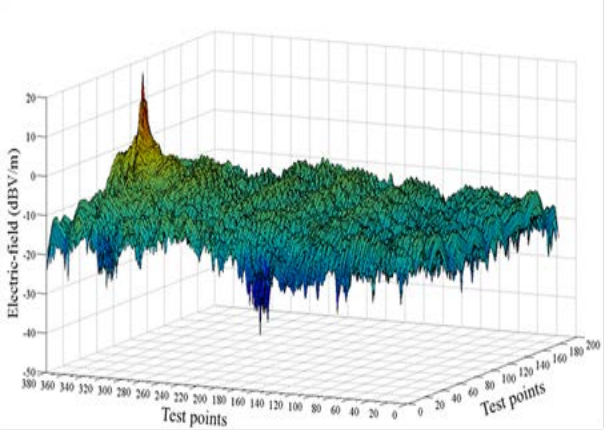

(b) Simulation

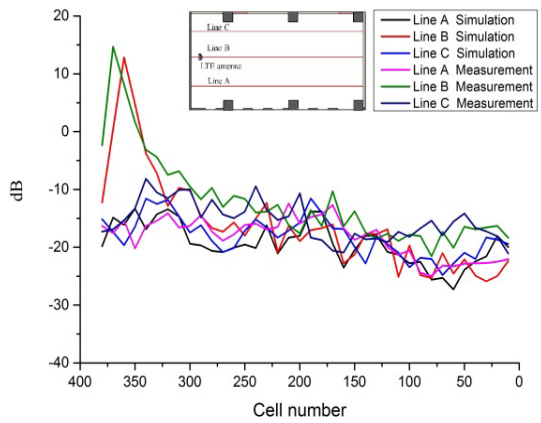

(c) Comparison of measured and simulated electric fields at lines A, B, and C

Fig. 4. Measurement and simulation results of electric field distributions on a horizontal plane with a height of 1 m above the floor inside the empty office at 700 MHz.

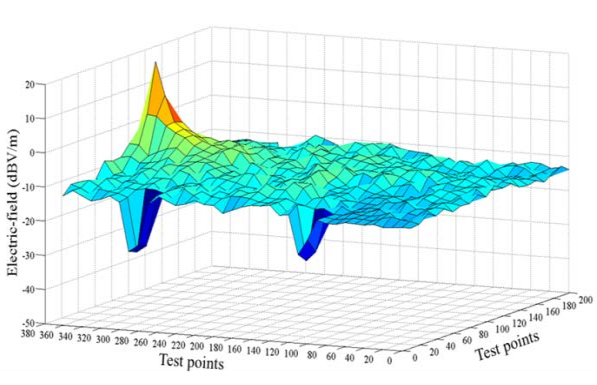

(a) Measurement

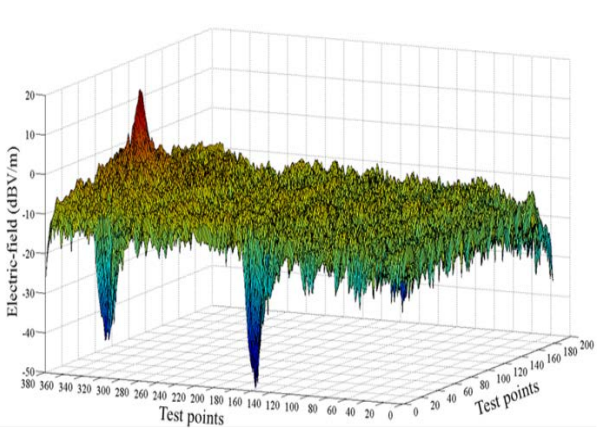

(b) Simulation

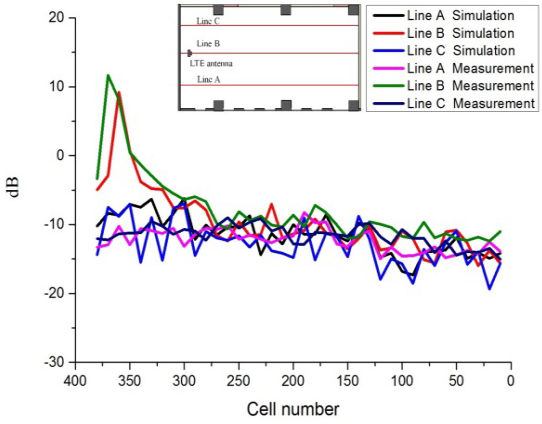

(c) Comparison of measured and simulated electric fields at lines A, B, and C

Fig. 5. Measurement and simulation results of electric field distributions on a horizontal plane with a height of 1 m above the floor inside the empty office at 860 MHz.

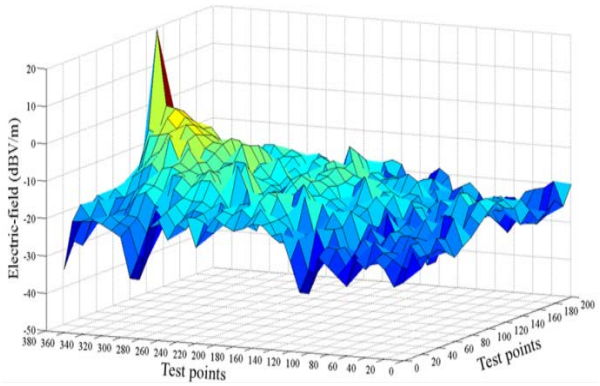

(a) Measurement

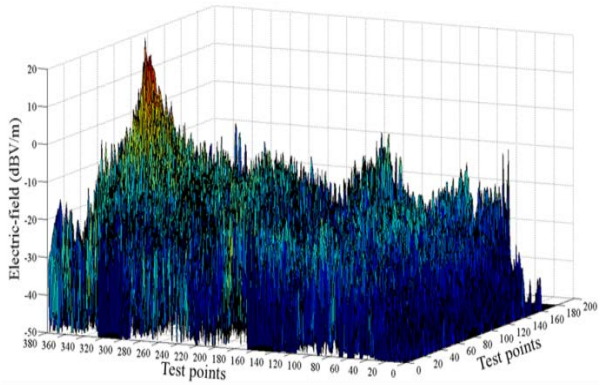

(b) Simulation

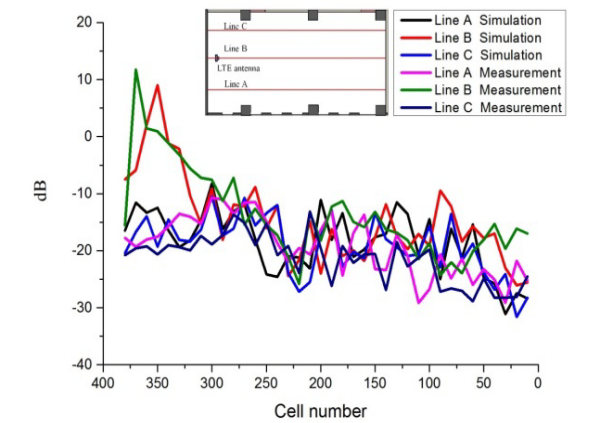

(c) Comparison of measured and simulated electric fields at lines A, B, and C

Fig. 6. Measurement and simulation results of electric field distributions on a horizontal plane with a height of 1 m above the floor inside the empty office at 1900 MHz.

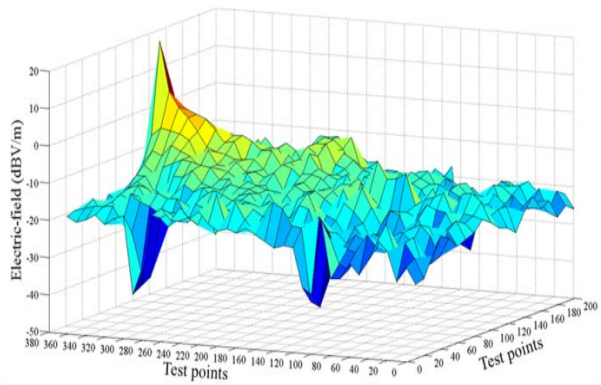

(a) Measurement

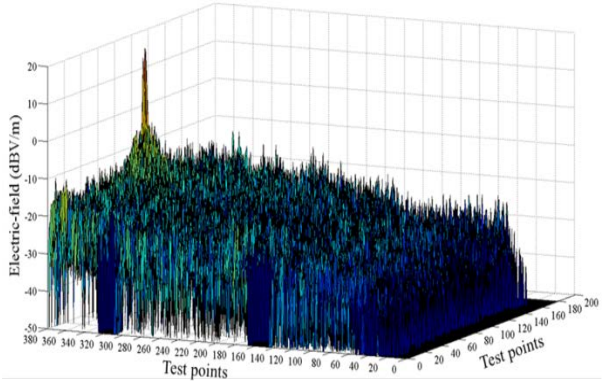

(b) Simulation

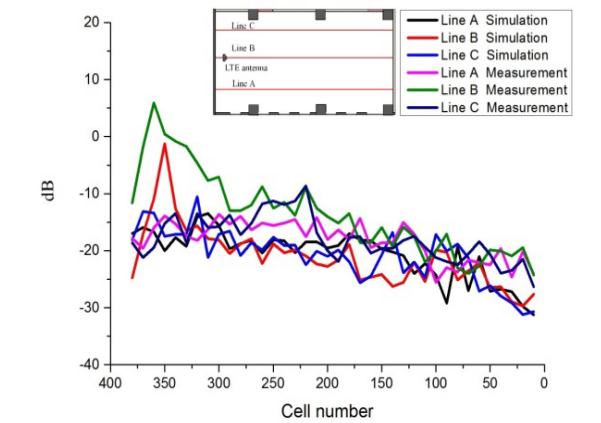

(c) Comparison of measured and simulated electric fields at lines A, B, and C

Fig. 7. Measurement and simulation results of electric field distributions on a horizontal plane with a height of 1 m above the floor inside the empty office at 2600 MHz.

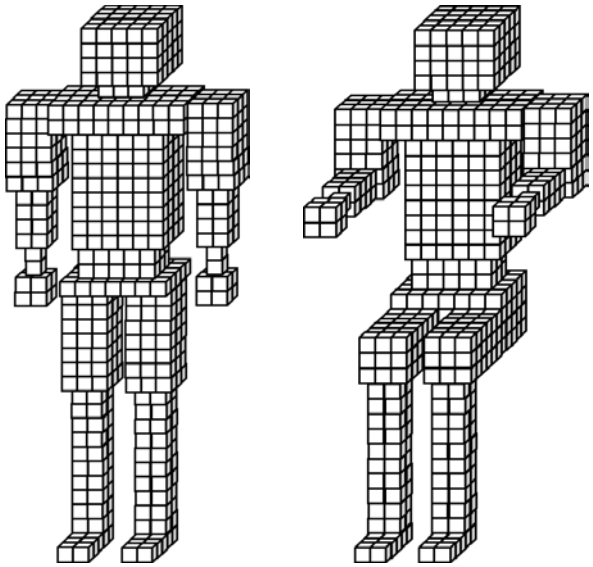

(a) Standing up (b) Sitting on a chair

Fig. 8. A homogeneous human model constructed with 808 cubical cells. The cell size is 5 cm.

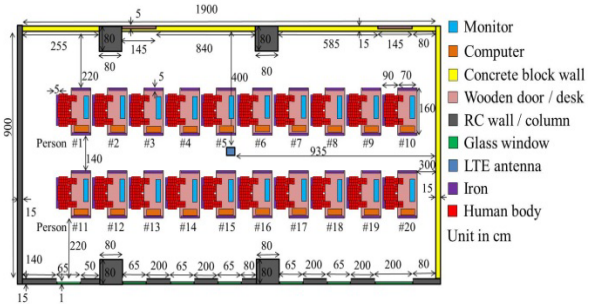

Fig. 9. Locations of 20 people and furniture inside the office.

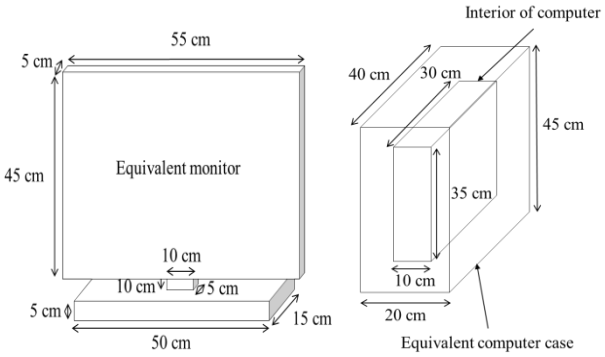

(a) Monitor (b) Mainframe

Fig. 10. A computer model used for FDTD simulations.

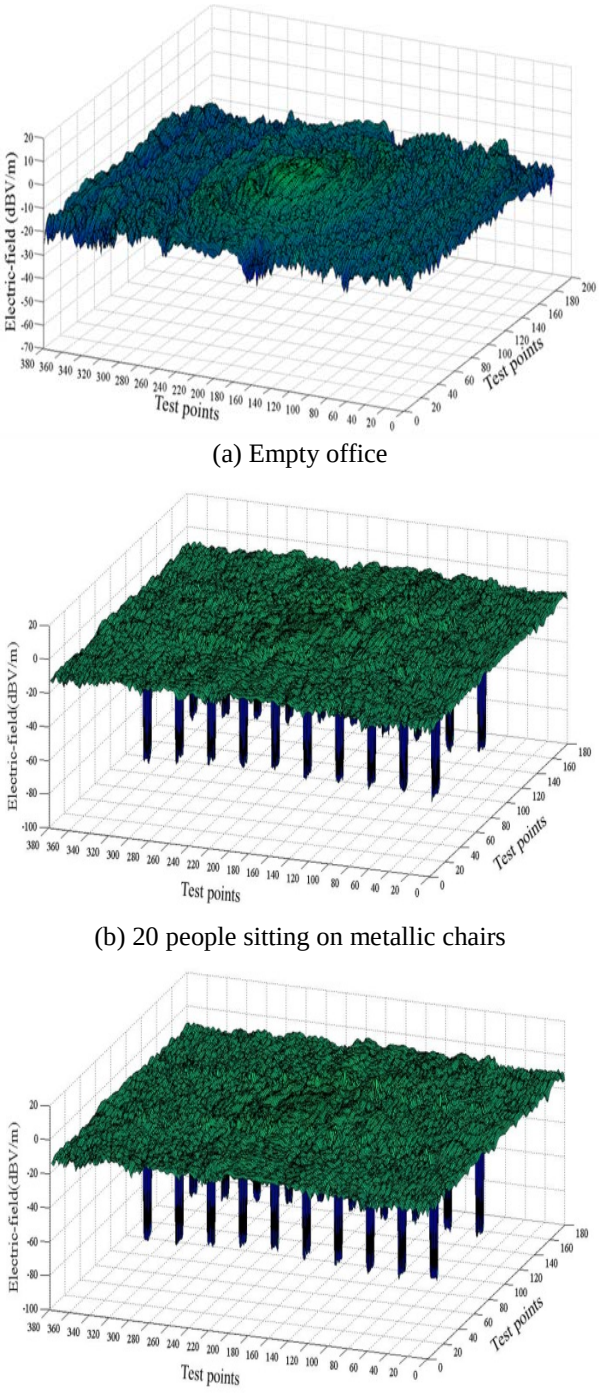

(a) Empty office

(b) 20 people sitting on metallic chairs

(c) 20 people standing up

Fig. 11. Comparison of electric field distributions on a horizontal plane with a height of 1.0 m above the floor for the office with and without the presence of 20 people and furniture at 700 MHz.

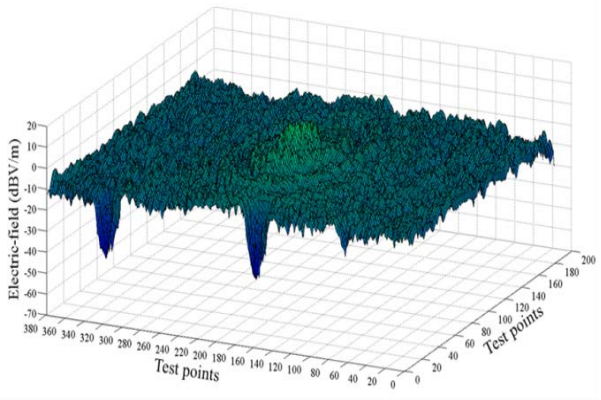

(a) Empty office

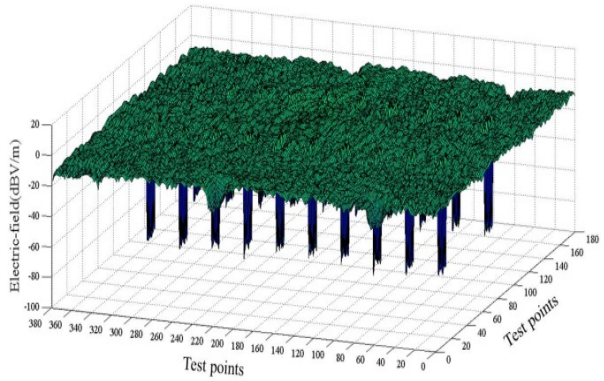

(b) 20 people sitting on metallic chairs

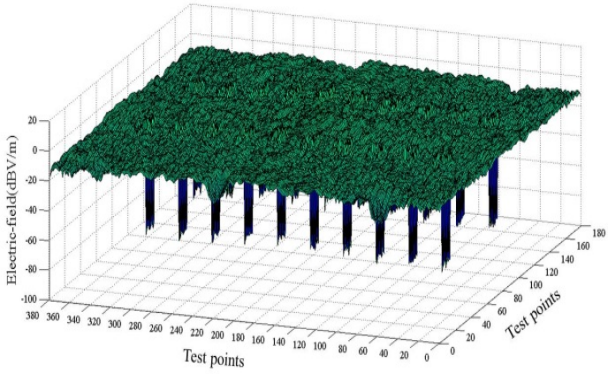

(c) 20 people standing up

Fig. 12. Comparison of electric field distributions on a horizontal plane with a height of 1.0 m above the floor for the office with and without the presence of 20 people and furniture at 860 MHz.

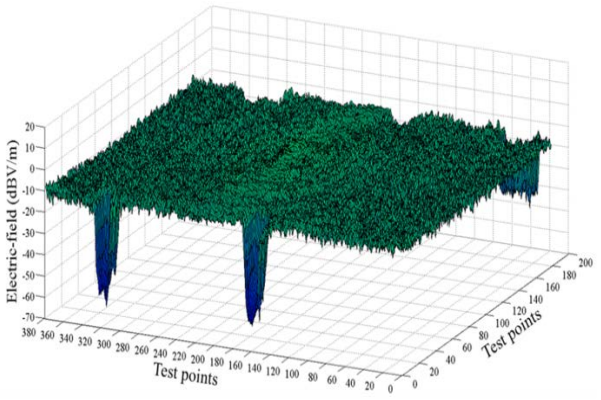

(a) Empty office

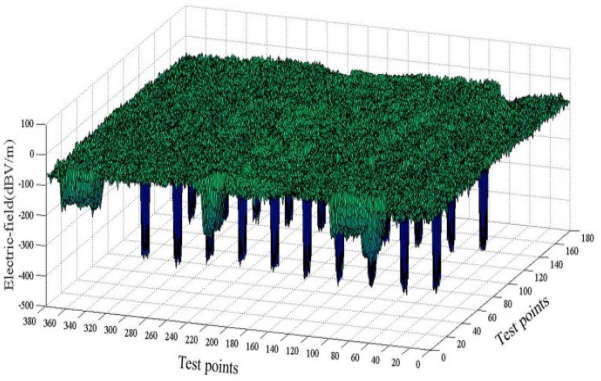

(b) 20 people sitting on metallic chairs

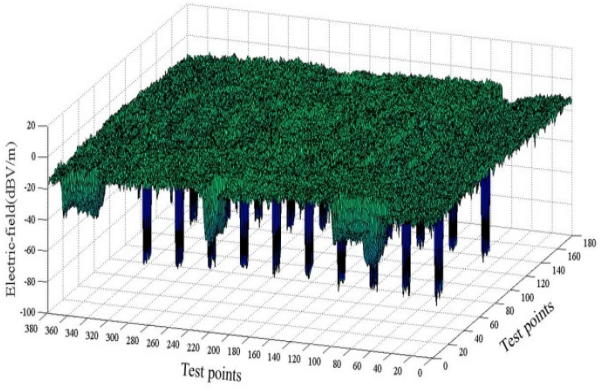

(c) 20 people standing up

Fig. 13. Comparison of electric field distributions on a horizontal plane with a height of 1.0 m above the floor for the office with and without the presence of 20 people and furniture at 1990 MHz.

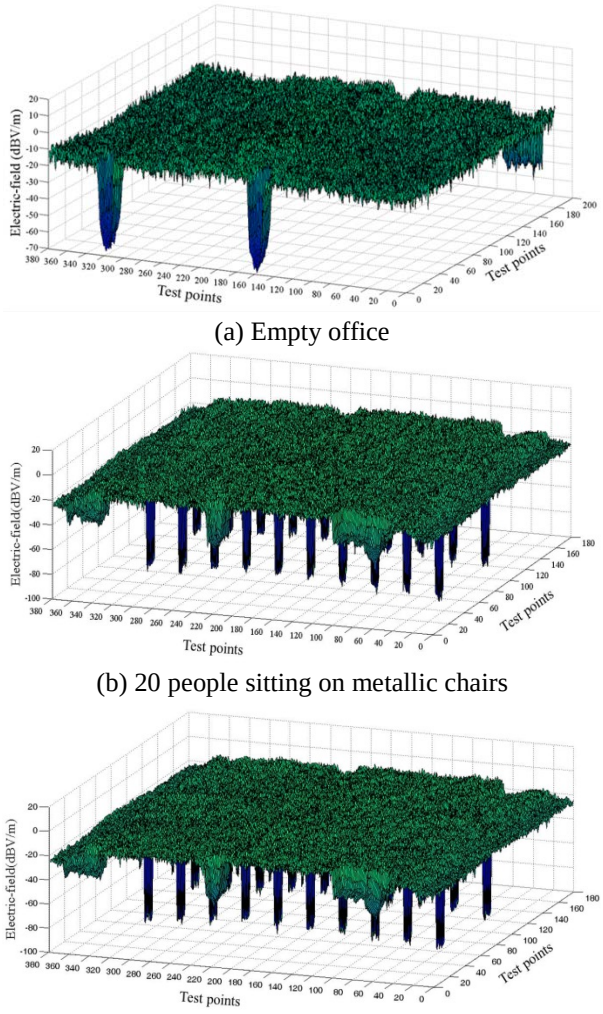

(a) Empty office

(b) 20 people sitting on metallic chairs

(c) 20 people standing up

Fig. 14. Comparison of electric field distributions on a horizontal plane with a height of 1.0 m above the floor for the office with and without the presence of 20 people and furniture at 2600 MHz.

In addition, the EM absorption in 20 people was also studied. The dielectric constants and conductivities of muscle tissue used for the homogeneous human model at various frequencies were obtained from the published literature [38] as shown in Table 1. The mass density of muscle was adopted to be 1040 kg/m^3. The human body was assumed to stand up or sit on a metallic chair in front of a wooden desk. After having obtained the induced electric field by the FDTD method, the localized SAR in each human body was calculated by the following equation:

$$\mathrm{SAR} = \sigma E^2 / 2\rho \qquad \mathrm{W/kg}, \qquad (2)$$

where σ, ρ, and E are the conductivity, mass density of muscle, and electric field induced in the human body, respectively. N = 808 is total number of cubical cells used in a human model. Figures 15-18 show localized SARs induced in the 20 people at 700, 860, 1990, and 2600 MHz, respectively. It is found that the maximum localized SARs of 1.07×10^{-5} and 9.14×10^{-6} W/kg are induced in the person numbered 5 when standing up and sitting on a metallic chair at 860 MHz, respectively. The minimum localized SARs of 4.03×10^{-11} and 2.21×10^{-11} W/kg are induced in the person numbered 12 when standing up and sitting on a metallic chair at 2660 MHz, respectively. From Figs. 15-18, it is obvious that standing people tend to have a higher SAR value than sitting people. This is because a standing person is much closer to the LTE femtocell than a sitting person. It is clear that the maximum localized SAR of 1.04×10^{-5} W/kg induced in the standing person numbered 5 is far below the ANSI/IEEE safety standard of 1.6 W/kg for public exposure in uncontrolled environments. Furthermore, the maximum localized SAR of 1.04×10^{-5} W/kg is also far below the SAR levels of 1-4 W/kg which can be subject to biological effects [39].

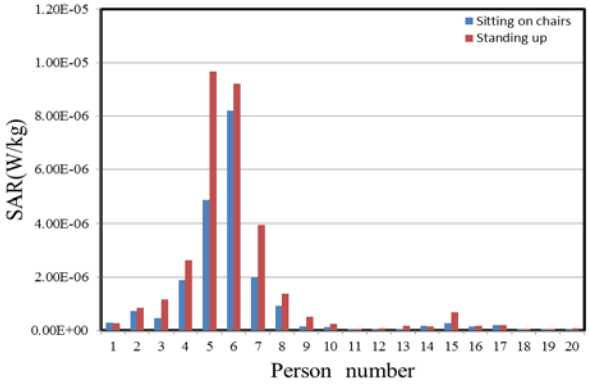

Fig. 15. Localized SARs induced in 20 people standing up and sitting on metallic chairs at 700 MHz.

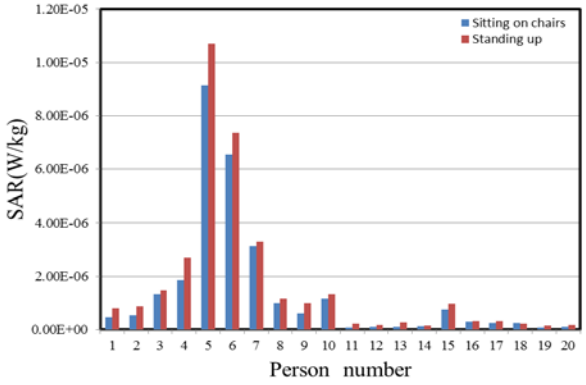

Fig. 16. Localized SARs induced in 20 people standing up and sitting on metallic chairs at 860 MHz.

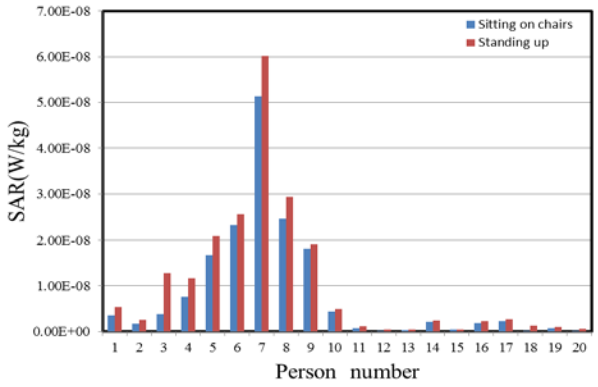

Fig. 17. Localized SARs induced in 20 people standing up and sitting on metallic chairs at 1990 MHz.

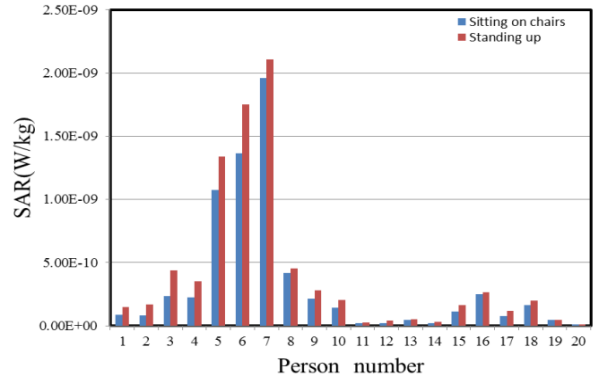

Fig. 18. Localized SARs induced in 20 people standing up and sitting on metallic chairs at 2600 MHz.

V. CONCLUSIONS

In this paper, the FDTD method was first proposed to calculate electric field distributions inside an empty office for a LTE femotcell placed at the left-hand-side of the office at frequencies of 700, 860, 1990, and 2600 MHz. The measurements of electric field distributions inside the empty office were carried out by a Narda Model NBM-3006 high frequency selective radiation meter. The validity of simulation results of electric field distributions is further checked by measurement data. After validating the accuracy of the FDTD method, the FDTD method was used to calculate electric field distributions on a horizontal plane with a height of 1 m above the floor of the office with and without the presence of 20 people and furniture for the LTE femtocell placed near the center of a horizontal plane with a distance of 1.0 m from the ceiling and transmitting a power of 10 dBm. It is found that furniture and people's existence affects distribution of the electric field strengths inside the office. The electric field strengths in the vicinity of 20 wooden desks have 5-10 dBV/m drops due to the impact of shadowing effect of 20 people and furniture. EM field distribution and variability are an important issue in the design of indoor wireless networks. Simulated electric fields at most of all locations on the horizontal plane with a height of 1.0 m above the floor for the office with and without the presence of 20 people and furniture are found in the range of -10 to -30 dBV/m which means a good signal will be picked up in the office. According to ANSI/IEEE standards for public exposure in uncontrolled environments, the maximum power density of 1.326×10^{-4} W/m^2 emitted from the LTE femtocell is far below the ANSI/IEEE safety standard of 4.6-17.3 W/m^2 for public exposure at frequencies of 700-2600 MHz. Localized SARs induced in the 20 people due to radiation from the LTE femtocell were also evaluated. It is found that the maximum localized SAR of 1.04×10^{-5} W/kg is induced in the person numbered 5 when standing up at 860 MHz. The minimum localized SAR of 7.67×10^{-12} W/kg is induced in the person numbered 12 when sitting on a metallic chair at 2660 MHz. It is found that standing people tend to have a higher SAR value than sitting people. This is because a standing person is much closer to the LTE femtocell than a sitting person. It is also found that the maximum localized SAR of 1.04×10^{-5} W/kg induced in a standing person is far below the ANSI/IEEE safety standard of 1.64 W/kg for public exposure in uncontrolled environments. Knowledge of electric field distributions and RF exposures is useful for indoor wireless network planning. The FDTD method provides a time efficient and cost effective solution for calculating electric fields emitted from LTE femtocells inside an office environment without measurements and for checking the EM absorption for public exposure to LTE femtocells.

ACKNOWLEDGMENT

The authors would like to thank Professor Heng-Tung Hsu of the Department of Communications Engineering, Yuan Ze University for providing the LTE femtocell for this study.

REFERENCES

[1] *LTE-Advanced: The 3rd Generation Partnership Projected*, 2011 [Online]. Available: http://www.3gpp.org/LTE-Advanced

[2] S. Sesia, I. Toufik, and M. Baker, *LTE-The UMTS Long Term Evolution-From Theory to Practice*, 2nd ed. including Release 10 for LTE-Advanced, New York: John Wiley & Sons, 2011.

[3] F. Khan, *LTE for 4G Mobile Broadband-Air Interface Technologies and Performance*, Cambridge University Press, New York, 2009.

[4] G. M. Whitman, K.-S. Kim, and E. Niver, "A theoretical model for radio signal attenuation inside buildings," *IEEE Trans. Veh. Technol.*, vol. 44, no. 3, pp. 621-629, 1995.

[5] R. P. Torres, L. Valle, M. Domingo, and M. C. Diez, "CINDOOR: An engineering tool for planning and design of wireless systems in enclosed spaces," *IEEE Antennas Propagat. Mag*., vol. 41, no. 4, pp. 11-22, 1999.

[6] Z. Ji, B. H. Li, H. X. Wang, H. Y. Chen, and T. K. Sarkar, "Efficient ray-tracing methods for propagation prediction for indoor wireless communications," *IEEE Antennas Propagat. Mag.*, vol. 43, no. 2, pp. 41-49, 2001.

[7] A. Aragon-Zavala, B. Belloul, V. Nikolopoulos, and S. R. Saunders, "Accuracy evaluation analysis for indoor measurement-based radio-wave-propagation predictions," *IEE Proc.-Microw. Antennas Propag.*, vol. 153, no. 1, Feb. 2006.

[8] X. Ling and K. L. Yeung, "Joint access point placement and channel assignment for 802.11 wireless LANs," *IEEE Trans. Wireless Commun.*, vol. 5, no. 10, pp. 2705-2711, Oct. 2006.

[9] D. Plets, W. Joseph, K. Vanhecke, E. Tanghe, and L. Martens, "Simple indoor path loss prediction algorithm and validation in living lab setting," *Wireless Pers. Commun.*, vol. 68, pp. 535-552, 2013.

[10] V. Degli-Esposti, G. Falciasecca, F. Fuschini, and E. M. Vitucci, "A meaningful indoor path-loss formula," *IEEE Antennas Wireless Propag. Lett*., vol. 12, pp. 872- 875, 2013.

[11] M. Ayadi and A. Ben Zineb, "Body shadowing and furniture effects for accuracy improvement of indoor wave propagation model," *IEEE Trans. Wireless Commun*., vol. 13, no. 11, pp. 5999-6006, Nov. 2014.

[12] NCRP, "Biological effects and exposure criteria for radiofrequency electromagnetic fields," NCRP Rep. 86, 1986.

[13] *IEEE Standard for Safety Levels with Respect to Human Exposure to Radio Frequency Electromagnetic Fields, 3 kHz to 300 GHz*, IEEE Standard C95.1, 2005.

[14] ICNIRP, "Guidelines for limiting exposure to time-varying electric, magnetic and electromagnetic fields," *Health Phys.*, vol. 74, no. 4, pp. 494-522, Apr. 1998.

[15] P. Frei, E. Mohler, G. Neubauer, G. Theis, A. Burgi, J. Frohlich, C. Braun-Fahrlander, J. Bolte, M. Egger, and M. Roösli, "Temporal and spatial variability of personal exposure to radiofrequency electromagnetic fields," *Environ. Res.*, vol. 109, pp. 779-785, 2009.

[16] H. Y. Chen and C. Y. Chuang, "Currents induced in human bodies during RF exposure near a cellular phone base station," *Electromagn*., vol. 29, no. 1, pp. 13-23, Jan. 2009.

[17] W. Joseph, P. Frei, M. Ro¨osli, G. Vermeeren, J. Bolte, G. Thur´oczy, P. Gajsek, T. Trcek, E. Mohler, P. Juhasz, V. Finta, and L. Martens, "Between-country comparison of whole-body SAR from personal exposure data in urban areas," *Bioelectromagn.*, vol. 33, no. 8, pp. 682-694, Dec. 2012.

[18] J. Cooper, B. Marx, J. Buhl, and V. Hombach, "Determination of safety distance limits for a human near a cellular base station antenna, adopting the IEEE standard or ICNIRP guidelines," *Bioelectromagn.*, vol. 23, no. 6, pp. 429-443, 2002.

[19] T. Alanko, M. Hietanen, and P. von Nandelstadh, "Occupational exposure to RF fields from base station antennas on rooftops," *Ann. Telecommun.*, vol. 63, pp. 125-132, 2008.

[20] D. Plets, W. Joseph, K. Vanhecke, and L. Martens, "Exposure optimization in indoor wireless networks by heuristic network planning," *Progress Electromagn. Res.*, vol. 139, pp. 445-478, 2013.

[21] G. Koutitas and T. Samaras, "Exposure minimization in indoor wireless networks," *IEEE Antennas Wireless Propag. Lett.*, vol. 9, pp. 199-202, 2010.

[22] A. Bamba, W. Joseph, J. B. Andersen, E. Tanghe, G. Vermeeren, D. Plets, J. O. Nielsen, and L. Martens, "Experimental assessment of specific absorption rate using room electromagnetics," *IEEE Trans. Electromagn. Compat*., vol. 54, no. 4, pp. 747-757, Aug. 2012.

[23] A. Boursianis, P. Vanias, and T. Samaras, "Measurements for assessing the exposure from 3G femtocells," *Radiation Protection Dosimetry*, vol. 150, no. 2, pp. 158-167, 2012.

[24] A. Bamba, W. Joseph, A. Boursianis, T. Samaras, G. Vermeeren, A. Thielens, and L. Martens, "Fast assessment of RF power absorption in indoor environments by room electromagnetics theory," *Radiation Protection Dosimetry*, first published online Nov. 14, 2015.

[25] K. S. Yee, "Numerical solution of initial boundary value problems involving Maxwell's equations in isotropic media," *IEEE Trans. Antennas Propag*., vol. AP-14, no. 5, pp. 302-307, 1966.

[26] Narda Safety Test Solutions, 435 Moreland Road, Hauppauge, NY 11788, 2015.

[27] G. Mur, "Absorbing boundary conditions for the finite-difference approximation of the time-domain electromagnetic field equation," *IEEE Trans. Electromagn. Compat.*, *EMC-23*, pp. 377-382, 1981.

[28] Z. P. Liao, H. L. Wong, B. P. Yang, and Y. F. Yuan, "A transmitting boundary for transient wave analysis," *Scientia Sinica (Series A)*, vol. 27, no. 10, pp. 1063-1076, Oct. 1984.

[29] J. P. Berenger, "A perfectly matched layer for the absorption of electromagnetic waves," *J. Comp. Phys.*, vol. 114, pp. 185-200, Oct. 1994

[30] A. von Hippel, *Dielectric Materials and Applications*, The MIT Press, Cambridge, Mass., 1954.

[31] C. F. Yang, C. J. Ko, and B. C. Wu, "A free space approach for extracting the equivalent dielectric constants of the walls in buildings," *IEEE AP-S. Int. Symp. Dig.*, Baltimore, MD, vol. 2, pp. 1036-1039, July 21-26, 1996.

[32] D. J. Cichon, T. Zwick, and J. Lahteenmaki, "Ray optical indoor modeling in multi-floored buildings: simulations and measurements," In *AP-S. Digest, Antennas and Propagation Society Int. Symp.*, Newport Beach, CA, vol. 1, pp. 522-525, July 21-26, 1995.

[33] A. C. M. Austin, M. J. Neve, and G. B. Rowe, "Modeling propagation in multifloor building using the FDTD method," *IEEE Trans. Antennas Propag.*, vol. 59, no. 11, pp. 4239-4246, Nov. 2011.

[34] M. Thiel and K. Sarabandi, "3D-wave propagation analysis of indoor wireless channels utilizing hybrid methods," *IEEE Trans. Antennas Propag.*, vol. 57, no. 5, pp. 1539-1546, Nov. 2019.

[35] D. Pena, R. Feick, H. D. Hristov, and W. Grote, "Measurement and modeling of propagation losses in brick and concrete walls for 900-MHz band," *IEEE Trans. Antennas Propag.*, vol. 51, no. 1, pp. 31-39, Jan. 2003.

[36] S. K. Patil, M. Y. Koledintseva, R. W. Schwartz, and W. Huebner, "Prediction of effective permittivity of diphasic dielectrics using an equivalent capacitance model," *J. Appl. Phys.*, vol. 104, pp. 074108-1-074108-11, 2008.

[37] LessEMF.com, *Radio Frequency & Microwave Meters*, 2014 [Online]. Available: http://www. lessemf. com/rf.html

[38] A. Christ, A. Klingenbock, T. Samaras, C. Goiceanu, and N. Kuster, "The dependence of electromagnetic far-field absorption on body tissue composition in the frequency range from 300 MHz to 6 GHz," *IEEE Trans. Microw. Theory Tech.*, vol. 54, no. 5, pp. 2188-2195, May 2006.

[39] J. A. Elder and D. F. Cahill, "Biological Effects of Radiofrequency Radiation," U.S. Environmental Protection Agency, EPA Rep. no. EPA-600/8-83-026F, Research Triangle Park, NC. 1984.

Hsing-Yi Chen was born in Taiwan, in 1954. He received the B.S. and M.S. degrees in Electrical Engineering in 1978 and 1981 from Chung Yuan Christian University and National Tsing Hua University, respectively. He received the Ph.D. degree in Electrical Engineering from University of Utah, Salt Lake City, Utah in 1989. He joined the faculty of the Department of Electrical Engineering, Yuan Ze University, Taiwan, in September 1989. He was the Chairman of Electrical Engineering from 1996 to 2002, the Chairman of Communications Engineering from 2001 to 2002, the Dean of Engineering College from 2002 to 2006, the Dean of Electrical and Communication Engineering College from 2006 to 2012, and the Dean of Research and Development Office from 2012 to 2013. Currently, he is the Dean of General Affairs Office, Yuan Ze University. His current interests include electrostatic discharge, electromagnetic scattering and absorption, waveguide design, radar systems, electromagnetic compatibility and interference, bioelectromagnetics, electromagnetic radiation hazard protection, and applications of frequency selective surface.

He is a member of Phi Tau Phi. He was also a member of the editorial board of the *Journal of Occupational Safety and Health* from 1996 to 1997. He was elected an Outstanding Alumnus of the Tainan Second High School in 1995. He has been the recipient of numerous awards including the 1990 Distinguished Research, Service, and Teaching Award presented by the Yuan Ze University, the 1999 and 2002 YZU Outstanding Research Award, and the 2005 Y. Z. Hsu Outstanding Professor Award for Science, Technology & Humanity Category. He was awarded Chair Professor by Far Eastern Y. Z. Hsu Science and Technology Memorial Foundation in 2008. His name is listed in Who's Who in the World in 1998.

Shu-Huan Wen was born in Taiwan, in 1991. He received the B.S. degree in Electronic Engineering from Oriental Institute of Technology in 2013. He is currently working toward the M.S. degree in Communications Engineering at Yuan Ze University, Taiwan. His research interests include patch antenna design, frequency selective surfaces, EM field measurement, and computational electromagnetics.

Light-Weight Wide-Band Metal-Only Reflectarray Antennas

Babak Honarbakhsh

Department of Electrical Engineering
Shahid Beheshti University, Tehran, IRAN
b_honarbakhsh@sbu.ac.ir

Abstract ─ A new class of metal-only reflectarray antennas (RAs) is reported. The proposed RA is based on a unit-cell constructed from a short-circuited conducting square. This, compared to the previously reported metal-only designs, leads to less weight and fabrication complexity. In addition, bandwidth enhancement can be accomplished by extending the idea to multi-layer unit cells. Gain stability with less than 0.1 dB variation over 1 GHz bandwidth at 12 GHz center frequency is achieved using the proposed two-layer reflector.

Index Terms ─ Antenna, ethernet, light-weight, metal-only, reflectarray, wideband, WiMAX.

I. INTRODUCTION

One of the advantages of microstrip reflectarray antennas (MRAs) over parabolic reflectors are their less manufacturing complexity, especially at high microwave frequencies [1]. Nevertheless, MRAs are not regarded as low-cost antennas, due to expensive low loss microstrip substrates. As well, MRAs are not reliable solutions at extra high temperatures, which is likely in near-sun space applications. In such situations, the dielectric substrate may become nonlinear and the thin metallization made by the printed circuit board (PCB) technology may become melted or deformed. Furthermore, the substrate blocks a fraction of electromagnetic (EM) energy due to surface wave excitation which deteriorates the overall gain. Thus, if it becomes possible to design MRAs without substrate, the application range of such antennas can be further extended. The idea of a metal-only RA is not new. The first RA was metal-only, constructed from an array of short-circuited (sc) rectangular waveguides as the reflector [2]. Another metal-only solution is suggested in [3], which is made from rectangular grooves in a metallic plate. Both of these designs are neither low-cost, nor light-weight, particularly below 10 GHz, due to large amount of metal and high fabrication complexity. Besides, it is unclear how their bandwidth can be broadened.

In the present work, a metal-only RA is proposed. This RA is based on a unit-cell constructed from an sc conducting square. This, compared to the previously reported cases, leads to less weight and fabrication complexity. In addition, bandwidth enhancement can be accomplished by extending the idea to multi-layer unit cells. Possible applications of such RAs are high-power applications, e.g., base stations, high-temperature applications, e.g., near-sun orbiting satellites, and terrestrial fixed-point wireless bridges, e.g., WiMAX and ethernet links. The proposed antennas can also be used for armature radio, since in less than 10 GHz, they can be constructed by elementary tools and materials. It is worth mentioning that the incident power must be kept sufficiently small to avoid electric discharge.

Applicability of the suggested method is verified using method of moments (MoM). Simulation results are carried out using FEKO® suite software.

II. THE IDEA

The idea supporting the proposed method stems from the fact that when a conducting patch, suspended over an infinite ground, is excited by a plane wave, the induced electric current density over its surface is mostly concentrated on the edges and the amount of EM energy at the patch center is negligible. Therefore, short-circuiting a patch from its center to the ground plane underneath may not significantly affect its radiation characteristics. This idea is validated in two steps.

First, the current density distribution over half-wavelength suspended and sc square patches over an infinite ground plane is computed. The results are reported in Fig. 1, for different shorting pin thicknesses and illumination angles. The gap between the patch and the ground is assumed to be $0.3\lambda_0$. The patch lies on the xy plane with the z axis perpendicular to it. The patch is excited by plane wave at normal and oblique incidence with, respectively, $\theta = 0°$ and 40°. As usual, θ is the elevation angle in spherical coordinate. In addition, the wave and electric field vectors lie in the xz plane in both cases. The radii of sc pins are taken to be $r = 0.005\lambda_0$ and $0.05\lambda_0$, respectively, as thin and thick cases. We note in Fig. 1 that, the current distributions on suspended and sc patches are effectively the same.

Submitted On: January 10, 2016
Accepted On: March 18, 2016

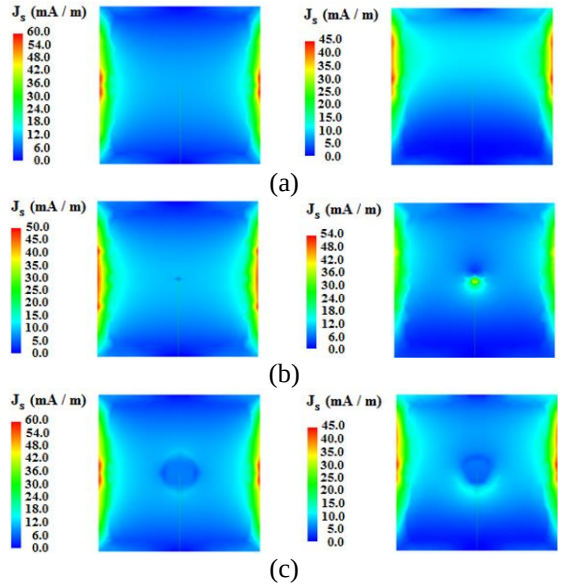

Fig. 1. Current density over $\lambda_0/2$ square patch at normal (left column) and oblique (right column) incidence: (a) suspended, (b) sc by thin pin, and (c) sc by thick pin.

At the second step, the magnitude and phase of the scattered near-field (NF) of the aforementioned patches are computed over a semi-circle of radius $10\lambda_0$ laying on the $\varphi = 0°$ plane and reported in Figs. 2 and 3. From these figures it is evident that the scattered fields are essentially the same at $\theta = 0°$, regardless of the pin thickness. While, for the case of thick shorting pins, discrepancy is undeniable as the observation angle increases.

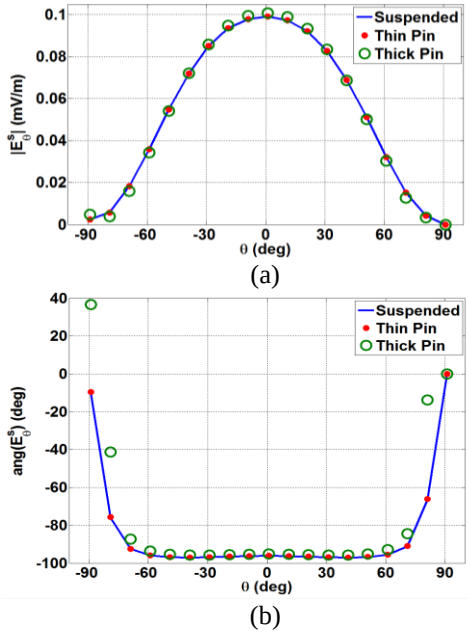

Fig. 2. Scattered NF of $\lambda_0/2$ square patch excited at normal incidence: (a) magnitude and (b) angle.

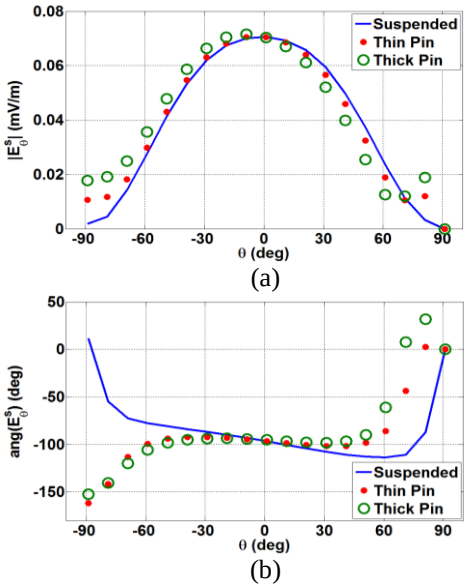

Fig. 3. Scattered NF of $\lambda_0/2$ square patch excited at oblique incidence: (a) magnitude and (b) angle.

III. PROPOSED UNIT CELLS

In this section, delay characteristics of single-, two- and three-layer unit-cells, designed by the proposed method, are reported. The geometries of the cells are selected based on [4-6]. The center frequency and the cell periodicity are 12 GHz and 14 mm, respectively. The inter-layer spacing is 3 mm. For the two-layer cell, the side-length ratio of the first to second layer is 0.7. For the three-layer cell, the side-length ratios of the first to the third and the second to the third layers are 0.7 and 0.9, respectively. The side views of two- and three-layer cells are depicted in Fig. 4, wherein the suspended case is included for clarity. It should be noted that all the reported results during the paper are restricted to sc cases. Two short-circuiting pin thicknesses are studied with radii $r = 0.5$ and 1.25 mm, which are equal to $0.02\lambda_0$ and $0.05\lambda_0$, respectively, where λ_0 is the working wavelength. All unit-cells are excited at $\theta = 0°$ and 40°, at 11.5 GHz, 12 GHz and 12.5 GHz. Computed phase-shifts are reported in Figs. 5 and 6. As can be seen from Fig. 5, the delay characteristics at different frequencies are effectively in parallel for the single-layer cell with thin sc pin. Similar results were observed for multi-layer cases with thin pins which are not included for brevity. Yet, the parallel phase range decreases for cells with thick sc pins at oblique incidence. Nevertheless, by considering Fig. 6, this reduction can be compensate by increasing the number of layers. These observations can be explained noting that at normal incidence, the pin is properly shielded by the patch. On the contrary, when the cell is excited obliquely, the pin is illuminated and thus its contribution to the scattered field becomes significant. Logically, the role of shorting pins is more

evident as they become thicker at oblique incidence. However, as noted before, the destructive effect of the pins can be compensated by increasing the number of layers.

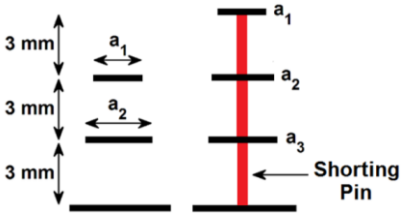

Fig. 4. Side view of multi-layer unit-cells: (a) suspended two-layer: $a_1 = 0.7a_2$, and (b) short-circuited three-layer: $a_1 = 0.7a_3$, $a_2 = 0.9a_3$.

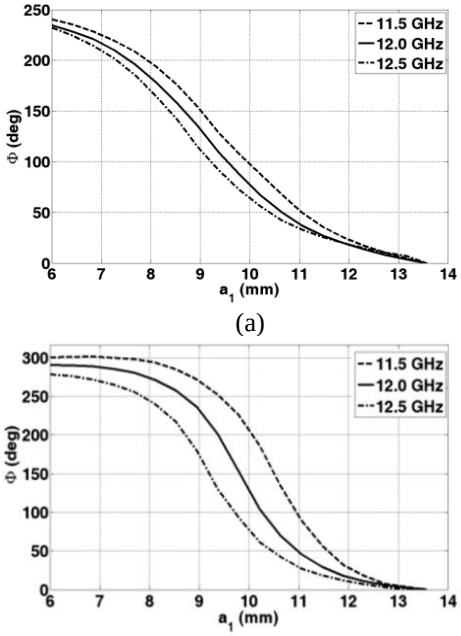

Fig. 5. Delay characteristic of the proposed single-layer unit-cell with thin sc pin at: (a) normal and (b) oblique incidence.

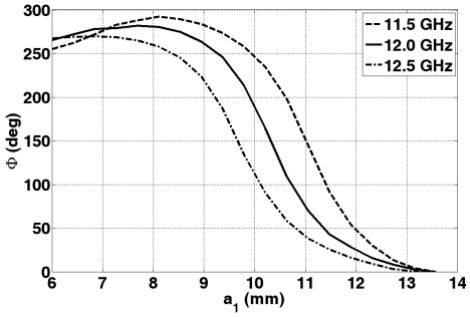

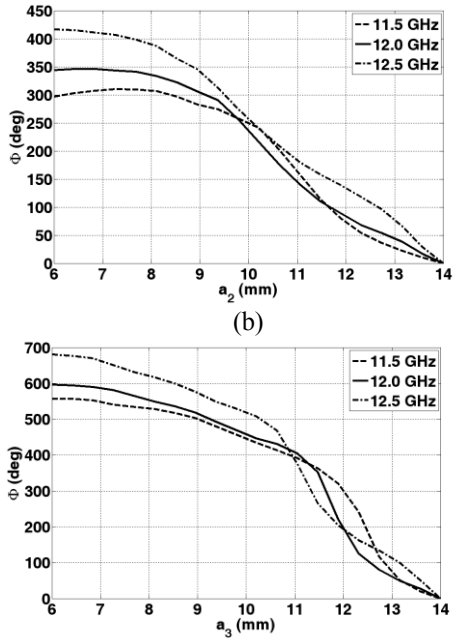

Fig. 6. Delay characteristic of the proposed unit-cells with thick sc pins at oblique incidence: (a) single-layer, (b) two-layer, and (c) three-layer.

IV. PERFORMANCE ESTIMATION

In this section, performance of the RAs designed based on the proposed method is estimated in the sense of overall gain using MoM. For efficient analysis, the multi-level fast multi-pole method (MLFMM) is exploited. Additionally, the reflector ground plane is assumed to be of infinite extent. The analysis frequency and radius of shorting pins is set to 12 GHz and 0.5 mm, respectively. The inter-element spacing of the RA elements is 14 mm. By designating the focal length and the reflector diameter with, respectively, *F* and *D*, the *F*/*D* ratio is computed following [7]. Specifically, the feed pattern is fitted by $\cos^n \theta$ function and then the optimum focal length is estimated based on the classical expression reported in [8]. The study is carried out for two configurations. The feed antennas in both cases are small-size and metal-only. This further reduces the computational complexity and makes it possible to analyze the whole structure, i.e., feed plus reflector.

In the first case, a large square-shaped RA with 30×30 single-layer elements is illuminated by a probe-fed square patch antenna with 13 mm side length and air substrate. For decreasing the blockage, the patch is placed over a finite square ground plane with 37.4 mm side length. This corresponds to $F = 48$ cm which is the distance of the feed from the center of the patch. Both center- and offset-fed arrangements are considered, where the offset angle is assumed to be 40° with respect to reflector normal direction. The corresponding gain

patterns are reported in Fig. 7, which verifies the applicability of the proposed single-layer cells for high-gain applications.

The second case is a small square-shaped RA with 10×10 elements, illuminated by a short metallic horn antenna in center-fed arrangement. The optimum position of the feed is computed to be 15 cm from the reflector center. The radiation pattern of this feed is depicted in Fig. 8 which shows its gain stability over 1 GHz bandwidth about the center frequency. The simulated gain patterns for RA with single- and two-layer elements are reported in Fig. 9. As can be clearly seen, perfect gain stability is achieved using the proposed two-layer elements. Additionally, increasing the number of layers has decreased the side-lobe level (SLL). Thus, the suggested multi-layer unit-cells are responsive for wideband applications.

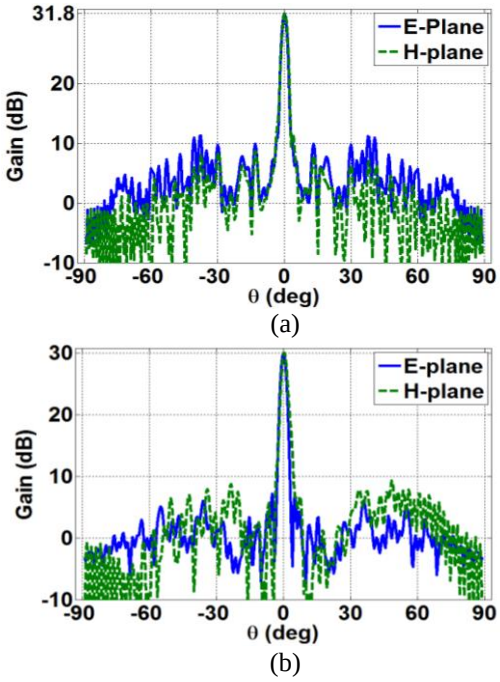

Fig. 7. Gain pattern of the 900 element RAs: (a) center-fed and (b) offset-fed.

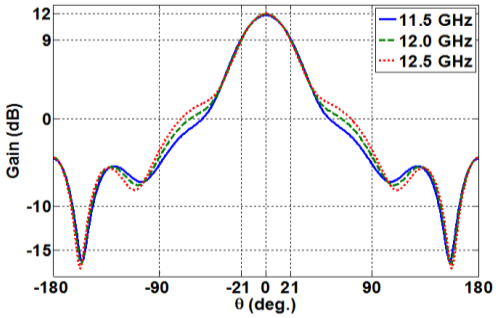

Fig. 8. Gain pattern of feed horn.

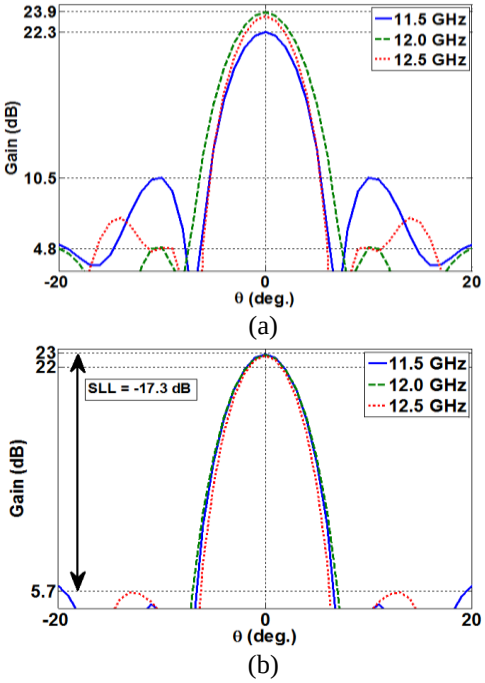

Fig. 9. Gain pattern of the 100 element RAs with: (a) single-layer and (b) two-layer elements.

V. CONCLUSION

Light-weight metal-only reflectarray antennas can be constructed based on short-circuited conducting patches. It is shown that delay characteristics of square patches are essentially unchanged when they are short-circuited from center using thin shorting pins. As the pin radius increases, discrepancy between delay characteristics of the suspended and the short-circuited patches become undeniable as the observation angle increases, although responses remains essentially the same at normal direction. These elements are shown to be a candidate for metal-only unit cells in designing light-weight metal-only reflectarray antennas. It is demonstrated that bandwidth of such reflectarrays can be broadened by extending the idea to multi-layer unit cells. It is observed that the sensitivity of the delay response to the thickness of shorting pins decreases as the number of layers increases.

REFERENCES

[1] J. Huang and A. Encinar, *Reflectarray Antennas*, New York: IEEE/John Wiley, 2008.

[2] D. G. Berry, R. G. Malech, and W. A. Kennedy, "The reflectarray antenna," *IEEE Trans. Antennas Propag.*, vol. 11, no. 6, pp. 645-651, Nov. 1963.

[3] Y. H. Cho, W. J. Byun, and M. S. Song, "High gain metal-only reflectarray antenna composed of multiple rectangular grooves," *IEEE Trans. Antennas Propag.*, vol. 59, no. 12, pp. 4559-4568, Dec. 2011.

[4] J. A. Encinar, "Printed circuit technology multilayer planar reflector and method for the design thereof," *European Patent EP 1120856*, June 1999.
[5] J. A. Encinar, "Design of two-layer printed reflectarrays using patches of variable size," *IEEE Trans. Antennas Propagat.*, vol. 49, no. 10, pp. 1403-14010, Oct. 2001.
[6] J. A. Encinar and J. A. Zornoza, "Broadband design of three-layer printed reflectarrays," *IEEE Trans. Antennas Propagat*., vol. 51, no. 7, pp. 1662-1664, July 2003.
[7] B. Honarbakhsh, "FR4-only microstrip reflectarray antennas," *ACES J*., accepted.
[8] J. Huang, "Analysis of a microstrip reflectarray antenna for microspacecraft applications," *JPL TDA Progress Report No. 42-120*, Feb. 15, 1995.

Babak Honarbakhsh born in Tehran, Iran, in 1981. He received his B.S., M.S. and Ph.D. degrees in Electrical Engineering, all from Amirkabir University of Technology (Tehran Polytechnic), in 2004, 2007 and 2012. He is currently an Assistant Professor in the Department of Electrical Engineering at Shahid Beheshti University. His research interest is CEM.